Microstructural Characterization and Analysis of Laser-Powder Bed Fusion GRCop-84 by Metallurgical and Neutron Scattering Methods

A Dissertation Presented for the
Doctor of Philosophy
Degree
The University of Tennessee, Knoxville

Robert Paul Minneci
May 2021

DEDICATION

I dedicate this to the love of my life and wife, Tommie Jean. She is my light in my darkest times, my biggest cheerleader, and my everything. I only wish I had found her sooner because the time we have spent together has been the best part of my life. Thank you for your love and emotional support through what has also been the most challenging time in my life.

ACKNOWLEDGEMENTS

I would like to acknowledge:

My advisor, Dr. Claudia Rawn, for pushing me to enter the graduate program and supporting me throughout the process. You have been incredibly patient and supportive of me through thick and thin. I appreciate everything that you have done for me as I do not think I could have made it through this process with anyone else.

My best friend and best man, soon-to-be Dr. Aaron. We have been through practically our entire lives together, and I will forever cherish the time we spent together in our college careers. If you had not been there, I would not be here. I truly believe that. My greatest strength is my friends.

My parents, brothers, and sisters. Each one of you has had a fingerprint on the development of my life, and you are all irreplaceable and inescapable. Thank you for always being there for me when I have needed you.

My new family for supporting both my newly-wed wife and I. Thank you for teaching me new things and taking care of us.

Furthermore, I acknowledge all my friends, my committee members, extended family, co-workers, and peers. There are too many of you to name, but know that you are appreciated.

ABSTRACT

GRCop-84 or Cu-8Cr-4Nb (atomic %) is a structural high-heat-flux Cu alloy that is dispersion strengthened by C15 Laves Cr_2Nb [Niobium Chromide] that has seen significant development with laser additive manufacturing (AM), specifically laser-powder bed fusion (L-PBF) in recent years. A review of the development, properties, and performance of GRCop alloys has been conducted and provides pertinent background. The body of research provides fundamental understanding regarding microstructure evolution and phase interaction of GRCop-84 through characterization by neutron and X-ray scattering and metallographic techniques. This research is intended to bridge fundamental research of L-PBF, Cu alloys, structural thermal conductors, and ex-situ and in-situ neutron diffraction techniques. Little is understood regarding the additive microstructure evolution and phase interaction in the Cu-Cr-Nb system. Understanding of melting and crystallization behavior are critical to laser-based processing and can be used to improve the final performance and properties. The microstructure and phases of GRCop-84 have been characterized with scanning electron microscopy (SEM), back-scattered diffraction (EBSD), and X-ray diffraction (XRD). Residual stress mapping with constant wavelength neutrons revealed unexpectedly high residual stress in the Cu matrix that should exceed the yield strength. The high loading of Cr_2Nb [Niobium Chromide] is theorized to provide significant balancing of stress to the Cu phase which allows for relatively easy processing and evidence to this persists in time of flight (TOF) diffraction results where both phases are visible.

TABLE OF CONTENTS

LIST OF TABLES

LIST OF FIGURES

INTRODUCTION

From memory foam to CAT scans, a variety of technological innovations have been made in the aerospace industry that have had a tremendous impact on the world. These innovations often pushed the limits of what was possible, surpassed those limits, and set ever-higher goals. A rocket is a perfect example of this. What began with achievable distances measured in meters can now be measured in kilometers, and as the limits progress, the measurement will be light-years. However, a major limiting factor in space flight and future development is cost. The answer to this issue in the early 1980s was the Space Shuttle which was a reusable launch vehicle built to support the construction of the International Space Station. The reusability was critical to reduce cost in the 135 total launches, but the reusability was limited and required significant refurbishing or replacement of components. The Space Shuttle Main Engines (SSME) in particular were a limiting factor to reusability due to one key engineering concept: structural components at high temperatures are susceptible to fatigue.

Glenn Research Copper or GRCop alloys were developed to improve the metallurgical limits by allowing for higher operating temperatures by having higher thermal stability. One GRCop alloy, GRCop-84 or Cu-8Cr-4Nb (at%), a publicly available, advanced copper alloy, that has shown potential for numerous high-heat-flux applications including rocket engine hardware, resistance welding electrodes and holders, permanent metal casting molds, vacuum plasma spray nozzles, fusion reactor first walls, or any high temperature heat exchanger. GRCop-84's creep, conductivity, low-cycle fatigue, tensile strength, and thermal expansion properties are among the best available of copper alloys at high temperatures. However, its high material, fabrication, and machining costs have limited its use in industry, and recent application of additive manufacturing (AM) has extended its utility and revitalized interest. NASA has developed internal build parameters for GRCop-84 for laser-powder bed fusion (L-PBF) and conducted practical hot-fire tests on full-scale hardware, but has limited available characterization work. AM's disadvantages often outweigh its benefits and is seldom used in practical industrial applications outside of prototypes, but GRCop-84 used in high-heat-flux applications is a case where AM outweighs traditional manufacturing in areas of cost, lead time, geometry control, and performance.

AM is a developing technology that creates unique microstructure-property relationships that still under investigation. Thorough characterization and metallurgical understanding is necessary to support future endeavors and ensure that AM components will be able to meet design specifications. GRCop-84 has demonstrated unusual L-PBF microstructures due largely to the high alloying fraction of Cr_2Nb which is also the source of the unusually high thermal stability. The focus of this dissertation seeks to assist future AM efforts by providing microstructure-processing and microstructure-property relationships. Several materials characterization techniques including scanning electron microscopy (SEM), electron back scattered diffraction (EBSD), ex-situ X-ray diffraction (XRD), in-situ high temperature X-ray diffraction (HTXRD), in-situ neutron time-of-flight (TOF) diffraction, and fixed-wavelength ex-situ neutron strain mapping have been utilized towards better understanding these relationships.

This body of research provides fundamental understanding regarding microstructure evolution and phase interaction of GRCop-84 through characterization by neutron and X-ray scattering and metallographic techniques. This research is intended to bridge fundamental research of SLM, Cu alloys, and structural thermal conductors. Little is understood regarding the additive microstructure evolution and phase interaction in the Cu-Cr-Nb system. Understanding of melting and crystallization behavior are critical to laser-based processing and can be used to improve the final performance and properties, and GRCop-84 has demonstrated unusual microstructures compared to typical SLM alloys. The gas-atomized powder used for SLM has a bimodal distribution of Cr_2Nb ranging from μm to nm scale with high loading fraction of 12 wt% which will provide a multitude of nucleation sites for the matrix grains, and high thermal conductivity of the alloy will provide extreme cooling gradients between the melt pool and surroundings. We hypothesize that these factors are the cause of non-equilibrium, heterogeneous grain structures and metastable precipitate phases observed in SEM, HTXRD, and EBSD results. Residual stress mapping with constant wavelength neutrons have revealed unexpectedly high residual stress in the Cu matrix that should exceed the yield strength. We hypothesize that the high loading of Cr_2Nb provides significant balancing of stress to the Cu phase which allows for relatively easy processing and evidence to this persists in time of flight (TOF) diffraction results where both phases are visible.

Improved understanding of the processing and phase interactions of SLM GRCop-84 directly benefits reusable rocket technology in the aerospace industry where the alloy is currently applied. Within the 700-900 K temperature range, there is a dramatic loss of mechanical strength that makes the majority of high-heat-flux Cu alloys unviable or non-reusable as the microstructure deteriorates from high temperature exposure, but the higher temperature range can provide significantly better fuel efficiency and safety factors. GRCop-84's practical use and development has been limited by the preferred use of single-use components, but its properties provide significantly longer fatigue and creep lifetimes that allow it to be useable within the 700-900 K range. This can result in a dramatic reduction of cost to the rocket and aerospace industry. Without SLM, GRCop-84's development would likely have stagnated due to its high material and machining costs. SLM and GRCop-84 allow for the production of highly customizable and reusable structural heat exchangers that can benefit a variety of industries. The advantages shown in this research are partly intended to improve awareness of the alloy and increase the quantity of interested researchers.

This is a multi-part dissertation with four main chapters and concludes with the primary intellectual merits and broader impact of the body of research:

Chapter 1: The first chapter is a comprehensive review of the historical development and available properties and performance of GRCop alloys. The goal of the review is to condense the available literature into a single source for future researchers. The initial development of GRCop-84 is covered in-depth since choices and observations were made that still impact its development today. The available properties, characteristics, and fabrication methods of GRCop-84 are reviewed with emphasis on creep and low-cycle fatigue.

Chapter 2: The second chapter provides microstructural characterization of as-built and HIPed L-PBF GRCop-84. The investigation covers formation of microstructural features,

phase evolution, and development during post processing. The objective of this chapter is to explore and evaluate the

Chapter 3: The third chapter is the result of in-situ neutron diffraction study that investigates the phase-specific mechanical response of as-built and HIPed L-PBF GRCop-84. The objective of this chapter is to define key structure-property relationships including lattice strain response, effect of dislocation density, and stress partitioning behavior.

Chapter 4: The fourth chapter is the result of an ex-situ neutron diffraction study that investigates the residual thermal strain distribution in as-built and HIPed L-PBF GRCop-84. The objective of this chapter is to correlate complementary neutron diffraction methods for residual stress calculations bridging in- and ex-situ techniques.

CHAPTER 1: COPPER-BASED ALLOYS FOR STRUCTURAL HIGH-HEAT-FLUX APPLICATIONS: A REVIEW OF DEVELOPMENT, PROPERTIES, AND PERFORMANCE OF CU-RICH CU-CR-NB ALLOYS

A version of this chapter was originally published by Robert P. Minneci, Eric A. Lass, Jeffrey R. Bunn, Hahn Choo, and Claudia J. Rawn:
Robert P. Minneci, *et al*. "Copper-based alloys for structural high-heat-flux applications: a review of development, properties, and performance of Cu-rich Cu-Cr-Nb alloys." *International Materials Reviews* (2020). https://doi.org/10.1080/09506608.2020.1821485

This work is co-authored by Robert P. Minneci[1], Eric A. Lass[1] Jeffrey R. Bunn[2], Hahn Choo[1], and Claudia J. Rawn[1].

[1]Department of Materials Science and Engineering, University of Tennessee, Knoxville, Tennessee 37996-2100, U.S.A. [2]Neutron Scattering Division, Oak Ridge National Laboratory, Oak Ridge, Tennessee 37831-6475

The article has only minor formatting changes. RPM wrote the initial manuscript draft, and all authors contributed to, revised, and approved of the final manuscript. CJR and JRB contributed to early editing and direction. EAL and HC contributed thorough editing and review of the structure-property correlations throughout the article.

Abstract

This review examines the development and current state of Cu-rich Cu-Cr-Nb alloys commonly referred to as GRCop or Glenn Research copper alloys with emphasis on Cu-8Cr-4Nb (at%), or GRCop-84, and Cu-4Cr-2Nb, or GRCop-42. GRCop alloys were originally developed as candidates for the Space Shuttle Main Engines' (SSME) combustion chamber liner which is a demanding high-heat-flux application with flux in excess of 100 MW m^{-2} and service temperatures ranging from 673 – 973 K. GRCop alloys are strengthened by Cr_2Nb, an intermetallic C15 Laves phase, which is highly stable and resistant to coarsening at high temperatures and provides characteristics of precipitation and dispersion strengthening. The SSME liner serves as context for discussing the relevant technological importance, unique challenges, extreme conditions, re-usability requirements, and failure modes typical of similar high-heat-flux applications. Relevant Cu metallurgy background is provided to highlight the challenge of balancing mechanical strengthening while maintaining thermal conductivity. Recent additive manufacturing efforts have increased interest in GRCop alloys, and full-scale hardware has been fabricated using AM techniques and practical hot-fire tests have been conducted, but structure-property relationships are still under development. The development, processing, and current microstructure-property relationships of GRCop alloys are reviewed along with comparisons to similar high-heat-flux Cu alloys including NARloy-Z, GlidCop Al-15, AMZIRC, Cu-1Cr-0.1Zr, and Cu-0.9Cr. The review concludes with an assessment of future prospects for GRCop alloys and overview of advantages provided by additive manufacturing.

Introduction

Excessive heat flux from or onto surfaces has been a major limiting factor in the development of various technologies such as turbines, rockets, or electronics [1]. The term

‘high-heat-flux applications’ is used to describe these and similar uses where the heat flux is subjectively high and difficult to manage and has been ascribed to a multitude of applications from welding equipment to fusion reactor components [1-4]. Defining a range for high-heat-flux is difficult since its perception has evolved with time and differs between different fields and industries. Most engineering disciplines consider >1 MW m^{-2} as high-heat-flux [5]. In the realm of microprocessor cooling for example, Ebadian et al. classify 1-10 MW m^{-2} as high-heat-flux and denote 10-100 MW m^{-2} as ‘ultra-high-heat-flux’ and >100 MW m^{-2} as ‘extreme-heat-flux’ [5]. However, these terms are rarely used outside of the microprocessor field, so the term high-heat-flux will primarily be used broadly here to encompass everything above 1 MW m^{-2}. For reference, a typical burning room during a house fire releases heat flux on the range of 0.001 – 0.01 MW m^{-2}, while the maximum allowed heat flux in a fission reactor is roughly 1 MW m^{-2} in the fuel cladding which is 1% of the heat flux at the surface of the sun [6, 7]. One method of mitigating excessive heat flux is to use a high thermal conductivity material to rapidly transfer heat by active or passive cooling. Copper is a standard for heat transfer media due to its relative cost, formability, and conductivity, and numerous alloys with a variety of elements have been used to fulfill various roles in industry. One of these alloys is Cu-8Cr-4Nb (at%) or GRCop-84 (Glenn Research Copper alloy 84) which was formulated for NASA’s Space Shuttle Main Engine (SSME) for a component with heat flux on the order of 100 MW m^{-2} but was not put into service due to large time and monetary investments in its predecessor, NARloy-Z. The term ‘GRCop-84’ will be used to specifically denote Cu-8Cr-4Nb and GRCop will classify similarly Cu-rich Cu-Cr-Nb alloys like GRCop-42, although the focus will be on GRCop-84 which has more available literature. GRCop-84’s creep, conductivity, low cycle fatigue, tensile strength, and thermal expansion properties are among the best available at high temperatures up to approximately 973 K [2]. GRCop-84 has shown potential for numerous high-heat-flux applications including resistance welding electrodes and holders, permanent metal casting molds, vacuum plasma spray nozzles, fusion reactor first walls, or any high temperature heat exchanger in the past, but recent advances in additive manufacturing (also known as 3D printing) and metallurgy have extended its utility [2, 8, 9]. While this has renewed interest in GRCop-84, the majority of the development of the alloy remains in technical documents and older papers that are overshadowed by more recent publications. GRCop-84 has become an intrinsic component to NASA’s additive manufacturing based Low-Cost Upper Stage Propulsion (LCUSP) project and Rapid Analysis and Manufacturing Propulsion Technology (RAMPT) and full-scale, quality tested hardware has been developed [10-12]. The objective of this review is to provide the context of GRCop-84 from the perspective of the Space Shuttle development and relevant properties and scientific theory to help facilitate its continued development and application.

Background

Following the historic moon landing in 1969 during the Apollo project, the largest arguable obstacle to further human operated space exploration and development was its high cost. Concepts from as early as the 1950s advocated the use of reusable launch vehicles for reducing cost but were not technologically viable [13]. The majority of the

necessary developments in technology were made during the Apollo project and led to the eventual approval of the Space Shuttle program in 1972 [13]. The primary goal of the Space Shuttle was to provide a consistent and reliable mode of transportation for the parts and crew to the International Space Station with high payload and safety requirements. The final design of the Space Shuttle consisted of the Orbiter Vehicle which held the crew and cargo, expendable tanks of liquid hydrogen and oxygen, and a pair of recoverable solid rocket boosters. Entry into orbit could be achieved by combining the thrust from the solid rocket boosters and Orbiter Vehicle's engines, but NASA engineers found that existing engines would not be sufficient to meet the weight and safety requirements [13]. As a result, a development contract was awarded to Rocketdyne in 1971 to develop a new engine that would eventually become the RS-25 engine or Space Shuttle Main Engine (SSME), which is shown in its relative position to the Space Shuttle in Fig. 1.1 [13, 14].

A key component of the SSME was a new high-performance combustion chamber design that raised the throat heat flux of previous designs from 32 MW m^{-2} (20 Btu in^{-2} s^{-1}) to 114 – 164 MW m^{-2} (100 Btu in^{-2} s^{-1}), which could accommodate the increased payload requirements [15, 16]. The SSME's combustion chamber contains the combustion reaction of propellants and generates thrust through supersonic expansion in the throat that is passed out the nozzle; these essential components are shown in Fig. 2.1 [17]. The combustion chamber was predicted to have operating conditions of 3600 K and ~20 MPa, though these predicted values vary between sources, and required regenerative cooling and a high thermal conductivity structural liner to dissipate heat and resist thermal strain [15, 17]. The temperature environment of the nozzle is significantly lower, so a lower cost, from a fabrication and raw material perspective, steel alloy or superalloy can be used instead. The pressure generated by the combustion reaction is mostly negated by mechanical support provided by an external jacket of IN718, but the rigid reinforcement does not aid in reducing the high thermal strains [16, 17].

Regenerative cooling was achieved by flowing liquid H_2 through rectangular cooling channels machined into the liner that also functioned as the path to the fuel injectors, see Fig. 2.1. These channels were machined by milling into the edges of the liner in a rectangular configuration parallel to the length with a subsequently added shell to enclose the channels with a close-out by electro-forming, or a similar process[18, 19]. Due to the complicated geometry of the liner, this was likely the most reliable method to add cooling channels at the time despite high machining costs and limited tolerances. Forming a combustion chamber in a single piece with built-in cooling channels without the need for machining would likely improve cooling rates, overall reliability, and cost efficiency but was effectively impossible at the time. Higher machining tolerances or built-in channels would allow for overall improvements to the design geometry such as the aspect ratio, number, and position of the channels [18].

Future computer analysis and fabrication methods would eventually be found and used to optimize the channels to some extent [18]. Under the high active-cooling gradient between the heat of combustion and liquid hydrogen, respectively, a typical rocket engine liner will have an operating temperature, often referred to as a 'hot-wall' temperature, ranging from 673 to 973 K depending on cooling efficiency from thickness and

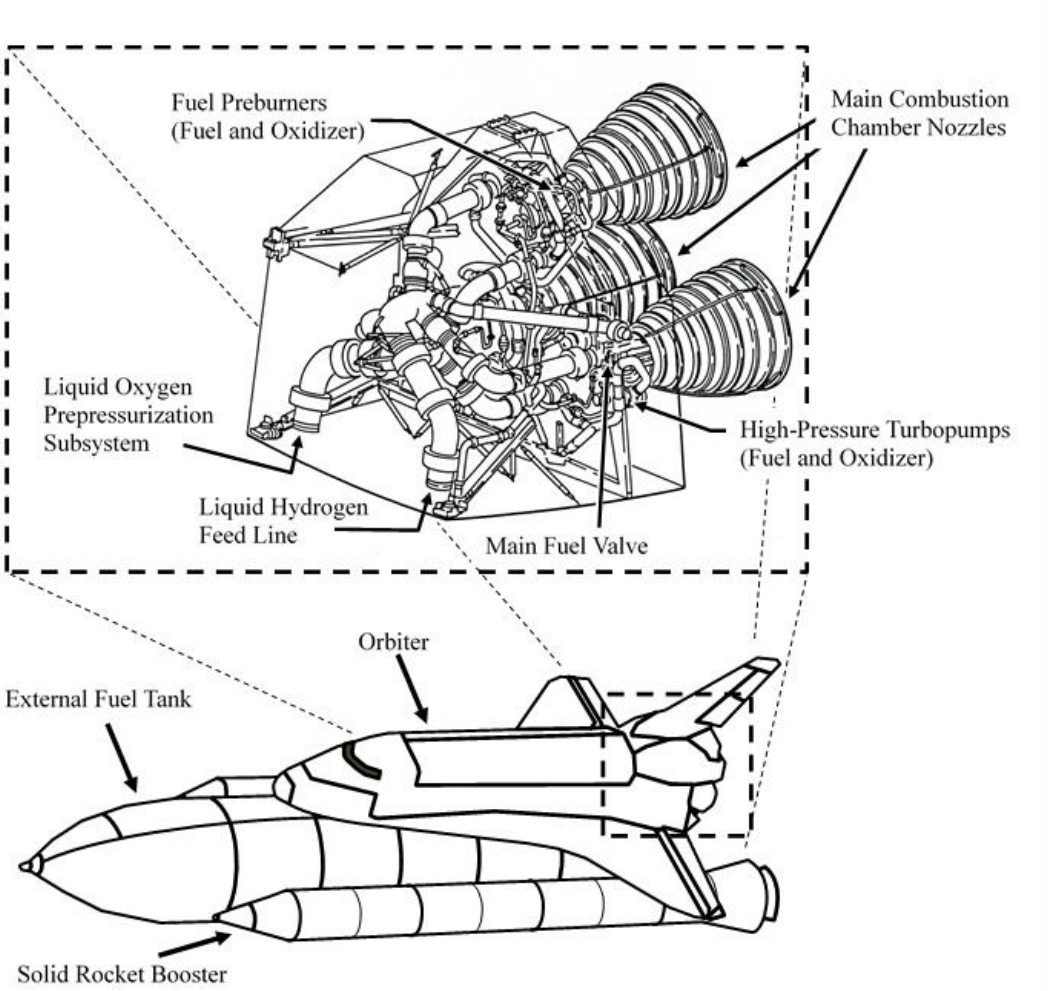

Figure 1.1. General Space Shuttle outline and inset of diagram of the RS-25 SSME adapted from [20].

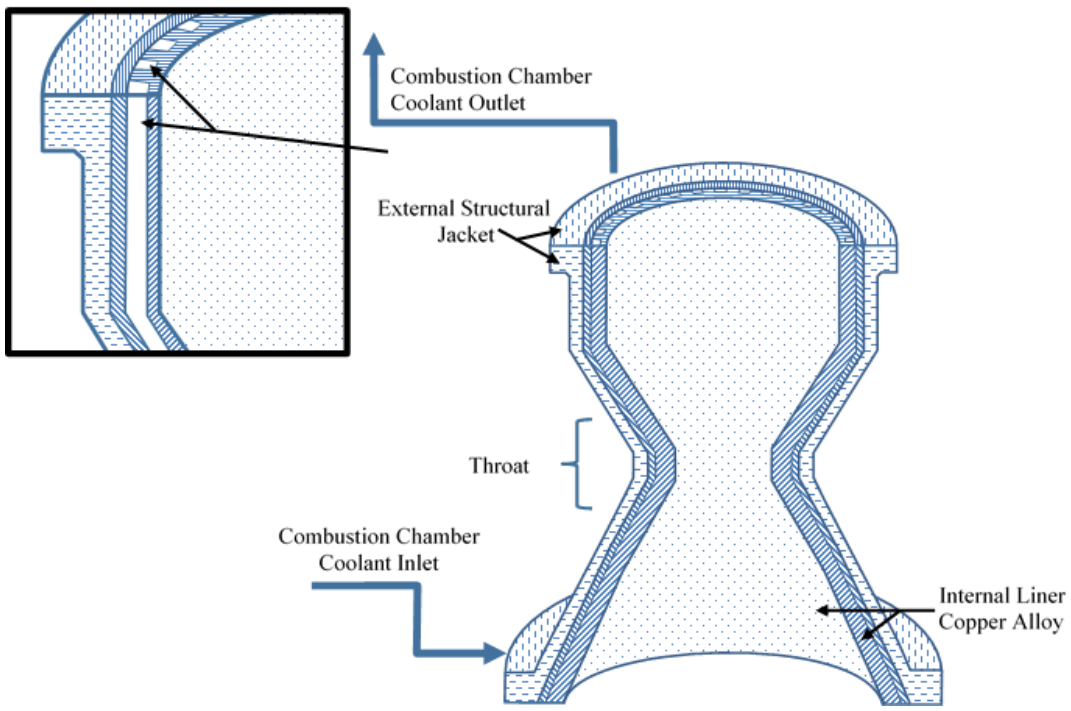

Figure 2.1. Sketch of essential components of SSME combustion chamber and nozzle without injector demonstrating path of cooling chambers built parallel to height of the nozzle; not to scale.

conductivity of the channel walls [2]. This hot-wall temperature range could be endured by a variety of materials, but NASA had another critical requirement that would prove to be the most difficult to meet: the SSME needed to be reusable with limited repair and re-conditioning to reduce cost. Even if a material could initially meet initial property requirements set by NASA, performance considerations of creep, low-cycle fatigue (LCF), and other time dependent mechanisms dramatically increased the design challenge.

A new alloy was needed to fulfill these conditions and Rocketdyne developed a copper alloy based on their previous work with NARloy-A, a cast Cu-3.5Ag (wt%) alloy, by adding Zr to a ratio of Cu-3Ag-0.5 Zr (wt%) and vacuum melting and vacuum centrifugally casting [16]. Copper was the base material due to its ability to function as a structural material along with its balance of cost, thermal conductivity, and mechanical strength. Cu-3Ag-0.5 Zr was trademarked NARloy-Z and formed into combustion chamber liners by a combination of hot spun forging and machining by Rocketdyne [16]. After the original production, the equipment was dismantled, and NASA had to reproduce a chemically equivalent version of the alloy with conventional melting, casting, and forging methods, designated as NASA-Z, when new liners were needed [16]. Other groups have had similar success including Krishna et al. who reproduced a similar Cu-Ag-Zr alloy with a combination of vacuum induction melting, hot forging, and rolling [21]. AMZIRC, a Cu-Zr alloy, was the primary competitor at the time for fatigue resistance, but NARloy-Z demonstrated longer and more uniform cycle lifetimes under realistic thrust chamber conditions [16]. Despite being the best available alloy, NARloy-Z was not able to fully meet reusability specifications and reusability life requirements were reduced from 100 missions in 1973 to 55 in 1980 [17, 22].

Regardless of its limitations, NARloy-Z was used in each space shuttle engine until the last launch in 2011 with roughly 40 years of development and investment focused on ensuring the reliability of the NARloy-Z engines. Replacing a critical component like the liner requires thorough testing and evaluation over many years, even though relatively small improvements from a new alloy could be economically worthwhile by improving load capacity or safety margins [23]. Although NARloy-Z remained in service, it was limited by its maximum operating temperature and reusability, leaving an opportunity for the development of a more optimized replacement. NASA and independent researchers were investigating new alloys capable of meeting the original standards of the SSME. Their goal was to develop a reusable copper alloy that would be thermally and mechanically stable during operation as a combustion chamber liner with primary criteria of mechanical strengthening, thermal conductivity, thermal expansion, creep, fatigue, and environmental resistance. Relevant theory and background for these criteria will be discussed to highlight the challenge and differences in performance between alloys in high-heat-flux applications.

Structure Property Correlations of High-Heat-Flux Copper Alloys

High-heat-flux Cu Alloying

Copper's mechanical strength can readily be improved through combinations of alloying, work hardening, and heat treatments, but the viable choices are considerably reduced at high temperatures. Most metals, including copper, become mechanically unstable and exhibit decreased mechanical properties at elevated temperatures. An alloy chosen for high temperature applications requires strong resistance to microstructural evolution in addition to mechanical strengthening. Solid solution strengthening (SSS), precipitation hardening (PH), dispersion hardening (DH), mechanical alloying, and oxide dispersion strengthening (ODS) are all commonly used to introduce a variety of secondary phases in copper, although their efficacy at high temperatures can vary. State-of-the-art copper alloys are compared in terms of composition and strengthening mechanisms in Tables 1.1 and 2.1. Solid solution strengthened alloys are the result of soluble elemental additions in either substitutional or interstitial atomic positions within the solvent metal. For high substitutional solubility, the two elements should have the same crystal structure and similar atomic radii, while interstitial solubility requires the atomic radii of the solute atom be sufficiently smaller than the base element (<15 %). In both cases, the elements' valences and electronegativities should be similar to help with bonding. Comparing the alloying elements of NARloy-Z and GRCop-84 to Cu provided in Table 3.1., only Ag has the same crystal structure (FCC) as Cu, and has significant solid solution solubility in Cu; although it's slightly larger atomic radius limits its solubility in Cu to about 4.9 at%. Cr is similar in size to Ag, but has a different crystal structure (BCC), and therefore has limited solubility in Cu. Nb and Zr have both different atomic radii and different crystal structures, and have limited solubility in Cu. However, both elements do form intermetallic phases with Cu that could be used as precipitation or dispersion strengthening particles.

Precipitation hardening, also called age hardening, is the result of a secondary heat treatment after initial fabrication where second phase particles form, or precipitate, within the primary matrix phase. Precipitation hardened alloys require a matrix-phase solubility that decreases with decreasing temperature [24, 25]. Quenching from an elevated temperature, followed by aging, causes supersaturation of solute and secondary-phase precipitation, respectively. The amount of secondary-phase precipitation is proportional to the concentration of solute in supersaturation and the solubility at the aging temperature [25]. Precipitation occurs because of the materials tendency to reduce free energy, and most often the precipitates nucleate at defects, such as dislocations or grain boundaries, as spherical particles (low surface area to volume, minimizing interfacial energy) [24-26].

The Ag in NARloy-Z contributes both SSS in the matrix and PH by forming various reported intermetallic phases with Cu and Zr [21, 27]. The Zr, in addition to contributing to Ag's intermetallic phases, can add SSS or form Cu_4Zr or Cu_5Zr precipitates or oxides depending on the processing methods [27, 28]. Singh et al. asserted that Zr in solid solution should contribute considerably to observations of higher

Table 1.1. Primary composition of Cu alloys by wt% [at%]; additional intentional or impurity elements may be present depending on the quality of the raw materials and processing, and exact values of elements can vary; united numbering system (UNS) identifier provided when available; adapted partially from [29]; rounded to first decimal when calculated.

Alloy	*UNS*	*Ag*	*Al*	*Cr*	*Cu*	*Nb*	*O*	*Zr*
NARloy-Z		3.0 [1.79]	-	-	96.5 [97.86]	-	-	0.5 [0.35]
AMZIRC	C15000	-	-	-	99.85 [99.9]	-	-	0.15 [0.10]
GlidCop AL-15	C15715	-	0.15 [0.08]	-	99.68 [99.8]	-	0.17 [0.12]	-
GRCop-84[*]		-	-	6.2-6.8 [7.6-8.3]	88.4-87.2 [87.3-88.69]	5.4-6 [3.7-4.1]	-	-
GRCop-42[*]		-	-	3.1-3.4 [3.8-4.2]	94.2-93.6 [94.4-93.8]	2.7-3 [1.8-2.1]	-	-
CuCrZr-IG[+]		-	-	0.6-0.9 [0.73-1.10]	Balance	-	-	0.07-0.15 [0.05-0.10]

[*] GRCop-84 and GRCop-42 based on powder chemistry from [30]

[+] CuCrZr-IG represents ITER grade Cu-Cr-Zr, adapted from [29]

Table 2.1. Comparison of high temperature Cu alloys' general composition, strengthening mechanisms, secondary phases, particle descriptions with key references; CW indicates cold work is optional but common.

Alloy Name	*Composition*	*Strengthening Mechanism(s)*	*Secondary Phase(s)*	*Particle Description*	*Ref.*
NARloy-Z	*Cu-Ag-Zr*	*PH, SSS, & CW*	*Ag, Cu_xZr**	Zr serve as oxygen traps at grain boundaries by forming oxides which prevents Cu oxide formation and promotes homogenous precipitation, while intermetallic Cu-Zr phases form that can pin grain boundaries and slow grain boundary growth; Ag's role is primarily strengthening: after aging, semi-coherent Ag nanocrystalline precipitates form that strengthen the matrix by pinning the Cu matrix grain boundaries and slowing grain boundary growth; above 866 K Ag precipitates coarsen in the matrix becoming incoherent and degrading material strength	[21, 31]
AMZIRC	*Cu-Zr*	*PH & CW*	*Cu_xZr**	Approximately 80% of strengthening from CW rather than particle strengthening; aging has limited effect; strength retained up to 773 K; Zr provides benefits similar to NARloy-Z, and intermetallics form as relatively large μm-sized precipitates	[29]
GlidCop	*Cu-Al_2O_3*	*DH*	*Al_2O_3*	Finely dispersed, nanometer oxide particles inside grains or at grain boundaries provide most of GlidCop's strengthening, though CW can be used to enhance mechanical performance; alumina prevents recrystallization and softening at elevated temperatures; noted as immune to coarsening	[32]
GRCop	*Cu-Cr-Nb*	*PH & DH*	*Cr, Cr_2Nb (C15)*	Slight excess of Cr suppresses detrimental Nb formation; can be CW but strengthening is not dependent on it; Cr_2Nb is resistant to coarsening at high temperatures, pins the Cu matrix grain boundaries, and slows grain boundary growth. Cr_2Nb forms bimodal distribution with μm and nano-scale particles that refine the matrix and provide strengthening respectively	[5, 33]
CuCrZr-IG	*Cu-Cr-Zr*	*PH*	*Cr, Cu_xZr**	Can be used in aged condition after CW to maximize mechanical properties; provides similar Zr benefits described in NARloy-Z; Cr believed to precipitate from the matrix and intermetallic Laves Cr_2Zr are possible but not observed; susceptible to over-aging and recrystallization at high temperatures; Cr also prevents grain growth following recrystallization	[32, 34-36]

* Indicates exact phase is inconclusive or dependent on processing conditions, typically specified as Cu_5Zr or Cu_4Zr

Table 3.1. Characteristics of select metals and maximum solid solubility in Cu from the indicated references.

Element	*Melting Temperature (K)*	*Approximate Maximum Solubility in Cu (wt% [at%])*	*Pure Thermal Conductivity 0-100 °C (W m^{-1} K^{-1}) [37]*	*Atomic Radii (Å)*	*Crystal Lattice*
Ag	1234	8.04 [4.9] [38]	425	1.65	FCC
Cr	2180	0.73 [0.89] [39]	91.3	1.66	BCC
Cu	1358	--	397	1.45	FCC
Nb	2750	1.31 [0.9] [40]	54.1	1.98	BCC
Zr	2128	0.17 [0.12] [41]	22.6	2.06	HCP

microstructural and thermal stability and non-equilibrium conditions introduced by rapid melting and solidification extending the solid solubility of Zr [28].

Dispersion hardening is distinguished from PH in that the second phase particles do not form via solid-state phase transformation in the matrix. Instead, DH particles can be directly added to a liquid metal (i.e. oxide or carbide particles), or can be formed in the melt prior to solidification. The other major difference between dispersion and precipitation strengthening is the particle/matrix interface. Precipitation hardening second phase particles typically have an orientation relationship with the matrix phase, are often fully or partially coherent (matching of the atomic lattice planes across the interface) [24]. Dispersoids typically have no lattice correspondence between matrix and particle [24].

DH can be difficult to distinguish from PH because their secondary phases have similar particles and strengthening mechanisms. Complicating matters, precipitate particles have been referred to as dispersions based on size or distribution in a matrix, but precipitates specifically refer to particles that come out of solution from additional heat treatments. DH alloys can be also be distinguished from PH by mechanical behaviors such as creep characteristics. However, it is rare to find an alloy with only one form of strengthening mechanism, so the dominant mechanism is often considered for classification. DH alloys are not limited by solubility like PH alloys and a variety of ceramic particles and intermetallic compounds can be readily introduced into a metal matrix by a variety of techniques, including mixing incoherent particles with an alloy melt, internal oxidation, precipitation by a chemical reaction, mechanical alloying, and rapid solidification [24].

The lattice correspondence between particle and matrix results in a greater increase in strength from PH compared to DH [24]. However, PH is limited to alloy systems with the appropriate phase equilibria conditions and are limited in maximum temperature capability by the solvus temperature of the precipitate phase at which the precipitate dissolves. PH alloys are further limited by diffusive coarsening of the precipitate particles at temperature well below the solvus temperature. These limitations leave DH as the only particle strengthening mechanism available for many alloy systems.

Specifics of Strengthening Mechanisms

Solute atoms generally provide SSS by impeding dislocation motion. More specifically, solute atoms locally distort the matrix lattice structure which provides a strain field around the solute atom. The solute strain field interacts with and impedes the strain field of dislocations by providing a frictional resistance force. The strength of the field is dependent on a variety of factors such as shear modulus, concentration, or relative size of the solute atom. SSS is limited by the solid solubility of the strengthening phases, and excess will form secondary phases. Typically, SSS alloys are made intentionally with excess solute to ensure that maximum solubility, and therefore strengthening, is reached [42].

Particles in alloys from DH or PH generally provide strengthening by hindering dislocation motion, similar to SSS, either by the dislocation shearing through the particle or by bypassing it (Orowan strengthening or bowing). There are six properties of

particles that affect shear including coherency strains, stacking-fault energy, ordered structure, modulus effect, interfacial energy and morphology, and lattice friction stress [24]. Most strengthening particles found in high-heat-flux Cu alloys are incoherent or much stronger than the Cu-matrix (i.e. resistant to particle shear), so Orowan strengthening is the primary precipitate/dispersoid strengthening mechanism [24].

Orowan strengthening relates to direct dislocation interactions with discrete particles in a matrix. The original derivation of Orowan strengthening has been adjusted to account for estimates of the dislocation line tension, mean free path, corrections of the interaction between dislocation segments on either side of a particle, type of dispersion, or particle type leading to many forms of the Orowan equation [24]. Most of these equations are semi-empirical and serve as estimates of strengthening for comparing similar alloys. As an example, the Orowan-Ashby equation for oxide dispersion strengthening is shown in Eq. 1.1.

$$\Delta\sigma = \frac{0.13Gb}{\lambda_{LD}} ln \frac{r}{b} \qquad (1.1.)$$

where $\Delta\sigma$ represents the increase in strength of the bulk alloy, G is the shear modulus of the matrix, b is the Burger's vector of the lattice, r is the average particle radius, and λ_{LD} is the linear mean free path of dislocations between the particles [24]. The mean free path can be described in many ways, but a simple expression is provided in Eq. 2.1.

$$\lambda_{LD} = \frac{4(1-f)r}{3f} \qquad (2.1.)$$

where f is the volume fraction of particles assumed to be spheres with radius r [24]. A high volume fraction of small particles should minimize the mean free path and provide the highest degree of Orowan strengthening due to the mean free path's inversely proportional relationship shown in Eq. 1.1.

The Orowan-Ashby equation for a random distribution of impenetrable particles goes by the form

$$\Delta\sigma = \frac{0.84 \text{ M Gb}}{2\pi(1-\upsilon)^{0.5}(\lambda_{PD} - 2r)} \ln \frac{r}{b} \qquad (3.1.)$$

which takes additional factors into account including the Poisson's ratio of the matrix, υ, and the Taylor factor, M, which is roughly 3 for face centered cubic (FCC) metals [43]. The linear mean free path term, λ_{LD}, changes to the mean planar particle spacing, λ_{PD} in Eq. 3.1., calculated by

$$\lambda_{PD} = r \left(\frac{2\pi}{3f}\right)^{0.5}. \qquad (4.1.)$$

This derivation of the Orowan-Ashby equation provides a better estimate of particle strengthening that the shear resistant particles in PH and DH will provide to the matrix. However, there are also a variety of other mechanisms that might be active depending on alloy composition.

The strengthening contribution from matrix grain size is described by the Hall-Petch mechanism, given in Eq. 5.1.

$$\sigma = \sigma_0 + k_y d^{-0.5} \quad (5.1.)$$

where d is a measured average grain size, k_y is a material constant for the ease of slip transfer and σ_0 is yield or friction stress of a single crystal, 0.16 MPa $m^{-1/2}$ and 26 MPa for pure copper, respectively [44]. Using these constants, the strength for Cu with an average grain size of 1 cm, 1 mm, 1 μm, and 100 nm is approximately 27.6, 31.1, 186, and 532 MPa, respectively. At 1 cm there is effectively no strengthening above σ_0 and considerable strengthening at 1 μm and 100 nm. Hall-Petch strengthening is possible because grain boundaries, like solute atoms and second phase particles, act as glide dislocation barriers. Smaller grains require that dislocations are positioned closer together, and the interaction of the stress fields associated with the dislocations themselves further impede their motion [43]. At equilibrium, the driving forces for coarsening are prevented or balanced by various pinning forces like Hall-Petch and Orowan strengthening, but as the temperature increases, the driving force for coarsening will eventually overcome the pinning forces. Additionally, small matrix grains are typically thermally unstable. For example, nano-crystalline copper has good Hall-Petch strengthening at room temperature, but its surface energy is high, and the grains are likely to grow, or coarsen, as the temperature is increased to reduce the surface energy and driving force for grain growth. Precipitates and dispersions can indirectly aid Hall-Petch strengthening by inhibiting grain boundary motion, preventing matrix grains from coarsening. However, the initial matrix grain size must be small, which can readily be achieved through rapid solidification techniques.

Rapid solidification broadly describes methods with cooling rates on the order of 10^2 to 10^{12} K s^{-1} that form unique microstructures with non-equilibrium phases and structures [9, 45]. Rapid solidification is often used to produce fine matrix grains and particles, but these have inherently high interfacial area, and consequently a large interfacial energy contribution to the total free energy and will readily grow unless they form in a stable configuration or are resistant to coarsening. Rapid solidification's high cooling rates typically prevents time-dependent particle or grain growth, so the microstructure is often more homogenous than other methods which can help prevent particle coarsening.

Particles of different radii have differences in free energy arising from capillarity effects, providing a driving force for particle coarsening, known as Ostwald ripening, which tends to decrease the free energy of the system by forming a more homogeneous distribution of larger particles [9, 46]. The free energy gradient between two particles, including grains, driving coarsening can be expressed as

$$\mu_p = 2\,\gamma_s\,V\left(\frac{1}{r_1} - \frac{1}{r_2}\right) = \frac{k_B\,T\,\Delta C_B}{C_B} \qquad (6.1.)$$

where μ_p represents the difference in chemical potential, V is the atomic volume, $r_1$and r_2 are the radii of two particles, k_B is Boltzmann's constant, γ_s is the surface energy of the precipitates, ΔC_B is the solute concentration gradient between the particles, and C_B is the average concentration of solute in the matrix [46]. While intended for comparing particles, this effect can largely be ignored because the inverse relationship of both $r_1$and r_2 has a larger impact on the chemical potential than their difference. Unless the distribution is unusually homogenous, the smaller the particles, the greater the tendency to grow. By Eq. 6.1., coarsening could be readily reduced by increasing the precipitate size, r, but this change would likely result in an undesirable decrease in the mechanical strengthening.

The Lifshitz-Slyozov-Wagner (LSW, formerly referred to as Lifshitz-Wagner) theory provides a better understanding of particle size development as the following derivation

$$r^3 - r_0^3 = \frac{D_B\gamma_s\,C_B\,V^2 t}{k_B\,T} \qquad (7.1.)$$

allows for the calculation of the average precipitate size where r is the average precipitate radius at the end of the growth stage, r_0 is the initial precipitate radius D_B is the diffusivity of the solute in the matrix, and t is time [9, 47]. The particular LSW derivation, given in Eq. 7.1., has the benefit of including diffusivity which can be used as a qualitative means of assessing the coarsening kinetics. Precipitates consisting of elements with low diffusivity will help decrease coarsening, and precipitate elements with larger atomic radii than the matrix atoms generally have slower diffusion.

Conductivity

Strengthening copper can be readily achieved by adding a secondary phase or solute, but if thermal conductivity is a critical design property, such as the case with the SSME combustion chamber liner or high-heat-flux applications, the alloy choice becomes significantly more complex. The principles of conductivity in metals will be discussed to help understand alloy choice and relationships between thermal and electrical conductivity.

Thermal energy is often attributed to atomic vibration in a given material, but a solid's vibration can further be defined by quantum mechanics as a wave carrying vibrational energy between the lattice or a phonon [48]. All crystalline materials conduct thermal energy through phonon interactions such as lattice or phonon thermal conductivity, κ_p, but phonon interactions contribute nearly all of non-metals thermal conductivity [49]. Phonons are dependent on the lattice, so the more defect-free the structure is, the higher the thermal conductivity. Researchers like Groza and Gibeling stress matrix purity as essential for high-heat-flux applications for this reason [50].

One of metals' unique qualities is the presence of free conduction electrons that readily transfer and serve as point charge entities for charge and heat which collectively contribute to electronic thermal conductivity, κ_{el}, in addition to phonon thermal conductivity, κ_p [49]. The Sommerfeld model treats the conduction electrons of metals as an electron gas (or sea) that obey the laws of quantum mechanics and can readily transfer better than phonons [51]. While non-metals may have some electronic contribution, it is significantly less than metals' electronic contribution which are overall better conductors [49]. Both phonon and electronic contributions are treated independently and contribute to the overall thermal conductivity, κ, by

$$\kappa = \kappa_{el} + \kappa_p. \quad (8.1.)$$

The electronic thermal conductivity is given by the following

$$\kappa_{el} = \frac{\pi^2\, n_e\, k_B^2\, T\, \lambda_{el}}{3\, m_e\, \bar{V}_F} \quad (9.1.)$$

where n_e is the number of free electrons per cm^3, T is temperature, λ_{el} is the mean free path between collisions, m_e is the mass of an electron, and $\bar{V}_F$ is the electron velocity at the Fermi surface as given in Eq. 10.1.

$$\bar{V}_F = \left[\frac{2\, \varepsilon_F}{m_e}\right]^{\frac{1}{2}} \quad (10.1.)$$

where ε_F is the Fermi energy [48].

Copper, silver, and gold each have a half-filled 4*s* conduction band that is highly mobile and permissible to electronic transfer. Since electrical conductivity is a direct measure of electron transport, this accounts for their high conduction. Thermal and electrical conductivity are intrinsically linked as both are measurements of the ease of transport of energy; thermal conductivity is under the influence of a thermal gradient, and electrical conductivity is under an applied electric field. Additionally, the Wiedemann-Franz-Lorenz law, shown in Eq. 11.1., provides a relation of electrical conductivity, σ, to thermal conductivity, κ, and temperature, T

$$\frac{\kappa}{\sigma\, T} = C_{WFL} = \frac{\pi^2\, k_B^2\, e^2}{3} \quad (11.1.)$$

where the remaining term is a constant known as the Lorenz number (or Wiedemann-Franz-Lorenz coefficient) C_{WFL} commonly approximated to 2.44 x 10^{-8} W Ω K^{-2} where e is the electron charge [52]. The Lorenz number is material specific and can vary between materials, but this law is well obeyed at room temperature and above for most pure metals and alloys [52]. This relationship can make determining thermal conductivity easier

since electrical resistivity, ρ, can be readily measured and converted to electrical conductivity by the inverse where $\sigma = \rho^{-1}$.

Eq. 9.1. predicts the electronic contribution to thermal conductivity will increase with temperature, if mean free path, λ_{el}, is ignored. Fig. 3.1. shows the relationship between thermal conductivity and temperature for several pure metals between room temperature and melting. Fe decreases initially but the trend increases at higher temperatures suggesting that the electronic contribution to thermal conductivity eventually overwhelms the phonon contribution at high temperatures [48]. However, most metals, including Cu, experience a constant decrease in thermal conductivity with increasing temperature. Most of the other terms in Eq. 9.1. are constants, λ_{el} would need to decrease to account for the loss of conductivity since they are directly proportional.

Prediction of phonon and electron interactions are limited, so the mean free paths of electrons, λ_{el}, and phonons, λ_p, provide a qualitative means of assessing the thermal conductivity of metals [48]. More scattering sites or interactions will result in decreased mean free path. Phonons are known to have three interaction processes: electron-lattice potential scattering known as Umklapp collisions, scattering by solute atoms and defects, and interactions between phonons and free electrons [48]. Electrons have three main interaction processes as well: scattering by solute atoms and defects, electron-electron interactions, and electron-phonon interactions [48]. At low and high temperatures, the lattice contribution to conductivity is low due to electron-phonon and Umklapp scattering, respectively [48]. In pure metals, the lattice contribution is largely ignored except at intermediate temperatures due to dominance of the electronic contribution [48]. This may seem counterintuitive for low temperatures since electron-phonon interactions are shared between lattice and electron contributions, but electrons more strongly suppress the phonon contribution than phonons affect the electron contribution. Scattering by defects, such as solute atoms or dislocations, has the opposite effect; electrons scatter more in the presence of defects, deceasing λ_{el} and their contribution to conductivity [49]. In alloys, the electronic contribution is still considered dominant; however, the lattice contribution becomes more prevalent over all temperatures. Conductivity interactions between alloyed elements is dependent on multiple factors, but usually, the higher the alloying content, the lower the conductivity since more defects are present. Part of what makes retaining both mechanical stability and thermal conductivity difficult is that both Orowan strengthening and conductivity are dependent on mean free paths of interaction. While Orowan is based on dislocations and conductivity is based on electron and phonon scattering, they are correlated. Orowan strengthening prefers a high-volume fraction of particles to decrease the path length that dislocations travel, and the presence of more particles provides more potential scattering centers decreasing conductivity. A compromise, depending on the design requirements, of conductivity and strengthening is necessary.

Thermal Expansion

Alloy choice for a high-heat-flux application like combustion chamber liners must also consider thermal expansion alongside mechanical strengthening and conductivity.

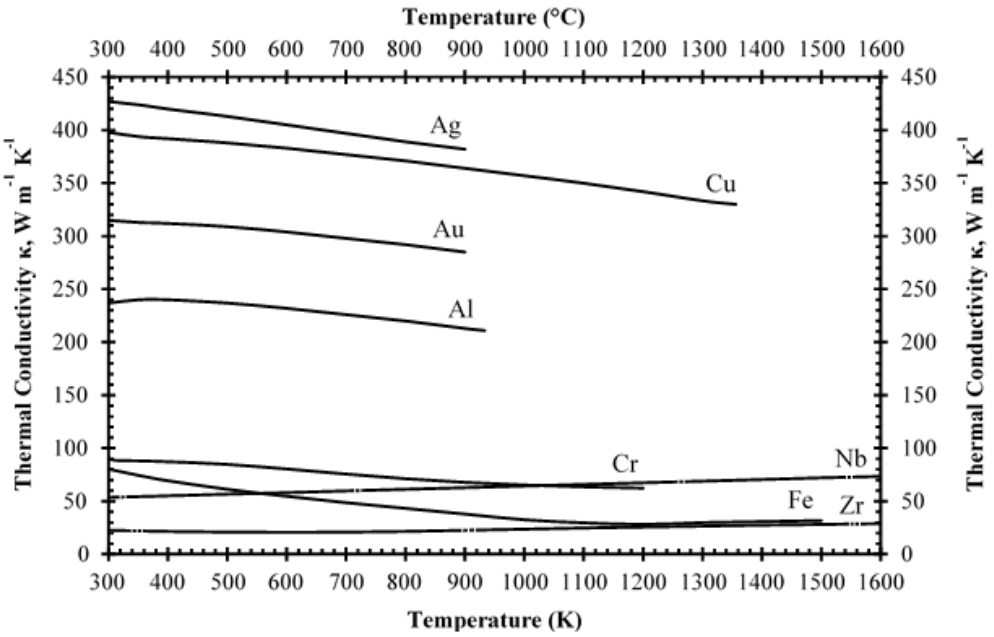

Figure 3.1. Thermal conductivities as a function of temperature of relevant high-heat-flux solid pure metals inspired by a similar plot from Poirier and Geiger [48] using data from Touloukian's TPRC Data Series [53] up to 1600 K with markings on Nb and Zr for clarity.

Thermal expansion in the combustion chamber liner contributes the majority of the stress and strain by the presence of high thermal gradients in the liner's wall rather than mechanical sources [2, 19]. The material's coefficient of thermal expansion and can be calculated volumetrically using Eq. 12.1. or linearly by exchanging the volumetric terms for length

$$\frac{\Delta V}{V_0} = \alpha_v \Delta T \qquad (12.1.)$$

where ΔV and V_0 represent the volume change and initial state, respectively, and α_v is the volume coefficient of thermal expansion. However, Eq. 12.1.'s coefficient of thermal expansion approximates thermal expansion to a linear relationship which will hold for most cases, but most materials' expansion does not hold to a linear relationship when at either excessively low or high temperatures, such as the hot-wall temperature of the combustion chamber liners which is 50 – 85% of the melting temperature of pure Cu.

Analysis of the thermal strain and distribution was conducted by Andrus and Bordeau [19] of Pratt & Whitney on NARloy-Z liners with nickel close-outs, demonstrated in Fig. 4.1., in 1989 which were used on the SSME revealed hot-wall temperatures ranging from 477 K in the nickel close-out to over 977 K in the liner [19]. The nickel close-out has lower thermal expansion and operating temperature which radially restrains the hotter NARloy-Z liner which demonstrated a tendency to expand radially outward [19]. During a single cycle of operation, the restraint of the nickel close-out generates compressive thermal loads in the hoop direction followed by relaxation during shutdown [19].

Rupture, Fatigue, and Creep

The combustion chamber liner's complex geometry and thermal loading during operation produces similarly complex stress and strain throughout the liner. As a result, predicting failure in the SSME was challenging and sources of failure were used to better understand alloy design and implementation. The main mechanical failure in the nozzle of rockets is rupture of the cooling channels from wall thinning and is referred to as the "dog house" effect due to the profile that the originally rectangular channels assume over time, shown in Fig. 4.1. [19, 54]. In Fig. 4.1., the web, also called the rib or land, separates the cooling channels, and the wall separates the channel from the hot side. The close-out chemistry varies depending on the fabrication methods, and the thickness of the wall depends on fabrication limitations. The wall separating the cooling channel and hot side of the liner was observed gradually deforming without material loss over operating cycles and eventually rupturing when sufficient biaxial ductility was lost [19]. Wall thinning is a complex failure mode that has been the subject of debate and has been attributed to different forms of fatigue and creep with dominant mechanisms dependent on geometry, alloy choice, and liner environment [19, 33, 54]. Better understanding each of these contributions to wall thinning led to better designs throughout the SSME's lifetime and into new rocket design.

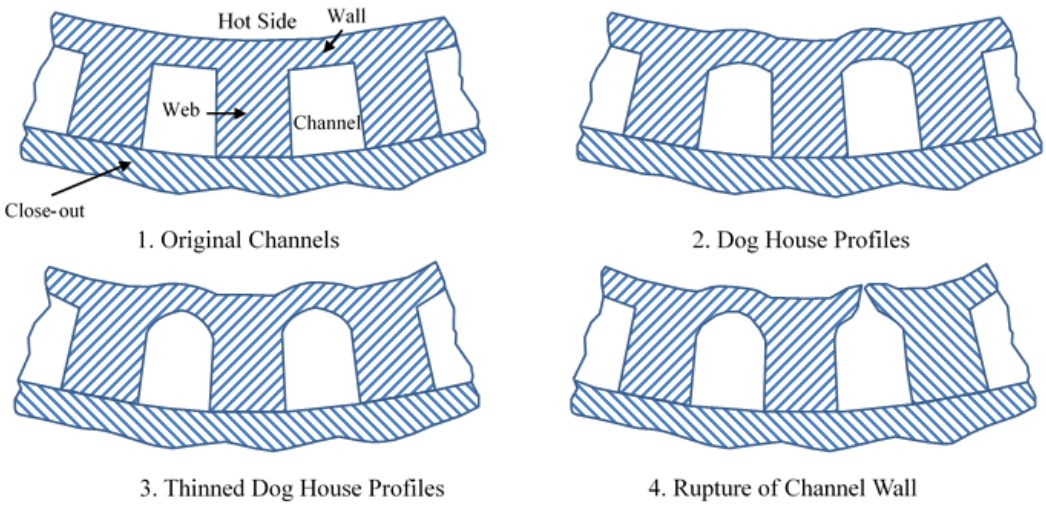

Figure 4.1. Channel thinning or dog house effect failure mode development of combustion chamber liners in order of progression and top view, not to scale; redrawn/modified from [19].

Fatigue is a failure mode that occurs when a material is subjected to repeated cycles of stress and accumulation of plastic strain. The number of cycles to failure or fatigue life is dependent on the magnitude of the applied stress. High-cycle fatigue involves low applied strain in the elastic regime that takes a long time to initiate failure, often above 10,000 cycles [24]. By contrast, low-cycle fatigue (LCF) is caused by relatively high plastic strain that initiates failure below 10,000 cycles [24]. If the source of strain is from thermal expansion and generates plastic strain, it is referred to as low-cycle thermal fatigue (LCTF) and is one of the dominant failure modes of high temperature structural components [55]. Under the original design constraints presented by Cook and Coffey, the SSME combustion chamber liner would require a fatigue life of at least 400 cycles at 700-900 K [17]. If the strain exceeds elastic limits, plastic strains accumulate in the liner during each cycle, producing LCTF [19].

Low-cycle fatigue from thermal cycling also presents concern of thermal mismatch strain, ε_{th}, between the reinforcing particles and matrix following the relationship

$$\varepsilon_{th} = \Delta\alpha \, \Delta T \qquad (13.1.)$$

where $\Delta\alpha$ is the difference between the coefficients of thermal expansion and ΔT represents the change in temperature [50]. While deformation may appear sufficiently elastic, thermal mismatch strain can account for intergranular plastic strain accumulation. Lowering $\Delta\alpha$ by particle selection, improves the likelihood of increased fatigue and creep resistance. However, copper's high thermal expansion coefficient, 17 x 10^{-6} C^{-1} at room temperature, relative to most strengthening particles, compared in Table 4.1., increases the selection challenge.

Creep is associated with progressive deformation as a function of time under applied stresses at constant temperature [24, 56, 57]. Creep can occur over a wide range of temperatures and stress levels and has multiple mechanisms responsible for progressive plastic deformation mostly based on diffusion and dislocation motion. Although the operating time of each cycle is short, creep can accumulate between cycles in a phenomenon called cyclic creep if the thermal strain is high enough [58]. Another creep term that is often attributed to failure in the combustion chamber liners is creep ratchetting which is accumulated plastic deformation specifically from unequal tensile and compressive loading and incomplete stress-strain loops in temperature cycling [59]. The rate of ratcheting and wall thinning strongly depend on the degree of heat flux and channel geometry [60].

During the Space Shuttle's operation, the cooling channel geometry and cooling efficiency were better optimized with improved machining, fabrication, and prediction technologies which significantly reduced the concern of the dog house effect [61]. Regardless of improvements, wall thinning from LCF and creep remain a concern for future designs and effort should be made to separate the effects of creep and LCF if the hot-wall temperature is high enough to facilitate creep.

Table 4.1. Characteristics of common particles used in strengthening Cu and Cr_2Nb, GRCop alloys' strengthening phase, with Cu for comparison.

Phase	*Heat of Formation (kJ mol^{-1})*	*Melting temperature (K)*	*Modulus of Elasticity (GPa)*	*Density (g cm^{-3})*	*Coefficient of Thermal Expansion 10^{-6} (K^{-1}) [at Temperature]*
Al_2O_3 [50]	-1667	2323	380	3.97	7.6 [773 K]
SiC [50]	-67	2700	207	3.18	4.3 [293 K]
Cr_2Nb *(C15)*	-21 [62]*	1858**	205 [63]	7.71	6.4* [293 K] [63]*
Cu	0	1358	110 [64]	8.96	17 [293 K]

*Average of reported values

** C15 Cr2Nb transforms to C14 above 1858 K and melts congruently at 2043 K based on the Cr-Nb phase diagram in Fig. 5.1(c)

Environmental Resistance

The thrust chamber environment has serious hydrogen embrittlement and blanching concerns due to high temperatures and the mix of liquid H_2 and O_2 fuels undergoing combustion that can cause failure in the liner if left unchecked. Other examples of detrimental environmental effects include orange peel roughening and cracking at inclusions but have been more easily detected, prevented, and understood [19].

Hydrogen embrittlement is largely dependent on the alloying elements in the Cu liner since Cu's crystal structure is FCC which is not susceptible to H embrittlement [65]. BCC and HCP metals are susceptible to H embrittlement, but only if they are present as separate phases. NARloy-Z has demonstrated adequate H embrittlement resistance despite its Ag (BCC) and Zr (HCP) content because Ag and Zr are either in solid solution or as an intermetallic compound, further described in Table 2.1. [66, 67].

Blanching is thought to be caused by oxidation-reduction cycles initiated by fluctuations, caused by hot spots in the geometry or the eventual degradation caused by constant combustion cycling during operation, in the oxygen-hydrogen fuel system. Blanching is represented by surface discoloration and corrosion of the liner wall and has been observed preceding channel wall failure in failed NARloy-Z chambers [19, 68, 69]. Inspection of blanched regions of NARloy-Z chambers revealed pits, cracks, fissures, and sponge-like appearance which damages the thin-walled coolant channels which roughen and decrease their cooling efficiency [65]. Unlike H embrittlement, blanching has been the primary cause of failure in NARloy-Z liners and rocket engines in general [69]. This may appear to contradict with wall thinning as the primary failure mode, but blanching has been observed proceeding wall thinning and is likely a strong contributor due to how it impacts the surface.

Various researchers have proposed and experimented with thermal barrier coatings (TBCs) to improve the thermal resistance and reduce blanching of the chamber liners, turbine blades, and other SSME hardware [61, 70-76]. TBC's are a thin coating of a low thermal conductivity material such as ZrO_2, ZrO_2-Y_2O_3, and NiCrAlY (used as a bond coating) that can reduce surface oxidation, improve corrosion resistance, and lower the temperature of the substrate on the hot side of a thermal gradient [73, 74]. TBCs could significantly lower thermal strain have been estimated to improve the life of a combustion chamber liner by a factor of 3 to 30 [60].While TBCs with NiCrAlY were applied to the turbine blades of the SSME, it doesn't appear that any were used on the NARloy-Z liner due to issues of coatings failing to retain adherence to the liner and spalling or flaking after repeated thermal cycles [70, 75]. During the coating of TBCs, the copper substrate (NARloy-Z) would oxidize and the coating would develop compressive residual stresses that formed a rough coating surface that performed poorly [70]. Various groups like Butler and Pindera have attempted functionally grading the TBC into combustion chamber liner alloys to improve cohesion, but the barrier's effectiveness decreases when the chemistry is altered [76].

Development of Cu-rich Cu-Cr-Nb Alloys

Relevant Phase Diagrams and Cr_2Nb

While NARloy-Z was used successfully on the SSME, researchers were looking for and developing alternatives with better long-term properties and overall reusability. Ellis and Michal of Case Western Reserve University formulated Cu alloys with additions of Cr and Nb in the 1980's as candidate SSME liner alloys in collaboration with NASA Lewis Research Center (LeRC and now NASA Glenn Research Center) [9]. At this time, limited to no Cu-Cr-Nb alloys had been developed or publicized [9]. During a phone interview in March 2020, Dr. David Ellis explained that the original idea for the project was conceived by then-Branch Chief Dr. Tom Glasgow of NASA LeRC who demonstrated that chill block melt spinning (CBMS) could be used to form desirable Cu-Cr-Nb alloys [77]. Glasgow then used a NASA graduate fellowship to bring Ellis and his graduate advisor, Dr. Gary Michal, onto the project and conduct more thorough alloying and characterization [77]. CBMS's high cooling rates were leveraged in an attempt to form a supersaturated solid solution with Cr and Nb. The supersaturated solution could then theoretically be precipitation hardened by the formation of a stable Cr_2Nb intermetallic that would provide similar strengthening methods compared to NARloy-Z's Ag and Zr. The intermetallic was expected to have a low solid solubility which would enhance conductivity of the matrix and provide a hard precipitate resistant to shear and coarsening effects [77]. The majority of Ellis and Michal's decisions and hypothesis on the new alloy were based on the best available alloys and limited available literature including the Cu-Cr, Cu-Nb, and Cr-Nb phase diagrams, shown in Fig. 5.1.

At the time to their knowledge, no ternary phase diagram was available, however, a Russian article by Nikolayev and Rozenberg presented ternary phase diagrams and a quasi-binary Cu-$NbCr_2$ phase diagram from 1972 which they were likely unaware of at the time [9, 78]. The existence of a binary Cu-Cr_2Nb phase diagram was important to Ellis and Michal because they inferred that an intermetallic Cu-Cr_2Nb phase might form from substitution of Cu for Cr, although no such intermetallic has been observed [9]. Michal later calculated a Cu-rich pseudo-binary phase diagram, but it would remain internal until it was presented by Anderson without additional context or details regarding its calculation [79]. It would not be until 2009 that Liu et al.'s [80] experimentally and thermodynamically calculated phase equilibria provided thorough ternary phase information on Cu-Cr-Nb and a binary Cu-Cr_2Nb phase diagram, presented in Fig. 6.1., covering the full range of Cu which agreed with Nikolayev and Rozenberg's work [78]. However, the binary phase diagram in Fig. 6.1 does show a solid solution gradient with temperature that will allow for precipitation strengthening. The maximum solid solubility of Cr_2Nb is less than 1 wt% at the solidus (or on final solidification), and it continues to decrease with temperature allowing for more precipitation that can be enhanced with supersaturation.

The Cr-Nb phase diagram, shown in Fig. 5.1.(c), shows that the intermetallic Cr_2Nb phase has two polymorphs. Since the intermetallic has an AB_2 stoichiometry, they both belong to what are commonly referred to as 'Laves' or 'Friauf-Laves' family of phases [81]. The older Cr-Nb phase diagram presented is likely outdated but was the newest available to Ellis

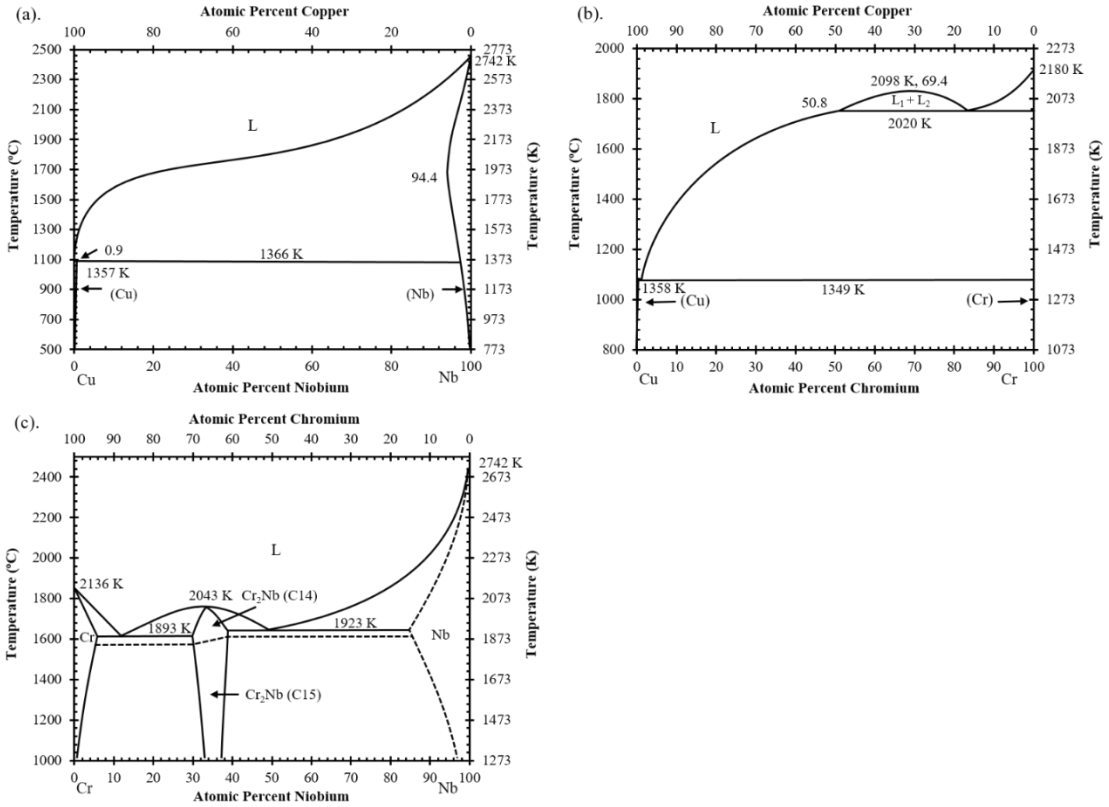

Figure 5.1. Phase diagrams for (a) Cu-Nb [82], (b) Cu-Cr [39] with updates from [83], and (c) Cr-Nb [84].

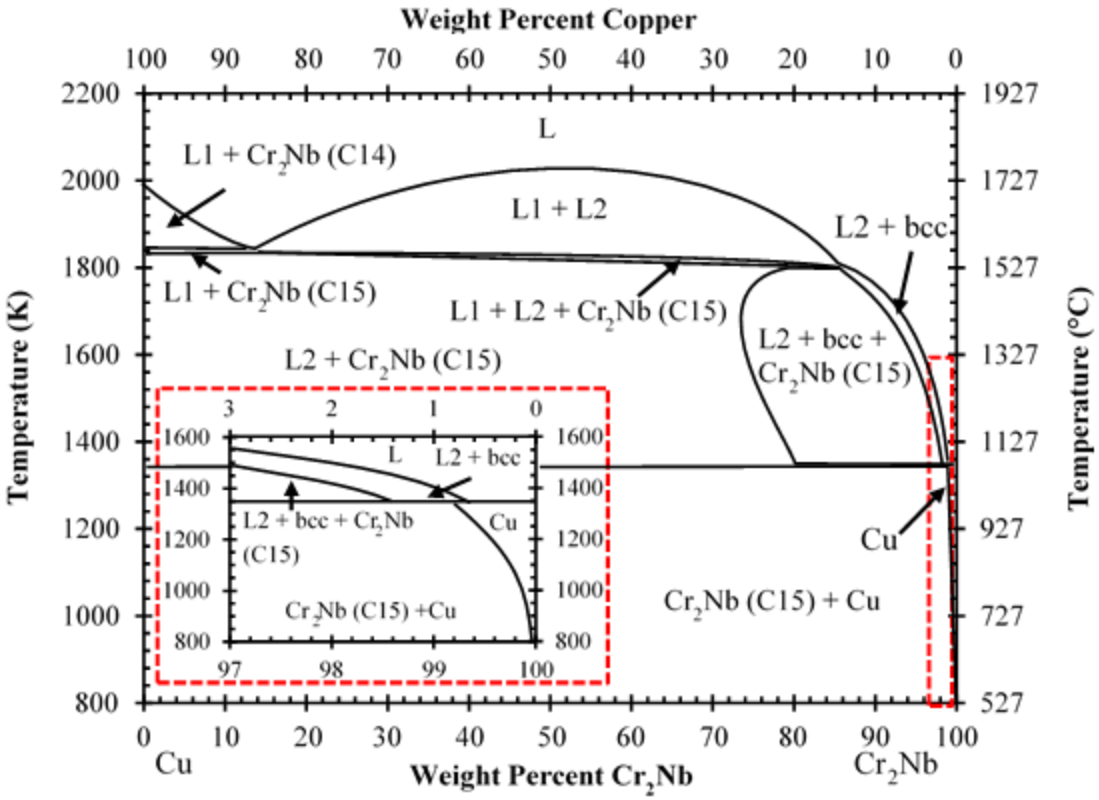

Figure 6.1. Calculated binary Cu-Cr_2Nb phase diagram and Cu-rich insert calculated by and redrawn from [80].

and Michal during development. Based on the phase diagram of Fig. 5.1.(c), Cr_2Nb solidifies first as the hexagonal C14 Laves phase or $MgZn_2$ structure type and transforms to the cubic C15 Laves phase or Mg Cu_2 between 1893 and 1923 K [81, 85]. The existence of the C14 phase in the Cr-Nb phase diagram has been brought into question with some researchers concluding that it is a metastable phase [86]. These arguments are summarized well by Jiang et al. and seem to be a matter of current debate, and our focus will be on C15 Cr_2Nb and Fig. 7.1. shows its crystallography [87].

The Nb atoms in C15 Cr_2Nb are arranged the same as the zincblende structure, though with only Nb instead of with Zn and S, and the smaller Cr atoms fill every available tetrahedral interstitial site. This structure is fairly stable, but from a temperature perspective, Cr_2Nb is not as stable as Al_2O_3 or other oxides with melting temperatures ranging from 2100 to 3400 K, some of which are shown in Table 4.1. [50]. Cr_2Nb melts congruently at 2006 K, well above the hot-wall temperature of 700 – 900 K and was assumed to have limited diffusion and interaction with Cu, which was based on the existing phase diagrams and results of Cu-Cr and Cu-Nb alloys [9, 39, 82, 88]. Low solubility and diffusivity of Cr and Nb in liquid Cu reduces the likelihood of Cr and Nb in solid solution, and results in the formation of most of the Cr_2Nb during solidification and general coarsening behavior. C15 Laves phases are known to be brittle at ambient temperatures and are currently commonly paired with a ductile matrix to leverage their high strength at high temperatures, but during the time of Ellis and Michal's work, it seems that the general focus was more on integrating ceramic particles [9, 23, 50, 81].

Initial Chill Block Melt Spinning Alloying

Ellis and Michal tested a range of stoichiometric Cr_2Nb or 2:1, Cr:Nb atomic ratios balanced by Cu including 2:1, 4:2, 6:3, 8:4, and 10:5 [9]. The 10:5 ratio was expected to be an over-alloyed condition that would form an incomplete solid solution, and 2:1 was set as an arbitrary minimum [9]. Master alloys in these ratios were first produced by induction melting and casting, then re-melted and solidified into ribbons and flakes by CBMS under an Ar atmosphere with a chilled Cu wheel [9, 89, 90]. Although commonly used for producing bulk metallic glasses, CBMS is useful for testing small volumes and can yield high cooling rates of 10^5-10^6 K s^{-1} under optimum conditions [45]. Some of the ribbons were consolidated for by vacuum hot pressing at 124.2 MPa and 923 K for 1 hr [90].

Examination of the induction melted alloys using X-ray diffraction and optical microscopy showed evidence of a largely pure Cu matrix with large, centimeter-sized FCC Cr_2Nb precipitates [9]. Cr precipitates were expected to be present but were not detected [9]. Using transmission electron microscopy (TEM) and select area diffraction (SAD) to interrogate the CBMS produced ribbons, Ellis and Michal asserted that Cu matrix was largely pure with distinct Cr_2Nb particles in the HCP C14 phase with no evidence of bulk metallic glass formation [9]. In the available literature for Cu-Cr-Nb alloys, CBMS is the only case where C14 has been detected which is likely the result of the extreme cooling rates. Differential thermal analysis was run in an attempt to detect the transformation between C15 and C14, but the results were inconclusive [9].

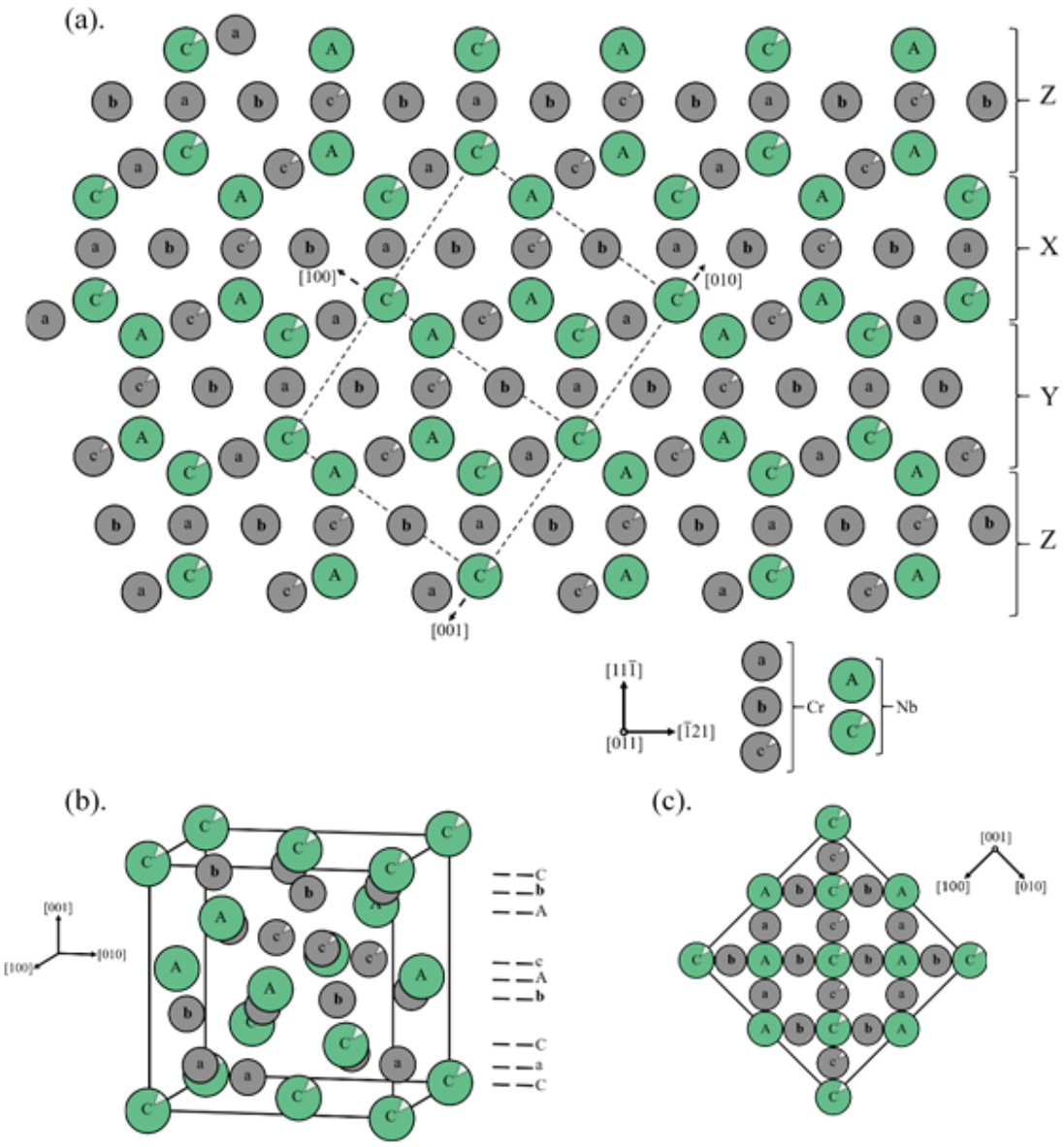

Figure 7.1. Crystal structure of the Cr_2Nb cubic C15 Laves phase drawn from atomic coordinates from [91]: (a) 2 dimensional sequential stacking orientation with atom layers representing positions, modified partially from [85], with dotted line representing one unit cell; (b) unit cell of C15 Cr_2Nb; (c) extended two dimensional (001) projection.

Microstructural characterization of the various ratios showed the 2:1 ratio ribbons' had long, columnar grains, the 8:4 and 10:5 had fine, equiaxed grains, and the 4:2 and 6:3 ratios had mixed grain morphology [9]. The Cr_2Nb precipitates were small and on the order of 10 nm for all of the alloy ratios which is unusually small and likely due to the rapid cooling rate. Additionally, the precipitates demonstrated limited coarsening by only growing to 20.6 nm after aging at 773 K for 100 h [9]. Nb precipitates were not detected in any of the samples [9].

The work by Ellis and Michal was successful in developing a new alloy with high mechanical and thermal stability. However, their mechanical and thermal property results are not comparable to current production properties due to variation in the processing methods. In this initial study, many important concerns were voiced that would be addressed in later studies with focus given to the 8:4 and 4:2 Cr:Nb ratios based on their preliminary performance. The 8:4 and 4:2 ratios have experienced the most development and were eventually given the commercial designations 'GRCop-84' and 'GRCop-42' representing Glenn Research Copper alloy and their respective ratios in the early 2000s by Dr. Michael V. Nathal of NASA GRC to represent the GRC's efforts in developing the alloy [77].

Following their preliminary work, Ellis and Michal performed extensive testing on the 8:4 and 4:2 Cr:Nb ratio alloys and directly compared NARloy-Z fabricated and tested under the same conditions in 1996 [27]. Instead of alloying with CBMS, both GRCop alloys were first alloyed by gas atomization, hot-extruded into cylindrical bars at 1130 K, and tested in the as-extruded condition with no additional heat treatments [27]. Thermal conductivity, yield strength, UTS, LCF, and creep were extensively tested and the results of these tests provided statistically significant evidence that the GRCop alloys' properties were a viable replacement option for combustion chamber liners or other high-heat-flux applications.

Difficulties of Comparing High-Heat-Flux Cu Alloys

High-heat-flux Cu alloys are difficult to compare because of concerns with conductivity and the condition of tested specimens including heat treatment history, exact chemical composition, and testing equipment. Conductivity is a critical design consideration and dependent on the microstructure and processing conditions, but few studies measure conductivity due to lack of equipment or time constraints. In order to provide an accurate representation of an alloy's properties for comparison, the best available processing condition should be used with testing conducted under the same standards and testing conditions for each individual alloy. Under ideal circumstances, thermal and mechanical measurements should be made on the same batch of samples with descriptions of processing conditions. It is problematic to show thermal conductivity and mechanical strength as a function of temperature for alloys with different thermal histories due to the strong microstructure dependence of conductivity. Comparisons of creep and LCF can be particularly difficult since considerable time is required to collect data, and there is a considerable range of stress and temperature conditions that are rarely consistent between experiments.

Experimental or literature-based comparisons of high-heat-flux Cu alloys including NARloy-Z, GRCop-84, GRCop-42, GlidCop, and AMZIRC for nuclear reactors or rocket nozzle hardware have been conducted by various researchers [2, 4, 6, 15, 29, 60, 92-96] that are each valuable for their particular trends and observations.. The majority of the reference-based data used to compare NARloy-Z, GlidCop, or AMZIRC can be traced to a series of experiments by Conway et al. of NASA LeRC in the 1970s, and new, high-quality data is needed for better comparisons [94-96]. Arguably, the best and most current comparison is de Groh et al.'s 2008 publication [29] which compares GRCop-84, AMZIRC, NARloy-Z, GlidCop Al-15, Cu-1Cr-0.1Zr, and Cu-0.9Cr. Each alloy was produced to current standards in the same geometry, subjected to the same heat treatment, tested under the same conditions, and compared for performance as high-heat-flux alloys, with the exception of NARloy-Z which used existing data [29]. Microstructures, thermal expansion, elongation, yield strength, reduction in area, and general creep properties as a function of temperature are presented [29]. However, GRCop-42 and more current processing methods of GRCop-84 are not included in the comparison, and thermal conductivity data was not collected which should have a significant impact on the comparison. Tests could be done with new material under the same conditions to add to the comparison but results may differ, hopefully only minor differences, due to changes in equipment or operator. In the case of GRCop alloys, processing conditions have changed dramatically over time, and limited data has been published, so a comprehensive comparison of processing conditions is challenging. The following sections will instead focus on the literature available for GRCop alloys, and comparisons to similar high-heat-flux alloys will prioritize de Groh et al.'s data when possible.

Processing, Microstructure, and Properties of Cu-rich Cu-Cr-Nb Alloys

Fabrication of GRCop Alloys

One of GRCop alloys' largest limitations is that they cannot be solidified by methods with low cooling rates like conventional casting for high-heat-flux applications. Cr_2Nb will form large precipitates over 1 cm in diameter, exceeding those shown in Fig. 8.1.(b), that will not aid in mechanical strengthening or retention of conductivity [2]. Serviceable GRCop-84 hardware has been produced by a variety of fabrication and post-processing techniques but is typically first alloyed in a melt and solidified into bulk powder by gas atomization with Ar.

The resulting powder has a fine distribution of Cr_2Nb precipitates in powder particles visible in Fig. 8.1.(a) [2, 97]. While other rapid solidification techniques could be used to produce fine microstructures, gas atomization is more affordable and produces powder with high purity and consistency. Gas atomization is a rapid solidification technique where a liquid metal stream is reduced to small particles by gas jets and is often used for its high production volume and relative cost. The number of jets and configuration can vary, but gas atomization consists of three primary stages: breakup of a liquid metal stream, secondary breakup of large molten droplets, and solidification of the final small (10-100 μm) powder particles [98]. When gas is used, the breakup of the liquid metal stream occurs above the focal point of the gas stream as a result of a vacuum

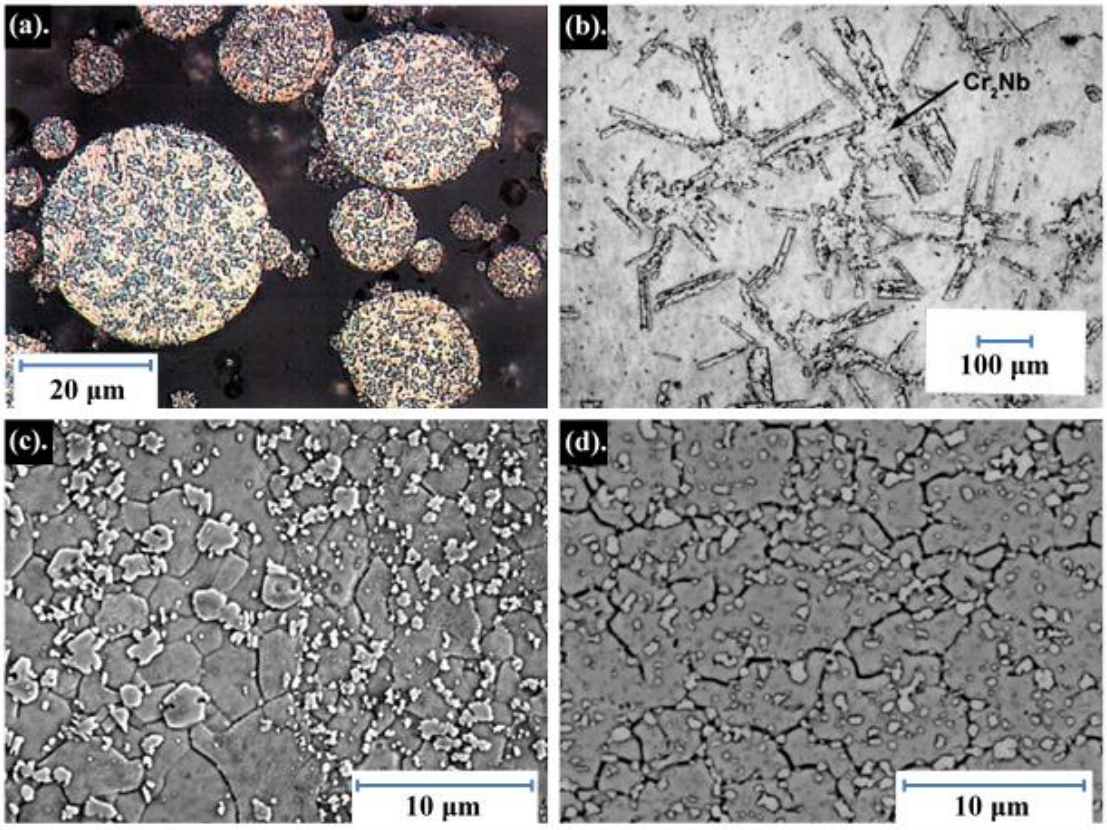

Figure 8.1. Micrographs of GRCop-84; (a) Gas atomized powder showing pure copper matrix with Cr_2Nb particles represented by the gray phase [2]; (b) Typical cast microstructure showing large, elongated Cr_2Nb [99]; (c) Etched, as-extruded with visible matrix grains and Cr_2Nb particles and agglomerations represented by the lighter phase [2]; (d) Extruded microstructure after 1273 K exposure for 30 minutes demonstrating more visible grain and particle boundaries [2], adapted with permission.

generated by the gas streams' pressure, which helps improve the efficiency of the secondary breakup [98]. Depending on cost and reactivity with the metal, gasses like Ar or N_2 are used, forming smooth, spherical particles from the liquid stream [98]. Water and steam are inexpensive but form more irregular shapes with high oxide content, so these methods are used primarily for low and high alloy steels [98, 100]. Standard gas atomization with inert gas has a lower cooling rate of 10^2-10^3 K s^{-1} compared to CBMS, while supersonic and close coupled gas atomization techniques have cooling rates comparable to CBMS [9].

GRCop-84's gas atomization specifications are fairly strict to help preserve the thermal conductivity of the end product and are partly listed by Gradl et al. [30]. High purity of the raw materials is critical to minimize Fe and O contamination, shown by Ellis to have a significant impact on the performance as shown in Fig. 9.1. [2]. According to Gradl et al, GRCop-42 is simpler to produce through gas atomization compared to GRCop-84 based on anecdotal evidence from powder suppliers. The alloy will react with N_2 and form nitrides, so Ar is necessary for gas atomization and should be used to backfill containers to minimize oxygen exposure. Additionally, a slight off-stoichiometric excess of Cr is added to suppress Nb precipitate formation and H embrittlement concerns ranging from 2.02 to 2.05 Cr/Nb based on powder compositions presented in Table 2.1. Cr precipitates are expected to be present but are often difficult to detect due to their small size and quantity.

Following powder production, most powder metallurgy and welding techniques can be applied to GRCop alloys without issue as well as warm and cold rolling, bump forming, stamping, metal spinning, and tube drawing [2]. NASA has demonstrated GRCop-84 consolidation methods including direct extrusion, hot isostatic pressing (HIP) to form, and vacuum plasma spraying (VPS) into shape and densifying with HIP [2]. NASA has also demonstrated a variety of welding techniques including diffusion bonding, inertia welding, friction stir welding, electron beam welding, and brazing, but limited information on these techniques is available currently [2, 101, 102]. Combustion chamber liners of GRCop-84 have been produced by VPS, conventional wrought processing, and by powder bed additive manufacturing (AM), with AM proving to be the most versatile processing technique [30, 103]. The term 'wrought' is used in GRCop literature to represent conventional processing methods like extrusion or rolling and the terminology used by the original authors will be maintained. Fabrication of GRCop-42 has been demonstrated with several techniques including hot extrusion and AM, any methods that work with GRCop-84 should be viable with GRCop-42. The specifications of extrusion, HIPing, and commercial rolling are detailed by Ellis et al. [104].

Prior to AM, several concepts were available for fabricating new liners and nozzles with GRCop alloys to improve SSME designs. These are described by Ellis et al. [104] and include metal spinning plate, directly HIPing into a cylinder or hourglass shape, diffusion bonding platelets, and forming tubing, but these processes all require considerable machining to produce cooling channels which are intrinsic to the operation of the liners. Annealing and cold work have a demonstrable effect on the room-temperature tensile properties, but Ellis et al. showed that recovery and recrystallization occurs between 473 and 873 K depending on the degree of cold work, so the benefits of

cold work will be lost in high-heat-flux operations [104]. At temperatures where cold work could improve GRCop-84's mechanical properties, other alloys with more optimal properties should be considered.

Additive Manufacturing

Cu alloys present two main challenges with powder bed AM: reflectivity with conventional lasers and high thermal conductivity of the powder [105]. Copper has high reflectivity with infrared light (1 μm) used in conventional lasers, so the majority of the energy used by conventional laser additive systems will not be absorbed by Cu powder and can inhibit melting. If sufficient energy is absorbed to initiate melting, the melt zone will have high local thermal gradients that will either inhibit melting or cause delamination, layer curling, and build failure [105]. A review of AM of pure Cu has been published by Tran et al. on selective laser melting (SLM), electron beam melting, binder jet, and ultrasonic AM [105]. Green lasers, which have a shorter wavelength of 515 nm, have been used for Cu with laser-based AM, but they are more expensive and less common [105].

As Gradl et al. discuss, GRCop-84 is unusual because it is easily melted by conventional SLM, a form of laser-powder bed fusion (L-PBF) AM [106]. As the more generic term, L-PBF will be used to represent sources that reference SLM. Gradl et al. postulate that the presence of the Cr_2Nb precipitates is responsible for initiating melting by lowering the initial reflectivity of the powder [106]. Cu's reflectivity decreases rapidly with temperature, so as long as enough initial energy can be absorbed, melting should initiate [106]. Additionally, the thermal conductivity is reduced by the high alloying content which likely contributes to the ease of AM by reducing heat dissipation. GRCop-42 has been shown to have a similar affinity with conventional L-PBF [30]. Measuring the reflectivity of the GRCop alloys would likely provide evidence to support their relative ease of AM.

Additive manufacturing often results in inherent porosity, anisotropy, and reproducibility concerns that must be addressed before implementation. Post-production annealing and HIP, often standard on aerospace hardware, are usually sufficient to ensure near theoretical density and homogeneity [106]. NASA's L-PBF development of GRCop-84 and GRCop-42 has progressed to the point where L-PBF build parameters have been established and practical hot-fire tests of L-PBF GRCop liners have been performed [30, 106]. NASA has demonstrated GRCop-84's versatility with L-PBF in forming combustion chamber liners and was a key component of the low-cost upper stage propulsion (LCUSP) project [10, 103], but the majority of NASA's build parameters and characterization efforts are internal and not currently available to the public. However, Gradl et al. mention that process parameters and characterization data are available to industry to expand NASA's supply chains, and that their GRCop-42 L-PBF process parameters are different than GRCop-84 [107].

A technical memorandum by Cooper et al. [108] provides NASA's basic process parameters for GRCop-84 and initial parameter testing for GRCop-42 on a ConceptLaser M2 system though the focus of the memorandum is on GRCop-42, and the parameters may not be current. Their ConceptLaser uses a single 400 W Nd:YAG laser with a spot

size of 52 μm, travel speed of 50 – 5,000 m s^{-1}, and the build chamber is filled with Ar [108]. The default parameters for GRCop-84 include a core laser power of 180 W, core scan speed of 800 mm s^{-1}, hatch width of 0.105 mm, build layer thickness of 0.03 mm, and core energy density of 95.2 J mm^{-3}. The coolest, fastest parameters in this memorandum for GRCop-42 are 270 W, 1,025 m s^{-1}, 0.099 mm, 0.045 mm, and 59.1 J mm^{-3} in the same order as the parameters for GRCop-84 [108]. Cooper et al. were able to improve on the build parameters of GRCop-84 by successfully increasing the build layer thickness and scan speed which improves the print time by about 20% [108]. Characterization work by Hayes et al. provides some general metallography and mechanical properties of L-PBF GRCop-84, and computed tomography of small-scale L-PBF GRCop-84 liners including demonstration of a new cooling channel design and orientation that can be achieved by AM, but more thorough characterization is necessary for future development [103]. The design freedom allowed by AM for the cooling channels provides a strong motivation to pursue AM as GRCop alloys main method of fabrication for high-heat-flux applications in the future.

Microstructure of Wrought GRCop-84

There are few microstructure-focused studies available for GRCop alloys with the exception of gas-atomized powder and extruded GRCop-84, the majority of which have been contributed by Groza and Anderson [43, 44, 79, 97, 109]. While there are newer fabrication methods available, such as AM, the available literature is developing, so gas-atomized powder and extruded GRCop-84 are the best available representation of the alloy and should be comparable to newer methods.

Groza and Anderson investigated the microstructural features of gas-atomized GRCop-84 powder which had a powder particle size of less than 106 μm [97]. The powder used in this study is not directly comparable to current gas-atomized powder used for powder bed AM which has a powder particle size of 25 – 40 μm, shown in Fig. 8.1.(a), but the general precipitate distribution and trends are comparable. The more current powder of Fig. 8.1.(a) is used as a visual reference for Groza and Anderson's work because it is the best available micrograph which shows distinct separation of the Cu matrix and Cr_2Nb particles, but it is not the same powder. Groza and Anderson identified a bimodal distribution of primary and secondary Cr_2Nb precipitates on the order of 1 μm and 10-100 nm, respectively [97].

Groza and Anderson suggest that the primary particles solidify and grow rapidly during atomization before the surrounding Cu matrix can solidify which yields large primary particles [97, 109]. The primary particles are irregular in shape, which can be observed in the more current powder of Fig. 8.1.(a), from their lack of constraint in the liquid and serve partially as nucleating sites for the Cu matrix. The secondary particles are hypothesized to precipitate out of the matrix grains because the secondary particles are primarily observed within the matrix grains and the matrix should be supersaturated considering the cooling rates [97, 109].

The bimodal distribution observed in the gas-atomized powder persists in extruded GRCop-84, shown in Fig. 8.1.(c) and 8.1.(d). The average diameter and distribution of the primary and secondary particles in the extruded material remains

roughly the same as the powder [110]. This demonstrates that the starting powder microstructure has a significant impact on the final microstructure, so powder quality and optimization might improve the final microstructures. Both the primary particles and Cu matrix grains had limited coarsening behavior during heat treatments which is ideal for high temperature performance. Following aging treatments at 773 and 973 K, below the Cu-Cr_2Nb solvus temperature (see Fig. 6.1.), further precipitation was observed in the extruded material as a distinct secondary distribution of particles which indicates that the matrix is supersaturated [110]. Even after an aging of 1323 K for 100 h, the mean primary precipitate diameter only increased from 0.93 ± 0.04 to 1.35 ± 0.03 μm, where the ± represents standard error [110]. This is consistent with statements that the coarsening of Cr_2Nb is slow in GRCop-84.

Anderson et al. estimated the strengthening contribution of the primary and secondary particles using the Orowan-Ashby equation for a random distribution of impenetrable particles (Eq. 3.1.) [110]. The primary particles were found to contribute little to strengthening based on estimates of the Orowan-Ashby equation, while the secondary particles provided a high degree of strengthening. However, the large particles contribute to grain boundary (Hall-Petch) strengthening by pinning the matrix grains and preventing grain growth [44], evidenced by the copper matrix grains exhibiting slow growth with a maximum size of 4 μm from 0.9 μm in the as-extruded condition [43]. Based on particle size and stress measurements, Anderson et al. calculated the contribution of Orowan and Hall-Petch strengthening with good agreement to experimental results with Eq. 3.1. [44]. The Hall-Petch strengthening is dominant with roughly two-thirds of the contribution to strength, and Orowan contributes roughly one-third, contrary to prior estimates [44]. This appears to reveal the true strengthening nature of the Cr_2Nb precipitates and their role in the high temperature properties of GRCop-84 keeping the matrix grains small by pinning the grain boundaries and preventing coarsening while keeping the matrix as pure as possible for high conductivity. This strengthening ratio has been cited for newer fabrication methods but has not been reproduced and should be reevaluated for the new microstructures.

Room-temperature Properties of GRCop Alloys

Room-temperature properties are somewhat unnecessary for high-heat-flux applications, but they are the most common type of tests and can provide a baseline comparison between alloys. A selection of extruded GRCop-84's properties relevant to high-heat-flux applications are presented in Table 5.1. There is data available for other processing conditions, but they are often incomplete, with unknown aging or annealing history, or only data is available in the as-fabricated condition. Furthermore, the properties of extruded GRCop-84 have improved with better processing and aging conditions, so comparisons between sources is challenging. Some of GRCop-42's properties have recently been published [30], but a general properties table has not been published and would be useful for future development.

Alloys used at high temperatures are best demonstrated by temperature dependence, so GRCop-42 and -84's thermal conductivity, yield strength (YS), ultimate tensile strength (UTS), creep, LCF, and thermal expansion as a function of temperature

Table 5.1. Room temperature properties of GRCop alloys including some mechanical brazing data and some SLM GRCop-84 and -42 data; all data is from the indicated references and should be considered approximate due to limited statistics.

Alloy	*YS (MPa)*	*UTS (MPa)*	*Elongation (%)*	*Reduction in Area (%)*	*Modulus of Elasticity (GPa)*	*Density ($kg\ m^{-3}$)*	*Specific Heat ($J\ kg^{-1}k^{-1}$))*	*Thermal conductivity ($W\ m^{-1}K^{-1}$)*
	196.2 [29]	368 [29]	21.7 [29]	39.7 [29]	112 [111]	8.81 - 8.83[+] [112]	381.8[++] [112]	284[i] [2]
Extruded GRCop-84	187[*] [29]	361[*] [29]	25.5[*] [29]	40.6[*] [29]				304[ii] [2]
	226 [30]	368.2 [30]						
Extruded GRCop-42	200 [30]	422 [30]	30 [30]			8.88 - 8.89[+] [112]		346 [30]
SLM & HIP GRCop-84	208 [30]	390 [30]	30 [30]					
SLM & HIP GRCop-42	173 [30]	357 [30]	32.9 [30]					

[*] Brazed at 1208 K

[i] <20 ppm Fe interpreted from graphical data

[ii] 200 ppm Fe interpreted from graphical data

[+] Theoretical density range based on powder alloying composition of Table 1.1., measured density not available

[++] Calculated from temperature dependent equations at 300 K

are compared with oxygen-free high thermal conductivity (OFHC) Cu serving as the baseline example when available.

Thermal Conductivity

GRCop-84's thermal conductivity compared to similar high-heat-flux alloys is its weakest property due to its high alloying content and can be significantly impacted by impurities In 2000, Ellis and Keller with Thermophysical Properties Research Laboratory (TPRL), Inc. in West Lafayette, IN [112] calculated thermal conductivity and electrical resistivity of extruded GRCop-84 using the Kohlrausch method. Since both conductivity and resistivity are calculated, the Lorenz number could be determined and was measured between 29 and 480 K with 5 powder lots [112]. The Lorentz number was significantly higher than pure Cu's and demonstrated a mild temperature dependence, but these results had not taken Fe impurity into account and are not accurate to current GRCop-84 chemistry. Although the Lorenz number increased, Ellis and Keller believed that this was caused by the thermal conductivity increasing and electrical resistivity decreasing in response to the material dynamically annealing during the measurements [112]. So, it is possible that the Lorenz number is constant for GRCop-84, though an updated and more accurate measurement has not been acquired. In 2005, Ellis found that Fe impurities on the order of 200-250 ppm from the Cr melt stock had a significant impact on GRCop-84's conductivity, illustrated in Fig. 9.1. and Table 5.1., and new processing guidelines ensure or require the concentration of Fe to be <20 ppm, so the mechanical properties should remain largely unaffected [2]. This distinction makes comparisons problematic with results prior to this publication because the Fe concentration was not commonly measured and often unknown and unreported.

Gradl et al. [12] present a significant amount of data for L-PBF GRCop-84 and GRCop-42 including thermal conductivity which is shown in Fig. 9.1. However, the data collection method and thermal history are not presented, and they are assumed to be in the as-built condition. Both GRCop alloys have significantly lower thermal conductivity than their wrought counterparts which is likely due to a detrimental microstructural change by additive processing. This could be caused by residual stress, stoichiometry change, or dissolved content and could likely be reversed by heat treatment or HIP, so these results may not be indicative of the optimal properties. L-PBF GRCop-84's thermal conductivity demonstrates a significant decrease starting at ~850 K, and Gradl et al. [12] postulate that the decrease is caused by excess Cr dissolving into the Cr matrix. GRCop-42 also decreases but at a much lower rate, which is likely due to a higher degree of excess Cr. In practical application of GRCop-84, the amount of excess Cr should be optimized to reduce this effect with care taken to retain hydrogen-embrittlement resistance.

At room temperature, extruded, <20 ppm Fe, GRCop-84's thermal conductivity is ~76%, based on Fig. 9.1., of OFHC's room temperature thermal conductivity, ~400 W mK^{-1} [29], while NARloy-Z's is ~91%. For comparison, AMZIRC has the highest available thermal conductivity of high-heat-flux copper alloys at 92.5% OFHC Cu, and GlidCop Al-15's is approximately 80% OFHC Cu [29]. Extruded GRCop-42's lower alloying content provides significantly fewer scattering sites, which results in a thermal

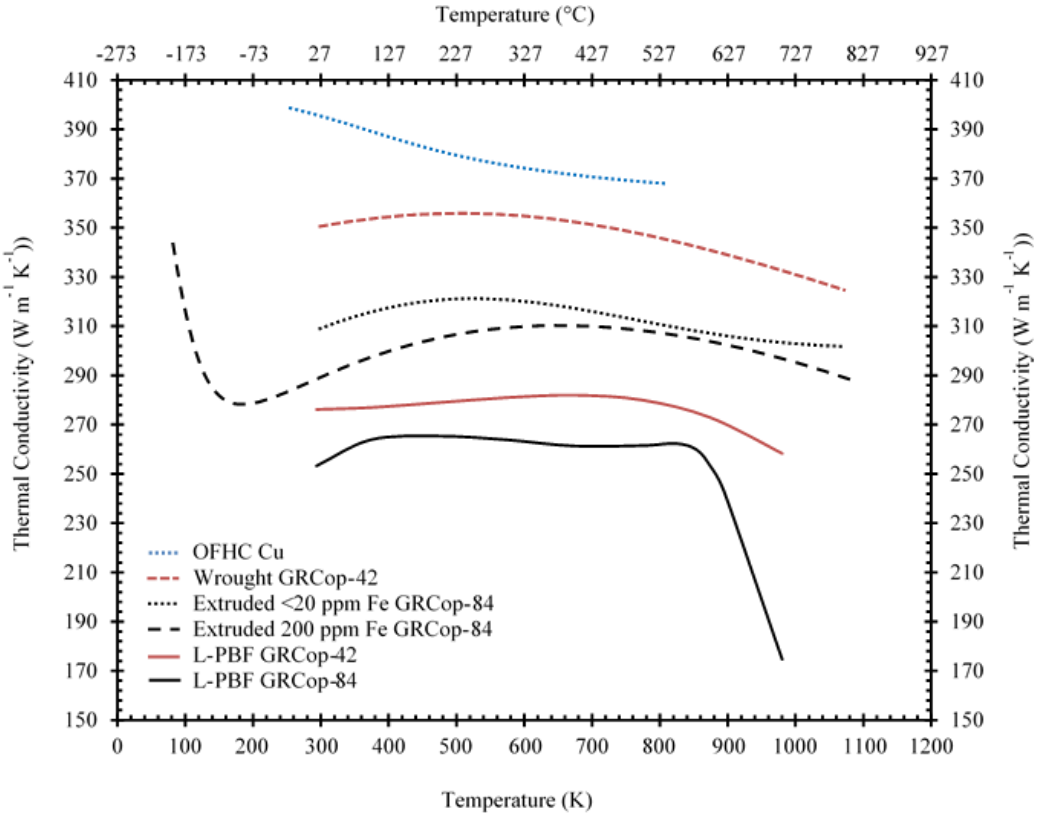

Figure 9.1. Thermal conductivity as a function of temperature for existing data on GRCop alloys including wrought, extruded, and L-PBF (SLM) and oxygen-free high conductivity (OFHC) Cu for comparison; redrawn from plots from [2, 12, 15, 30, 112] with permission.

conductivity ~86.5% OFHC Cu at room temperature which is a significant improvement over GRCop-84. Extruded <20 ppm Fe GRCop-84's thermal conductivity, shown in Fig. 9.1., demonstrates some temperature dependence. The thermal conductivity first increases to a maximum value of ~79.5% OFHC Cu at ~535 K and then decreases steadily up to ~900 K. At temperatures above 900 K, the thermal conductivity continues to decrease but at a noticeably lower rate. These regions may help identify changes in the microstructure between these temperature ranges, but this data is from a single sample and more, repeated data sets would be necessary to be certain that these shifts are not anomalous.

Tensile Properties

According to Ellis et al., optimization of tensile strength at high temperatures is not the primary design consideration of the combustion chamber liner, but tensile strength provides a readily tested macroscopic indicator of thermal stability against thermal cycling [104]. This 2012 study by Ellis et al. presents a thorough characterization of GRCop-84 tensile properties fabricated by various methods including extrusions, HIPed billet, rolled plate, rolled sheet, drawn tube, and VPS, under a variety of heat-treatment conditions including annealed, brazed, and cold worked [104]. They reported that processing methods had a minimal effect on the tensile properties, though the HIPed billet had the worst performance, likely due to the higher consolidating temperatures and longer thermal exposures resulting in larger grain and precipitate particle sizes [104]. Regardless of processing or heat-treatment conditions, the GRCop-84 samples were noted to exhibit similar stress-strain behavior with the exception of cold work [104].

As-extruded, annealed, and brazed GRCop-84 revealed similar general tensile behavior, demonstrated by the as-extruded results in Fig. 10.1., with a minimal elastic region less than 0.5% strain and long plastic region greater than 20% [104]. When the yield point is reached, as-extruded GRCop-84 rapidly reaches a stress near its UTS and remains near that stress for 10 to 20% elongation followed by 5 to 15% elongation during necking prior to failure [104]. Ellis et al. studied strain-rate dependence for annealed and 47% cold-worked GRCop-84 tensile specimens in a range of strain rates of 0.01 to 0.0008 s^{-1}. The annealed samples demonstrated limited dependence while the cold-worked samples had some dependence [104]. Tensile data for as-built L-PBF GRCop-84 and -42 specimens, collected at room temperature, also presented in Fig. 10.1., demonstrate significantly more brittle behavior with a higher UTS and reduced elongation [30, 104]. L-PBF samples that were HIPed demonstrate a similar tensile behavior compared to as-extruded GRCop-84, though slightly more ductile with a ~16 to 33% increase in final elongation [30, 104]. In both L-PBF cases, GRCop-42 demonstrated reduced strength but longer elongations compared to GRCop-84 [30].

In high-heat-flux applications, changes to UTS and YS with temperature help demonstrate an alloy's loss of mechanical strength at high temperatures. The UTS and YS as a function of temperature for OFHC Cu and GRCop-84 and GRCop-42 in a variety of conditions are presented in Figures 11.1. and 12.1. Gradl et al. discuss that the operating pressures in the cooling channel walls of combustion chamber liners can be up to 40 MPa, so the benefit of higher YS and UTS is that thinner walls can be used

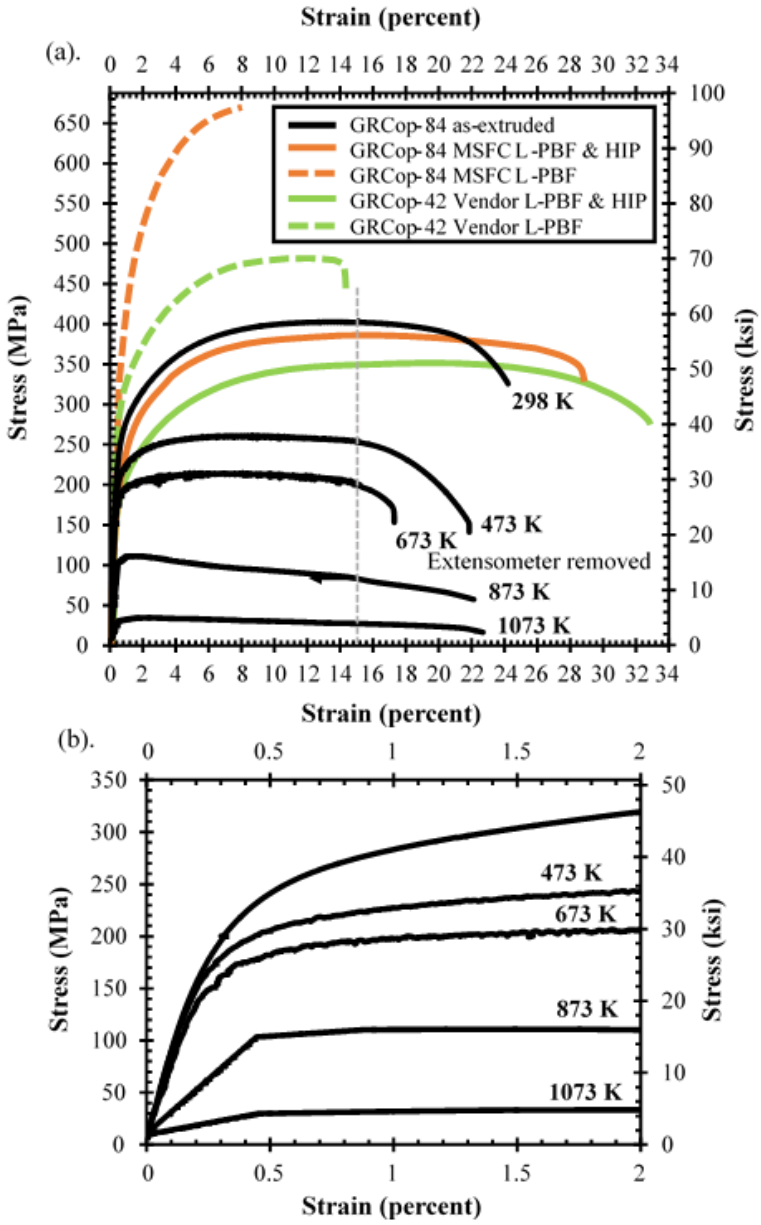

Figure 10.1. Stress-strain plots (tensile) (a) data collected on GRCop-84 and -42, processed using a variety of techniques with post processing treatments, and several temperatures between room temperature and 1073 K; If not specified, data was collected at room temperature [30, 104]. Marshall Space Flight Center's (MSFC) tensile specimens were fabricated on a Concept M2 SLM system, and the vendor's were built on an EOS M400. (b) Low strain regime of as-extruded GRCop-84 data from (a) redrawn with permission.

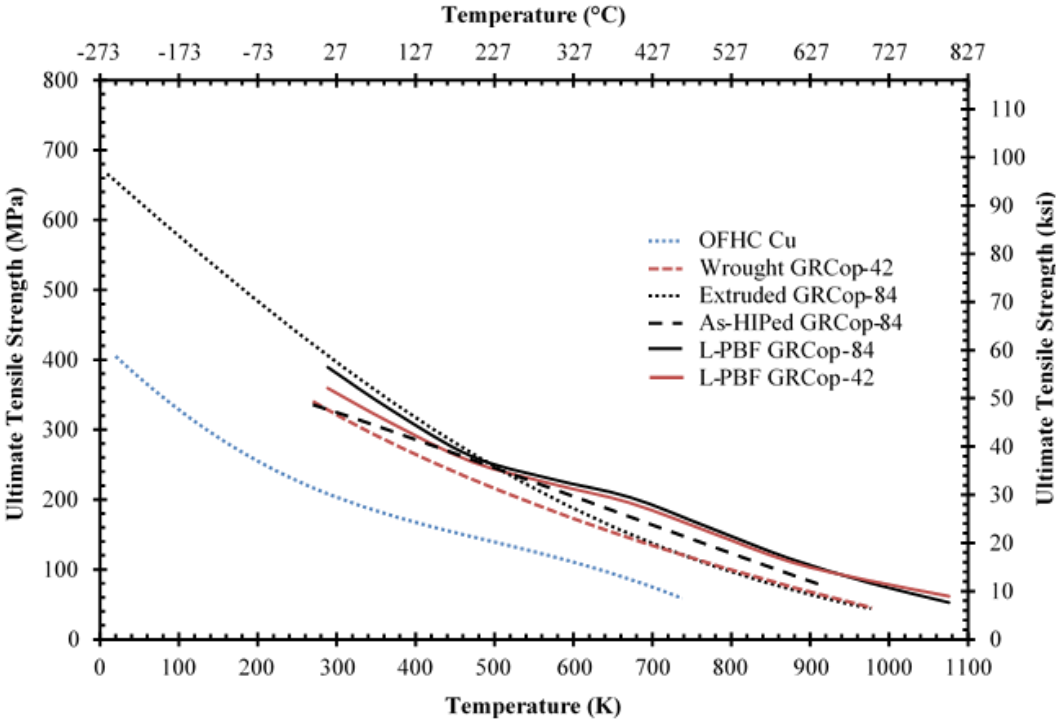

Figure 11.1. Ultimate tensile strength as a function of temperature for existing data on GRCop alloys in wrought, extruded, and L-PBF (SLM) conditions with OFHC Cu for comparison; redrawn and combined from [2, 12, 15, 30, 112].

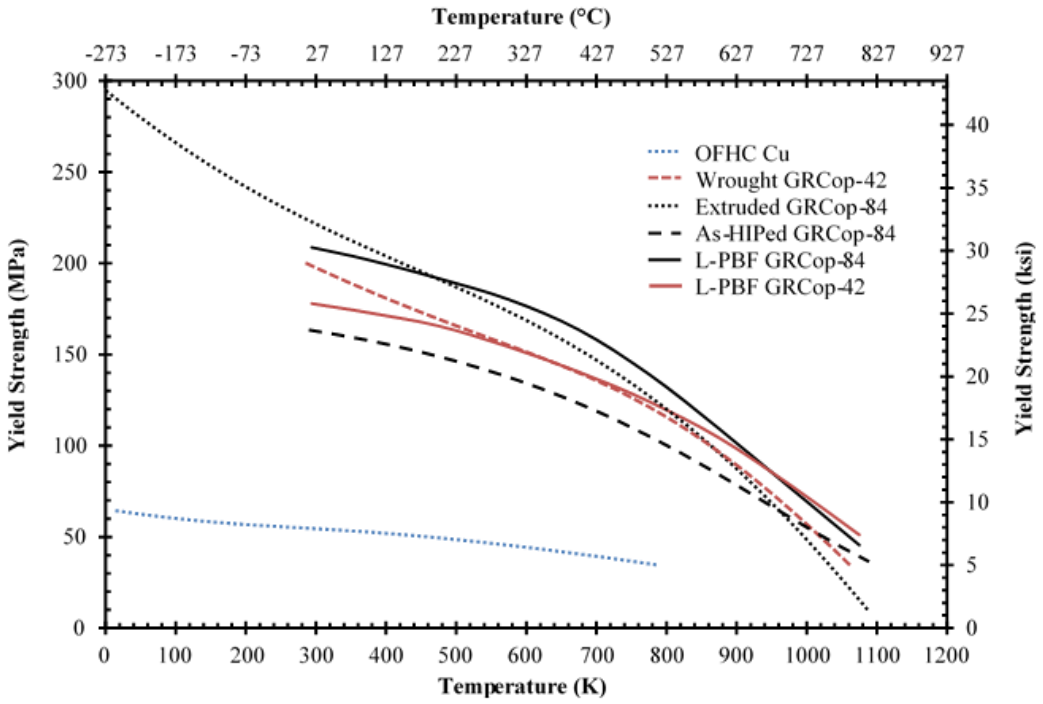

Figure 12.1. Yield strength as a function of temperature for existing data on GRCop alloys in wrought, extruded, and L-PBF (SLM) conditions with OFHC Cu for comparison; redrawn and combined from [2, 12, 15, 30, 112].

resulting in better cooling efficiency and lower hot-wall temperatures [30]. Similar to the thermal conductivity, the L-PBF samples are assumed to be in the as-built condition. The UTS and YS of the L-PBF samples are significantly higher, 20-30 MPa in some cases, than the wrought conditions at elevated temperatures which is a significant improvement. The improvement of mechanical properties may help balance the lower thermal conductivity at high temperatures in practical use. Below ~873 K for YS and ~700 K for UTS, GRCop-84's mechanical properties are better than GRCop-42 which compensates somewhat for the shortcoming of GRCop-84's lower thermal conductivity. Above these temperatures, GRCop-42 performs better in YS and roughly the same in UTS, which is likely caused by the comparatively weak Cu matrix dominating the strength [30].

Compared to similar high-heat-flux alloys, GRCop alloys demonstrate low loss of UTS and YS at high temperatures and after high temperature exposures. This is best demonstrated by de Groh et al.'s comparison of common high-heat-flux alloys in as-received and brazed at 1208 K conditions, shown by data points extracted in Table 6.1. The alloys were subjected to the braze to simulate a brazing operation typical of a main combustion chamber liner to apply a brazed structural jacket [29]. The simulated braze demonstrates how the alloys' properties will change after a braze (if required) or exposure to the highest realistic temperatures in the combustion chamber liner, and the same simulated braze was used for each brazed sample in de Groh et al.'s experiment. These results should be used more for comparison of high temperature exposure rather than property change after a braze cycle because the requirements for the individual alloys after a braze cycle have not been taken into account. At all temperatures, GRCop-84 and GlidCop Al-15 are the least effected by the brazing cycle and exhibit limited UTS and YS loss compared to the other alloys. This can be related to their microstructures which are strengthened with thermally stable Cr_2Nb and Al_2O_3 precipitates. While other alloys demonstrate better UTS and YS below 773 K, brazed GlidCop Al-15 and GRCop-84 have superior UTS and YS values above 773 K. Although as-received Cu-1Cr-0.1Zr and Cu-0.9Cr have better UTS and YS then GRCop-84, their brazed counterparts are at least half that of brazed GRCop-84, and the as-received values are likely to drop after continued high temperature exposures similar to those in practice [29]. L-PBF GRCop alloys and wrought GRCop-42 in brazed conditions will likely perform similar to wrought GRCop-84 but should be tested to the benefit of the literature.

Creep Properties and Characteristics

Decker et al. in 2004 and Ellis et al. in 2015 conducted creep tests with GRCop-84 over a range of temperatures and strain rates that could be experienced by the combustion chamber liner in service [33, 113]. At the time of Decker et al.'s study, the most common production methods of GRCop-84 were as-extruded or as-rolled following the extrusion, and these two forms were both creep tested [113]. The creep tests were performed in tension with a constant stress creep instrument under vacuum. A range of temperatures from 764 to 1068 K and stresses from 12.5 to 200 MPa were examined to determine the activation energies needed for creep, and analysis included applying several creep models to the results.

Table 6.1. Comparison of (a) UTS and (b) YS of high-heat-flux data from [2, 29] in rough descending order between 300 and 773 K and separated/reorganized at 923 K to help demonstrate the shift in strength; OFHC Cu condition is unknown, but provides baseline value; estimated from data points of figures by [29] with GRCop-84's data based on the average of HIPed and extruded material with five tests at each temperature, and all others are estimates of two tests; OFHC Cu and NARloy-Z data estimated from trend lines [2].

(a)

Ultimate Tensile Strength (MPa)						
Alloy	*Condition*	*300 K*	*773 K*	*923 K*	*Condition*	*Alloy*
Cu-1Cr-0.1Zr	*As-received*	564	293	125	*As-received*	*GlidCop Al-15*
AMZIRC	*As-received*	509	264	125	***Brazed***	*GlidCop Al-15*
Cu-0.9Cr	*As-received*	495	206	118	*As-received*	*Cu-1Cr-0.1Zr*
GlidCop Al-15	*As-received*	464	184	104	*As-received*	*Cu-0.9Cr*
GlidCop Al-15	***Brazed***	408	174	86	*As-received*	*GRCop-84*
GRCop-84	*As-received*	368	153	82	***Brazed***	*GRCop-84*
GRCop-84	***Brazed***	361	148	46	***Brazed***	*Cu-1Cr-0.1Zr*
NARloy-Z[*]	*STA*	315	187	33	***Brazed***	*Cu-0.9Cr*
Cu-1Cr-0.1Zr	***Brazed***	266	89	34	***Brazed***	*AMZIRC*
Cu-0.9Cr	***Brazed***	245	62	32	*As-received*	*AMZIRC*
AMZIRC	***Brazed***	231	104			
OFHC Cu[*]	*Unknown*	217	84			

(b)

Yield Strength (MPa)						
Alloy	*Condition*	*300 K*	*773 K*	*923 K*	*Condition*	*Alloy*
Cu-1Cr-0.1Zr	*As-received*	551	284	126	*As-received*	*GlidCop Al-15*
AMZIRC	*As-received*	501	261	126	***Brazed***	*GlidCop Al-15*
Cu-0.9Cr	*As-received*	442	207	112	*As-received*	*Cu-1Cr-0.1Zr*
GlidCop Al-15	*As-received*	465	184	100	*As-received*	*Cu-0.9Cr*
GlidCop Al-15	***Brazed***	409	175	73	*As-received*	*GRCop-84*
GRCop-84	*As-received*	196	114	69	***Brazed***	*GRCop-84*
GRCop-84	***Brazed***	187	105	55	*STA*	*NARloy-Z*[*]
NARloy-Z[*]	*STA*	138	93	36	***Brazed***	*Cu-1Cr-0.1Zr*
Cu-1Cr-0.1Zr	***Brazed***	107	67	29	*As-received*	*AMZIRC*
Cu-0.9Cr	***Brazed***	90	43	23	***Brazed***	*Cu-0.9Cr*
OFHC Cu[*]	*As-received*	52	33	16	***Brazed***	*AMZIRC*
AMZIRC	***Brazed***	32	25			

[*] Indicates estimated and interpreted from trend lines

[**] STA indicates solution treated and aged.

Ellis's [33] creep study was more focused on liner application and generating statistically significant data to help qualify and provide to potential models predicting GRCop-84's creep response during service while investigating the effect of processing on creep. Large and small extrusions, plate, brazed plate, production sheet, HIP billets, pre-production sheet, and friction stir welded sheet were creep tested at 773, 923, and 1073 K to determine the influence of processing on creep properties with constant load tests [33]. The creep tests were conducted in both vacuum and in air at three separate laboratories so special consideration was given to errors in their comparison. Ellis et al. focused on formulating a forward stepwise regression analysis to compare fabrication and only the power law creep model was fit to the data [33].

Typical creep curves of GRCop-84 generated by Decker et al., Fig. 13.1.(a), show three distinct regions of creep, and the strain is often in excess of 10% in contrast to dispersion strengthened alloys which usually have low ductility. Most of the strain is within the secondary and tertiary regions, with a short primary. GRCop-84 also lasts longer in the secondary creep regime with an easy transition to tertiary creep, Fig. 13.1., which results in total elongations of 8 – 14%, which resembles creep curves of pure metals according to Decker et al. [33]. Another constant stress study by Lerch et al., Fig. 13.1.(b), shows that extruded GRCop-84's creep behavior at lower temperatures have only two distinct creep regions and stays mostly within the steady-state, secondary creep [33].

The majority of Decker et al.'s measured stress exponents ranged from 7.6 to 10 with an outlier of 4.7 at 1068 K under low stress conditions which could indicate evidence of dislocation climb controlled creep in that region [113]. Ellis et al. calculated similar stress exponents ranging from 6.6 – 8.26 for the eight fabrication methods tested [33]. The general range of stress exponents for both studies are indicative of creep behavior of dispersion strengthened alloys or metal matrix composites. Decker et al. found that GRCop-84's diverse creep characteristics of pure metal strain and high creep exponents made applying a model of creep behavior difficult [113]. They attempted to apply a power law relationship, but almost all of the data was well above power-law breakdown and instead applied a hyperbolic sine relationship, which incorporates an exponential dependence on stress, to interpret data.

Both studies applied a Monkman-Grant relationship to compare fabrication conditions. The Monkman-Grant relationship is simple to test; if the slope is constant for minimum creep rate as a function of rupture time, fabrication does not impact the creep properties. Decker et al. found a slope of -1.08 and determined the fracture mechanism was the same between rolled and extruded material [113]. Ellis et al. calculated a slope of -1.11 in agreement to Decker et al.'s results; however, the forward stepwise regression analysis showed a statistically significant impact of processing on creep response, though differences in texture, testing environment, or scatter of the data could also contribute to explaining the results [33]. In 2011, Ellis and Loewenthal [114] conducted a follow-up study to assess the variation of previous creep results. By improving the specimen temperature measurement and control, the scatter in the data was from 2 to ½ orders of magnitude for extruded GRCop-84, demonstrating that the scatter in data collected prior to the 2011 study is largely due to complications of the testing environment [114]. In particular,

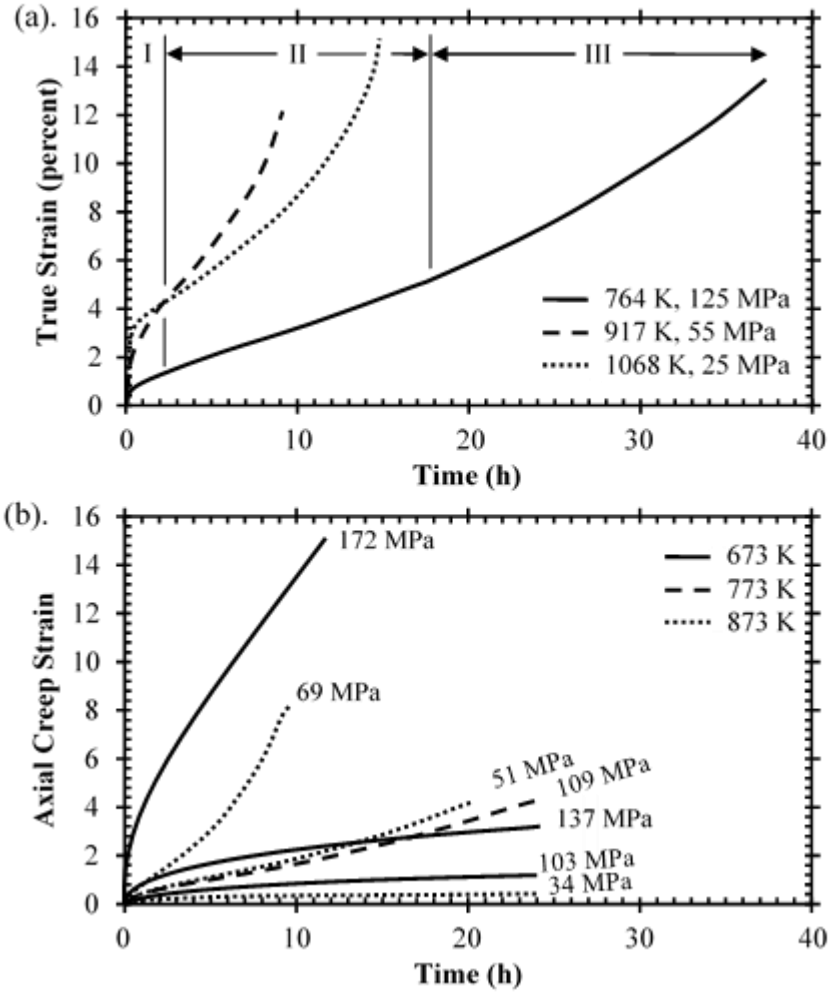

Figure 13.1. – (a) Creep results for three temperatures and constant-stress conditions of extruded GRCop-84, redrawn from [113]; primary (I), secondary (II), and tertiary (III) creep regions are labeled for the 746 K creep test; (b) – Axial creep results for three constant temperatures and various constant stress conditions tested at a strain rate of 0.0001 s^{-1}, only the 69 MPa - 873 K sample broke during testing [115].

different fabrication methods produce roughly the same grain size, but changes to texture can have a substantial impact on creep properties [33]. For the small extrusions, plate, and pre-production sheet there was evidence of texture having an impact on creep, though the change is minimal [33]. Therefore, fabrication method should not be fully excluded from future creep studies of GRCop alloys and could be utilized to improve creep properties by texture control.

Regardless of fabrication, wrought GRCop-84 has generally good creep characteristics compared to the other high temperature Cu alloys studied by de Groh et al. [29]. The step loaded and constant load creep results are compared in Table 7.1. based on the rate equations at a strain rate of $1x10^{-6}$ s^{-1}. Not all of the samples reached this strain rate, so some have been extrapolated for comparison. Creep results should not normally be extrapolated as the strain rate or creep mechanism could change outside of these regions and is only included here to compare a limited data set. Additionally, the condition of the GRCop-84 creep samples was not explicitly stated with the presented data, so comparison of the as-received and brazed GRCop-84 is based on de Groh's analysis. Their results revealed that GlidCop Al-15 had the best creep properties at high temperatures followed by brazed GRCop-84, similar to UTS and YS behavior [29]. AMZIRC, Cu-1Cr-0.1Zr, and Cu-0.9Cr's creep stress was significantly reduced after the simulated braze and were well below GlidCop and GRCop-84's creep stress at the same strain rate and temperatures. At similar temperatures and stresses, NARloy-Z's creep response is relatively poor and has been observed to have creep lifetimes up to a third of wrought GRCop-84's life [2].

Compared to GRCop-84, GRCop-42 has limited available creep data. Ellis and Michal's 1996 study compares the creep behavior of GRCop-84, GRCop-42, and NARloy-Z [27]. Though, these results are best used for qualititative comparisons. Specifically, both GRCop alloys' data were not consistent between tests, with over 2% strain difference between tests conducted at the same stress level in some cases and did not fit well to linear trends [27]. In general, GRCop-42's creep properties were slightly inferior but comparable to those of GRCop-84 [27]. Ellis and Michal noted that the as-extruded GRCop-84 showed limited stage III creep, as shown in the creep curves in Fig. 13.1.(b) from a 2017 study by Lerch et al. [115], whereas GRCop-42 was more likely to exhibit more stage III creep [27]. A more recent comparison of extruded GRCop-84 and -42 from Gradl et al. in 2019 [30] shows that the creep rate and lifetimes are similar, shown in Fig. 14.1. While there are some deviations, both alloys still demonstrate similar creep rates and lifetimes under the tested conditions [30]. Gradl et al. postulate that while the Cr_2Nb precipitates of the GRCop alloys prevent or reduce grain boundary sliding, grain growth, and grain boundary diffusion, the similarities in macroscopic creep properties are likely caused by the Cu matrix dominating the creep properties [30].

At this time there is little data available on the creep of AM GRCop with the exception of the work conducted by Gradl et al. [106] in 2017, which compared creep rates of L-PBF, wrought, plate, brazed plate, and sheet GRCop-84. Limited data is presented but a thorough discussion of the observed trends is provided instead. Compared to the other fabrication methods, the creep results of the L-PBF samples were more consistent, more repeatable, and better fit a linear trend [106]. Gradl et al. state that "… the properties

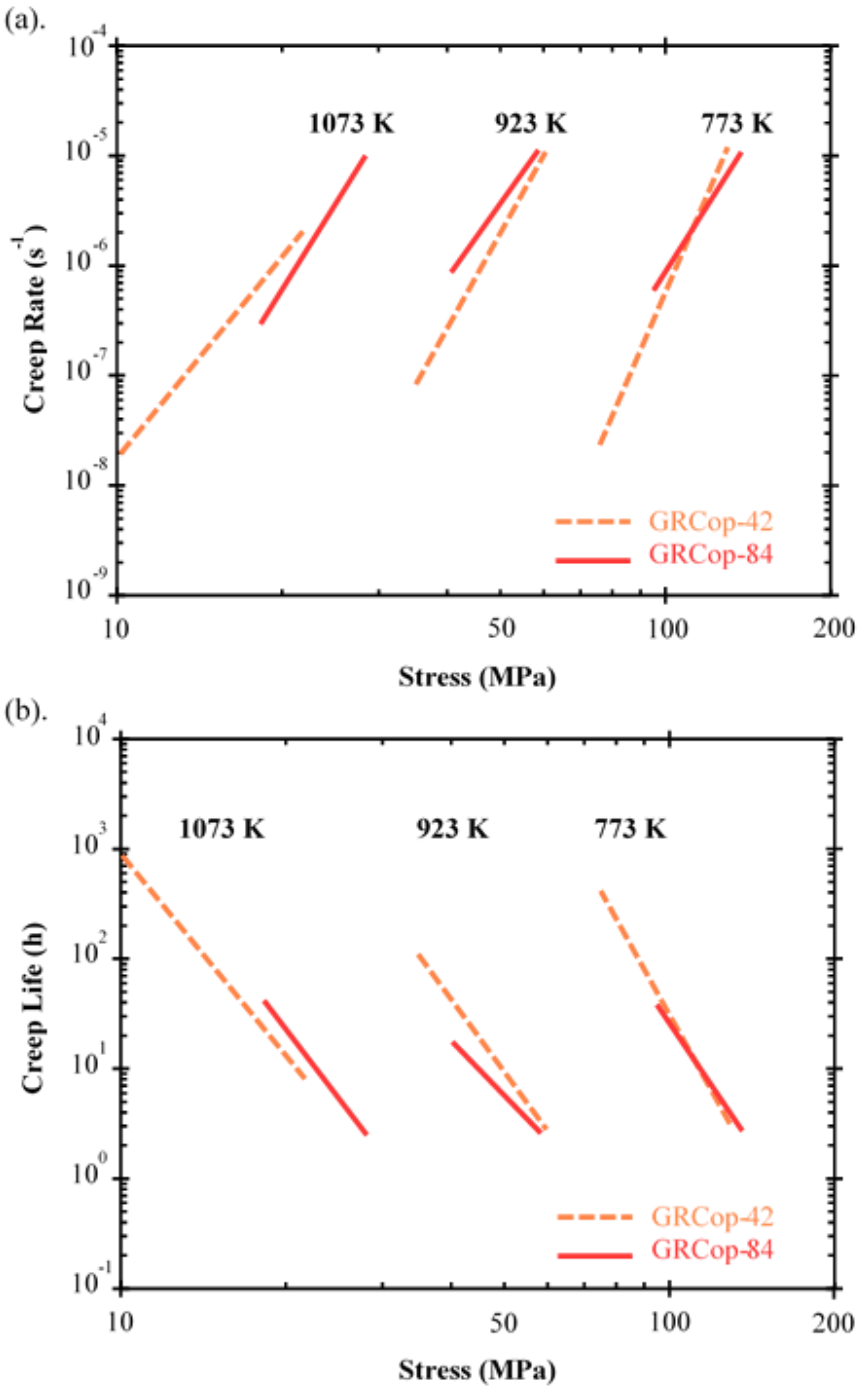

Figure 14.1. (a) - Creep rates and (b) creep lives of wrought GRCop-84 and GRCop-42 alloys; the GRCop-84 data is from warm rolled plate, rather than as-extruded, for higher consistency, and the GRCop-42 data is assumed to be as-extruded; redrawn with permission from [30].

Table 7.1. Power function constants for high-heat-flux Cu alloys (a) step loaded secondary steady state creep and (b) constant load, secondary, steady state tensile creep; with calculated stress based on the power function constants of the form $\dot{\varepsilon} = A\sigma^{n}$ converted to $\sigma = \sqrt[n]{\frac{\dot{\varepsilon}}{A}}$, where n is the stress exponent, A is the pre-exponential factor constant, $\dot{\varepsilon}$ is creep rate in units of s^{-1}, and σ is stress; reused from [29] with added calculated stress and some as-received data removed for clarity.

(a)	*Alloy*	*Condition*	*Temperature (K)*	*A*	*n*	*Estimated Step Loaded Creep Tensile Stress (MPa)*
	*GlidCop**	*As-received*	773	7.71E-57	22.93	153
	*GlidCop**	***Brazed***	773	3.72E-34	12.4	163
	*GlidCop**	*As-received*	923	4.58E-39	15.9	108
	*GlidCop**	***Brazed***	923	8.48E-38	15.5	101
	GRCop-84	*Not Specified*	773	4.77E-26	9.49	109
	GRCop-84	*Not Specified*	923	7.17E-24	10.32	46
	*AMZIRC**	***Brazed***	773	4.18E-13	3.73	51
	AMZIRC	***Brazed***	923	2.99E-11	3.65	17
	Cu-1Cr-0.1Zr	***Brazed***	773	5.94E-17	5.71	62
	Cu-1Cr-0.1Zr	***Brazed***	923	1.50E-14	5.52	26
	*Cu-0.9Cr**	***Brazed***	773	4.00E-14	5.08	29
	Cu-0.9Cr	***Brazed***	923	1.27E-10	3.83	10

(b)	*Alloy*	*Condition*	*Temperature (K)*	*A*	*n*	*Estimated Constant Load Stress (MPa)*
	*GlidCop**	*As-received*	773	2.392E-87	36.40	164
	*GlidCop**	***Brazed***	773	1.195E-205	91.21	152
	GlidCop	*As-received*	923	3.312E-61	26.74	109
	*GlidCop**	***Brazed***	923	2.762E-56	24.70	102
	GRCop-84	*Not Specified*	773	1.042E-22	7.67	121
	GRCop-84	*Not Specified*	923	3.400E-21	8.52	50
	*AMZIRC**	***Brazed***	773	1.633E-23	9.49	59
	*AMZIRC**	***Brazed***	923	2.141E-17	7.80	23
	*CuCrZr**	***Brazed***	773	2.489E-14	4.46	51
	CuCrZr	***Brazed***	923	8.059E-17	7.07	27
	CuCr	***Brazed***	773	7.363E-13	4.17	30
	CuCr	***Brazed***	923	6.047E-11	4.06	11

* Indicates that the stress has been extrapolated beyond the existing data and is only used for the purpose of comparison

of L-PBF GRCop-84 are equal to or exceed the properties of conventionally processed GRCop-84 with the exception of the LCF lives" [106] . Under the same level of stress, the creep rate of L-PBF GRCop-84 is roughly two orders of magnitude lower than that of wrought alloys. For example, the minimum creep rate at 40 MPa and 923 K is $3x10^{-9}$ s^{-1} for the L-PBF alloy and $3x10^{-7}$ s^{-1} for sheet GRCop-84 (when interpreted from its trend line) [106]. The L-PBF GRCop-84's creep exponent was comparable to the other fabrication methods which agrees with the previous Monkman-Grant relationships, and its dominant mechanism should be the same, although the exact value was not presented for a comparison [106]. Finally, while the creep rate is lower, the improved consistency is considered a major benefit to predicting the performance of the AM alloy [106]. The basic understanding of the origins of L-PBF GRCop-84's higher creep rate is a subject for future studies and can be potentially related to the characteristics of AM microstructure and defect structure such as (1) strong build texture and its relationships to build/creep directions, (2) AM defects such as gas porosity and lack-of-fusion defects, (3) grain morphology and grain boundary properties, and (4) the characteristics of precipitates.

Thermal Expansion

Thermal expansion is a primary factor when evaluating LCTF performance for high-heat-flux applications, especially in the case of the combustion chamber liner where the primary failure mode is driven by LCTF. Ellis stated that thermal expansion in the combustion chamber liner contributes the majority of the stress and strain rather than mechanical sources [2].The thermal expansions of NARloy-Z, AMZIRC, GlidCop Al-15, GRCop-84, and GRCop-42 are compared in Fig. 15.1. and Table 8.1. as a function of temperature. These alloys have similar thermal expansion characteristics which makes visual comparison and interpretation of the data difficult, so these are also presented as quadratic equation forms of thermal expansion as a function of temperature in Table 8.1. Of these alloys, both GRCop alloys' thermal expansion is consistently lower at temperatures exceeding 700 K which should aid in lowering thermal strain and producing longer LCTF lives. The GRCop alloys' thermal expansions are comparable up to 900 K, though GRCop-84's thermal expansion is slightly lower above 900 K which should be the result of its higher loading content.

Low-Cycle Fatigue Behavior

Similar to creep, there are currently only a few available studies on LCF of GRCop alloys and effectively none for LCTF. Mechanical fatigue is not the same as thermal fatigue, but mechanical fatique is more readily tested by LCF and the trends of LCF and LCTF are typically similar. Ellis and Michal's 1996 publication provides LCF results for only GRCop-84. This LCF experiment was strain controlled with a triangular waveform at a constant strain rate of 0.12 min^{-1} [27]. Unlike its creep data, GRCop-84's LCF results were more reproducible and consistent [27]. This is one of few publications to present LCF hysteresis loops, and two representative hysteresis loops from this study are shown in Fig. 16.1. The loops' shapes and slopes were noted to remain relatively constant and marginally increase in stress during cycling indicating minimal work hardening under the tested conditions [27]. Compared to NARloy-Z, Ellis and Michal found that GRCop-84's

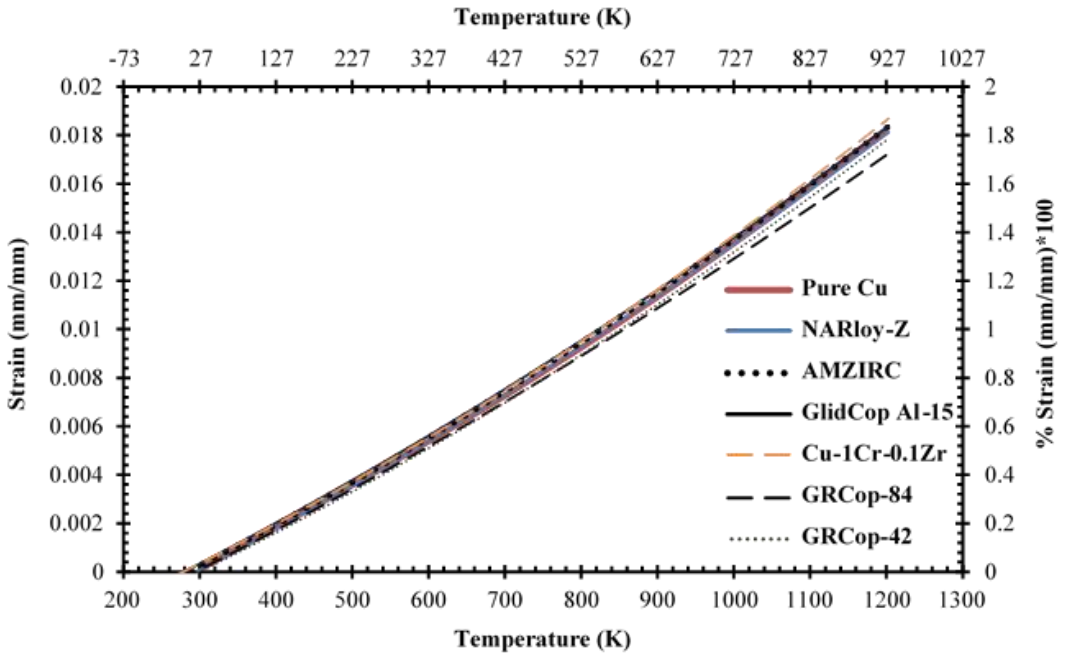

Figure 15.1. Thermal expansion calculated from quadratic equations included in Table 8.1.; adapted with permission from [2].

Table 8.1. Quadratic thermal expansion equations of high heat flux alloys where thermal expansion, α (mm/mm), is a function of temperature, T, in units of K from $\alpha(T)=A(T)^2+B(T)+C$; these values are accurate only above room temperature and should be considered estimates.

Alloy	*A*	*B*	*C*	*Approximate Calculated % Thermal Expansion, 100*(mm/mm) at 700 and 900 K*
Pure Copper[o]	4.718E-9	1.268E-5	-4.210E-3	0.74 – 1.15
NARloy-Z[*]	3.883E-9	1.414E-5	-4.498E-3	0.73 – 1.13
AMZIRC[**]	4.132E-9	1.384E-5	-4.257E-3	0.75 – 1.15
GlidCop, Al-15[**]	3.989E-9	1.401E-5	-4.223E-3	0.75 – 1.16
Cu-1Cr-0.1Zr[**]	4.947E-9	1.289E-5	-3.968E-3	0.75 – 1.16
GRCop-84[+]	3.420E-9	1.387E-5	-4.380E-3	0.70 – 1.09
GRCop-42[++]	4.718E-9	1.268E-5	-4.210E-3	0.70 – 1.10

Based on recommended values of average literature from [116]

[*] Estimated from graph of thermal expansion [15], assume ±5% accuracy

[**] Converted from quadratic equation where T (°C) and has ±1% reported accuracy [29]

[+] In the extruded condition with 95% confidence; converted from power law to quadratic equation [112]

[++] In the extruded condition; estimated from graph assume ±5% accuracy [30]

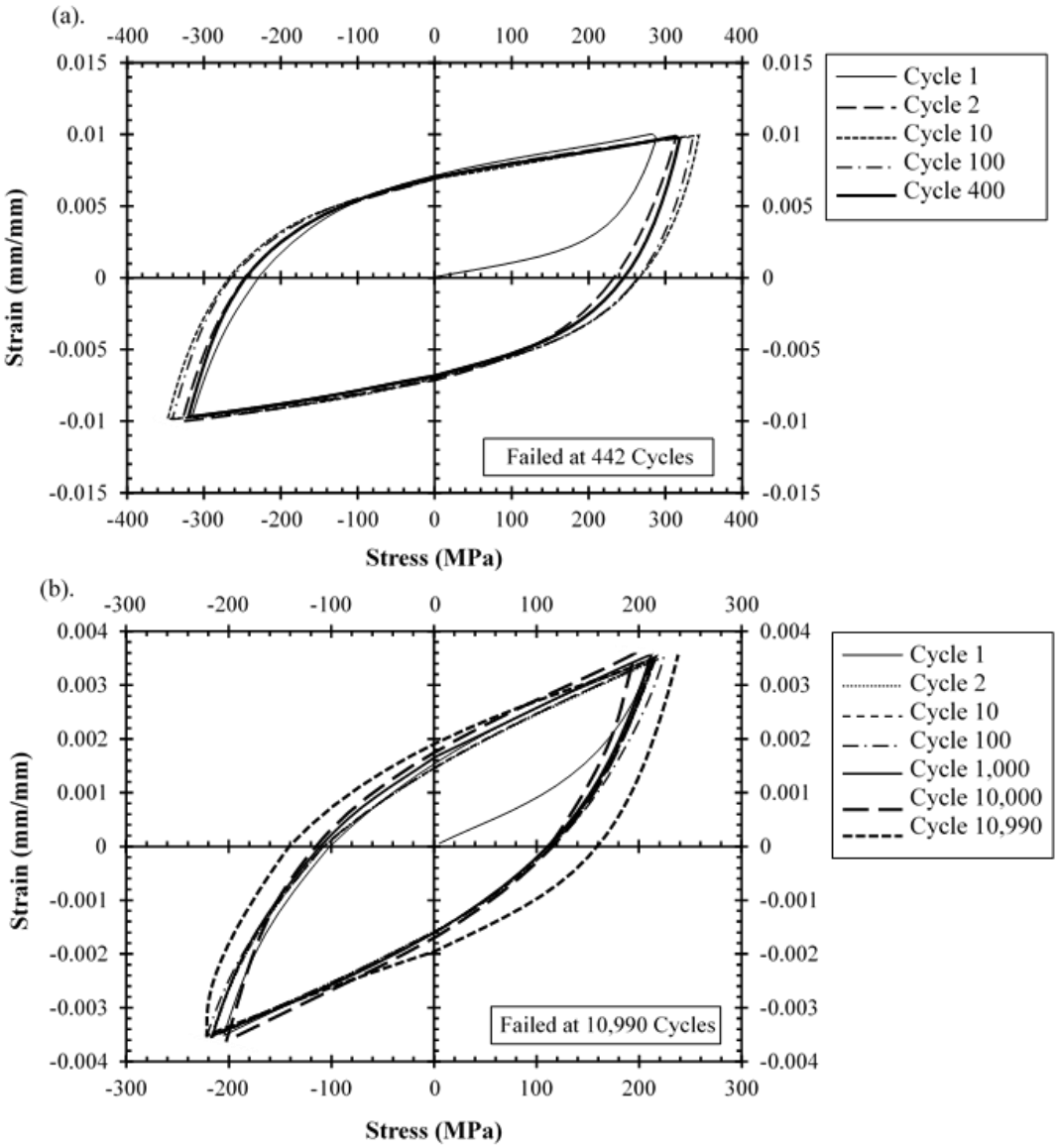

Figure 16.1. LCF stress-strain hysteresis loops (a) GRCop-84 tested at room temperature and 2% total strain; (b) GRCop-84 tested at 811 K and 0.7% total strain; data collected using strain-controlled fatigue tests with a triangular waveform at a constant strain rate of 0.12/min; redrawn with permission from [27].

LCF performance was either as-good or better depending on the degree of strain [27]. The relatively high volume fraction of hard Cr_2Nb particles are believed to be the cause of this increase, by either preventing or minimizing the development of persistent slip bands, NARloy-Z's particles are too low in volume fraction to have a similar effect [2, 27].

Gradl et al. also presented LCF results on wrought GRCop-84 and GRCop-42 at room temperature, 673 K, and 873 K with a fully reversed triangular waveform under strain control [30]. The GRCop alloys were tested according to the total strain range with plastic strain and shown in Fig. 17.1. [30]. Gradl et al. observed limited statistical difference or temperature dependence between the GRCop-42's strain data, so it was combined into a single trendline [30]. Gradl et al. observed that both alloys did not fail below 0.7% total strain and have nearly equivalent performance from a practical engineering perspective [30]. GRCop-84's strain data was similarly temperature independent with the exception of the 873 K data. The plastic strain, Fig. 17.1.(b), shows significant scatter for both GRCop-42 and GRCop-84 data points.

While the strain results were similar between the alloys, the stress range, Fig. 17.1.(c), shows the difference between the loading fractions. GRCop-84's stress is consistently higher than GRCop-42's, and the difference between them increases with temperature. As Gradl et al. indicate, this means that GRCop-42 has a lower load bearing capacity, consistent with the GRCop-84's higher strength [30]. These tests are not a full representation of the combustion chamber liner because mimicking the liner environment in standardized test equipment is not feasible. The liner's LCF is primarily LCTF where thermal expansion should play a significant role, though, as Fig. 14.1. shows, the GRCop-84 and -42's thermal expansions are largely similar up to 873K. Compared to GRCop alloy's UTS, YS, thermal conductivity, and creep response, GlidCop appears to be a better choice for high-heat-flux applications like the combustion chamber liner. However, fatigue is a major failure mode in combustion chamber liners, and GlidCop Al-15's fatigue behavior has been described as poor, particularly at high temperatures, compared to GRCop-84 by several sources [2, 29, 96, 101]. Similar to creep, LCF results are difficult to compare due to the variety of factors, and a comparison of GRCop alloys and GlidCop in the same source could not be located. Takahashi et al. [117] performed LCF tests on GlidCop Al-15 similar to the experiment presented by Gradl et al. [30]. At a total strain range of 1% under vacuum and at 473, 543, and 673 K, GlidCop Al-15 failed at approximately 6000, 3000, and 1500 cycles, respectively [117]. Based on the Fig. 17.1. at the same strain, GRCop-84 fails at approximately 6000 cycles between room temperature and 673 K and 5500 cycles at 873 K compared to GRCop-42 which fails at 4500 cycles between room temperature and 873 K [30]. GRCop alloys demonstrate significantly longer lives than GlidCop Al-15 which is in agreement with previous assessments.

Environmental Resistance

Outside of creep and LCTF, the combustion chamber liner's remaining concerns, stemming from the harsh environment, are resistance to H embrittlement and oxidation. High volumes of liquid and high pressure gaseous hydrogen in the combustion chamber liner is a major concern. The Nb content of GRCop alloys is known to be the most susceptible component to embrittlement by forming a solid solution and hydrides with

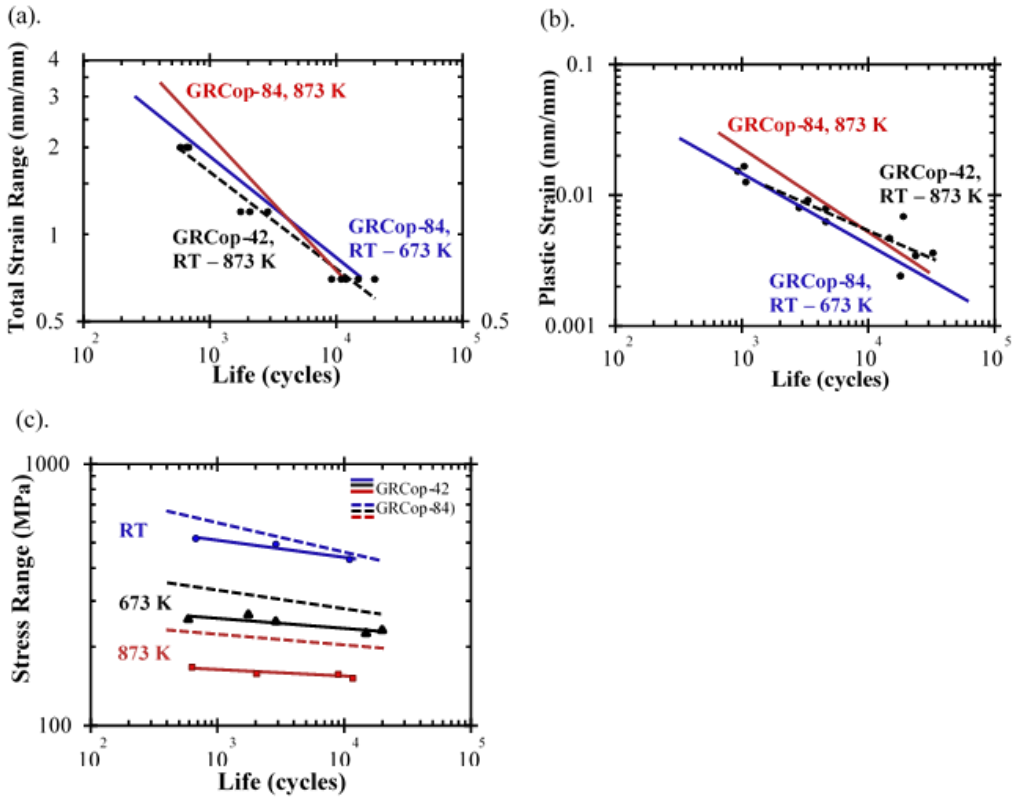

Figure 17.1. LCF trends of extruded GRCop-42 (reported as wrought) with data points and GRCop-84 from [30, 106] (a) LCF strain ranges; (b) LCF plastic strains; (c) LCF stress range; RT - 673 K and RT - 873 K indicate that data has been combined from these temperatures to produce these trend lines (as there was no discernible difference in trend between them); redrawn with permission.

hydrogen [118-120]. Ellis et al. [120] performed thermodynamic calculations with GRCop-84 based on activity and partial pressures. The primary conclusion from this study was that the chemistry of the Cr_2Nb precipitates would control, by reducing, hydrogen embrittlement. By adding an excess of Cr, the activity of Nb is reduced along with the risk of hydrogen embrittlement [118, 120]. Ellis and Hastings performed tensile, notched tensile, stress, rupture, and LCF tests on extruded GRCop-84 in high pressure environments including high pressure H_2, high pressure He, and samples charged in high pressure H_2 for 8 h at 922 K [119]. They were unable to find evidence of the formation of hydrides by either optical or electron microscopy, changes in fracture morphology, or statistically significant difference in the mechanical tests [119]. The susceptiblility may change slightly between GRCop alloys and fabrication methods and should be tested, but ultimately, the H embrittlement is largely dependent on the Nb content that is available. The slight excess of Cr appears to be sufficient to consume the majority of the Nb in forming the intermettalic Cr_2Nb leaving GRCop-84 with good stability in hydrogen environments.

Rocket combustion chamber liners made with NARloy-Z were susceptible to blanching during operation, so extruded GRCop-84's oxidation behavior was investigated by Thomas-Ogbuji and Humphrey and compared to NARloy-Z and OFHC Cu with thermogravimetric analysis (TGA), scanning electron microscopy, electron dispersive spectroscopy, and X-ray diffraction [68, 121]. They found that the alloys had similar oxidation rates at or above 1023 K, but at intermediate temperatures closer to the operating temperatures between 773 – 1023 K, GRCop-84 exhibited significantly higher oxidation resistance [121]. In a later study, Thomas-Ogbuji and Humphrey determined that GRCop-84's enhanced resistance is time dependent and longer exposures result in a greater difference compared to the other alloys [68]. These results are likely tied to the formation of stable Cr or Nb oxides on the surface which require lower temperatures and longer times to form an outer barrier. Thomas-Ogbuji and Humphrey determined likely oxide candidates from X-ray diffraction data collected on oxide scale removed from their samples [121], but changes in the powder chemistry and fabrication methods are likely to have changed this list of candidates and should be reassessed. The reduced Cr and Nb content of GRCop-42 may reduce the formation and efficacy of the oxide layer.

Summary and Future Prospects

Several microstructural trends are apparent when comparing the state-of-the-art high-heat-flux Cu alloys and Cu metallurgy presented in this review that help understand the essential qualities for optimizing high-heat-flux performance. Thermal conductivity is critical and should be preserved by reducing impurities in the FCC Cu matrix. Higher thermal conductivity results in lower operating temperatures which helps prevent thermo-mechanical instability. Conventional alloying limits the fraction of alloying content to preserve thermal conductivity, so their strengthening instead relies on reducing the size of microstructural features. Below 773, GRCop alloys' have lower thermal conductivity and mechanical strength compared to other alloys but has a highly stable microstructure due largely to the high alloying content of Cr_2Nb which is resistant to coarsening and prevents recrystallization of the microstructure. In high-heat-flux applications with

operating temperatures above 773 K and significant LCF concerns, GRCop alloys are among the best available. Cu-rich Cu-Cr-Nb alloys, like GRCop, have potential for use in the next generation of aerospace rockets and structural high-heat-flux applications where reusability and long-term use are desired. Small capability improvements achieved by replacing an existing material can translate to large economic savings and enhanced safety margins and design freedom. In high-heat-flux applications, GRCop-84 and GRCop-42 have similar properties and performance, however GRCop-84 exhibits slightly higher mechanical strength while GRCop-42 exhibits slightly higher thermal conductivity. More statistically relevant data, microstructure information, and cost metrics will help determine which should be chosen for any given application though both have merits.

GRCop alloys have potential in future space-oriented or high-heat-flux applications, e.g. resistance welding electrodes and holders, permanent metal casting molds, vacuum plasma spray nozzles, and fusion reactor first walls. Fusion reactor first walls carry an additional irradiation concern with the Nb content of GRCop alloys because Nb can cause H embrittlement by absorption of tritium or deuterium [122]. As long as the Cr excess is sufficient in suppressing the formation of Nb by consuming it in forming Cr_2Nb, this should not be an issue, but the long term effects and low level waste requirements need to be fully exhausted before practical use. As candidate combustion chamber liner alloys, AM GRCop has shown unique potential for liner fabrication when compared to conventionally wrought material. After HIPing, fully-dense AM GRCop-84 liners have been produced faster and with properties equal to or better than their wrought counterparts. AM of GRCop alloys combined with the intricate geometries of combustion chamber liners represents a rare case where AM provides optimal processing. The greatest advantage AM provides is the ability to manufacture built-in cooling channels. New cooling channel designs with thinner walls and more customizable paths, impossible by traditional machining constraints, will improve the cooling efficiency and design constraints of liners. One development is the cooling channels can be wrapped around the liner and split from one channel at the bottom to three at the top rather than being machined straight down the walls [106]. However, both cooling channel design developments introduce new wall thinning and stress concentrating concerns. L-PBF's surface finish is relatively poor as it is limited by multiple factors including the quality, size, and sintering of the powder which can serve as crack initiation regions in fatigue, particularly LCF [123]. The exterior of parts can be polished to alleviate these concerns, but internal channels are not easily inspected or smoothed. These concerns must be addressed in qualification testing, and the improved cooling efficiency provided may lower the temperature sufficiently to reduce fatigue. The composition of GRCop alloys is also likely to be optimized or adjusted in the future for either cost or performance reasons. Ellis et al. [124] have shown that relatively low 0.1 – 0.5 wt% additions of Zr in extruded GRCop-84 (to GRCop-84Z) can improve the mechanical properties through the formation of Cu_5Zr precipitates [8, 124]. These Cu_5Zr precipitates are smaller than the Cr_2Nb precipitates and add 2 vol. % more to the existing 14 vol.% of Cr_2Nb precipitates in GRCop-84 and are estimated to improve the strength by 23 – 39% [8, 124]. The thermal conductivity is expected to decrease from new potential scattering centers, but

conductivity results have not been published [8, 124]. It is unknown how additions of Zr would interact in L-PBF and future testing and characterization is necessary. The additions of Zr demonstrated improved creep performance and elongation compared to extruded material, and HIPed L-PBF GRCop-84 has demonstrated similar improvements, so it is unknown if Zr will significantly benefit L-PBF GRCop.

It is the opinion of the authors that there are potentially three main obstacles to the development of GRCop alloys for future and current scientists and researchers. The first is that the current literature of GRCop alloys is somewhat limited; past experiments should be reproduced and expanded with updated GRCop alloys, and AM GRCop needs considerably more research. Secondly, the literature lacks a thorough, empirical assessment of microstructure-property relationships for AM GRCop alloys. Comparisons of wrought and AM material may help to better understand the microstructure-property relationships. A prime example is understanding why the creep results of AM GRCop have less scatter than wrought. The last obstacle is a need for more interest in GRCop alloys by industry and researchers outside of NASA. Expansion of the literature and understanding of the alloy will likely bring in new researchers who may elucidate the principles supporting these observations and add to the literature.

Acknowledgements

The authors would like to acknowledge the Manufacturing and Materials Joining Innovation Center (Ma^2JIC), made possible through awards NSF IIP-1540000 (Phase I) and NSF IIP-1822186 (Phase II) from the National Science Foundation Industry University Cooperative Research Center program (IUCRC). RMC also acknowledges the financial support of the Center for Materials Processing at the University of Tennessee, Knoxville and Oak Ridge National Laboratory's Graduate Opportunities (GO!) Program. Special thanks to David Ellis of NASA GRC and Paul Gradl of NASA MSFC for their discussions and comments on this review and historical information as well as various NASA staff who have supported this project.

CHAPTER II
MICROSTRUCTURE CHARACTERIZATION OF LASER-POWDER BED FUSION (L-PBF) CONSOLIDATED GRCOP-84

A version of this chapter is intended for separate publication under the same title at a future date with the current co-authors in a future journal article.

This work is co-authored by Robert P. Minneci [1], Michael P. Haines [2], Paul R. Gradl [3], David L. Ellis [4], Eric A. Lass [1], Jeffrey R. Bunn [5], Hahn Choo [1], Zachary C. Jones [3], Suresh S. Babu [1,2], and Claudia J. Rawn [1]

[1]Department of Materials Science and Engineering, University of Tennessee, Knoxville, Tennessee 37996-2100, U.S.A. [2]Mechanical, Aerospace, Biomedical Engineering Department, University of Tennessee, Knoxville, TN 37996-2100, U.S.A. [3]NASA Marshall Space Flight Center, Huntsville, Al 35808, U.S.A. [4]NASA Glenn Research Center, Cleveland, OH 44135, U.S.A. [5]Neutron Scattering Division, Oak Ridge National Laboratory, Oak Ridge, Tennessee 37831-6475.

The article has no current changes but is expected to have minor changes in its future publication. RPM wrote the initial manuscript draft, and all authors contributed to the final manuscript. CJR contributed to collection of data, editing, direction, and writing throughout. MPH contributed writing to the analysis of the results and writing of the initial draft. PRG, DLE contributed editing and analysis of the metallographic results and methods. EAL, JRB, and HC contributed editing of the entire paper and analysis of the metallographic and diffraction-based results. ZCJ contributed early direction, fabrication of samples, and support. SSB contributed resources, direction, editing, and analysis of the metallographic result and methods.

Abstract

GRCop-84 or Cu-8Cr-4Nb (at%) samples with simple geometries were built with laser-powder bed fusion (L-PBF). In order to evaluate the microstructure, specimens were sectioned to produce cross-sections parallel or perpendicular to the build direction and were compared in the as-built and hot isostatically pressed (HIP) conditions. The microstructure and phase evolution were evaluated with optical microscopy, scanning electron microscopy (SEM), electron backscattered diffraction (EBSD), high temperature X-ray diffraction (HTXRD) up to 1223 K, and time-of-flight (TOF) neutron diffraction. The as-built specimens demonstrated a heterogeneous nucleation with mixed columnar and equiaxed grains dependent on the laser weldment geometry. Cr_2Nb precipitate particles were dispersed uniformly throughout but are expected to serve as nucleation sites and promote the formation of equiaxed grains. Gas-atomized GRCop-84 powder from the same build lot as the samples was compared in HTXRD along with as-built and HIPed solids. HTXRD revealed unusually low phase fractions of Cr_2Nb in both the powder and as-built samples and high residual stress in the Cu matrix that was annealed between 473 and 873 K. Following HTXRD, the as-built phase fraction of Cr_2Nb was increased to the expected alloying fraction. The HIPed samples showed evidence of recrystallization and the presence of Cr-rich particles that precipitated from the Cr_2Nb particles and/or Cu matrix grains, and no annealing behavior was demonstrated during HTXRD.

Introduction

GRCop-84 or Cu-8Cr-4Nb (at%) is an alloy developed originally in the 1980s for the Space Shuttle Main Engines' combustion chamber liners and similar structural high-heat-flux applications. The GRCop notation represents Glenn Research Copper and reflects NASA Glenn Research Center's (NASA GRC) efforts in developing Cu-rich Cu-Cr-Nb alloys, and includes GRCop-42 also known as Cu-4Cr-2Nb (at%). GRCop alloys are currently being developed and considered for use with rocket projects like the Space Launch System (SLS) through NASA's Low Cost Upper Stage-Class Propulsion (LCUSP) effort and Rapid Analysis and Manufacturing Propulsion Technology (RAMPT), and thermonuclear fusion reactor components including novel lower hybrid current drive (LHCD) radio-frequency (RF) launcher designs [12, 30, 125]. GRCop-84 provides higher strength and better fatigue properties than GRCop-42 which are desirable for applications requiring reusability. Although GRCop-42 has seen a significant increase in interest recently, GRCop-84 has been the focus of most development and is the subject of investigation for this study.

Structural high-heat-flux applications require high thermal conductivity, retention of mechanical strength at high temperatures, and resistance to fatigue and creep. One example is re-usable rocket combustion chamber liners which have extreme conditions with heat flux on the order of 100 MW m^{-2}, in-service temperatures ranging from 673 – 973 K, and considerable low-cycle fatigue (LCF) and creep [126]. The best performing Cu alloys typically listed for these applications include NARloy-Z, AMZIRC, GlidCop, Cu-Cr, Cu-Cr-Zr, and GRCop alloys. The typical methodology behind these alloys is to strengthen the Cu matrix with minimal alloying content, usually less than 1 wt%, to preserve Cu's high thermal conductivity. Higher thermal conductivity results in better cooling efficiency and lower operating temperatures; however, the compromise is that these alloys are often subject to long- or short-term thermal and mechanical creep and fatigue issues. GRCop-84 contains roughly 8 wt% Cr and 4 wt% Nb which is unusual compared to the other alloys; for comparison, NARloy-Z has the second most at 3 wt% Ag and 0.5 wt% Zr. The 12 wt% of alloying content limits GRCop-84's thermal conductivity, and other alloys outperform GRCop-84 below 773 K as a consequence. However, GRCop-84's highly stable microstructure results in better performance above 773 K, up to 1073 K. Longer lifetimes result in increased reusability of rocket components which has significant cost-benefits, and higher allowed temperatures improve safety margins and fuel efficiency.

GRCop alloys are produced by rapid solidification through gas atomization followed by powder metallurgy routes [126]. Cr and Nb have low solid solubility in Cu and preferentially form C15 Laves Cr_2Nb, and rapid solidification is necessary to limit their growth which also reduces the size of the Cu matrix grains [2, 9, 90, 127]. Typical GRCop microstructures consist of a largely pure Cu matrix grains and distinct, μ scale C15 cubic Laves (Cr_2Nb) precipitate particles. A slight excess of Cr is added in alloying to prevent Nb precipitates from forming which could cause embrittlement under an H-rich atmosphere [128]. A variety of wrought consolidation methods have been applied to GRCop-84, including extrusion, metal spinning, vacuum plasm spraying, and tube drawing, but these methods are limited for high-heat-flux applications due largely to

geometry restrictions [2, 126]. In contrast, additive manufacturing (AM) allows for near net-shaped production of complex geometries with internal geometries that are unachievable by traditional methods and provide a significant improvement to performance. Recent efforts with AM GRCop-84 through laser-powder bed fusion (L-PBF) has provided evidence that AM is arguably the best available consolidation method for GRCop-84 [12, 30, 106, 107]. Additional background on high-heat-flux applications and the development of GRCop alloys can be found in a review [126].

Overview of L-PBF

L-PBF is a general term for AM techniques that combine laser melting technology with powder bed fusion (PBF) [129]. For clarity, this term will be used to replace another commonly used term, selective laser melting (SLM), a registered trademark, and L-PBF will only refer to laser methods that fully melt the feedstock. L-PBF is distinguished from other PBF techniques including electron beam melting (EBM) and laser sintering (LS) by fusion method and hardware. PBF systems consist primarily of a powder bed that rests on top of a build platform where powder is selectively fused together, a piston to lower the fused layer, and method to redistribute powder on top of the previous layer for successive fusion [129]. In L-PBF, fusion is achieved by fully melting metallic powder with a complete melting/solidification mechanism [130]. To ensure full melting, L-PBF uses thin layers, high laser power, and small focused laser spot sizes for higher energy density necessary for full melting [130]. Thinner layers and smaller laser spot size allow for a higher degree of geometry control, but the build times can be significantly longer. Full melting allows for production of near- or fully dense components requiring less post-processing. The disadvantages of L-PBF's high energy density and melting includes significant concerns regarding melt pool instability, shrinkage, and complex thermal residual stresses that can cause premature failure in builds through crack formation, delamination, and other defects [131]. Process parameters and laser scan strategies can help alleviate these concerns but are rarely sufficient to negate them.

L-PBF is essentially a micro-welding technique with resulting solidification grain structures similar to those seen in welding but on a smaller scale. As the laser beam passes over the build area, a melt pool forms which will fully melt the powder in its path and partially melt the previous layer and surrounding area. This is similar to a fusion weld, and the previous layer serves as a crystallographic template for solid fusion zone growth [132-134]. When the laser passes, a localized solidification process occurs spontaneously beginning with epitaxial growth where the solidifying grains orient their crystal structure with respect to the molten pool border, which acts as nucleation sites, and competitively solidify towards the center of the melt pool [131]. Face-centered cubic metals, including Cu, have preferred growth along the <100> family of crystallographic directions, suppressing growth in other orientations [131, 132, 135]. Horizontal growth (relative to the build direction) is similarly suppressed and elongated grain growth is favored resulting in a low probability of nucleation in the liquid ahead of the columnar zone [131, 136].

Classical welding solidification parameters apply to L-PBF and can be taken advantage of to influence the final microstructure. The two parameters commonly used to

understand solidification are temperature gradient, G, and the solid/liquid interface growth rate, also referred to as solidification rate or interface velocity, R. Both G and R are functions of position and time, and these terms are typically used as a ratio, G/R, to demonstrate the grain solidification morphology [132]. At the fusion line, the solidification rate, R, will be roughly zero as the previous layer has already solidified and will be unaffected by the laser pass, resulting in a G/R ratio that is effectively infinite and results in a planar-dominated grain structure at the bottom of the melt pool [131]. The interface then transitions sequentially into a cellular, columnar dendritic, and equiaxed dendritic interface as the ratio of G/R decreases. The exact G/R ratio necessary to switch between transitions is dependent upon a variety of factors including undercooling, solute diffusion, slope of the liquidus curve, nominal alloy composition, and equilibrium partitioning [135].

Typical L-PBF microstructures have either columnar or mixed columnar and equiaxed grain structures indicating that the solidification interface is mostly columnar dendritic and equiaxed dendritic, supporting the preference of epitaxial growth. Equiaxed grains are desirable for their higher degree of mechanical strength, and the preference for equiaxed grain formation can be adjusted by decreasing the ratio of G/R and increasing G*R through build parameters and additives. G*R has the same principle as rapid solidification; the higher the temperature gradient and solidification rate, the smaller the grain structure. This is why equiaxed grains are typically observed at the top of the laser path. Both the effect of L-PBF build parameters and additives are well reviewed by Zhang et al. [131], but generally, faster scan speeds and lower energy densities promote equiaxed grain growth. Additives, usually as nano-scale material impurities, promote equiaxed grain formation by serving as nucleation sites and help increase the solidification rate.

Current L-PBF GRCop-84 Efforts

Gradl et al. have successfully demonstrated GRCop-84 and GRCop-42's viability with L-PBF on conventional systems [30, 106]. Conventional L-PBF systems use infrared Nd:YAG or fiber lasers that are not usually compatible with Cu because Cu preferentially reflects infrared light (1 μm) preventing heating, and therefore melting, of the powder [105, 137]. This can be circumvented by changing laser parameters or using a shorter wavelength green laser (515 nm), however, this is not necessary with GRCop alloys, due likely to the alloying content. Gradl et al. hypothesize that this is possible due to the high loading of Cr and Nb which lowers the initial reflectivity sufficiently to absorb heat in the powder and initiate melting [106]. Reflectivity lowers as a function of temperature, and as the powder heats, more energy can be absorbed and initiate melting, though this should be effectively instantaneous. NASA is currently producing near fully dense, full-scale serviceable hardware with GRCop alloys with both AM and post-processing parameters developed largely by efforts at Marshall Space Flight Center (MSFC) [108]. Typical post-processing includes annealing and hot isostatic pressing (HIP) under Ar to relieve thermal residual stresses and shrink porosity. NASA's HIP parameters have been shown to be effective by Carter et al. [138]. While HIP adds significant post-processing cost, it is specified by NASA for L-PBF builds to ensure consistency and qualification [139].

NASA's L-PBF GRCop-84 processing parameters are at a development stage where they are optimized to fabricate reproducible parts and are becoming standardized for NASA's purposes. The parameters produce parts with low probability of failure during the building process with properties better or equal to traditionally fabricated components. However, the structure-processing relationships involved with L-PBF and GRCop-84 are not fully understood which limits the understanding of the performance and properties.

Microstructure Predictions

The GRCop powder feedstock used in NASA's L-PBF efforts is effectively the same as traditional powder metallurgy routes, Ar gas-atomized powder. The powder has a bimodal distribution of Cr_2Nb particles with primary precipitate particles on the order of 1 μm that form during solidification and secondary 10-100 nm that precipitate out of solution during cooling [2, 126]. In most GRCop-84 powder-processing routes, the bimodal distribution remains after consolidation with either a slightly reduced size from break-up of larger particles or slight overall growth from coarsening during heating events like those in hot rolling or secondary annealing. Based on results of wrought GRCop-84, the as-built L-PBF microstructure is hypothesized to be similar to the powder with a bimodal particle distribution. However, L-PBF has a full melting stage, unlike most powder metallurgy routes. If the melt pool temperature exceeds the melting temperature of Cr_2Nb (~2006 K), then it is possible that the precipitate particle distribution is likely to change. However, the cooling rates of L-PBF are expected to be comparable to gas-atomization, so the bimodal distribution of the powder is expected to remain. Exact cooling rates have not yet been measured for L-PBF GRCop-84 or Ar gas-atomized GRCop-84, but typical L-PBF cooling rates are approximately 10^6 K s^{-1} while Ar gas atomization ranges from 10^5-10^6 K s^{-1} [140, 141]. The Cu matrix grain structure is expected to be strongly influenced by the processing and resemble typical L-PBF microstructures with dominant columnar grains through the build height. GRCop-84 has a significant amount of precipitates which are expected to solidify well before the Cu matrix grains that have a melting temperature of roughly 1358 K. The high density of particles will likely serve as nucleation points and promote equiaxed grain formation. At 14 vol% and μm to nm scale precipitates, it would be difficult to produce a uniformly columnar microstructure with L-PBF. While the grain structure is not clearly defined, Hayes et al. [103] revealed distinct laser weldments in as-built L-PBF GRCop-84. The matrix grain shape and orientation should be dependent upon the laser path velocity and overlap. Hayes et al. also showed that the edges of the laser weldments have a high density of precipitate particles [103]. This demonstrates a bias in the particle distribution caused by the laser motion, and the matrix grains may be affected by regions with different particle densities.

Following HIP, the matrix grains and precipitates are expected to grow minimally based on previous high temperature experiments by Anderson et al. [110] on extruded GRCop-84 . GRCop-84 has a relatively low recrystallization range between 473-873 K, so the HIPed material is expected to be in an annealed state [104, 126]. Equiaxed grains are expected to form from columnar grains due to recrystallization which is a common observation in columnar grain dominated AM microstructures. Song et al. [142] with L-

PBF iron and Brandl and Greitemeier with wire-fed directed energy deposition (DED) Ti-6Al-4V [143] have demonstrated this phenomena. Typically, cold working is necessary to provide the driving force for recrystallization, but it is theorized that thermal residual stresses generated during AM can provide the driving force [129].

The goal of this paper is to provide microstructural characterization and analysis to support future L-PBF efforts with GRCop-84. Gas atomized powder, as-built L-PBF solids, and HIPed L-PBF solids are investigated to assess the effect of processing and provide evidence to support or disprove the predictions.

Materials & Methods

Sample Geometry and Conditions

L-PBF GRCop-84 samples were fabricated at NASA MSFC on a Concept Laser M2 using the build parameters summarized in Table 1.2. Ar-gas atomized powder was also provided from the same powder lot for characterization.. The L-PBF samples characterized were either 10 mm cubes or 10 x 10 mm^2 pillars with heights of 22 and 40 mm's. As part of the L-PBF process, a layer of Inconel 625 was printed onto the stainless-steel build plate on a separate additive system, the build plate was cleaned of powder, and then the GRCop-84 build was started on top of the Inconel layer. Prior work [30] has shown that GRCop-84 did not wet or adhere well to the build plate but was compatible with Inconel 625. The Inconel 625 remains behind on the build plate when the part is wire electrical discharge machined (EDM) from the build plate and limited diffusion is expected to occur. All samples were removed from the build plate by wire EDM and were either in the as-built condition or HIPed under Ar.

Various geometries of the samples are shown in Fig. 1.2.(a) with additional cube samples used in future studies. Visually, the surface finish is of high quality compared to most additive methods with no observable external abnormalities. The sides of the samples are relatively smooth, and the chess scan strategy used to produce the samples is observable on the top surface from differences in the roughness caused by the laser being rotated 45°, shown in Fig. 2.2. with respect to the sample edges. Figure 2.2. further demonstrates how the laser path's rotation and direction is changed between layers and overlapping regions. The surface of the HIPed samples were significantly darker which is likely caused by the formation of a thin oxide layer. The oxidation effect is only visible on the surface and can be readily removed with simple polishing methods.

Chemical analysis was conducted at NASA GRC to estimate the elemental fractions present in the as-built condition samples from the same lot as described here. These are presented in Table 2.2. The results were well within the target composition and are unusually pure. At 10 ppm, the Fe content was significantly lower the target of 50 ppm, and O could not be detected reliably. Some additional impurities were present but totaled ~14 ppm.

Micrographic Analysis

Microscopy samples were wire EDMed parallel or perpendicular to the build direction (referred to as XY where Z represents the build direction), mounted, and ground

Table 1.2. Laser parameters used with Concept Laser M2 for the experimental samples.

Parameter	*Setting*
Core Laser Power	178 W
Core Scan Speed	585 mm s^{-1}
Hatch Spacing	0.105 mm
Layer Thickness	0.030 mm
Scan Pattern	Chess

Figure 1.2. L-PBF GRCop-84 samples built on a Concept Laser M2 (a) 4, 7, 10, and 20 mm cubes and 10x10x40 mm pillars and (b) top of a 20 mm cube.

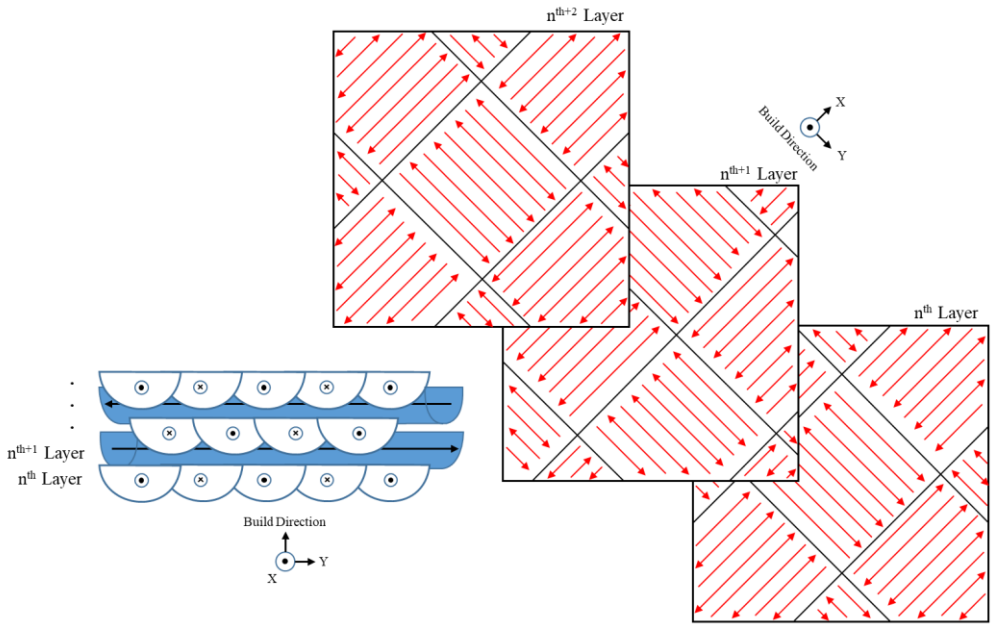

Figure 2.2. Schematics demonstrating the idealized weld pool overlap in the X-build direction plane and X-Y plane showing an example of a possible pattern shift; X and Y are arbitrary but orthogonal to the build direction.

Table 2.2. Comparison of experimental and target compositions of GRCop-84 samples.

Element	*Cu*	*Cr (wt%)*	*Nb (wt%)*	*Fe (ppm)*	*O (ppm)*	*Other (ppm)*
Experimental	Bal.	6.47	5.78	10	---	<14
Target	Bal.	6.2 - 6.8	5.4 - 6.0	<50	<400	<100

to 4000 grit SiC paper on an autopolisher. The samples that were cut parallel to the build direction (XZ or YZ) were sectioned square with the sample edges. XZThe ground samples were polished to 0.5 μm with a diamond suspension and finished with a vibratory polisher and colloidal silica (Syton HT-50). Electron back-scattered images were collected with a Phenom ProX scanning electron microscope (SEM) at 15 kV. Electron backscatter detection (EBSD) mapping was conducted with a TESCAN MIRA 3 instrument. The EBSD maps were collected at 800x magnification with a step size of 250 nm, sample incline of 70° to the incident beam, working distance of 20-25 mm, beam intensity of 20 kV, current of 2.3 nA, and spot size of 26 nm. C15 Cr_2Nb could not be readily refined in the EBSD, so only FCC Cu is refined in the maps. Cr_2Nb is visible, but as black, unrefined dots in the EBSD maps.

X-ray and Neutron Diffraction

X-ray diffraction data were collected on as-built, HIPed, and powder GRCop-84 samples with a Malvern PANalytical Empyrean X-ray diffractometer with a PIXcel detector. For in-situ high temperature X-ray diffraction (HTXRD) experiments the samples were contained in an Anton Paar HTK1200N environmental chamber. The incident beam was Cu radiation with a wavelength of ~1.54 Å with a radius of 240 mm, soller slits of 0.02 radians, mask of 10 mm, and fixed divergence slit of 1/8°. The diffracted beam has a similar radius, anti-scatter slit of 0.25°, and soller slit of 0.02 radians. HTXRD data were collected at 1223 K with a temperature ramp of 3 K min^{-1} with data collected every three minutes. The HTXRD data collected on the powder sample was conducted to a lower maximum temperature of 1223 K to ensure the powder remained in the solid state. Melting was avoided to prevent additional cleaning and potential damage to the instrument. Data was collected over a narrow range of 35-53 °2θ during ramping to allow for the short time period to produce interpretable results. This range provided two primary Cu peaks (111) and (200), two Cr_2Nb peaks, and other present phases. Samples for X-ray diffraction were sectioned from pillar samples, both from as-built and HIPed samples, conditions with a laboratory saw perpendicular to the build direction to produce a 10 x 10 mm^2 cross-section and lightly polished by hand to a consistent surface to remove any artifacts. Long scans up to 100 °2θ were collected at room temperature prior to heating, at the maximum respective temperature, and again at room temperature after cooling down. The HTXRD samples were held at their maximum temperature for approximately 10 minutes before collecting a long scan to help achieve equilibrium. Although HTXRD was conducted under vacuum, the surface of each sample had significantly oxidized from oxygen trapped within the system after heating. Repeated purging may have helped reduce this effect, but the oxidation effect is also of interest. The surfaces were removed with a high grit grinding paper and a room temperature diffraction profile was collected under the same conditions; this could not be repeated for the powder sample. Time-of-flight (TOF) neutron powder diffraction data were collected on as-built and HIPed samples, from the same build lot, using the VULCAN beamline at Oak Ridge National Laboratory's Spallation Neutron Source (SNS). The TOF results are used solely for comparison. XRD is a strictly surface-level technique, and neutron diffraction should provide a more accurate representation of the bulk composition since

more of the volume is measured. The remainder of the TOF results will be presented in future work.

Analysis of the X-ray data was performed with the second iteration of the General Structure Analysis system (GSAS II) with Rietveld refinements [144]. Similar analysis was conducted on the TOF data using EXPGUI, which is a previous iteration of GSAS coupled with a graphical user interface [145, 146]. Crystallographic information files (CIF) were obtained from the Inorganic Crystal Structure Database (ICSD) [147] for FCC Cu [148] and cubic C15 Laves Cr_2Nb [149]. A limited number of parameters were chosen for the Rietveld refinements to help limit errors and retain consistency between the various samples; although, some exceptions did occur. These refinements are intended to provide a reasonable estimate of phase fractions and lattice behavior. The data collected during temperature ramping was refined using sequential refinements with similar parameters. Data collected during temperature ramping is not considered accurate due to systematic error between the exact sample temperature and the furnace temperature controller. However, the trends produced by the data should be reasonably accurate which allows for this methodology.

Results and Discussion

Scanning Electron Microscopy of As-Built Samples

Figure 3.2. shows SEM micrographs of the as-built samples, collected under high image contrast, exhibiting identifiable matrix grains and particles. Under this image contrast, the matrix grains appear to have significantly different contrast. In back scatter electron images (BSE), this implies that the matrix grains vary in composition since contrast is produced by variation in atomic number. However, energy-dispersive x-ray spectroscopy (EDS) line scans detected only a minor compositional change. The EDS results are used to help with interpretation but are not presented due to limited accuracy on the system. The XY samples show a matrix grain pattern that closely resembles the laser path, though it is difficult to observe from the images how the matrix grain distribution is influenced by the laser path. There is a distinct bimodal distribution of matrix grains in the XY micrographs showing either elongated, columnar-like or equiaxed grains. The XZ micrographs also demonstrate a mixed microstructure, though the vertical columnar growth is more evident.

EDS line scans suggest that the bright particles are Cr and Nb rich and are most likely Cr_2Nb, though the instrument's EDS resolution is limited. A line scan of two separate large particles are shown in Fig. 4.2.(a). Both particles are Nb-rich relative to the expected Cr_2Nb ratio. Three distinct particle types, labeled on Fig 3.2.(d), were identified including: (I) fine (<0.25 μm) particles; (II) large-semi-spherical (0.5 to 4 μm) distinct particles or agglomerates of the fine type I particles; (III) large Nb-rich spherical particles with similar size to II. Due to the similarity in size the type II and III particles can be difficult to distinguish, but the Nb-rich type III particles are brighter in the back-scattered images and slightly larger than the type II particles. The general distributions of particle types I and II seem to be dependent on the overlap of the melt zones with higher concentrations in the equiaxed grain regions. The particles are present at both grain

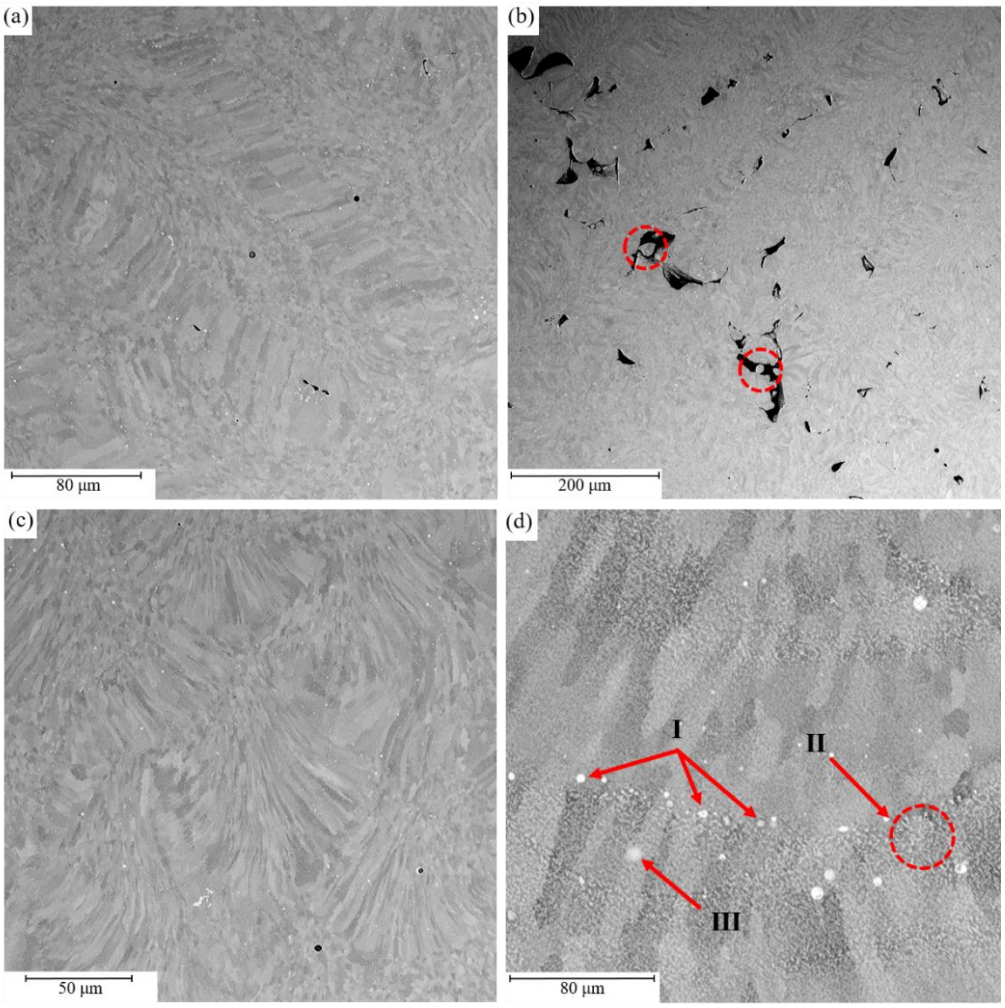

Figure 3.2. SEM micrographs for the as-built GRCop-84 samples (a) 880x XY, (b) 400x XY, (c) 1150x XZ, and (d) 7800x XZ with primary particle types.

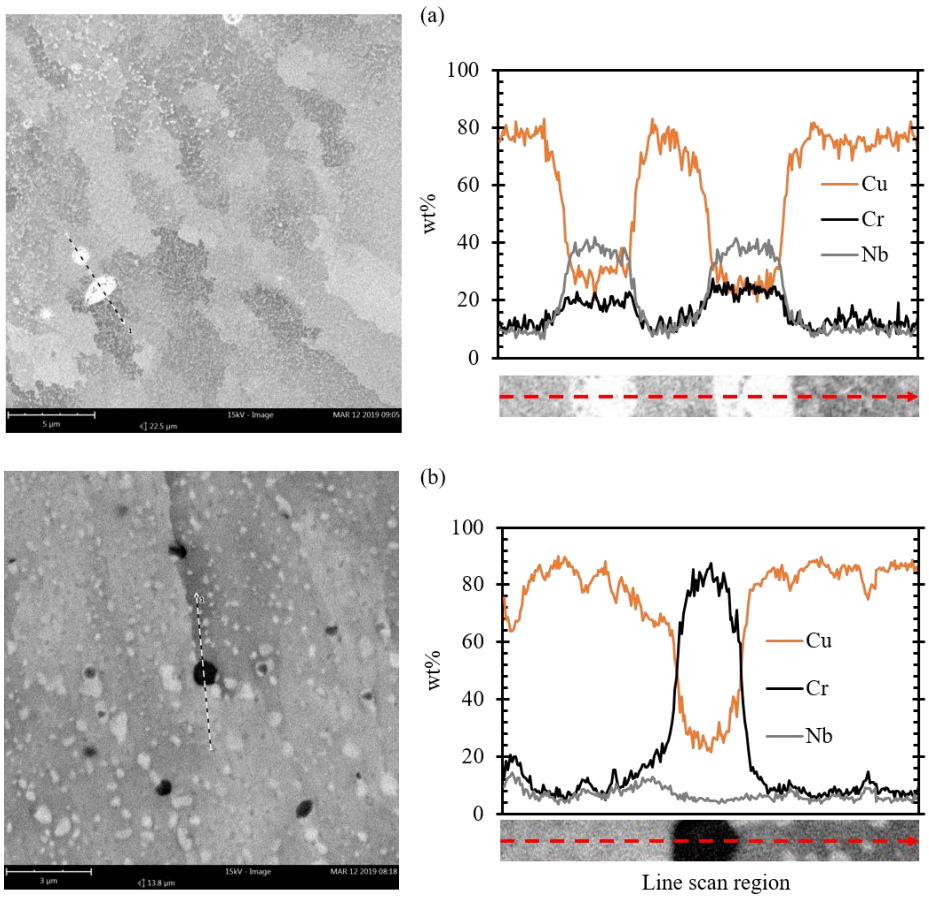

Figure 4.2. EDS line scans of (a) Nb-rich particle and surrounding region of as-built GRCop-84; (b) Cr-rich particle and surrounding region of HIPed GRCop-84 with reference image obtained on Phenom ProX SEM.

boundaries and within grains but are somewhat difficult to view. Compared to extruded GRCop-84, the distribution of the particles is more uniform and the size is smaller which agrees with previous work by Gradl et al. [106].

There were observable build defects (appearing with dark contrast) across the as-built samples. Samples sectioned near the edges of the build geometry revealed a high concentration of voids while samples sectioned near the interior were nearly defect free. Other as-built samples (not shown) with XZ cross-sections showed high defect densities at its respective edges. Figure 3.2.(a-c) shows circular pores (interpreted as dissolved or trapped gas) and Fig. 3.2.(b), the lowest magnification image, demonstrates observable lines of defects, which are most likely due to lack of fusion during the build. Evidence for this is powder-like shapes trapped within the voids, circled on Fig. 3.2.(b). Since the defects are concentrated at the edges of the builds, this may indicate that the n^{th+1} layers are necessary to complete fusion and densification of the below layer, and the edges of the build do not appear to receive sufficient energy density above them to complete fusion. Geometric abnormalities from the cooler exterior of the sample may also displace the build surface relative to the center and disrupt the energy density.

Scanning Electron Microscopy of HIPed Samples

Following the high temperature and pressure conditions of the HIP's post processing treatment, the microstructure coarsens slightly while retaining the heterogeneous distribution of the Cu matrix, shown in the representative images of Fig. 5.2. Annealing twins were present in HIPed samples, shown in Fig. 5.2.(d) which provides visual evidence that annealing and recrystallization occurred during the HIP. The twins are observed in regions surrounded by type II particles and are primarily Cu. These were not common within the HIPed samples, and 10 to 30 could be observed in a single 10 x 10 mm cross-section. Considering the lack of particles within the twins, it can be inferred that the presence of Cr_2Nb prevents and the absence allows the formation of annealing twins. Prior to HIP, the regions were annealing twins formed probably did not have a uniform distribution. So, this degree of recrystallization appears to be a localized phenomenon induced during L-PBF. The exact source is unknown and may be caused by overlap of laser paths, defects closed during the HIP, or particle agglomeration from diffusion during HIP.

The Cr_2Nb particles are more distinct from the matrix compared to the as-built images. The primary particle types, labeled in Fig. 5.2.(c), I, II, and III are still present after HIP, however, they have grown significantly, especially the type I particles. The type I particles are more present within the grains while the type II particles are present primarily at the grain boundaries There is another particle type, IV, which appears in the back-scattered images as dark particles that were not present in the as-built micrographs. The type IV particles are similar in size and distribution compared to the type II particles, though there are significantly less type IV particles. The contrast indicates that the type IV particles have a lower relative atomic number, and Cr has the lowest in the Cu-Cr-Nb system. EDS also provided evidence that these particles are Cr-rich, shown in Fig. 4.2.(b). These results demonstrate that the HIP has a significant impact on the chemistry of the microstructure.

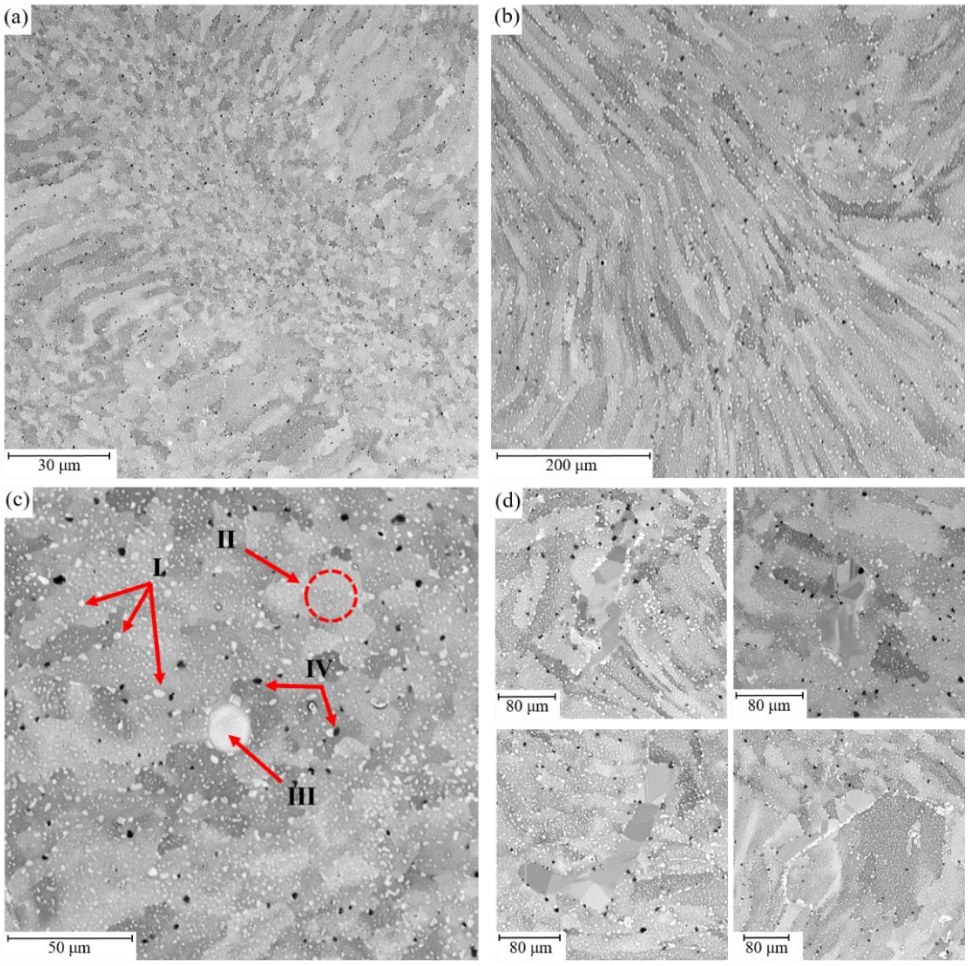

Figure 5.2. SEM micrographs for the HIPed GRCop-84 samples (a) 1900x XY, (b) 2900x XZ, (c) 7000x XY with primary particle types, and (d) four examples of annealing twins.

Electron Back Scattered Diffraction of As-built Samples

Four EBSD maps are shown in Fig. 6.2. for samples in the as-built condition. Again, only the Cu matrix is imaged. Cr_2Nb can be seen as non-indexed regions, and appear as small black dots at grain boundaries and within grains. However, it is difficult to distinguish these particles from similarly non-indexed voids and build defects. Larger black areas in the maps, like those in Fig. 6.2.(b) are voids. Although the matrix grains are visible under SEM, EBSD images better demonstrate the weld-line-like features for these samples. There are distinct regions in the XY EBSD maps of small equiaxed grains and long columnar grains that curve towards the equiaxed grains. Considering the lower magnification SEM images, this pattern of equiaxed to columnar regions can be confirmed to represent the laser weld path. The equiaxed grains are either at the center of the laser path or the edges. Based on welding literature, it is most likely that the equiaxed grains are at the center, where the thermal gradient is expected to be low. Equiaxed grain solidification at the fusion boundary is highly unlikely due to the high G/R ratio [131]. Since both equiaxed and columnar grains are present, it is, therefore, more likely that the equiaxed grains form where the G/R ratio is lowest at the center of the beam path. The expected position of the equiaxed and columnar grains with respect to the laser path are added to an as-built XY EBSD micrograph in Fig. 7.2. The ~14 vol% of precipitate particles provide a high amount of nucleation sites and can lower the G/R ratio to promote equiaxed solidification, and agrees with classic welding literature [150]. These likely contribute to the formation of equiaxed grains, but it is unlikely that they would promote the formation of equiaxed grains at the edge of the melt pool and not the center. In order for equiaxed grains to form at the edge, the particle density would have to demonstrate a significant distribution bias towards the edge. A bias is unlikely considering L-PBF's turbulent mixing and rapid solidification, and the distribution observed in the SEM results is relatively uniform.

The EBSD maps for the as-built samples, Fig. 6.2., were color thresholded in ImageJ [151] to separate the grains according to the principle directions and quantify the area fractions for each primary crystallographic orientation within the various images. Figure 8.2. shows an example of a thresholded EBSD XY map, and Figure 9.2.(a) provides the area fractions for all of the as-built EBSD maps. The values in Fig. 9.2. are not indicative of the entire cross-section and would require additional EBSD maps. The thresholding was conducted in the same manner for each map with a small fraction of voids and particles (V & P) that could not be resolved. Although all of the grains are not oriented perfectly with either of the three principle directions, this method provides an estimate for analysis. The fraction of voids and particles are used to represent the degree of error in the measurements.

The maps for the XZ samples have regions of strong (100) texture separated by randomly oriented equiaxed or thin, columnar grains. The area fraction calculation, Fig. 9.2.(b), of the (100) orientation in both XZ maps exceed 40% demonstrating preferential (100) growth. This is also demonstrated by the corresponding XZ (100) pole figures which were generated using MTEX [152] in Fig. 10.2.(c-d). The XZ samples have preferred orientation resembling cube texture [153]. Considering this preference, it is unusual that the XY samples do not show a similar preference in the (100) orientation. Instead, the XY micrographs show a periodic or random change in crystallographic orientations in the

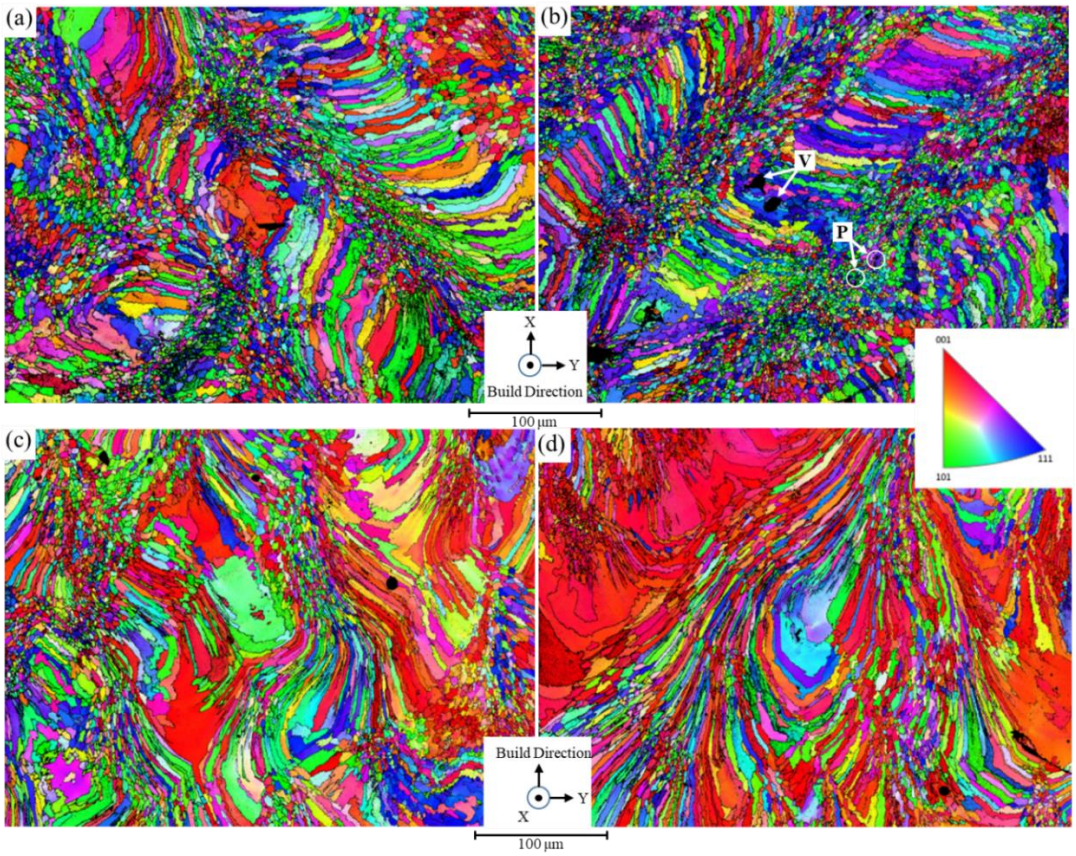

Figure 6.2. EBSD maps for (a-b) as-built GRCop-84 XY and (c-d) XZ samples; collected at 800x magnification with labeled examples of voids (V) and particles (P) in (b).

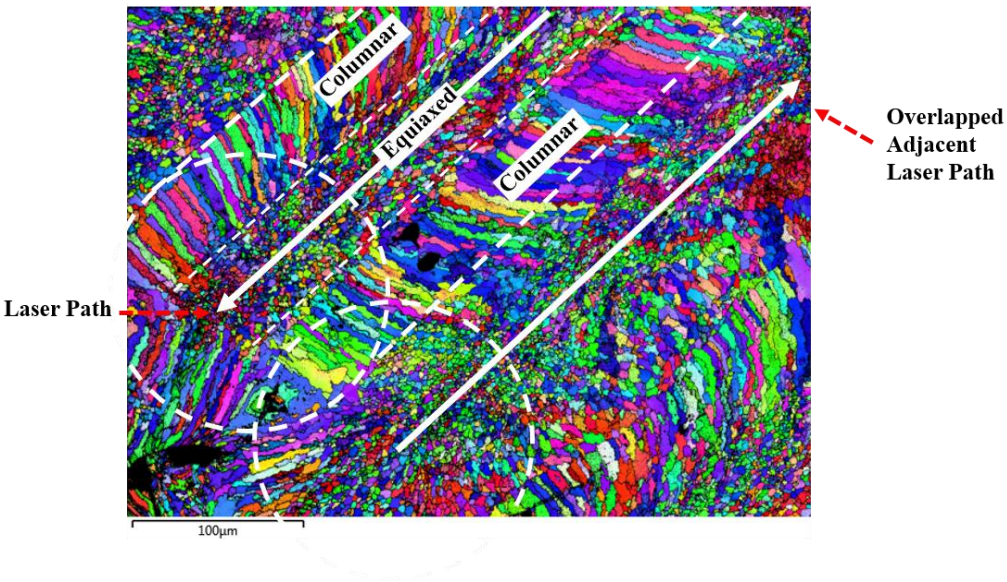

Figure 7.2. EBSD maps of as-built GRCop-84 XY sample with added separation of columnar and equiaxed regions with respect to a single laser path and expected overlap of adjacent laser path.

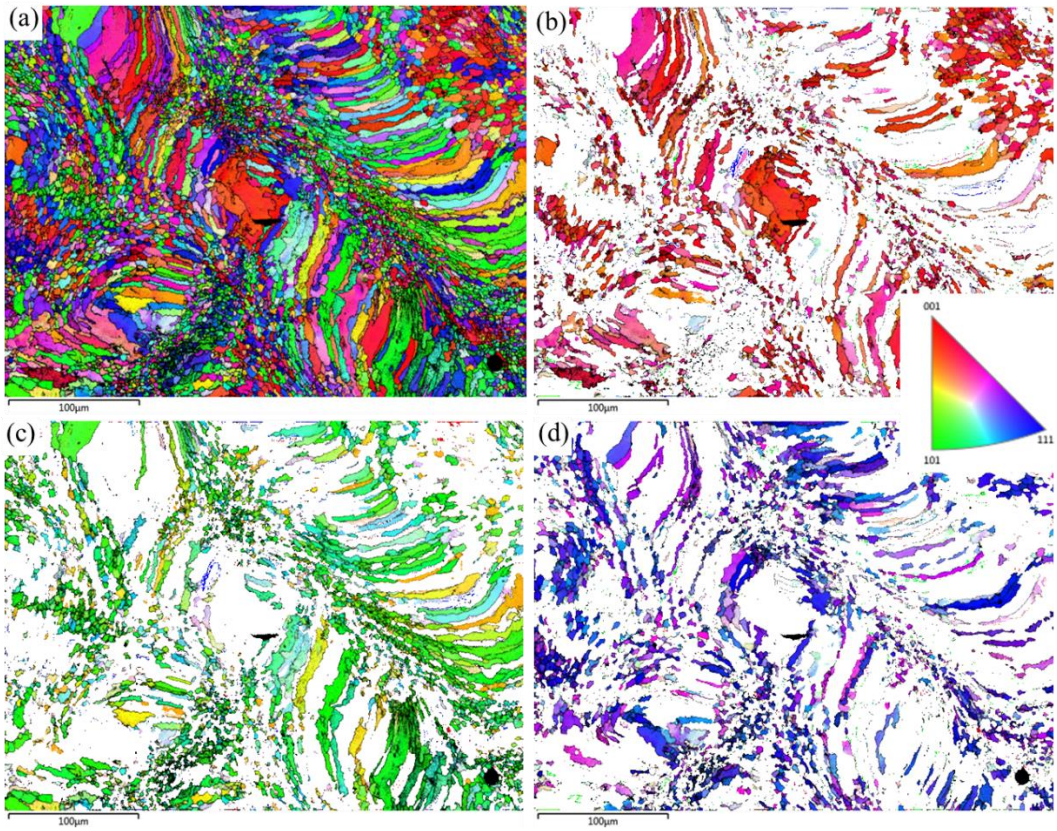

Figure 8.2. Isolation of principle crystallographic directions processed with ImageJ software (a) original EBSD image of as-built GRCop-84 XY (shown in Fig. 5.2.(a)), (b) primarily (001) oriented grains, (c) primarily (101) oriented grains, and (d) primarily (111) oriented grains.

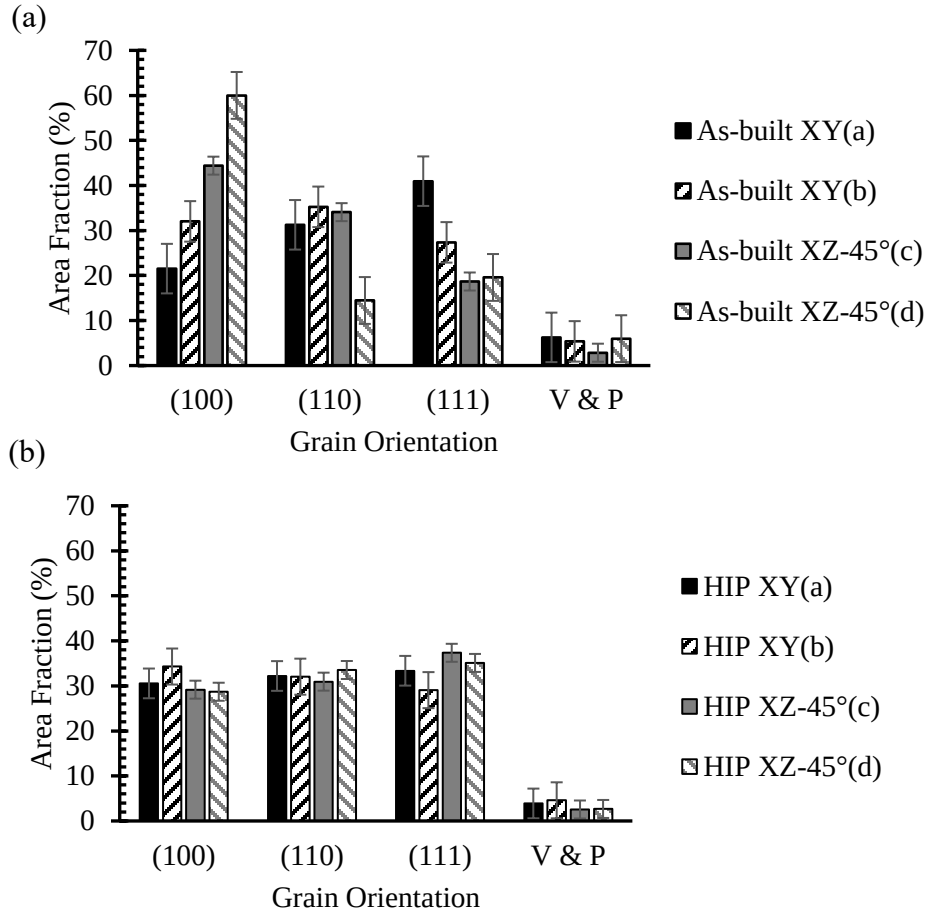

Figure 9.2. Area % determined for (100), (110), and (111) orientations, voids (V), and precipitate particles (P), determined from ImageJ analysis of the EBSD maps for both as-received and HIPed samples; with example shown in Fig. 6.2.

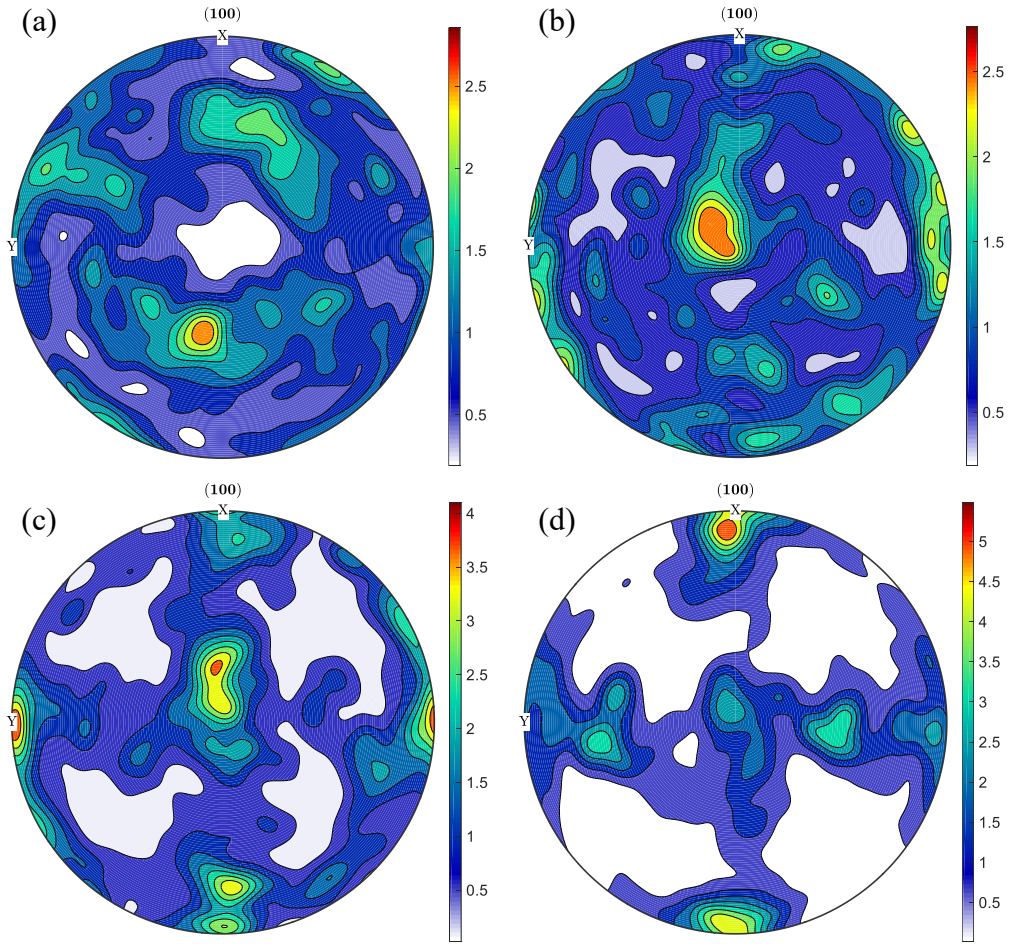

Figure 10.2. (100) Pole figures of Fig. 6.2.'s EBSD maps of (a-b) as-built GRCop-84 XY and (c-d) XZ samples generated using MTEX.

larger, columnar grains: i.e., changing between (100) (red), (110) (green), and (111) (blue). The pole figures for the XY micrographs, Fig. 10.2.(a-b) demonstrate some preferred orientation, but lack the cube texture shown in the XZ orientations. The source of the change likely relates to factors within the melt pool and heat affected zones during processing, but it may also be representative of horizontal grain growth within the system, as well as the orientation of the sectioning plane with reference to the overall of build and melt pool geometry orientations. The melt pool morphology is highly complex due to overlap both horizontal and vertical, so a substantive conclusion cannot be made without further modeling or study.

Some of the effects of overlap appear visible within the EBSD maps. At the center of Fig. 6.2.(a), there appears to be an overlap of two vertical laser weldments running perpendicular to each-other which has a dominating (100) orientation. Similarly, the XZ maps, Fig. 6.2.(c-d) show large regions dominated by (100) oriented grains which could be the result of overlapping weldments and strong epitaxial growth. When adjacent, horizontal weld pools overlap, there does not appear to be a preference for (100) growth, though the shape of the columnar grains changes; Fig. 6.2.(b) provides the best example of this observation.

Electron Back Scattered Diffraction of HIPed Samples

The EBSD maps of HIPed L-PBF GRCop-84, shown in Fig. 11.2., resembles the general Cu matrix grain structure of the as-built condition but with larger grains. The as-built EBSD images, fig. 6.2., demonstrate a significantly higher ratio of equiaxed grains than the HIPed images indicating that a significant amount of recrystallization and grain growth occurred throughout the microstructure. A significant amount of columnar grains are still present after the HIP. This may indicate that there was not a sufficient driving force to promote full recrystallization or that the high-volume fraction of Cr_2Nb particles suppressed the mobility of grain boundaries. Compared to the as-built micrographs, the distinct boundaries of the weldments from the as-built condition are less visible, similar to the SEM results. The overall texture appears more uniform or randomized in the HIPed maps than the as-built condition. This is partially supported by the pole figures, shown in Fig. 12.2. The texture is not perfectly random, and some preferred orientation is demonstrated, but the overall texture lacks the definition of the as-built samples and appears to have been changed. Considering the evidence of re-crystallization in the SEM results, the grains are likely re-orienting to a lower energy state. The area fractions of Fig. 9.2.(b) provide further evidence for this as the principle directions are roughly the same for each of the maps collected. Figure 13.2. provides an example of the ImageJ analysis for one of the HIP XY samples.

Particle Influence of Microstructure Evolution in L-PBF GRCop-84

The pattern of equiaxed and columnar matrix grain regions observed in the XY cross-sections of the SEM and EBSD micrographs is most likely representative of the laser weld path in a single horizontal layer. Additional vertical layers during L-PBF can be expected to have an influence on the layer that was randomly sectioned, but the equiaxed and columnar grain regions are unusually distinct in the horizontal sections. Either the laser

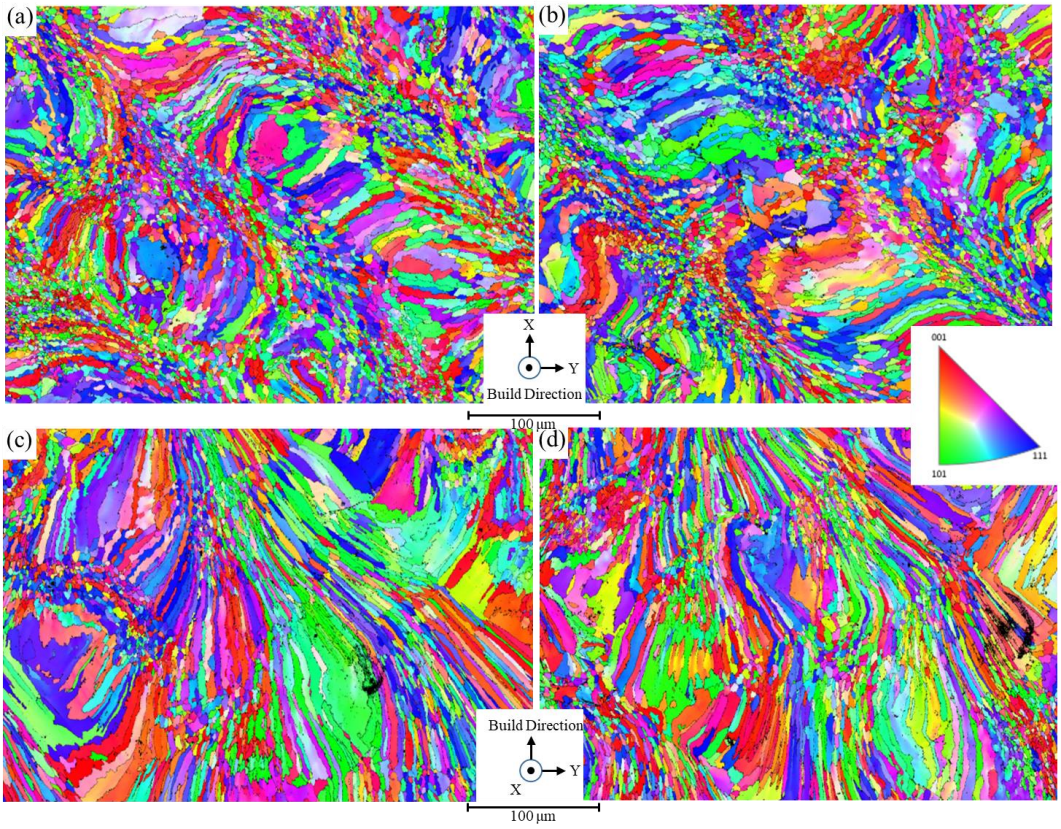

Figure 11.2. EBSD maps for (a-b) HIPed L-PBF GRCop-84 XY and (c-d) XZ samples; collected at 800x magnification.

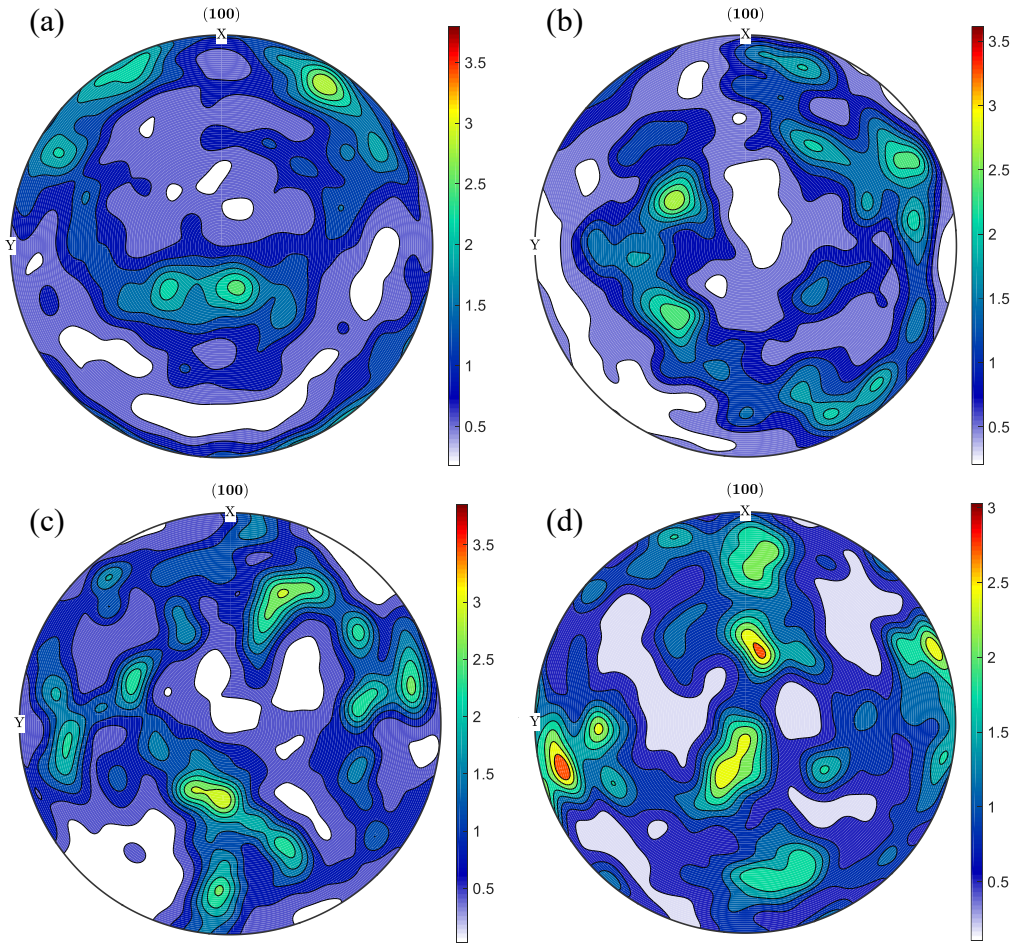

Figure 12.2. (100) Pole figures of Fig. 6.2.'s EBSD maps of (a-b) HIPedGRCop-84 XY and (c-d) XZ samples generated using MTEX.

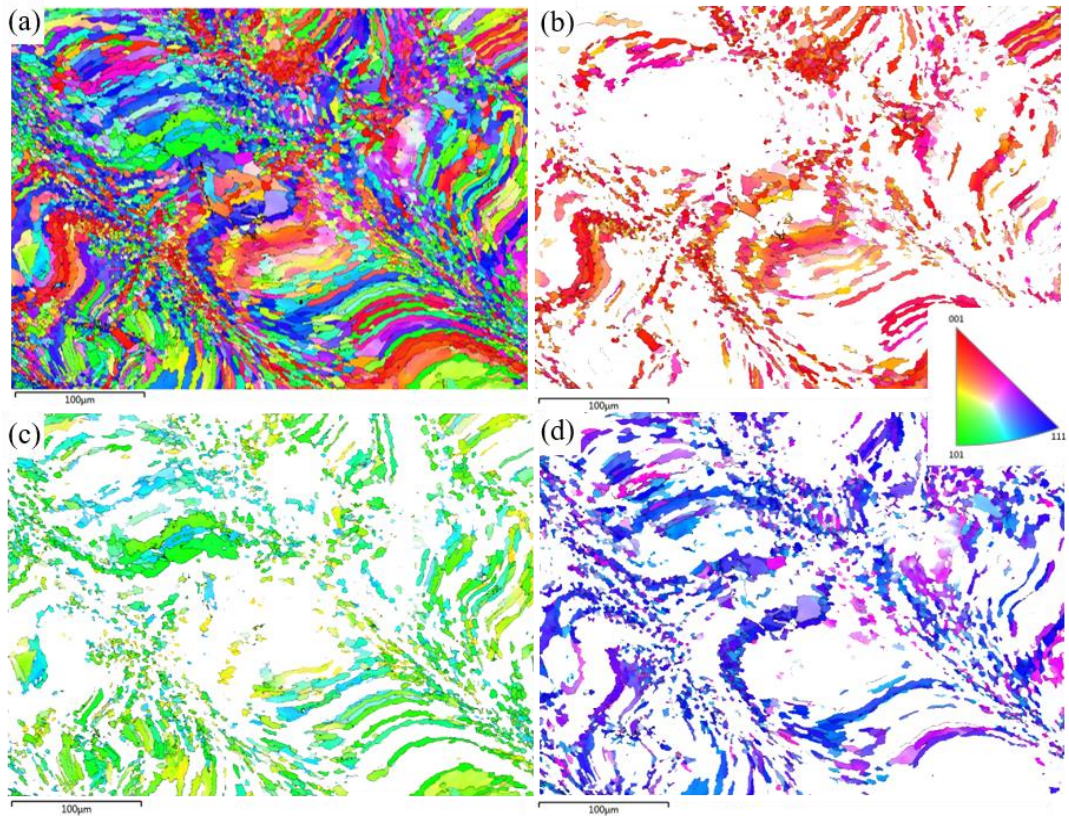

Figure 13.2. Isolation of principle crystallographic directions processed with ImageJ software (a) original EBSD image of HIP GRCop-84 XY (shown in Fig. 9.2.(b)), (b) primarily (001) oriented grains, (c) primarily (101) oriented grains, and (d) primarily (111) oriented grains.

parameters or amount of precipitates are sufficient to allow for equiaxed grain formation when columnar should be preferred. This study is limited a single set of build parameters, so the microstructure evolution will be considered primarily from the precipitate particle content. The microstructure can likely be modified by varying the build parameters to produce either more columnar or equiaxed grains and should be considered in the future.

The GRCop-84 powder used in L-PBF contains Cr_2Nb particles ranging from nm to μm-scale with the Cu matrix. During heating by the laser, both the matrix and particles are expected to fully melt though the particles should melt last and solidify first. Though, some fraction of the particles may remain un-melted during processing. Once the matrix is melted, the particles will be inserted into the matrix grains and may be whisked away from cold regions to regions with temperatures above the stability of the particles depending on spatial variations of fluid flow. As the particles travel through the melt pool, they may experience dissolution, growth or coarsening [154]. The extent of dissolution, growth or coarsening is related to the overall trajectory of these particles through the melt pool [155] and its thermal history. If some of these particles survive and end up in the constitutionally super-cooled region, the liquid may decompose into equiaxed grains [156]. The equiaxed grain formation would then inhibit the growth of columnar grains from the edges and produce the heterogeneous microstructure that is observed. However, the particle motion may simply be random due to turbulent mixing and rapid solidification effects in L-PBF. The particle distribution seems relatively uniform between the equiaxed and columnar grains which is partially a consequence of the high amount of alloying content.

With ~14 vol% of Cr_2Nb, there are a numerous nucleation sites present in the melt pool that can provide sufficient undercooling to promote heterogeneous nucleation. The equiaxed grains are most likely to form at the center-line of the laser path while the columnar grains should be at the edges where epitaxial growth is preferred. This agrees with finite-element modeling by Liu et al [157] with L-PBF IN718, and their results show that heterogeneous nucleation first occurs at the tail of the melt pool. IN718 has significant super-cooling from segregation effects which influences its heterogeneous nucleation, but significant segregation is not expected with GRCop-84 [44, 157]. Instead, the nucleation from the precipitate particles are more likely controlling the solidification.

Throughout the observations of the SLM metallographic data, there has been an assumption that the particles present outside of the matrix are more or less Cr_2Nb in the cubic C15 Laves phase. However, these techniques are incapable of providing confirmation of the formation of Cr_2Nb. It is critical to a high temperature application that the phases form a relatively pure Cu matrix and Cr_2Nb particles for the purposes of thermodynamic stabilization, thermal conductivity, and mechanical strengthening.

Gas Atomized GRCop-84 Powder HTXRD

X-ray powder diffraction data, collected on the as received gas atomized powder, before and after heating to 1123 K are shown in Fig. 14.2.(a). The data are compared in a smaller range, from 37-46 °2θ, for a more detailed view in Fig. 14.2.(b) and with the data collected at 1123 K in Fig. 14.2.(c). Results of analyzing the diffraction data collected initially at room temperature on the as received gas atomized powder, refined lattice parameters and phase fractions are provided in Table 3.2. When heated, the powder

Table 3.2. Refined lattice parameters and phase fractions (wt%) determined from analyzing X-ray powder diffraction data collected on as-received, gas-atomized GRCop-84 powder at ambient conditions.

	As-received Powder		
	Cu	**Cr_2Nb**	**Nb**
a (Å)	3.6229(1)*	7.019(3)	3.29(1)
wt%+	92(1)	7.2(3)	0.9(3)

* Estimated standard deviation (esd) reported as 3σ
+ Total wt% may exceed 100% due to rounding

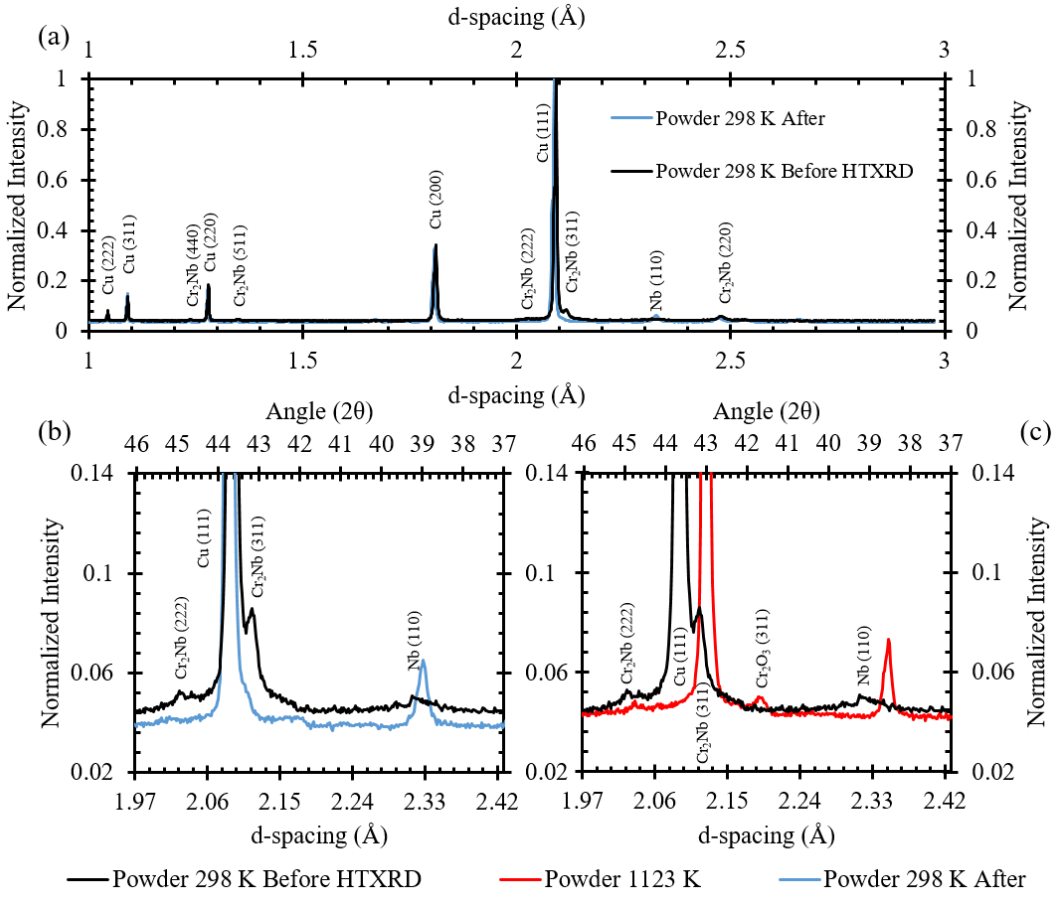

Figure 14.2. Normalized X-ray diffraction data of as-received gas atomized GRCop-84 powder (a) full scan range comparing data collected at room temperature before and after heating to 1123 K, (b) detailed view between 1.97-2.42 Å (converted to approximate 2θ) comparing data collected at room temperature before and after heating to 1123 K, and (c) detailed view between 1.97-2.42 Å (converted to approximate 2θ) comparing data collected before and at 1123 K.

readily oxidized demonstrated by weak diffraction maxima in the diffraction pattern. These were difficult to confident identify due to low intensity, matching reflections, and overlap with primary peaks but are most likely Cr and Nb oxides based on the powder chemistry. Oxide formation interferes with the phase fractions, so accurate values above ambient temperatures were not possible.

The as-received powder contains ~7 wt% cubic C15 Laves Cr_2Nb, significantly below the minimum alloying composition of 11.6 wt%. Two factors of gas-atomization are likely responsible for the low phase fraction. A significant fraction of the Cr_2Nb particles in gas-atomized GRCop-84 are between 10-100 nm from precipitation following gas-atomization [126]. This size is near the detection limit of laboratory XRD, reducing the detected phase fraction. Furthermore, rapid solidification can cause slight off-stoichiometry by freezing compositions in non-equilibrium states or defect structures that would be alleviated during slower cooling. If the amount of Cr and Nb in Cr_2Nb varies around the expected 2:1 ratio in Cr or Nb rich particles, then the diffraction peak will be more amorphous and not contribute to the overall phase fraction. Ellis, Misra, and Dreshfield [128] determined that Cr_2Nb is not strictly stoichiometric and has a narrow composition range supporting the prior observations.

Prior to heating, a diffraction maxima at 2.31 Å (38.8 °2θ) is barely visible. Based on the peak position and the composition of the alloy the diffraction maxima could indicate the presence of elemental BCC Nb. At and after cooling from 1123 K the peak increases in intensity and sharpens suggesting a decrease in disorder and/or crystallite size growth and refinement results determine that <1 wt% elemental Nb is present. Despite the low amount, this result is surprising since BCC Nb was not expected to be present in any of the conditions. GRCop alloys have a slight excess of Cr to prevent formation of Nb by lowering its activity and consuming it in forming Cr_2Nb which has been demonstrated by Ellis, Misra, and Dreshfield [128]. This leaves two possibilities to explain the presence of Nb in the powder. (1) The solidification is so rapid in gas atomization that Nb is able to precipitate. (2) A significant amount of Cr was dissolved into the Cu matrix and the majority of Cr_2Nb is in an Nb-rich state caused by rapid solidification. Possibility (1) is unlikely based on preferential formation of Cr_2Nb. In the case of (2), this could help explain the relatively low Cr_2Nb phase fraction and the increase in phase fraction observed at high temperatures could be caused by the Cr_2Nb rejecting Nb for a more favorable stoichiometry. Furthermore, the amount of dissolved content could be reasonably estimated by a rule-of-mixtures with Vegard's law if not for the high probability of microstrains in the gas-atomized powder that also influence the crystal lattice [158]. The two cannot be easily separated for such a measurement. In the future, the degree of solute present in the matrix could be assessed by atom probe tomography [159].

Refined lattice parameters for the HTXRD experiments are plotted in Fig. 15.2.(a). The lattice parameters are refined using the Rietveld method employing a least squares approached, however, in the data collection range only the (111) and (200) reflections were observed, and the lattice parameter is calculated through GSAS refinements from only two Cu peaks, Cu(111)&(200). This data is only intended for observing changes in the slope and direct comparison to the other sample types. For more

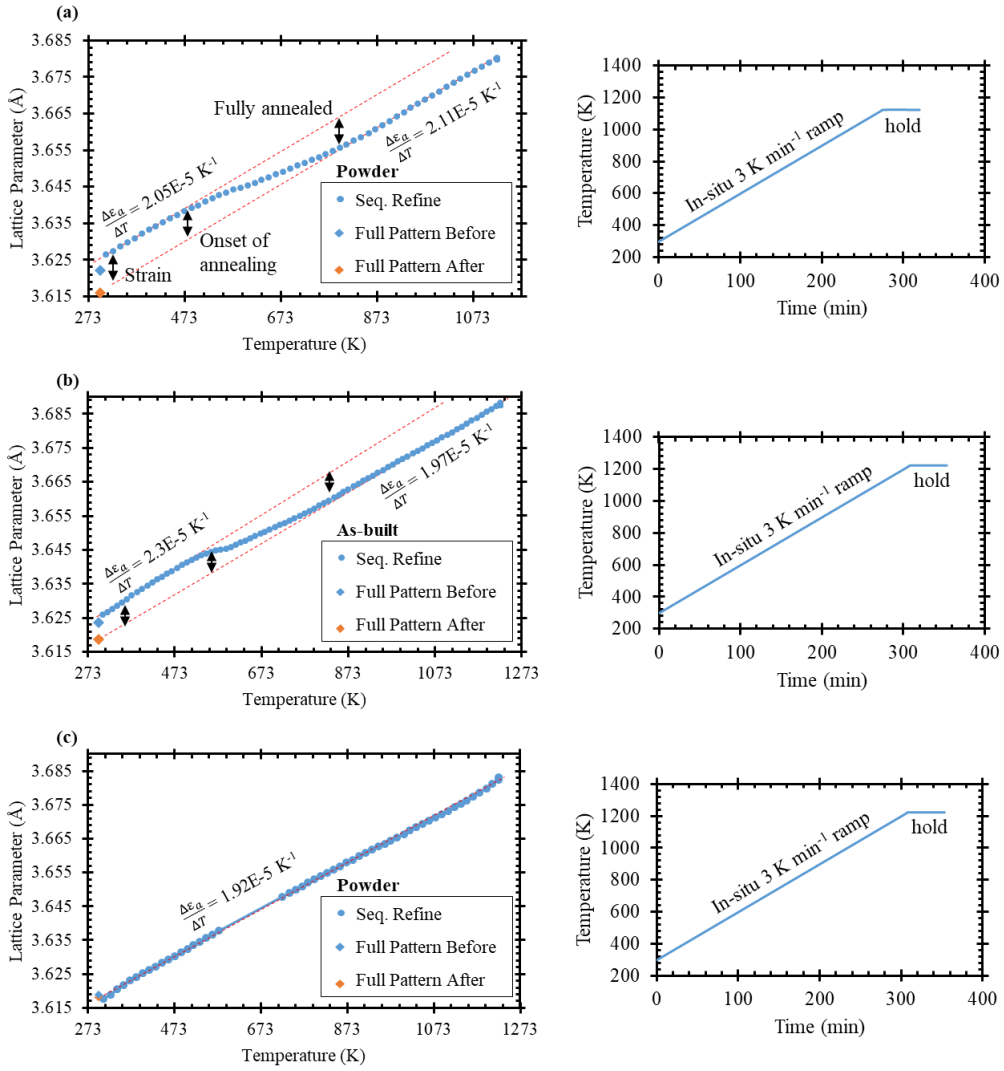

Figure 15.2. Refined lattice parameters for Cu from HTXRD experiments based on only the (111) and (200) planes and corresponding furnace schedules on the right for (a) powder, (b) as-built, and (c) HIPed samples. Each figure compares the refined lattice parameter, obtain from a larger two-theta range, on data collected at room temperature prior and after heating to 1123 K. Linear regions were fitted (dash lines) and the resulting slope is reported as thermal expansion using strain. Error bars were smaller than the data markers and are omitted.

accurate results, the data could have been measured over the entire diffraction profile at a slower temperature ramp to reduce any possible temperature fluctuations, but this would have taken significantly longer. Figure 15.2.(a) reveals a significant slope change between 473 and 873 K, which agrees with the annealing range described in literature [104]. Beyond 873 K, the expansion remains linear and follows that linear slope back to room temperature during cooling. The slope was converted to thermal expansion, $\frac{\varepsilon_a}{\Delta T}$, by converting the change in lattice parameter, a, to lattice parameter strain, ε_a, shown in Fig 15.2.(a-c). The slope before and after annealing the shift changes by ~2%. The primary factors that can influence lattice spacing include compositional changes, phase transformation, change in temperature (thermal expansion), and intergranular strains [160]. The effect of thermal expansion is observed but should not be responsible for the shift before and after, and no phase transformations are observed or expected. That leaves compositional changes and intergranular strains as the primary sources of the shift in the lattice parameter. The exact source is difficult to determine since both are expected and can be changed by annealing. Ultimately, this indicates that the gas-atomized powder has a significant amount of defects present as possible dissolved content or intergranular strains in the bulk powder composition. During annealing, the dissolved content may precipitate out and the intergranular strain may be relieved. Further analysis with TEM or atom probe would likely to be able to determine the exact source, and may help explain the low volume fraction of Cr_2Nb. The linear coefficient of thermal expansion of pure Cu is 1.6-1.7E-5 K^{-1},and GRCop-84's macroscopic expansion is ~1.9E-5 K^{-1}, converted from a quadratic form [126]. The thermal expansion of the Cu matrix in the GRCop-84 powder will not be directly comparable to either pure Cu or GRCop-84 due to the influence of Cr_2Nb but is similar in magnitude which adds to the confidence of the experiment. These measurements serve as the base-line for the as-built L-PBF and HIPed samples.

As-built L-PBF GRCop-84 Diffraction

The full collected ambient diffraction profiles before and after heating to 1223 K are shown in Fig. 16.2.(a) for the as-built sample, with comparisons in Fig. 16.2.(b-c) similar to those used in Fig. 14.2. Refined lattice parameters and phase fractions are provided in Table 4.2. for room temperature data collected prior and after heating to 1223 K. Significant oxidation occurred, so the specimen was cleaned of surface oxides after the exposure with a high grit grinding pad and water. This provides a method of assessing the bulk composition without interference from oxides.

The phase fraction of Cr_2Nb in the as-built samples prior to exposure was nearly below the detection level. The less than 1 wt% value in Table 4.2.(a) is an estimation from manually adjusting strain and size contributions in the calculated X-ray diffraction pattern to match the observed data. Only the Cr_2Nb (220) peak is distinguishable from the background intensity, and it is such an inconsistent peak that the lattice parameter could not be refined. Following the 1223 K exposure, the wt% of Cr_2Nb increases to ~11.7 wt% which is near the alloying amount. This implies that the degree of crystallinity of the Cr_2Nb particles, stoichiometry, microstrains during introduced during consolidation, and/or small crystallite sizes in the as-built condition are altered with annealing resulting in sharper, more intense reflection maxima. This is similar to the powder results where

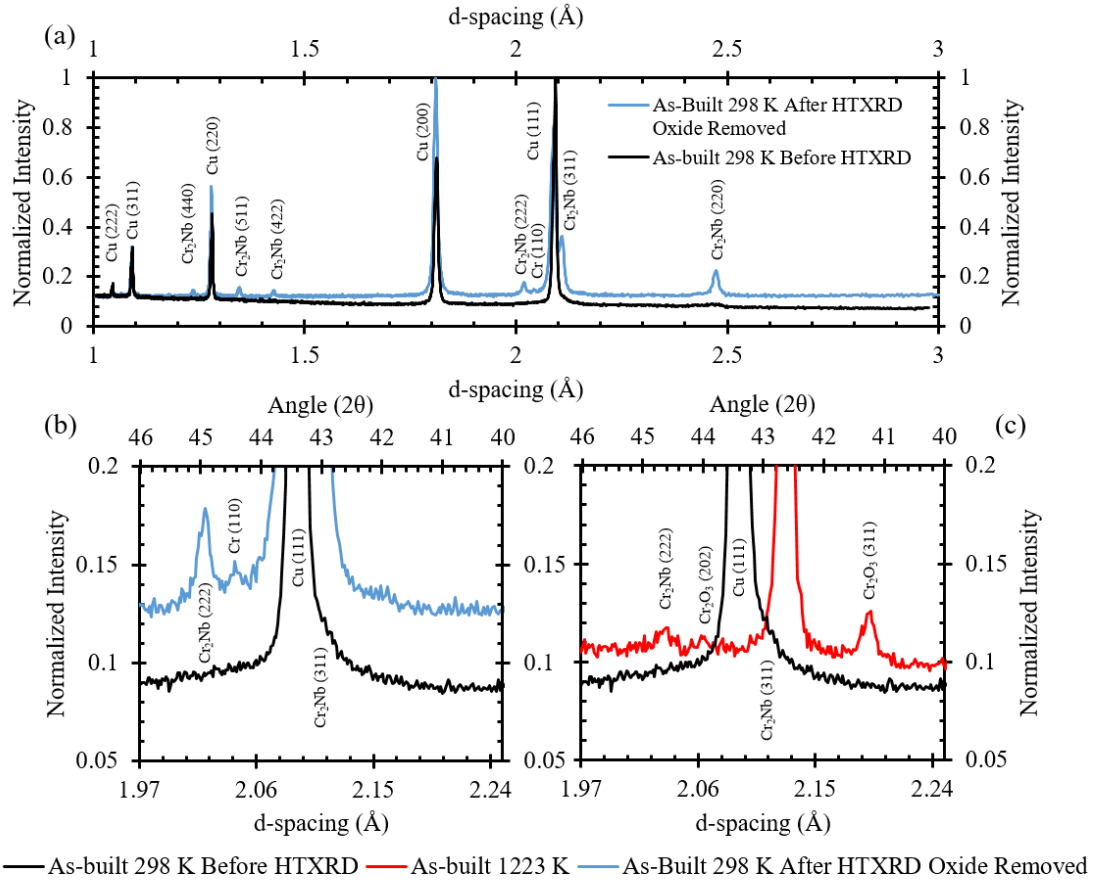

Figure 16.2. Normalized X-ray diffraction data of as-built L-PBF GRCop-84 samples sectioned from larger parts (a) full data range comparing data collected at room temperature before and after heating to 1223 K, (b) detailed view between 1.97-2.24 Å (converted to approximate 2θ) of data collected at room temperature before and after heating to 1223 K, and (c) detailed view between 2.15-2.7 Å comparing data collected before and at 1223 K.

Table 4.2. Refined lattice parameters and phase fractions (wt%) determined from analyzing X-ray powder diffraction data collected on as-built and HIPed GRCop-84 samples (a) refined from XRD data collected before and after heating to 1223 K and (b) refined from neutron powder diffraction data collected on four samples at room temperature.

	HTXRD As-built					HTXRD HIP			
	Before		After Firing			Before		After Firing	
	Cu	Cr_2Nb	Cu	Cr_2Nb	Cr	Cu	Cr_2Nb	Cu	Cr_2Nb
***a* (Å)**	3.6235(1)*	6.99**	3.6208(2)	6.997(2)	2.89(1)	3.6189(3)	6.994(2)	3.6141(3)	6.985(2)
wt%	99.1(7)	0.8**	87.7(9)	11.7(6)	0.6(4)	90(1)	10.2(7)	89.8(1)	10.2(8)

	Ambient Temperature TOF NPD As-built				Ambient Temperature TOF NPD HIP			
	Sample 1		Sample 2		Sample 3		Sample 4	
	Cu	Cr_2Nb	Cu	Cr_2Nb	Cu	Cr_2Nb	Cu	Cr_2Nb
***a* (Å)**	3.6162(4)	6.978(7)	3.6209(4)	6.991(7)	3.6153(3)	6.980(2)	3.6162(2)	6.980(3)
wt%	97.4(3)	2.6(8)	97.3(3)	2.7(9)	87.5(9)	12(1)	86(2)	14(2)

* Esd reported as (3σ) for lattice parameters and wt%

** Indicates a value calculate from peak position without esd; accurate refinement was not possible due to overlapping peaks

+ Total wt% may exceed 100% due to rounding

size and off-stoichiometry are expected but more pronounced. Unlike the powder, there is no detectable BCC Nb, however, following heating BCC Cr is present. This suggests that the melting and solidification cycles in L-PBF move the general stoichiometry of the Cr_2Nb particles from Nb-rich to Cr-rich.

The in-situ data for the Cu lattice parameter between ambient temperatures and 1223 K is shown in Fig. 15.2.(b). The trend of the as-built sample is nearly the same as the powder sample with observable slope changes between 473 and 873 K, and the magnitude of the shift is similar. This may indicate that the gas-atomized powder and as-built L-PBF material share a similar amount of dissolved content or intergranular strains but should be the subject of further study.

Neutrons are uncharged and more penetrating compared to X-rays and yield information about the bulk of a sample compared to the surface information provided by X-rays and should result better particle statistics due to the higher amount of sample being interrogated. Refined lattice parameters and phase fractions from analyzing the neutron TOF data are presented in Table 4.2. These results from data collected on as received samples consolidated via L-PBF, suggest that 2.6-2.7 wt% of Cr_2Nb is present, higher than that obtained from analyzing the XRD data collected on similar samples but confirms that the as-built condition has significantly less detected Cr_2Nb. The 2.6-2.7 wt% is most likely the type II particles observed in the SEM results that were beyond the detection limit of the laboratory XRD. The type I particles are less contribute to a consistent diffraction maxima due to presence of microstrain.

HIPed L-PBF GRCop-84 Diffraction

The full collected ambient diffraction profiles before and after heating to 1223 K are shown in Fig. 17.2.(a) for the as-built sample, with detailed comparisons in Fig. 17.2.(b-c). Refined lattice parameters and phase fractions are provided in Table 4.2. for room temperature data collected prior to and after heating to 1223 K. Prior to data collection after firing the sample, the surface was cleaned of oxides using the same method described for the as-built.

The phase fractions of the HIPed samples from the ambient XRD, Table 4.2., reveal that the detected phase fraction of Cr_2Nb is near the alloying amount. After the 1223 K exposure, the phase fraction and lattice parameter remains largely unchanged which demonstrates the stability of Cr_2Nb after HIPing. This demonstrates the stability of Cr_2Nb after HIP since the phase fraction is almost identical following the 1223 K exposure. Prior to firing, the HIP sample data showed a small diffraction maxima, distinguishable above the background in Fig. 17.2.(b), at approximately 2.042 Å (44.5^o 2θ), which most closely matches the (110) reflection of BCC Cr and agrees with the as-built results after heating. This supports the SEM results that found Cr-rich particles, and Cr-rich particles could likely be observed in the as-built samples after 1223 K. After heating the HIPed sample to 1223 K, the BCC Cr (110) reflection is no longer distinguishable from the background intensity which disagrees with the as-built sample. Considering that the ratio of Cu:Cr_2Nb remains effectively unchanged after the high temperature exposure, it is unlikely that the amount of BCC Cr in the alloy has changed. The cause of the change is currently unknown. The phase fractions determined from the XRD data of Cr_2Nb is 2-4 wt% lower than those

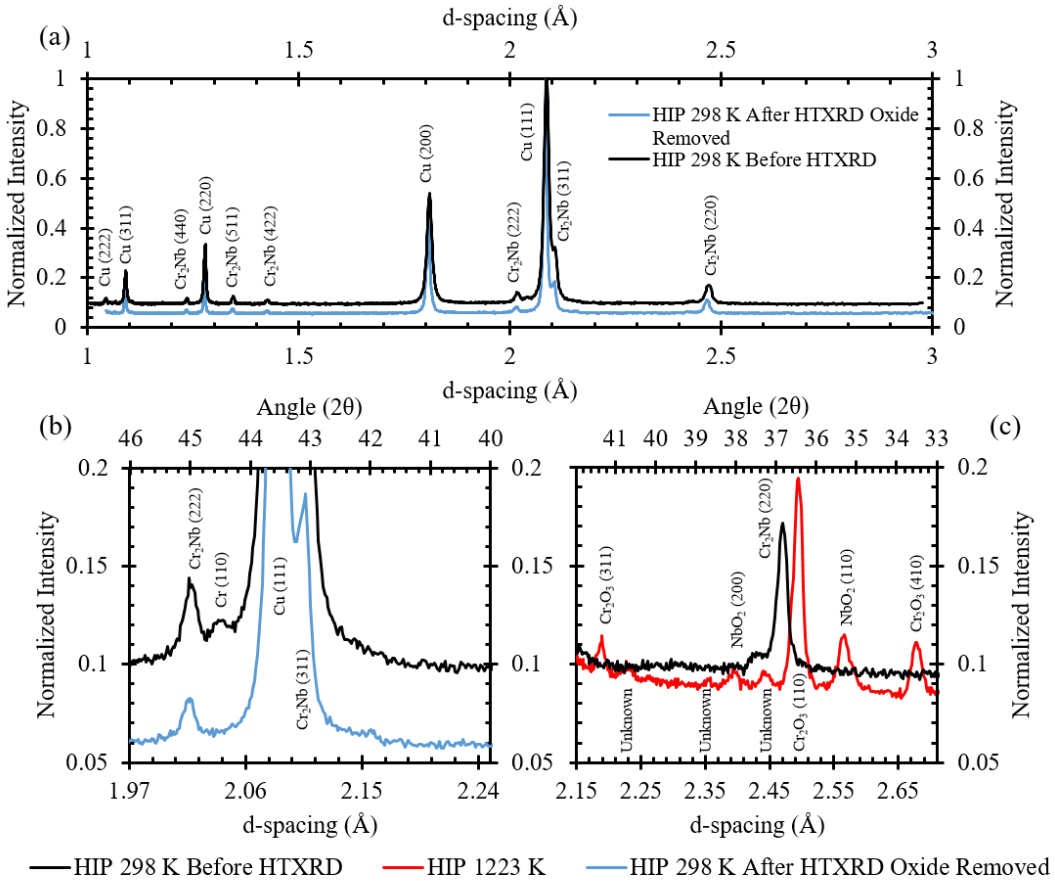

Figure 17.2. Normalized X-ray diffraction data of HIPed L-PBF GRCop-84 samples sectioned from larger parts (a) full data collection range comparing data collected at room temperature before and after heating to 1223 K, (b) detailed view between 1.97-2.25 Å (converted to approximate 2θ) comparing data collected at room temperature before and after heating, and (c) similar view comparing data collected before and at 1223 K.

determined from the TOF neutron data. This difference is within error, but may be representative of the higher diffracted volume and improved detection limits.

Summary and Conclusions

The influence of L-PBF on the microstructure of GRCop-84 was investigated on samples in the as-built and HIPed conditions using NASA's standardized build parameters. SEM, EBSD, HTXRD, and TOF neutron diffraction were used to characterize the evolution of microstructural features and phases. The major findings are summarized as follows.

(1) The as-built material retained the largely bimodal distribution present in the powder similar to other powder-processing methods. The distribution of particles throughout the microstructure remains largely uniform. Significant coarsening of 10-100 nm-scale particles is observed following HIP, but the larger, μm-scale particles demonstrated limited coarsening. Following HIP, Cr-rich particles are detected with size similar to the μm-scale particles.

(2) The current L-PBF build parameters result in a heterogeneous Cu matrix microstructure consisting primarily of equiaxed and columnar grains. From the view of a single XY layer, the equiaxed grains are at the center of the individual laser weldments while the columnar grains are at the edges following the laser path, and the texture is largely random. From the XZ view, strong (100) epitaxial preferential growth is observed, and bundles of (100) columnar grains traverse multiple layers.

(3) Minor and major abnormalities were observed in the calculated phase fractions of the Rietveld refinements. Approximately 40% less Cr_2Nb was detected in the gas-atomized powder than the alloying amount of ~12 wt%, and a non-negligible amount of BCC Nb was present that was not detected in any other samples. The lower phase fraction of Cr_2Nb can be attributed to diffraction limits but significant off-stoichiometry and amorphous content is expected. Less than 10% of the expected weight fraction of Cr_2Nb was calculated in the as-built material, but after HTXRD to 1223 K, the weight fraction is greater than 90%.

Acknowledgements

This research used resources at the Spallation Neutron Source, a US Department of Energy Office of Science User Facility operated by Oak Ridge National Laboratory. The authors would like to acknowledge the Manufacturing and Materials Joining Innovation Center (Ma^2JIC), made possible through awards NSF IIP-1540000 (Phase I) and NSF IIP-1822186 (Phase II) from the National Science Foundation Industry University Cooperative Research Center program (IUCRC). RPM also acknowledges the financial support of Oak Ridge National Laboratory's Graduate Opportunities (GO!) Program.

CHAPTER III
INVESTIGATION OF DEFORMATION MECHANISMS OF L-PBF GRCOP-84 WITH IN-SITU NEUTRON DIFFRACTION

A version of this chapter is intended for separate publication under the same title at a future date with the current co-authors in a future journal article.

This work is co-authored by Robert Minneci [1], David L. Ellis [2], Yan Chen [3], Ke An [3], Eric A. Lass [1], Jeffrey R. Bunn [3], Paul R. Gradl [4], Hahn Choo [1], and Claudia J. Rawn [1]

[1]Department of Materials Science and Engineering, University of Tennessee, Knoxville, Tennessee 37996-2100, U.S.A. [2]NASA Glenn Research Center, Cleveland, OH 44135, U.S.A. [3]Neutron Scattering Division, Oak Ridge National Laboratory, Oak Ridge, Tennessee 37831-6475. [4]NASA Marshall Space Flight Center, Huntsville, Al 35808, U.S.A.

The article has no current changes but is expected to have minor changes in its future publication. RPM wrote the initial manuscript draft, and all authors contributed to the final manuscript. CJR contributed to editing, direction, and writing throughout. DLE contributed to collection of data and analysis of results. YC and KA contributed to preparation of the experiment plan, collection of data, editing, and analysis. EAL, JRB, and HC contributed to editing and analysis. PRG contributed resources and editing.

Abstract

In-situ time-of-flight neutron diffraction measurements were conducted under compressive deformation of additively manufactured (AM) GRCop-84 (Cu-8Cr-4Nb at%) on the VULCAN beamline at the Spallation Neutron Source (SNS). Samples were built with laser-powder bed fusion (L-PBF) and were tested in as-built and hot isostatically pressed (HIPed) conditions and tested in compression at room temperature. In order to evaluate the effect of build anisotropy and texture, samples were sectioned parallel (referred to as XY) and perpendicular (Z) to the build direction and two detector banks provided axial and transverse strain response. The lattice response, strain partitioning between the primary face centered cubic (FCC) Cu and C15 Laves Cr_2Nb phases, diffraction elastic constants, and deformation behavior are investigated. The as-built material exhibited roughly 200 MPa higher stresses beyond 2% strain, but immediately enters plastic deformation characterized by an increase in the dislocation density. By contrast, the HIPed condition demonstrates a loading region more resembling elastic deformation with no increase to the dislocation density. In the HIPed condition, the Cr_2Nb phase is found to yield earlier than the Cu phase and reach a maximum strain value while the Cu phase supports the majority of the stress and significantly strain hardens.

Introduction

Additive manufacturing (AM) is a rapidly advancing technology that produces components by fusing feedstock material in a layer-by-layer approach. In metal AM, the feedstock can take a variety of forms including powder, wire, or sheets and can be fused with a secondary sintering step or directly by the use of lasers, electron beams, or ultrasonic vibrations [129]. AM allows for nearly full processing control of the geometry

which can be leveraged to produce complex shapes that reduce weight or improve performance that would not be achievable otherwise; though, each additive method has advantages and disadvantages associated with production time, achievable properties, cost, and dimensional accuracy that must be considered in selection for a given application. In most cases, AM falls behind traditional manufacturing methods, such as wrought, in production time and cost limiting its practical use in industry. AM is best suited for applications with low production volumes, inherently high material and processing costs, or cases where performance outweighs cost.

NASA's development of laser-powder bed fusion (L-PBF) GRCop-84 (Cu-8Cr-4Nb at%) demonstrates a rare case where AM is the ideal processing method in nearly every way. L-PBF is used here to specifically refer to laser melting methods and not laser sintering. GRCop-84 is a traditionally powder-processed alloy with strict purity requirements that is alloyed with Ar gas atomization for both traditional and AM use, so the material cost is effectively equal [30]. GRCop-84 is used in complex geometries, such as the combustion chamber liner of reusable rockets that are difficult to produce with traditional wrought or subtractive machining methods. The production speed of AM GRCop-84 is slow compared to traditional fabrication methods but is similar to the complex methods used in wrought GRCop-84. AM's layer-by-layer fabrication method can produce the desired geometry with limited material waste, equal or better thermal properties, the ability to control the internal geometry, and improved dimensional tolerance over traditional methods [106, 126]. Cooling efficiency is crucial for GRCop-84 selected applications with AM allowing for cooling channels to be built directly into the geometry. These are demonstrated by Hayes, Brown, and Kappes [103] with computerized tomography scans of complex internal cooling channels produced by L-PBF GRCop-84. By directly building the cooling channels, the design space is open to complex routes that wrap around the shape or branch off into multiple channels that can dramatically improve cooling efficiency. Higher cooling efficiency translates into improved safety qualifications and performance, directly impacting the end use.

Due in large part to the efforts at NASA Marshall Space Flight Center (MSFC), NASA has developed approved L-PBF process parameters for component fabrication. These parameters can reliably produce parts with limited build failures and a minimum density of 99.2% [30]. All L-PBF GRCop-84 parts are hot isostatically pressed (HIPed) with a standard procedure that helps negate deviations in processing by reducing porosity and improving tolerances and confidence in performance.

The microstructure of GRCop-84 consists primarily of an FCC Cu matrix and C15 Laves Cr_2Nb precipitates. More in-depth analysis of the microstructure can be found elsewhere [126]. The limited solid solubility and preferential formation of Cr_2Nb limits the presence of other phases, and Cr_2Nb is stable within Cu and provides a high degree of mechanical and thermal stability to the matrix at high temperatures ranging from 50-85% of the melting temperature of pure Cu [126]. Characterization efforts of as-built and hot isostatically pressed (HIPed) L-PBF GRCop-84 have revealed complex microstructures [103, 126]. With the NASA-approved process parameters, L-PBF produces a mixed microstructure of equiaxed and columnar Cu grains with Cr_2Nb precipitates present at both grain boundaries and within the grains. The high-volume fraction of Cr_2Nb (~14

vol%) in GRCop-84 provides sufficient nucleation sites to promote heterogeneous nucleation and suppress preferred epitaxial growth. Following the HIP, the microstructure demonstrates limited coarsening and retains the mixed microstructure, despite evidence of recrystallization.

GRCop-84 is strengthened primarily through a combination of Orowan and Hall-Petch strengthening. These represent direct and in-direct strengthening from the Cr_2Nb particles. In Orowan strengthening, the precipitate particles directly impede dislocation motion and increase strength [24]. The extent of Orowan strengthening is dependent upon the size of the particles, and the smaller, secondary particles of the bimodal distribution are predicted to provide the majority of the Orowan strengthening. The precipitate particles also serve as nucleation sites and are effective in pinning the Cu matrix grain boundaries at high temperatures, preventing coarsening. This indirectly strengthens the matrix by reducing the starting grain size and retaining the grain size at elevated temperatures and provides Hall-Petch strengthening. Anderson and Groza [44] estimated that 2/3^{rds} of the strengthening in extruded GRCop-84 is Hall-Petch and 1/3rd is Orowan, but little is known about the deformation of AM GRCop-84.

The overall understanding through characterization is advancing with the rapid progression of AM GRCop-84. It is critical to understand how the processing of L-PBF and post processing HIP controls the microstructure and properties for future development. Modeling can help predict properties and performance, but experimental results are necessary to provide a physical basis, provide modeling parameters, and validate models. Key information regarding internal strain, texture, and dislocation density is necessary for polycrystalline plasticity modeling [161]. This information can be obtained with in-situ neutron diffraction techniques that have been developed to measure lattice response. In this study, as-built and HIPed AM GRCop-84 have been deformed in an in-situ neutron study to provide data for future modeling efforts, better understand the role of Cr_2Nb in deformation, and assess the impact of processing.

Methods

Measurement of Lattice Strain with VULCAN

Time-of-flight (TOF) neutron diffraction data were collected on the VULCAN beamline at the Spallation Neutron Source (SNS) at Oak Ridge National Laboratory (ORNL). The configuration of the VULCAN instrument, shown as a diagram in Fig. 1.3., measures an entire diffraction profile simultaneously. During a TOF experiment the neutron flux is split over the entire diffraction spectrum rather than focused in a single range. Each diffraction event produces a wavelength, λ, that is determined by measuring the time of flight, t, from when the neutron pulse is generated in the moderator to the instant when the diffracted neutron is captured in the detector [160]. Diffraction events follow Bragg's law

$$\lambda = 2d_{hkl}\sin\theta \quad (1.3.)$$

where d_{hkl} is lattice spacing of a specific hkl plane and θ is the angle of incidence and scattering., The angle of the neutron beam is fixed, and the wavelength is given by

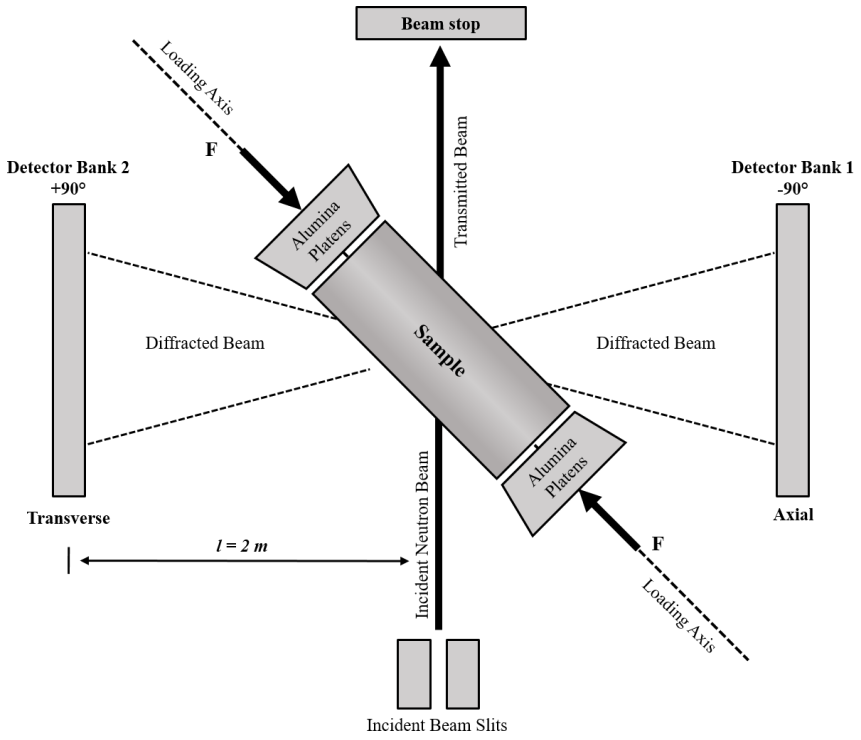

Figure 1.3. Diagram of VULCAN engineering diffractometer showing detector placement and neutron beam geometry with respect to the sample and loading axis with a compression sample; not to scale.

$$\lambda = \frac{h\,t}{m_n\,L} \quad (2.3.)$$

where h is Planck's constant, m_n is the mass of a neutron, and L is the distance between the detectors and the neutron beam is two meters from the detectors at the VULCAN instrument [160, 162, 163]. The wavelength accounts for the velocity of individual neutrons within each neutron pulse. Each volume element in the diffracted media produces Debye-Scherrer cones from planes normal relative to the sample. Each cone moves from low to high scattering angles proportional to the velocity and inversely proportional to the wavelength allowing for all crystallographic planes to be measured.

The VULCAN instrument is equipped with two sets of detector banks to collect both directions normal to the diffraction planes, ±90° with respect to the neutron beam [162, 164]. These are useful for in-situ studies with the goal of collecting lattice strain data during an external stimulus. The VULCAN instrument is equipped with a hydraulic Materials Test Systems (MTS) load frame that can apply compressive or tensile deformation for in-situ mechanical studies [162, 164, 165]. Samples are held 45° with respect to the incident beam. Compression cylinder samples are held in the load frame by compression with platens that have a matching diameter, depicted in Fig. 1.3., and tensile samples are held by grips.

Sample Preparation and Description

As-built and HIPed GRCop-84 samples were provided by NASA MSFC. The samples were produced by L-PBF on a Concept Laser M2 according to NASA's build parameters, shown in Table 1.2, and were built in the same sample lot as previous studies and share the same chemistry [166]. The HIPed samples were processed according to NASA's procedures, and all samples were removed from the build plate by electron discharge machining (EDM). Compression samples were prepared from 20 mm cubes by EDM into cylinders with an 8 mm diameter and 16 mm length. The cylinders were segmented parallel (xy) and perpendicular (z) to the AM build direction for a total of four samples. The sectioning method is demonstrated in Fig. 2.3. with added lines to illustrate the layers. The cylinders with length cut parallel to the build direction are labeled as 'Z' while the perpendicularly cut cylinders are labeled 'XY.' X and Y are arbitrary to the build axis or Z. The samples were cut in these orientations to compare the effect of the microstructural texture from the build layers. No additional polishing was performed as the EDMed surfaces were sufficiently uniform for the neutron TOF experiments to maintain a uniform scattering cross-section.

Experimental Procedure

An extensometer was attached to each sample prior to placement in the load frame, and zeroed after applying sufficient compression to hold the samples in place. Compression was applied with variation of the strain rate to investigate different regions. From a macroscopic perspective, the regions included elastic loading, plastic loading, and elastic unloading. Previous work with Cu alloys has shown that the initial elastic loading

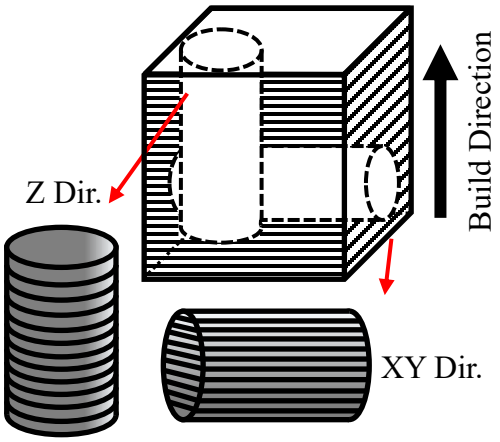

Figure 2.3. Sample sectioning and distinction of build layers between XY and Z samples.

region tends to be non-linear and relatively short, so the samples were strained below their expected breaking point and unloaded for calculation of elastic moduli. The maximum strain value was determined based on previous L-PBF results [106], and the maximum strain of the samples was varied slightly to investigate any potential differences. Prior to data collection, the samples were preloaded to 200 N in order to ensure consistent pressure from the platens and unloaded. The data collection for each sample began with a 30-minute period of data collection in an unstressed state to collect reference data prior to the experiment. Compression was slowly applied up to the anticipated yield point of 200 MPa to provide more data within the elastic loading region. Afterwards, a constant strain rate of ~1.4×10^{-5} s^{-1} was applied until reaching an intended strain value. The compression was then slowly relieved to measure the unloading response. This process is illustrated in Fig. 3.3. using the HIP XY sample for both stress and strain as a function of time and stress versus strain. To avoid confusion, the terms applied and macroscopic refer to the values recorded by the load frame, and lattice, planar, and phase refer to the diffraction data. Data were collected on a standard vanadium sample in the same configuration to normalize the detector efficiency and apply the appropriate correction.

Data Processing

At VULCAN, each neutron captured by the detectors is recorded with a timestamp based on a master time clock [162]. This allows for the mechanical loading to be applied continuously without the need for stepwise scans. The data requires additional processing with the VULCAN Data Reduction and Interactive Visualization Software (VDRIVE) which combines the data into useable subsets relative to a time interval [167]. A time interval of 300 s, which are represented as data points in Fig. 3.3., was chosen for providing a reasonable spacing between data in the plastic region while producing sufficient diffraction statistics.

The reduced data was then read into the General Structure Analysis System (GSAS) via the EXPGUI graphical user interface [145, 146] for Rietveld analysis. Crystallographic information files (CIF) for FCC Cu [148] and cubic C15 Laves Cr_2Nb [149] were obtained from the Inorganic Crystal Structure Database (ICSD) [147] for calculating diffraction patterns and providing initial parameters for refinements. A limited subset of parameters were refined to reduce errors including obtaining a false minimum. Consistency was achieved by refining on the parameters in the same order for each data set. Although a variety of structural information can be obtained from Rietveld refinements, the specific parameters refined in this study were the lattice parameters and phase fraction of each phase and the full-width half-maximum and peak position (d-spacing) of each diffraction maxima. Four family-independent planes were selected from the neutron data for the analysis of FCC Cu (200), (220), (111), and (311), reducing the amount of data into a more manageable subset. The (222) plane was also used in analysis and helped serve as a reference in calculations since the (111) and (222) planes should have similar behavior since they belong to the same planar family. As a minor constituent phase, Cr_2Nb had significantly less diffracted intensity, and the three best diffraction maxima were chosen and included the (440), (333), and (442) planes for their relative

intensity and isolation from other diffraction maxima.. The individual peaks were fit, and the planar spacing and other shape factors were obtained. Furthermore, these are real samples that are not perfectly crystalline and are subject to a variety of factors that can cause inherent scattering of data. AM samples, in particular, push the capabilities of neutron diffractometers to their limits, and similar experiments in literature usually focus only on the primary phase.These are samples intended to reflect materials that will be found in harsh service applications and are plagued with a variety of issues, including that the rapid cooling rates found in L-PBF, render the Cr_2Nb precipitates highly disordered. As a result, some of the diffraction maxima analyzed, especially in the as built condition, are broad and correspondingly low in intensity. This is often reflected in large estimated standard deviations in several of the refined parameters. In most cases, the intensity and coherence of the diffracted peak data can be improved by counting for longer times, however, with the high demand and limited sources neutron diffraction beamtime is often limited.

Results and Discussion

Macroscopic Compression Behavior

The macroscopic stress-strain behavior of the compression samples is shown in Fig. 4.3. Its axes and the axes of all subsequent stress-strain plots are reversed to resemble tensile stress-strain plots for ease of interpretation. The initial loading elastic region of each sample is somewhat non-linear while the subsequent unloading elastic region is nearly perfectly linear. The exact cause of this behavior is unknown but is likely due to rapid plastic deformation of the Cu. In Fig. 4.3., the HIP Z curve's stress dips at ~0.004 and ~0.056 stain, which is attributed to temporary beam loss at the neutron source. During periods of beam loss, the diffraction data is absent and was not caught during the allocated experiment time.

The behavior of L-PBF GRCop-84 strongly resembles the tensile behavior of a previous study by Gradl et al. [12] with L-PBF GRCop-84 built with similar parameters. The as-built samples exhibit brittle behavior while the HIPed samples are more ductile. During plastic deformation, the ultimate tensile strength (UTS) is not reached, though further strain likely would have reached the UTS, and the samples all continued to strain harden until unloading. Typical build-induced anisotropy of AM components is observed for as-built and HIPed samples comparing the XY and Z orientations. In the plastic deformation region, the as-built Z condition has at most ~4% less stress compared to the as-built XY curve, while the HIP Z condition has at most ~7% less stress compared to the HIP XY curve.

The elastic moduli were determined from the unloading curves and are presented in Table 1.3. The values are close to that expected for Cu with the HIPed specimens exhibiting a higher average modulus compared to the as-built, but only by ~10 GPa. The purpose of calculating the modulus is to confirm that the values are of a similar magnitude and provide a comparison to previous and future efforts.

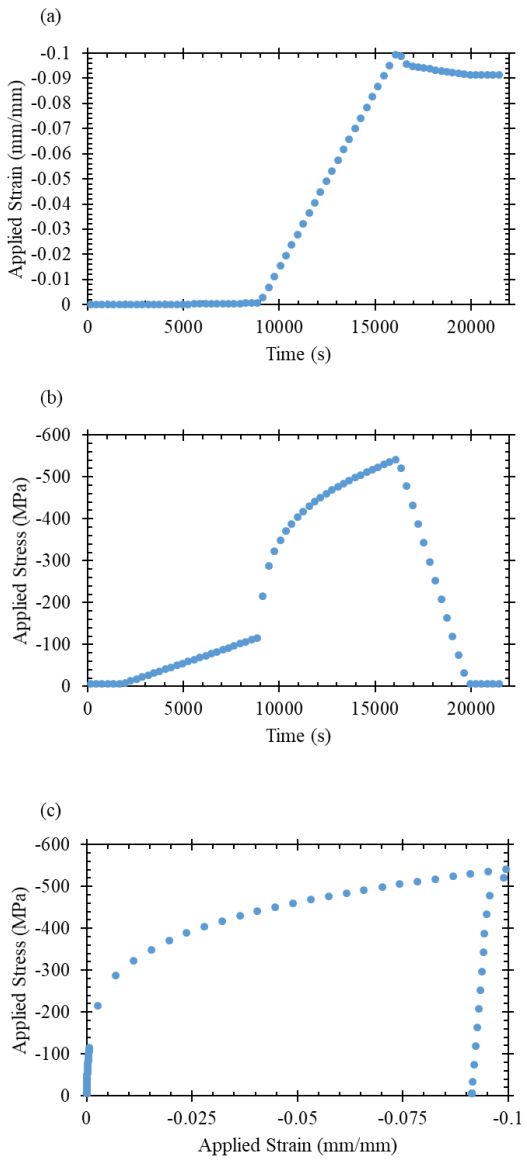

Figure 3.3. Data from the HIP XY sample illustrating the experimental procedure as (a) a function of time and applied strain, (b) time and applied stress, and (c) applied strain and applied stress; each marker represents data binned over the period of 300 s; both axes are reversed to resemble conventional tensile plots.

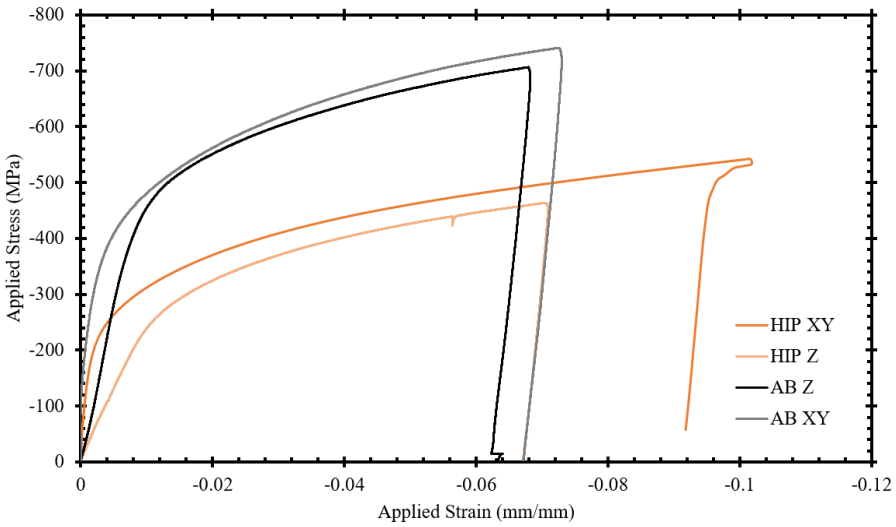

Figure 4.3. Macroscopic stress-strain plots for as-built (AB) and HIPed L-PBF GRCop-84 tested in compression; both axes are reversed to resemble tensile plots.

Table 1.3. Elastic modulus determined from the unloading curve of applied stress-strain results shown in Fig. 4.3.; the coefficient of determination, or R^2, of each value is >0.99.

		Bulk Elastic Modulus, E (GPa)	
		As-built	*HIPed*
Sample Orientation	XY	123	119
	Z	111	130

Phase Fractions

Rietveld analysis was used to refine lattice parameters and phase fractions of Cu and Cr_2Nb from data collected on the samples prior to compression and are reported in Table 2.3. TOF diffraction profiles collected on samples with the XY orientation prior to compression for the as built and HIPed conditions are compared in Fig. 5.3. During subsequent compression, the phase fractions did not change significantly. No stress-induced phase transformations were expected or observed. The Cr_2Nb phase fraction is low in the as-built condition with only 2.6(8) and 2.7(9) wt% refined for the XY and Z directions, respectively, compared to the ~12 wt% should be nominally present and the 12(1) and 14(2) wt% refined for the HIPed samples. This lower-than-expected weight fraction of the Cr_2Nb in the as built samples was also observed in X-ray studies [166] and is likely caused by rapid solidification effects of L-PBF and stoichiometric variance in C15 Laves Cr_2Nb resulting in diffraction maxima that are broad and have low intensity, shown in Fig. 5.3.(c). As a result, all analysis of the as-built samples is limited to the Cu phase. However, after HIPing the disorder from rapid solidification has been annealed out resulting in sharper more intense Cr_2Nb diffraction maxima allowing for analysis.

Evolution of Lattice Strain in Loading

The lattice spacing, or d-spacing, of a crystalline phase's lattice planes, *hkl*, will change under an applied load. Lattice strain, ε_{hkl}, is measured in the same manner as engineering strain using the unloaded state, d^0_{hkl}, as a reference point with

$$\varepsilon_{hkl} = \frac{\left(d_{hkl} - d^0_{hkl}\right)}{d^0_{hkl}} \quad (3.3.).$$

Unlike engineering strain, lattice strain, based on accepted theory, is intrinsically elastic [168, 169]. Under an applied load in a polycrystalline material, stress develops at each grain that can either be elastic or plastic, but diffraction methods only measure the elastic portion [169]. Diffraction measures crystallites that are in the correct orientation, or *hkl*, to diffract based on the relative orientation of the beam. This holds for lattice strain measurements of polycrystalline materials which measure an average displacement of crystallites, or grains, in the corresponding orientation that diffract.

The evolution of lattice strain in loading is presented in Fig. 6.3.(a-b), 7.3.(a-b), and 8(a-b) for the as-built XY, as-built Z, and HIPed XY samples, respectively. These figures are plotted against macroscopic stress to understand the link between crystallite and macroscopic behavior with both axial and transverse response. During deformation, each plane demonstrates a unique behavior. This is because, lattice deformation, and correspondingly oriented grains or crystallites, is typically anisotropic due the arrangement of atoms in a crystalline lattice [170]. Furthermore, the slope changes indicate a transition in the primary deformation mechanism or load sharing behavior. Four stages of deformation have been identified in the Cu lattice planes for each sample and are labeled on the appropriate figures. Dashed lines are placed between data points and are used to represent an approximation of where the slope change is occurring. Stages II-IV are marked on the axial figures with + or – signs to indicate the perceived change in

Table 2.3. Lattice parameters, *a*, and weight fractions from the as-built and HIP samples refined using Rietveld analysis and time-of-flight neutron powder diffraction data collected prior to mechanical loading at room temperature. Target alloying composition included for comparison.

	Ambient Neutron TOF As-built L-PBF GRCop-84			
	XY		Z	
	Cu	*Cr_2Nb*	*Cu*	*Cr_2Nb*
a (Å)	3.6162(4)*	6.978(7)	3.6309(4)	6.991(7)
Wt%[+]	97.4(3)	2.6(8)	97.3(3)	2.7(9)
	Ambient Neutron TOF HIP L-PBF GRCop-84			
	XY		Z	
	Cu	*Cr_2Nb*	*Cu*	*Cr_2Nb*
a (Å)	3.6153(3)	6.980(2)	3.6162(2)	6.980(3)
Wt%[+]	87.5(9)	12(1)	86(2)	14(2)
Target Wt%	Cu	87.8	Cr_2Nb	12.2

* Estimated standard deviation (esd) reported as 3σ
[+] Total wt% may exceed 100% due to rounding

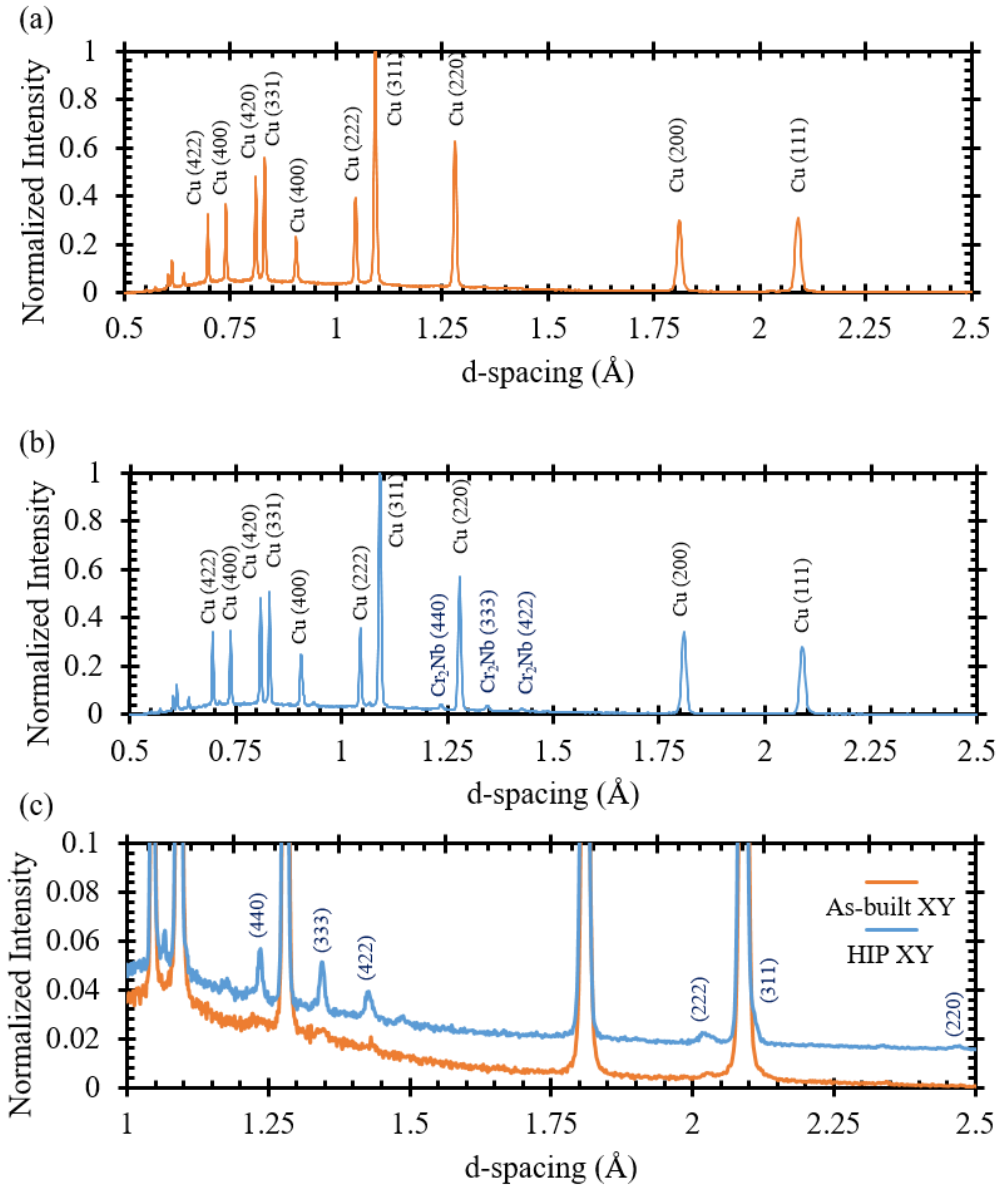

Figure 5.3. Normalized time-of-flight diffraction profiles of L-PBF GRCop-84 (a) XY sample in the as-built condition, (b) XY sample in the HIPed condition, and (c) comparison at low intensity.

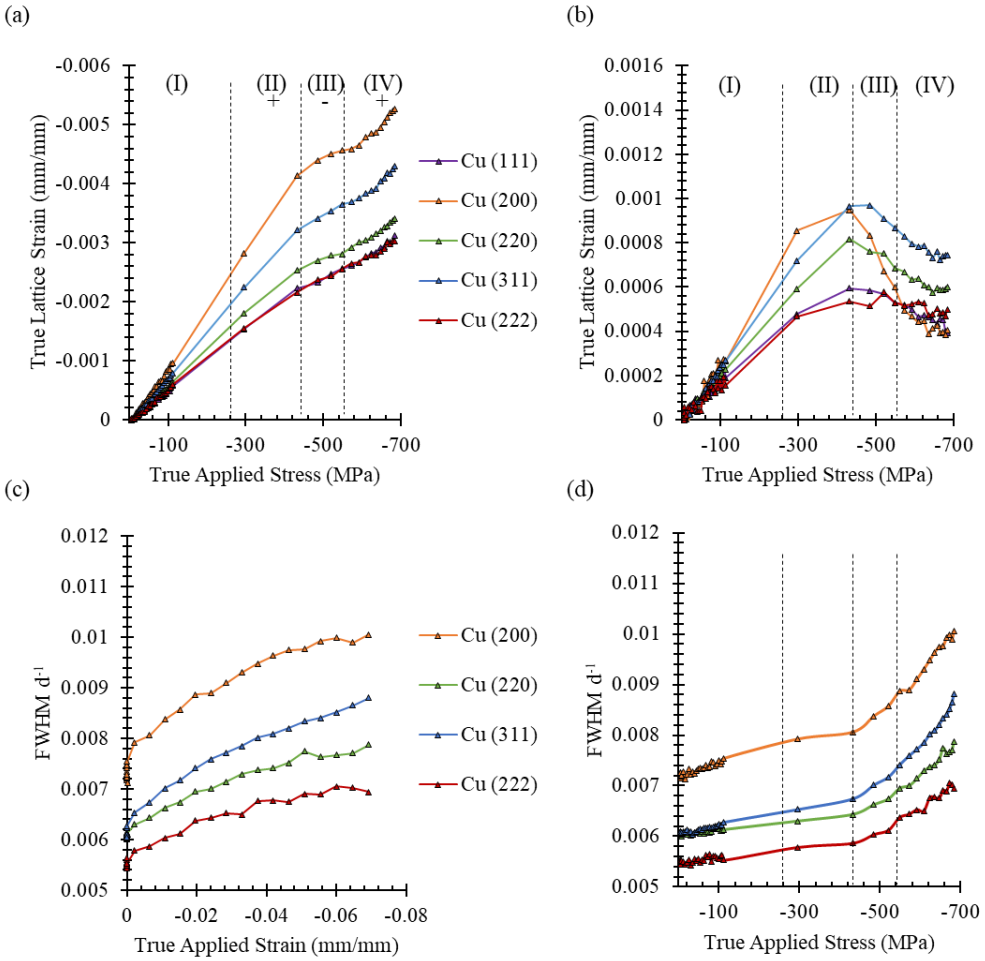

Figure 6.3. Cu lattice loading behavior under uniaxial compression of as-built XY L-PBF GRCop-84 comparing axial (left) and transverse (right) response; (a-b) lattice strain; (c-d) dislocation density behavior estimated by FWHM d^{-1} for the axial behavior plotted against macroscopic strain and stress respectively; dashed lines indicate possible changes in slope; some axes have been reversed for comparison.

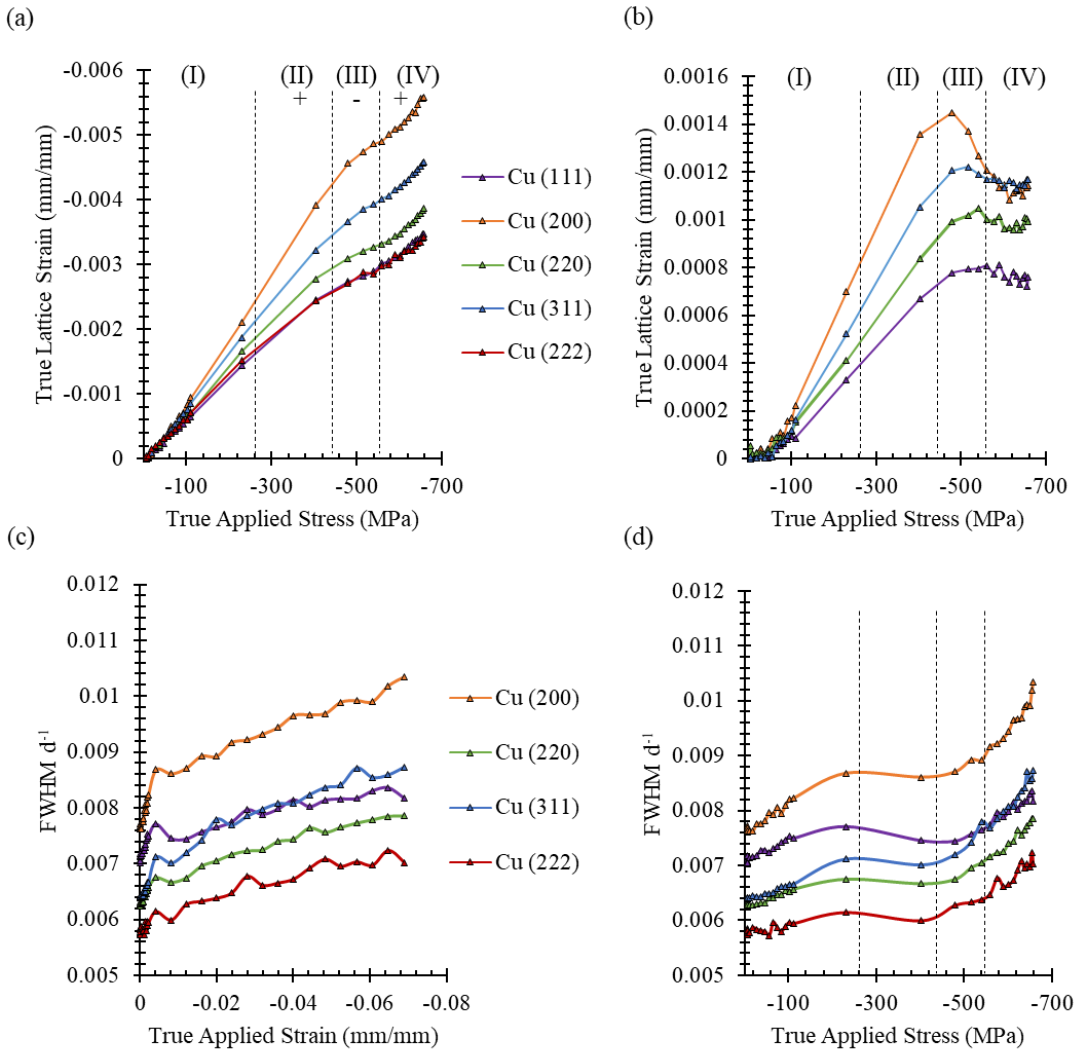

Figure 7.3. Cu lattice loading behavior under uniaxial compression of as-built Z L-PBF GRCop-84 comparing axial (left) and transverse (right) response; (a-b) lattice strain; (c-d) dislocation density behavior estimated by FWHM d^{-1} for the axial behavior plotted against macroscopic strain and stress respectively; dashed lines indicate possible changes in slope; some axes have been reversed for comparison.

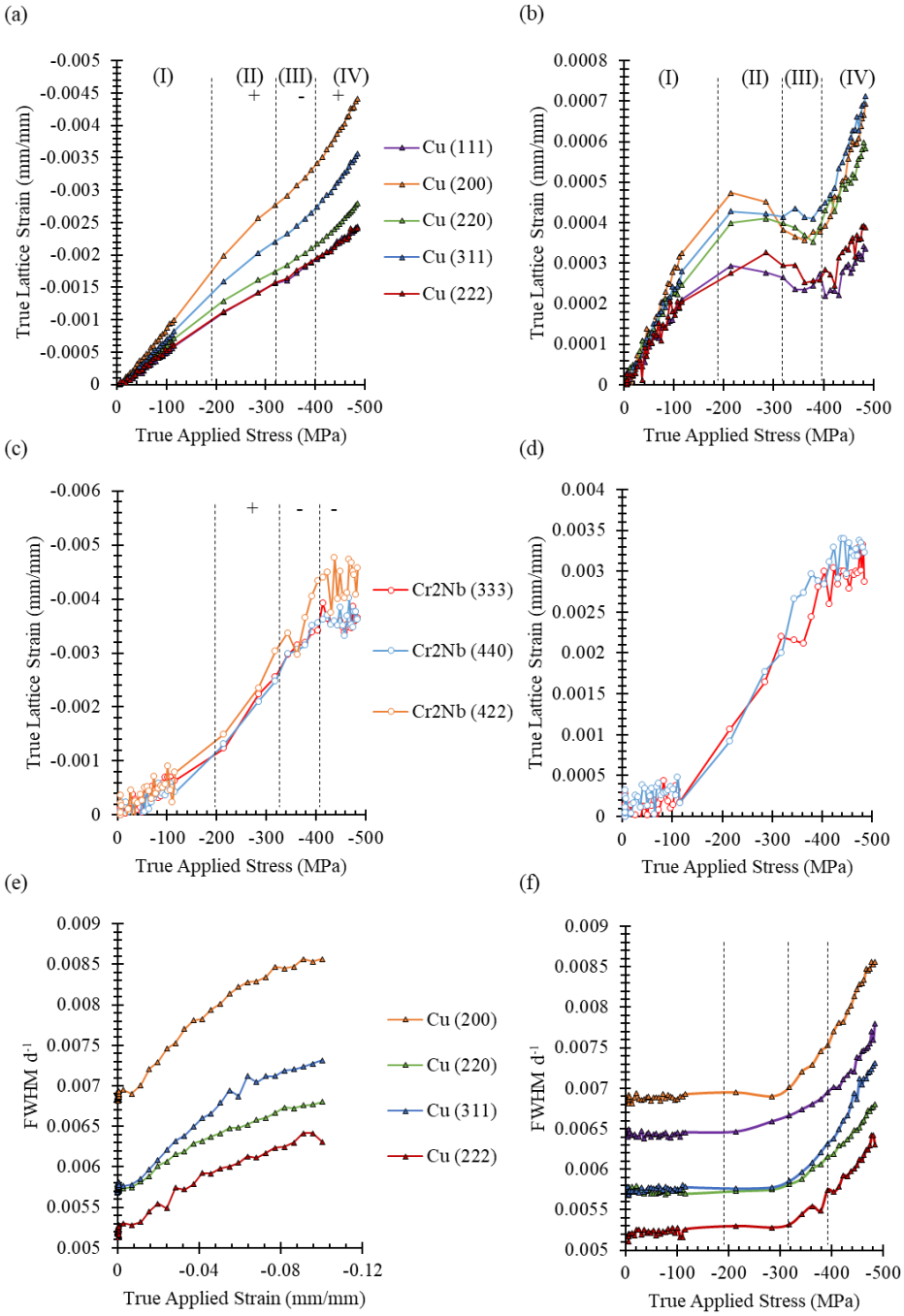

Figure 8.3. Loading behavior under uniaxial compression of HIP XY L-PBF GRCop-84 comparing axial (left) and transverse (right) response; (a-b) lattice strain of Cu; (c-d) lattice strain of Cr_2Nb; (e-f) dislocation density behavior of Cu estimated by FWHM d^{-1} for the axial behavior plotted against macroscopic strain and stress respectively; dashed lines indicate possible changes in slope; some axes have been reversed for comparison.

slope. In some cases, the axial behavior shows little distinction between the slopes of I and II, but the transverse shows a significant slope change. The behavior of the full width half maximum (FWHM) divided by the lattice d-spacing, FWHM d^{-1}, is presented in Figures 6.3.-8.3. against the macroscopic strain and stress values. FWHM d^{-1} is known to be proportional to the dislocation density and is commonly used as an indicator of hardening or softening in materials [168, 171-175]. The FWHM d^{-1} for the Cr_2Nb is not presented due to the low intensity and broad diffraction maxima just above background. The majority of the analysis will be based on the axial behavior because the transverse response is less statistically reliable. Clausen [176] explains this difference between the axial and transverse response as intrinsic to the measurements. The axial response is rotationally symmetric to the deformation direction while the transverse response is limited by higher stiffness deviation in the grains and lower strain levels from the Poisson effect, which can be seen by the limits of the y-axes of Fig. 6.3.(a) and Fig. 6.3.(b).

Stage I is expected to correlate with the elastic region of the macroscopic stress-strain response. Within this stage, two diffraction elastic constants (DEC) can be determined that are specific to their relative grain orientation or *hkl* including the modulus, E_{hkl}, and Poisson ratio, υ_{hkl}. As the name implies, these values are only relative to lattice behavior in the elastic region, and are not fully comparable to the correlating engineering constants. Lattice behavior of cubic materials is typically anisotropic, and the DEC's will vary between family of planes. The slope, E_{hkl}, is calculated from

$$E_{hkl} = \frac{\sigma_{macro}}{\varepsilon_{hkl}} \quad (4.3.)$$

where σ_{macro} represents the macroscopic stress and ε_{hkl} represents the lattice strain. The Poisson ratio DEC, υ_{hkl}, is the same as a macroscopic calculation with

$$\upsilon_{hkl} = -\frac{\Delta\varepsilon_{trans}}{\Delta\varepsilon_{axial}} \quad (5.3.)$$

where $\Delta\varepsilon_{trans}$ is transverse strain, and $\Delta\varepsilon_{axial}$ is axial strain. Calculating DECs requires a known macroscopic stress and a direct measurement of axial and transverse strain, and both of these are readily achieved at VULCAN with the load frame and two sets of detectors.

However, it is critical to understand that the DECs will change during deformation, as shown by the changes in the slope illustrated in figures 6.3, 7.3, and 8.3. Measurement of lattice strain remains intrinsically elastic, but if the slope changes, intergranular misfit from differential slip occurs that is effectively plastic [160]. In order to reverse the effect, reverse 'plastic' slip has to occur during unloading which is not feasible. This can result in residual intergranular strain after unloading that Hutchings et al. [160] refer to as pseudo lattice strains. To compensate for this, the DECs of both the initial loading region in stage I and the unloading region were calculated. Any non-linear behavior can be attributed to intergranular shape misfits but are difficult to distinguish.

Rather than use data points from the experiment and Eq. 5.3. alone, the Poisson ratios were calculated from the Young's moduli by substituting Eq. 4.3. into Eq. 5.3. by

$$\upsilon_{hkl} = -\frac{\Delta E_{hkl,axial}}{\Delta E_{hkl,trans}} \quad (6.3.)$$

with axial, $\Delta E_{hkl,axial}$, and transverse, $\Delta E_{hkl,trans}$, modulus DECs. Similar to macroscopic elastic region, the moduli within stage I were largely non-linear and difficult to measure, shown in Table 3.3. Only the values for the Cu phase are presented since the Cr_2Nb data still had too much scatter. Even the HIPed samples' loading curves were somewhat non-linear, and they are expected to be in an annealed state. The moduli were measured from six to eleven data points between 35 – 90 MPa of stress and should not be considered anything other than an estimate.

The moduli within stage I provide the best method of comparing load sharing behavior within the elastic region. The lower the modulus, the lower the relative strength and the higher strain at a given stress. Each sample had the same order of magnitude of strength for the Cu matrix with (200), (311), (220), and (111) from most compliant to least compliant. This is the same behavior predicted by the Kröner model, shown in Table 4.3., for pure Cu [160]. The Kröner model accounts for variations of stress and strain within the grains but assumes uniform crystallite size. The experimental results are reasonably consistent with the Kröner model values and deviations can be attributed to alloying content and influence of texture and non-uniform crystallite size.

Within stage I, both Cu and Cr_2Nb phases are expected to undergo elastic deformation; however, the FWHM d^{-1} plots for the as-built samples, Fig. 6.3.(d) and Fig. 7.3.(d), demonstrate an immediate increasing trend in the dislocation density within stage I. In contrast, the HIPed sample's dislocation density, Fig. 8.3.(f), does not increase and remains constant. These results indicate that the Cu phase of the as-built samples rapidly undergoes plastic deformation and strain hardening while the HIPed Cu phase elastically deforms. The source of this difference is hypothesized to be due to the presence of residual thermal stresses and higher dislocation density in the as-built material from AM that are relieved as part of the HIP process. A similar observation was made by Brown et al. [161] with austenite in AM 304L stainless steel, and they attribute the higher stresses of as-built material to the higher dislocation density. Lattice deformation and DECs are dependent on previous mechanical and thermal history, implying that the previous residual stresses either exceeded the 'true' elastic stage I or are at the maximum strain necessary to stay within stage I. Key differences between the XY and Z sample may provide further evidence for this hypothesis. During AM, the majority of the residual stress is expected to be present between the vertical layers from thermal expansion of the heat affected zone into cool layers [177]. The Z sample, which was sectioned parallel to the build direction, demonstrates a significantly higher slope in the FWHM d^{-1} plots compared to the XY sample and may indicate a higher degree of prior plastic deformation from residual stresses, though the general behavior is the same for both. These results indicate that stage I for the HIPed condition consists of elastic deformation for the Cu and Cr_2Nb phases and general macroscopic behavior. Stage I for the as-built samples consists

of plastic deformation of the Cu phase, partially dependent on the build orientation relative to the sample.

Stage II is expected to occur at the onset of macroscopic plastic deformation, around 200 MPa. Comparing the differences in the trends is useful for assessing changes in compliance and deformation behavior. In general, the relative increase or decrease between stages represents a change in compliance. An upward trend in the lattice strain curves versus macroscopic stress indicates more lattice strain increment and more correlating micro-stress increment [168]. The opposite holds for a decreasing trend. Considering that GRCop-84 consists of two phases, Cu and Cr_2Nb, it is likely that one begins to plastically deform in this stage while the other remains elastic. This trend of the Cr_2Nb can be seen in Fig. 8.3.(c-d) for the HIPed data. Despite the scatter in the data, the slope of the Cr_2Nb planes appears to increase significantly while the Cu planes slightly increases. Of the two phases, the Cr_2Nb is more likely to be plastically deforming. Further evidence for this is demonstrated by the FWHM d^{-1} behavior of the Cu phase in stage II. For each sample, the dislocation density in the Cu planes remains constant which is evidence of elastic deformation.

Although stage I of the Cu planes response of the as-built samples was indicative of plastic deformation, stage II's FWHM d^{-1} behavior indicates elastic deformation as the slope is roughly zero. Considering the change between stage I and II, the Cr_2Nb phase is expected to undergo plastic deformation similar to the HIPed results. The behavior of the as-built samples appears identical within stage II but not when plotted together, Fig. 9.3. The (200) trend is comparable for the XY and Z sample, but the remaining planes demonstrate significantly higher lattice strain in the Z direction. This indicates that more overall deformation is occurring in the Z sample which agrees with the macroscopic results in Fig. 4.3. and the calculated modulus DECs in Table 3.3. This difference is likely caused by a difference in texture, and the Z sample should have a higher proportion of (100) oriented grains due to epitaxial growth. A higher proportion of (100) grains decreases the proportion of the other grains and reduces the relative load carried. The (111) and (220) planes are the most affected by this difference.

In stage III, the trend of the Cu planes of the as-built and HIPed samples significantly decreases meaning that the Cu lattice is deforming less. This may indicate that the Cu phase is plastically deforming and strain hardening, and the dislocation density also increases and provides more evidence for this behavior. The as-built condition re-enters plastic deformation from stage I while the HIP condition begins plastic deformation of the Cu phase. The trend of the Z sample increases more than the XY sample, Fig. 9.3., in the (200) and (311) planes which may also indicate that they are preferentially slipping. The behavior of the Cr_2Nb planes in stage III for the HIPed sample is approximately the same as stage II and expected to continue strain hardening in stage III.

In stage IV, the trend of the Cu lattice of the as-built and HIPed samples increases, indicating that the Cu phase is carrying more lattice strain and micro stress at a higher rate of strain hardening than stage III. By contrast, the trend of the HIPed condition's Cr_2Nb does not appear to add strain during stage IV, though significant scatter of the data is present. This may indicate that the Cu phase is the only phase that is

Table 3.3. Diffraction elastic constants for L-PBF GRCop-84 calculated from loading lattice strain data; all elastic moduli reported as GPa.

As-built XY			***Cu***		
(hkl)	*(111)*	*(222)*	*(200)*	*(220)*	*(311)*
E_{hkl} *(GPa)Axial*	178	167	117	148	131
R^2	0.972	0.976	0.989	0.991	0.994
E_{hkl} *Transverse*	-423	-339	-255	-537	-380
R^2	0.570*	0.758*	0.708*	0.958	0.951
υ_{hkl}	-	0.492	0.461	0.276	0.345
As-built Z			***Cu***		
(hkl)	*(111)*	*-222*	*(200)*	*(220)*	*(311)*
E_{hkl} *Axial*	149	168	116	137	124
R^2	0.969	0.988	0.988	0.988	0.999
E_{hkl} *Transverse*	-678	-417	-389	-579	-517
R^2	0.922	0.517*	0.876	0.863	0.900
υ_{hkl}	0.220	-	0.298	0.237	0.239
HIP XY			***Cu***		
(hkl)	*(111)*	*(222)*	*(200)*	*(220)*	*(311)*
E_{hkl} *Axial*	173	127	111	156	144
R^2	0.962	0.997	0.982	0.957	0.990
E_{hkl} *Transverse*	-422	-347	-363	-284	-388
R^2	0.927	0.971	0.899	0.671*	0.813
υ_{hkl}	0.411	0.367	0.306	-	0.371

* Low R^2 imply low confidence in associated modulus and Poisson ratio

Table 4.3. Cu axial DECs values predicted by the Kröner model from [160] with experimental DECs calculated from data obtained during unloading; all elastic moduli value reported as GPa.

	Kröner Model	*As-built XY*	*As-built Z*	*HIP XY*	*HIP Z*
E_{bulk} *(GPa)*	129.4	134(5)*	132(5)*	141(5)	141(5)
υ_{bulk}	0.34	0.34(1)*	0.35(1)*	0.35(1)*	0.35(1)*
E_{111}	159	172	161	180	179
E_{222}	---	173	159	183	173
E_{200}	101.1	97	105	101	103
E_{220}	139.1	147	140	156	156
E_{311}	122	123	124	129	128
ν_{111}	0.31	0.351	0.372	0.341	0.332
ν_{222}	---	0.356	---	0.348	0.375
ν_{200}	0.38	0.322	0.404	0.343	0.335
ν_{220}	0.33	0.359	0.263	0.379	0.393
ν_{311}	0.35	0.341	0.367	0.339	0.340

*Experimental E_{bulk} and υ_{bulk} values are an average of the respective (111), (220), (311), and (222) values and are used as estimates with an estimated standard deviation in ( ).

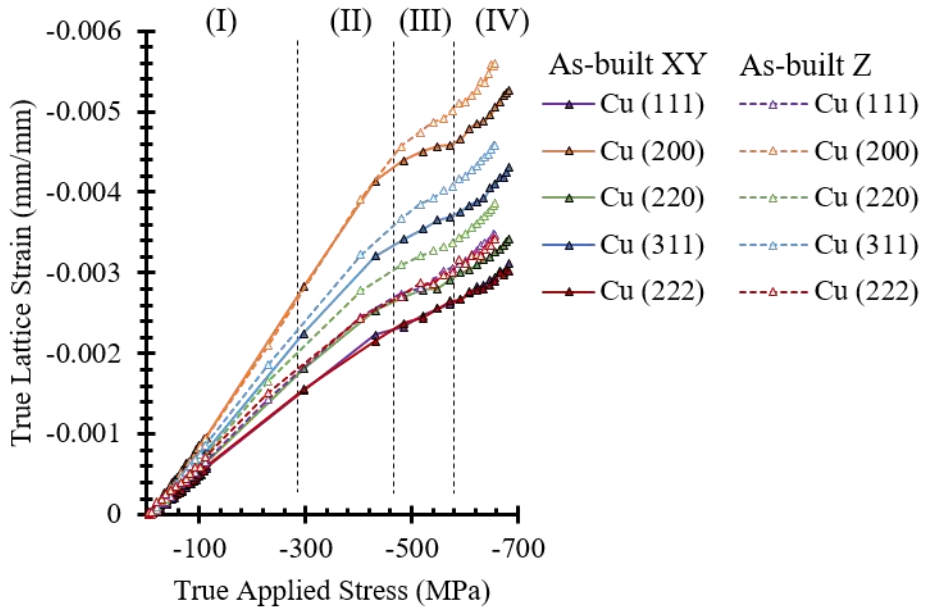

Figure 9.3. Comparison of axial Cu lattice strain of the as-built samples, combining Fig. 6.3(a) and Fig. 7.3(a), against the applied macroscopic stress; dashed lines indicate possible changes in slope; the trends of the (111) and (222) curves are overlapped.

carrying the load past the stress between stage III and IV and the Cr_2Nb has a maximum amount of strain it can support during deformation. A similar effect is expected for the as-built condition but cannot be confirmed.

At the end of stage IV, the final effect of the build direction on the as-built samples can be seen in Fig. 9.3., but the samples were also unloaded to measure the DECs and pseudo-residual strains for comparison. The unloading DECs were more linear and consistent than loading and are shown in Table 5.3 and compared to the Kröner model values in Table 4.3. These DECs are representative of stage IV, and should follow these values if reloaded until another deformation change occurs. The pseudo residual strains of each sample are shown in Fig. 10.3. The as-built XY sample has a high degree of strain that is 200-300% compared to the as-built Z, and the HIP XY sample has a low degree of strain, 33-66% less than the as-built Z. These values indicate the relative amount of intergranular lattice strain that have accumulated during deformation are tensile, rather than compressive. Using the modulus DEC for unloading for the as-built XY (311) plane, 123 GPa, and the residual lattice strain, ~0.0012, the corresponding lattice stress is 147 MPa. The as-built Z direction's (311) plane has a lattice stress of 72 MPa with a modulus of 124 GPa and ~0.0006 strain. This is somewhat confusing because the XY direction is known to be stronger, but this may show that the texture of the XY direction is able to hold more intergranular strains than the Z direction which is why it is stronger macroscopically. The XY texture is expected to be relatively uniform, and the (100) plane demonstrates the highest intergranular strain. The Z direction has preferential (100) texture and excess of intergranular strain in the higher relative proportion of (100) grains may have led to further slip and deformation at similar macroscopic stresses.

Unfortunately, this analysis lacks the context of the Cr_2Nb phase. The residual lattice stress of the Cr_2Nb in the HIPed sample, Fig. 10.3.(b), is compressive and is 200-300% higher than the Cu lattice strains demonstrating a balancing effect with the tensile strain of the Cu lattice. It is unknown how the Cr_2Nb interacts with the as-built samples, but it should balance the Cu phase with a similarly high value unless there is a limit to the amount of intergranular strain.

Evolution of Phase Strain in Loading

The lattice parameter, *a*, provides an effective average of the behavior of the phase. Most of the observations from the lattice plane response still hold, and the phase strain can provide improved statistics. Although some comparison of the Cu and Cr_2Nb phases has been completed with individual lattice strains, the best method of comparison is with the lattice parameter as it represents the average planar response. Phase strain, $\varepsilon_{\text{phase}}$ is represented by strain of the lattice parameter, a_{phase}, with

$$\varepsilon_{\text{phase}} = \frac{\left(a_{\text{phase}} - a^0_{\text{phase}}\right)}{a^0_{\text{phase}}} \quad (7.3.)$$

where a^0_{phase} is the lattice parameter prior to deformation.

Table 5.3. Diffraction elastic constants for L-PBF GRCop-84 calculated from unloading lattice strain data with Cr_2Nb values; R^2 >0.995 unless stated

As-built XY			***Cu***		
hkl	*(111)*	*(222)*	*(200)*	*(220)*	*(311)*
E_{hkl} *Axial (GPa)*	172	173	97	147	123
E_{hkl} *Transverse (GPa)*	-491	-487	-302	-409	-360
υ_{hkl}	0.351	0.356	0.322	0.359	0.341
As-built Z			***Cu***		
hkl	*(111)*	*(222)*	*(200)*	*(220)*	*(311)*
E_{hkl} *Axial (GPa)*	161	---[+]	105	140	124
E_{hkl} *Transverse (GPa)*	-434	---[+]	-259	-531	-339
υ_{hkl}	0.372	---[+]	0.404	0.263	0.367
HIP XY			***Cu***		
hkl	*(111)*	*(222)*	*(200)*	*(220)*	*(311)*
E_{hkl} *Axial (GPa*	180	183	101	156	129
E_{hkl} *Transverse (GPa)*	-529	-526	-294	-412	-379
υ_{hkl}	0.341	0.348	0.343	0.379	0.339
			Cr_2Nb		
hkl		*(333)*	*(440)*	*(422)*	
E_{hkl} *Axial (GPa)*		156	157	139	
R^2		0.975	0.953	0.943	
E_{hkl} *Transverse (GPa)*		-324[*]	-376	-307[*]	
R^2		0.726	0.954	0.653	
υ_{hkl}		0.482[*]	0.416	0.453[*]	
HIP Z			**Cu**		
hkl	*(111)*	*(222)*	*(200)*	*(220)*	*(311)*
E_{hkl} *Axial (GPa)*	179	173	103	156	128
R^2	0.999	0.998	1.000	1.000	1.000
E_{hkl} *Transverse (GPa)*	-540	-462	-306	-396	-376
R^2	0.995	0.973	0.995	0.996	0.999
υ_{hkl}	0.332	0.375	0.335	0.393	0.340

[*] Low R^2 imply low confidence in associated modulus and Poisson ratio
[+]Not calculated due to scatter low R^2 values

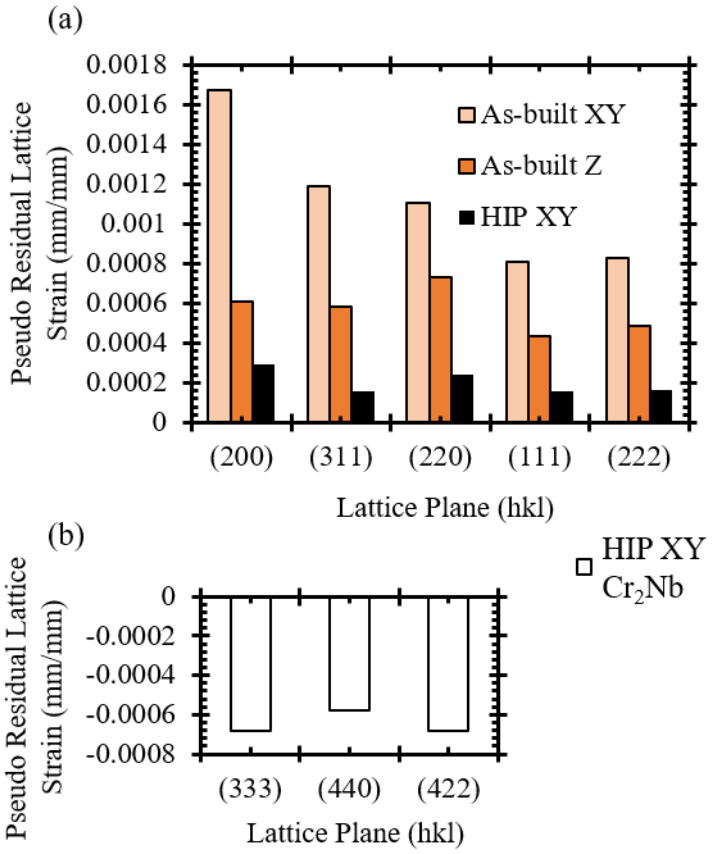

Figure 10.3. Calculated residual lattice strain for the (a) Cu and (b) Cr_2Nb planes with y-axis similar to (a) for comparison.

The Cu phase strain of each sample in loading is compared in Fig. 11.3., and the Cr_2Nb phase is compared to the Cu of the HIP XY sample in Fig. 12.3. Comparatively, the Cu phases of the as-built and HIPed samples have similar behavior and changes in slope but with different overall stresses due to macroscopic differences. The as-built XY sample has the highest compressive strength while the HIP XY sample has the highest degree of ductility. From a lattice perspective, the as-built Z sample has the highest amount of strain at any given stress and indicates that its Cu phase is the most compliant. The as-built XY's lower Cu phase strain is more effectively balanced by intergranular strains and likely exhibits a higher Cr_2Nb strain partitioning. By this logic, the Cu phase of the HIP XY sample is the least compliant but is difficult to directly compare due to significantly less compressive stress and higher ductility.

The lattice response of the Cu and Cr_2Nb phases of the HIP XY sample, Fig. 12.3., is effectively the same until ~200 MPa where the Cr_2Nb trend significantly decreases. This correlates with the transition from stage I to II in the individual planar results, Fig. 8.3., where Cr_2Nb was projected to begin plastic deformation. In the subsequent stages, Cr_2Nb strain hardens and reaches a maximum phase strain of approximately -0.35 %. This general behavior resembles similar work by Song et al.[178] which compared the matrix and precipitate lattice response of Fe-Cr-Ni-Al-Ti alloys.

Considering that HIPing increases the strain macroscopically at a given stress and the Cu in the HIPed condition has less strain, either the Cr_2Nb's role or efficacy changes or the microstructure is significantly different after HIP. Considering the balancing effect that Cr_2Nb had on intergranular strain in the HIP sample, it is more likely due to the Cr_2Nb. A similar balancing effect is present in the phase strain of the HIPed sample, Fig. 12.3. When the trend of the Cu phase increases, the Cr_2Nb trend decreases and vice versa. This indicates a strong partitioning effect between the phases, and the Cr_2Nb phase should be responsible for a significant degree of strengthening.

DECs from the refined lattice parameters of both Cu and Cr_2Nb were measured in the loading region and unloading regions and are presented in Table 6.3. The Poisson ratio of the axial and transverse values was calculated from the moduli according to Eq. 6.3., and the Poisson ratio of the axial and transverse response was unusually high for Cr_2Nb in both the loading and unloading regions. Normally, Cr_2Nb's Poisson ratio is within the range of 0.34-0.38, [179] and the experimental values were close to 0.5 which is indicative of an incompressible material. The loading region has significant scattering in the data, visible in Fig. 12.3., but the overall trend is linear. In unloading, there is low scatter in the data, so the calculated value there has higher confidence. The exact reason behind the change to the Poisson ratio is unknown and a similar literature result could not be readily found. It is also unknown if this behavior is indicative of particle strengthened (dispersion or precipitation hardened) alloys or unique to GRCop-84 or Cr_2Nb. The unloading Poisson ratio from the planar response of Cr_2Nb, Table 5.3., was similarly high.

Conversion of Phase Strain to Stress

Although lattice strain contains considerable information about the material, macroscopic stress behavior is often more desirable as it is more applicable to practical

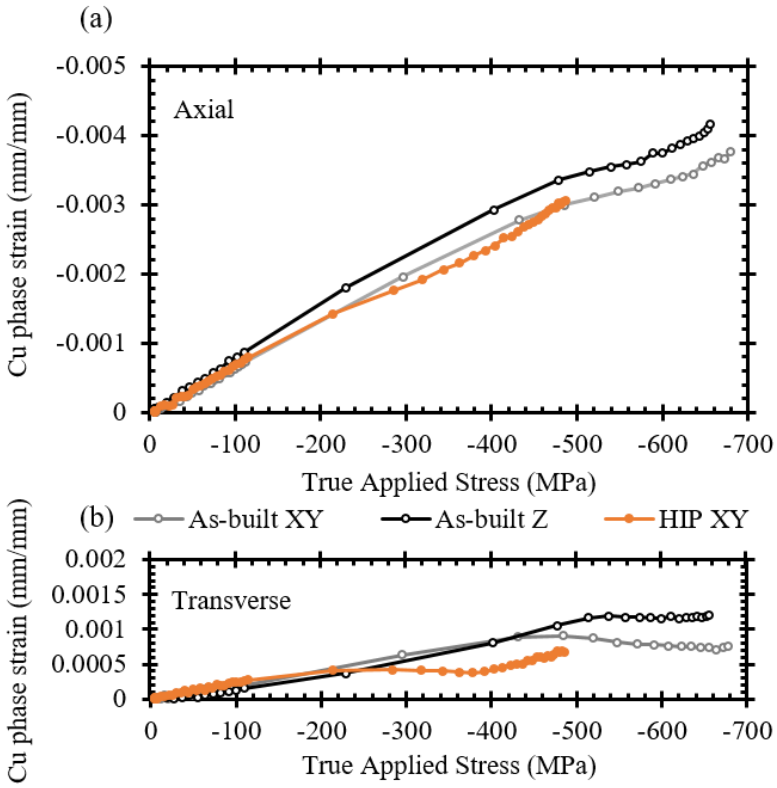

Figure 11.3. Comparison of Cu phase strain for each sample in the (a) axial and (b) transverse directions; some axes have been reversed for comparison.

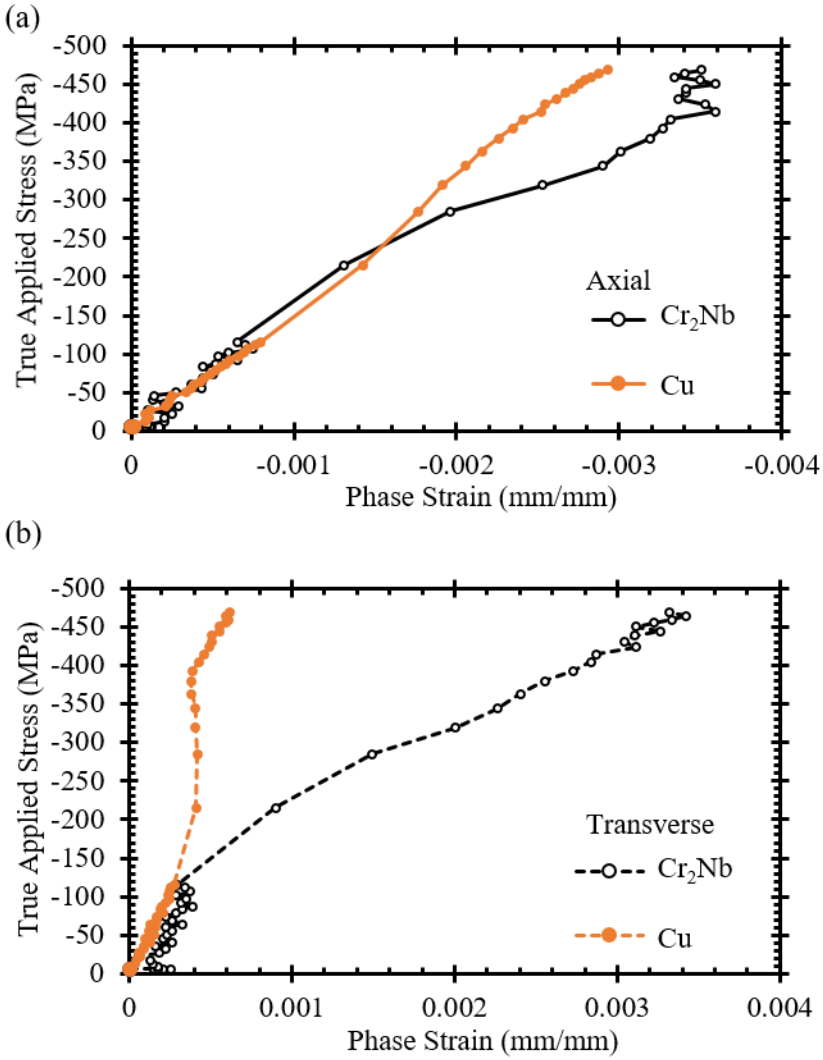

Figure 12.3. Comparison of Cu phase strain for HIPed GRCop-84 in (a) axial and (b) transverse directions; plotted with similar axes; some axes have been reversed for comparison.

Table 6.3. Lattice parameter based DECs for the HIP XY sample comparing Cu and Cr_2Nb in the initial loading (stage I) and unloading (from the end of stage IV) regions with estimated standard deviation in parenthesis.

HIP XY	***Loading***	
	Cu	***Cr_2Nb***
E_a Axial (GPa)	138(7)	153(8)
R^2	0.978	0.812
E_a Transverse (GPa)	-373(19)	-303
R^2	0.909	0.729
υ_a	0.371	0.504
HIP XY	***Unloading***	
	Cu	***Cr_2Nb***
E_a Axial (GPa)	159(8)	188(9)
R^2	0.999	0.993
E_a Transverse (GPa)	-411(20)	-405(20)
R^2	0.998	0.982
υ_a	0.388	0.463

design and implementation. All stress calculations from lattice strain are purely estimates due to complicated conversions from elastic stiffness tensors, *C*, and elastic compliance tensors, *S*, and it is not feasible to measure each independent variable of stress, strain to determine the tensors. The amount of independent components can be reduced by testing in isotropic conditions which reduces the elastic stiffness tensors to two independent elastic constants, Young's modulus, *E*, and Poisson's ratio, υ [160]. The phase-specific macroscopic stress can be calculated using a generalized Hooke's law equation

$$\sigma_i = \frac{E_i}{(1+\upsilon_i)}\left[\varepsilon_{11} + \frac{\upsilon_i}{(1-2\upsilon_i)}\left(\varepsilon_{11} + \varepsilon_{i,22} + \varepsilon_{i,33}\right)\right] \quad (8.3.)$$

where *i* represents either Cu or Cr_2Nb phase values, and ε_{11}, ε_{22}, and ε_{33} represent the principal strains. Each direction is an independent measurement, but only the axial and transverse response were measured. In uniaxial tension, the assumption is made that ε_{11} is representative of the axial strain, and ε_{22}, and ε_{33} are equal, $\varepsilon_{22} = \varepsilon_{33}$ where both are the transverse strain [168]. Equation 8.3. then becomes

$$\sigma_i = \frac{E_i}{(1+\upsilon_i)}\left[\varepsilon_{11} + \frac{\upsilon_i}{(1-2\upsilon_i)}\left(\varepsilon_{11} + 2\varepsilon_{i,22}\right)\right] \quad (9.3.).$$

The loading strain and DECs from the lattice parameter calculations were used with Eq. 9.3. for Cu to estimate stress; however, Eq. 9.3. could not be readily applied to the Cr_2Nb phase. An incompressible material with a Poisson ratio of 0.5 will cause the right side of the equation, $\frac{\upsilon_i}{(1-2\upsilon_i)}$, to divide by zero. A number near or greater 0.5, which is the case with Cr_2Nb, will result in a large, negative number. Attempts to use Eq. 9.3. with the Cr_2Nb data did not make physical sense, so the equation was simplified to

$$\sigma_{Cr2Nb} = \frac{E_{Cr2nb}}{(1+\upsilon_{Cr2Nb})}\varepsilon_{11} \quad (10.3.)$$

which only uses the axial strain. The phase stress was plotted with the applied strain in Fig. 13.3. along with the applied stress and a volume fraction average stress, $\sigma_{Average}$, calculated with a rule of mixtures. The rule of mixtures was based on the volume fraction with

$$\sigma_{Average} = \sigma_{Cu}(f_{Cu}) + \sigma_{Cr2Nb}(1 - f_{Cu}) \quad (11.3.)$$

where f_{Cu} represents the volume fraction of Cu, 0.86. Although the stress calculation of Cr_2Nb was unusual, its magnitude relative to the Cu phase lines up well with the average stress and applied stress and provides evidence that the values are representative of the true behavior. The Cu phase exhibits higher stress and strain hardening than the Cr_2Nb and is carrying the majority of the load. The Cr_2Nb strain hardens up to the macroscopic strain of -0.04 and plateaus. Use of the unloading DECs results in higher estimated stress by ~100 MPa for both Cu and Cr_2Nb that less resembles the macroscopic data.

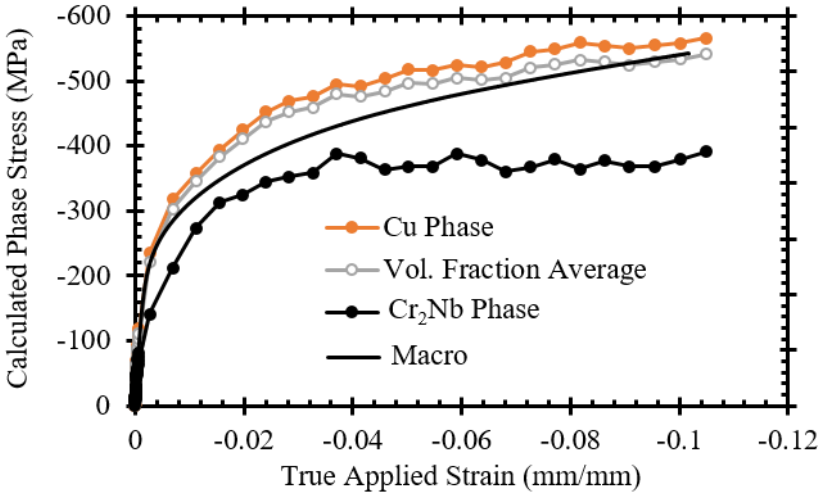

Figure 13.3. Comparison of axial phase-specific stress partitioning of calculated phase macroscopic stress versus applied strain from loading DECs; both axes have been reversed to resemble tensile plots.

In its pure form, Cu is a ductile, low strength metal that is not expected to exceed a maximum stress of ~250 MPa in compression [180]. In GRCop-84, the Cu phase of the HIPed condition was estimated to reach a maximum stress of over double the pure value and demonstrates strain hardening that pure Cu does not. Both Orowan and Hall-Petch strengthening are expected from Cr_2Nb, and considering the amount of stress partitioning from the Cu phase, the Hall-Petch strengthening may be the most effective.

Summary & Conclusions

The deformation behavior of Cu and Cr_2Nb was investigated in as-built and HIPed L-PBF GRCop-84 for compression samples sectioned with the length parallel, Z, and perpendicular, XY, to the build direction. The samples were macroscopically strained between 6 and 10% strain and unloaded to measure the unloading response. In-situ mechanical neutron diffraction data were collected to determine the response of the lattice spacing under macroscopic stress from both the axial and transverse directions. Some errors were present that limited the analysis due to the nature of the samples, but comparisons of the trends are expected to be accurate. In the as-built condition, Cr_2Nb has a low diffraction response and could not be accurately compared, reducing the analysis to the Cu phase. The HIPed condition had sufficient diffraction response, but the sample cut perpendicular to the build direction could not be used due to an experimental error.

The lattice strain was used to compare anisotropy of Cu and Cr_2Nb lattice planes and calculate DECs for the initial loading and unloading regions. If used in future work, the calculated DECs should be considered estimates. The DECs changed significantly with thermal and mechanical history. Cu and Cr_2Nb phase strain, measured from the changes to the calculated lattice parameter, were compared. DECs were calculated from the phase response and used to convert the phase strain to stress. The major findings are summarized as follows.

(1) Typical AM build induced anisotropy from texture was observed in the macroscopic and lattice response. Macroscopically, the Z samples of the as-built and HIPed condition demonstrated 4-7% less stress compared to the corresponding XY samples at comparable strains. Comparing the lattice response of the as-built XY and Z samples, the bulk anisotropy is present as higher lattice strain at a given stress indicating higher overall compliance in the Z sample. The response of the (200) plane of the as-built Z sample was the same as the XY sample until approximately 400 MPa, but the (111) and (222) planes of the Z sample were significantly more compliant at the onset. This indicates more load being carried by the (200) plane in the Z sample which agrees with the higher amount of (100) grains oriented with build direction from texture.

(2) Four stages of deformation were observed in the HIPed samples identified from changes in the slope of the lattice response. The initial loading region, stage I, was identified as elastic deformation of both the Cu and Cr_2Nb phases. In stage II which begins at ~200 MPa, the Cu phase continues elastic deformation while the Cr_2Nb phase begins plastically deforming. Beginning at ~325 MPa, stage III is

represented by plastic deformation of both phases. Beyond ~400 MPa, stage IV is dominated by plastic deformation and strain hardening of the Cu phase while the Cr_2Nb reaches a plateau and does not carry additional strain.

(3) Four similar stages of deformation were observed in the as-built condition, though the stresses to change between stages were different. The major difference between the conditions was present in stage I of the as-built condition which indicated that the Cu phase was immediately plastically deforming from an observed increase in the dislocation density. In stage I, the HIP condition did not indicate an increase to the dislocation density and is a significant difference in deformation behavior.

(4) Although further testing is necessary for confirmation, Cr_2Nb acts as an incompressible phase in GRCop-84 with an unusually high Poisson ratio of ~0.5. Cr_2Nb provides limited direct stress partitioning, and the majority of the stress is supported by the Cu phase.

Acknowledgements

This research used resources at the Spallation Neutron Source, a US Department of Energy Office of Science User Facility operated by Oak Ridge National Laboratory. The authors would like to acknowledge the Manufacturing and Materials Joining Innovation Center (Ma^2JIC), made possible through awards NSF IIP-1540000 (Phase I) and NSF IIP-1822186 (Phase II) from the National Science Foundation Industry University Cooperative Research Center program (IUCRC). RPM also acknowledges the financial support of Oak Ridge National Laboratory's Graduate Opportunities (GO!) Program.

CHAPTER IV
RESIDUAL STRESS MAPPING OF L-PBF GRCOP-84

A version of this chapter is intended for separate publication under the same title at a future date with the current co-authors in a future journal article.

This work is co-authored by Robert Minneci [1], Jeffrey R. Bunn [2], Eric A. Lass [1], Hahn Choo [1], Paul R. Gradl [3], and Claudia J. Rawn [1]

[1]Department of Materials Science and Engineering, University of Tennessee, Knoxville, Tennessee 37996-2100, U.S.A. [2]Neutron Scattering Division, Oak Ridge National Laboratory, Oak Ridge, Tennessee 37831-6475. [3]NASA Marshall Space Flight Center, Huntsville, Al 35808, U.S.A.

The article has no current changes but is expected to have minor changes in its future publication. RPM wrote the initial manuscript draft, and all authors contributed to the final manuscript. CJR contributed to editing, direction, and writing throughout. JRB contributed to preparation of the experiment plan, collection of data, analysis of the results, and editing. EAL and HC contributed editing and analysis of the results.

Abstract

Residual stress mapping was performed on GRCop-84 (Cu-8Cr-4Nb) samples built with laser-powder bed fusion using the (311) plane of the Cu phase. Samples consisted of simple cube and pillar geometries that were in the as-built and HIPed conditions and were removed from the build substrate to assess the thermal residual strains induced during laser-powder bed fusion (L-PBF) and following removal from the build substrate and after a HIP cycle. Three orthogonal strain directions were measured and stress was calculated using constants derived from literature and prior in-situ time-of-flight diffraction efforts. The strain distribution within the as-built samples resembled typical L-PBF strains with the highest strains present parallel to the build direction and with strong tensile strains at the edges of the samples and a balancing compressive strain at the center. Remnants of stress relief from removal from the build substrate was observed at the bottom of the samples, indicating the prior presence of a strong tensile strain. Calculated maximum stress values of both tensile and compressive strains exceeded the expected yield strength of the material by over a factor of two. Stress relief from HIP cycle resulted in low strains of ±100 μstrain

Introduction

Additive manufacturing (AM) is a layer-by-layer fabrication technique that builds three dimensional shapes from two dimensional layers with a variety of materials in various feedstock forms. Metal additive manufacturing has been embraced by a variety of industries for its unique flexible processing capability, and metal AM parts are starting to be used in practical applications. NASA has independently and collaboratively developed Cu alloys for AM including GRCop-84 (Cu-8Cr-4Nb), GRCop-42 (Cu-4Cr-2Nb), C-18150 (Cu-Cr-Zr), and C-18200 (Cu-Cr) with industry partners [12, 30, 107]. These alloys are intended for high-heat-flux applications including combustion chamber liners and nuclear reactor components that require high thermal conductivity and resistance to

thermal fatigue and creep [2, 4, 27, 122, 126]. AM is ideal for these types of applications since they have relatively low production volumes, high starting material cost, a need for optimal performance, and high geometric complexity [2, 30, 129]. These benefits are all exploited by the geometry control that AM allows with its layer-by-layer building method. Of the Cu alloys, GRCop-84 has undergone the most development and is the focus of this study [30].

Laser-Powder Bed Fusion

AM through laser-powder bed fusion (L-PBF) is a promising consolidation technique due to its high degree of geometry control. L-PBF technically refers to both laser melting and laser sintering processes, but the commonly used terms are registered trademarks [129]. Throughout this paper, L-PBF will used instead the more commonly used selective laser melting and will only refer to melting processes. In L-PBF, a thin layer of powder is spread onto a build plate with a blade or roller, and a laser melts the powder according to an input computer-aided design (CAD), forming the first layer. The powder bed is lowered according to the build height, and more powder is spread over the previous layer. The next layer is melted, and the process repeats until the desired shape is formed.

L-PBF uses relatively thin layers, small spot sizes, and higher laser powder than other methods [130]. This provides a high energy density that puts the powder through a full melting and solidification cycle and partially re-melts the previously solidified layers resulting in complex thermal history and cycling [177]. During a build, complex thermal stresses develop from thermal expansion mismatch between layers and adjacent laser paths. These can cause premature failure during AM builds by delamination, crack formation, or geometric distortion [131]. Furthermore, typical residual stresses induced during laser AM and similar welding techniques are well known to reduce the fatigue lifetime of components [181, 182]. It is standard practice to relieve the residual stresses in laser AM parts through annealing, but the parts must survive the build and the annealing phase must sufficiently reduce the undesirable residual stresses to optimize performance. Various methods have been utilized to predict residual stresses in AM like finite element modeling but require validation [182, 183]. When combining L-PBF and Cu alloys, the residual stress is expected to be difficult to predict due to Cu's high thermal conductivity and L-PBF's high energy density. Furthermore, the amount and locations of residual stresses in L-PBF GRCop-84 are unknown, and an improved understanding can help alleviate, predict, and monitor their evolution during builds. Lower failure rates during building and parts with improved properties should result from this improvement.

Types of Residual Stress

Residual stress is a mechanical stress which exists within a component without the application of any additional external forces. Residual stresses can arise due to mechanical stress, thermal gradients, or lattice misfit. Residual stresses are typically categorized by the length scale over which the stresses vary as type I, type II, and type III stress [160, 177]. Without an external stress, the stress state of a given component must be in equilibrium, and self-equilibration means that the sum of the total stresses over the length

scale is zero. Type I residual stress is commonly referred to as macrostress and varies over a length scale comparable to the dimension of the component (typically over mm) and are caused by macroscopic plastic deformation and thermal gradients [160]. Type II residual stresses, referred to as intergranular stresses, vary over a length-scale comparable to the grain size and arise from misfits between grains. An example of type II stresses is differential thermal contraction between adjacent grains [160]. Type III residual stresses, referred to as intragranular stresses, pertains to misfit within grains and form due to crystal defects such as atomic vacancies and interstitials. Both type II and III stresses combined are referred to as microstresses. The macroscopic type I residual stresses are usually the primary concern because they tend to be significantly higher in quantity than the microstresses. Furthermore, type II and III residual stresses are difficult to measure and separate from the type I stresses due to their size. If not specified, any further mention of residual stress will refer to type I residual stress. Residual stresses can be advantageous or disadvantageous to various applications, but those generated during welding or AM typically need to be mitigated and understood to improve performance.

Thermal Residual Stress in L-PBF

Mercelis and Kruth [184] describe two mechanisms of thermal residual stress in L-PBF including the temperature gradient mechanism (TGM) and cool-down phase mechanism. TGM accounts for residual stresses generated between hot and cool layers and is commonly used to account for laser bending of sheets along straight lines [184]. When the laser heats the upper surface, a high temperature gradient rapidly develops between the underlying material while heat conduction catches up [184]. The strength of the top layer simultaneously decreases from the high temperature and expands, causing a counter bending force that induces compressive strains between the restricting underlying material [184]. Residual stresses will generate between the layers if the strains exceed elastic levels. Without the instantaneous temperature gradient, the TGM mechanism would not occur. The cool-down phase mechanism is simpler and accounts for plastic strains retained during cooling.

In L-PBF, the heated zone expands by thermal expansion but is restrained by previous layers and surrounding material. As the heated zone cools, plastic strain develops at the edges of the heated zone that translates into a compressive stress that is partially balanced by tensile stress at the center of the heated zone and surrounding regions. If the thermal expansion of the heated zone into the cool regions, also known as transient stresses, exceeds elastic limits, permanent misfits or residual stresses will remain [160]. No thermal residual stresses will be generated unless the spatial gradient in temperature is sufficient to exceed the elastic limits, but in laser AM, localized, rapid heating and cooling commonly produces high thermal residual strains.

Measuring Residual Stress

Residual stress can be measured either destructively or nondestructively with a variety of methods but all of them measure some form of displacement to calculate strain and derive stress. Destructive methods measure the material's displacement in response to stress relief from removing material [185]. Non-destructive methods measure a

parameter that relates to stress and includes crystal lattice response, magnetic properties, conductivity through eddy currents, speed of sound, Raman excitations, and optical fluorescence [186-188]. Of the non-destructive methods, neutron diffraction is one of the most powerful due to the highly penetrating nature of neutrons. Neutrons and X-rays can both be used to evaluate residual stress through analysis of the diffraction maxima and Bragg's Law [189]. Diffraction peak shifts relate to changes in atomic spacing in relation to tensile or compressive stress, changes to peak intensity may indicate preferred orientation or phase fraction, and peak width can relate to crystallite size, dislocation density, microstresses and concentration gradients in non-stoichiometric compounds [190]. Typical laboratory X-rays diffract from atoms' electrons which restricts their penetration depth to the order of microns, depending on the material and are typically ideal for surface measurements. Neutrons scatter from the significantly smaller nucleus of atoms and can penetrate materials on the order of centimeters, depending on the material. The major disadvantage of neutrons is that they require a reactor or spallation source and beamtime is highly competitive and often only obtained in limited quantities. The penetrating power of X-rays can be increased to the order of millimeters through the use of a high energy synchrotron, but this has a similar quantity problem [190, 191]. Although diffraction measures an atomic-scale parameter, stress measurements are almost always of type I macrostresses due to the nature of the measurement; though microstresses can be inferred through peak width changes [160]. Diffraction measurements are volumetric and dependent on possible events. The incident beam of X-rays or neutrons can be separated into three potential outcomes (1) diffraction occurs and is collected by a detector, (2) no diffraction occurs, or (3) diffraction occurs but is either absorbed by the sample or is not detected. Individual events are impossible to predict and occur at a high volume. With sufficient counting time, the measurements are highly accurate to the diffracted volume. However, stress calculations require knowledge of the material and should always be treated as an estimate.

Although neutron diffraction is a powerful technique, it is not a viable option for the inspection large quantities of individual parts due to limited access but rather a way to interrogate stresses that result from processing parameters in order to provide guidance for future processing decisions. The work by Wang et al. [192] is an excellent example for a use case scenario of neutron diffraction. They developed thermomechanical models to predict the residual stress in AM Inconel 625 and used residual stress mapping to validate the model [192]. Various neutron diffraction studies have been performed on Inconel 625 prior to their work which likely contributed to their success. The available neutron characterization of AM GRCop-84 is currently limited in literature and needs further development for similar applications.

Microstructure of L-PBF GRCop-84

GRCop-84 contains ~88 wt% Cu, ~8 wt% Cr, and ~4 wt% Nb. Cr and Nb have low solid solubility with Cu and preferentially form C15 Laves Cr_2Nb [9, 120]. The Cr_2Nb provides strengthening to Cu matrix with precipitation and dispersion strengthening characteristics [126]. This phase is thermally stable, resistant to coarsening, and helps refine the Cu grain size. GRCop-84 is typically first alloyed by gas-atomization and can

then be consolidated by a variety of powder processing methods, including L-PBF [2]. NASA Marshall Space Flight Center (MSFC) has developed L-PBF build parameters on a Concept Laser M2 system that can achieve >99.2% density, and typically hot isostatically presses (HIP) components to reduce potential porosity and improve homogeneity [30, 108].

The microstructure and phases of as-built and HIPed GRCop-84 have been characterized in a previous study [166],. The microstructure is strongly influenced by the laser velocity and the laser scan pattern is partially visible under back scattered electron images. Columnar grains are observed at the edges of the laser melt pool following the solidification front while equiaxed grains are observed at the centerline of the laser path. Equiaxed grains were unexpected since FCC Cu tends to favor epitaxial growth in the (100) direction, but the high volume, ~14 vol%, of Cr_2Nb provides sufficient nucleation sites to initiate heterogeneous nucleation for the current build parameters [193, 194]. In the direction parallel to the build direction, the Cu matrix grains have preferred (100) texture while the texture of the direction perpendicular to the build direction is relatively even. The Cr_2Nb phase is present as a largely bimodal distribution that is relatively uniform throughout the alloy and can be found within grains and at the grain boundaries. In the as-built condition, the X-ray and time-of-flight neutron (TOF) diffraction calculated phase fraction of Cr_2Nb is <1 wt%. This is theorized to be the result of slight off-stoichiometry, residual stress, and crystallite size, but the alloying fraction of 12 wt% can be regained by either annealing or HIPing the alloy. The microstructural stability of GRCop-84 is demonstrated after the HIP by limited coarsening of the microstructure, but recrystallization occurs and less (100) texture is observed in the build direction.

In this study, the influence of L-PBF and HIP on the macro residual stress was evaluated in GRCop-84 through residual stress mapping. Experimental residual strain measurements were made with neutron diffraction and residual stress estimates were made using constants obtained from previous neutron studies and are discussed later.

Materials and Methods

Sample Geometry and Conditions

GRCop-84 samples were produced by L-PBF on a Concept Laser M2 system according to NASA's build parameters at MSFC and were built in the same sample lot as previous studies and share the same chemistry [166, 195]. The as-built samples were removed from their build plates with wire electron discharge machining (EDM), and duplicate samples were HIPed according to NASA's procedures. Little was known regarding the residual stress state prior to measurement, so the sample geometries were intentionally simple. Figure 1.4. shows the primary sample geometries. Samples were prepared in 4, 7, and 10 mm cubes and a larger 10 x 10 x 40 mm geometry referred to as a pillar. Thin 4 x 4 x 10 mm matchsticks were wire EDMed from larger samples to serve as reference samples but are not presented. Sectioning with EDM is expected to relieve the majority of the residual stresses, and the sample can serve as a reference for the stress-relieved state [196]. Each of the samples was assumed to have the same microstructure and chemistry, though some variation is expected, especially between the

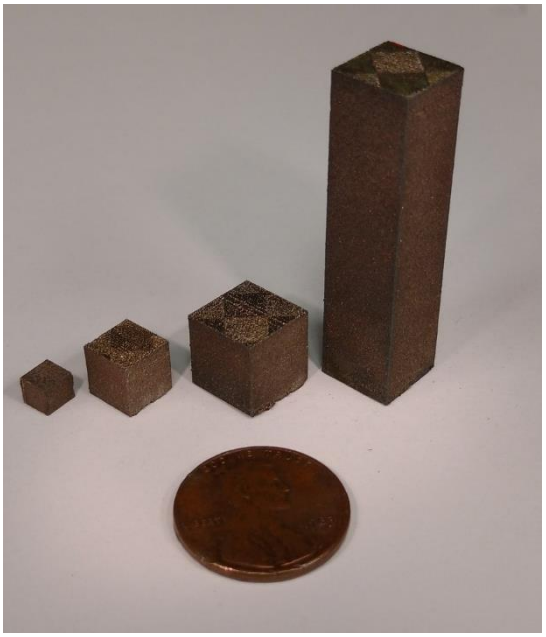

Figure 1.4. Photo of as-built L-PBF samples used in the experiment including a 4, 7, and 10 mm cube (from left to right) and 10 x 10 x 40 mm pillar with 1 cent coin for scale.

as-built and HIPed samples. The cubes were chosen to investigate a volumetric dependence on stress, and the pillar was chosen to investigate a dependence on the distance from the build plate.

Measurement of Lattice Behavior with HB-2B

Neutron diffraction was conducted on the High Flux Isotope Reactor's (HFIR) second generation neutron residual stress mapping facility (NRSF-2) diffractometer (HB-2B) [197]. This beamline has been upgraded since this experiment, and the capabilities of the instrument at the time of the experiment and discussion of the upgrades are described by Cornwell et al. [198]. This instrument was chosen for its high neutron flux and mapping capability. Figure 2.4. shows a diagram of the primary components of the instrument including a monochromator to select the wavelength of the radiation, incident slits to control the geometry of the incident neutron beam, goniometer to move the sample, and detector bank to collect the diffracted neutron beam. The incident slits can be changed depending on the experiment with dimensions ranging from 0.3 to 20 mm, the motorized goniometer is capable of precise vertical, horizontal, and rotational positions, and the detector bank consists of seven vertically stacked linear position-position sensitive detectors with a field of view of ~4° 2θ [198].

During a measurement, the incident beam diffracts from the sample according to Bragg's Law

$$\lambda = 2d\sin(\theta) \quad (1.4.)$$

which relates the angle, θ, to the wavelength of the radiation, λ, and interatomic spacing, d. The measured diffraction volume, commonly referred to as the gauge volume or voxel, is dependent upon the geometry of the incident slits and angle of the detector. The best mapping results are obtained near an angle of 2θ = 90°, demonstrated in Fig. 2.4., which produces a rectilinear gauge volume and prevents measuring a different volume upon rotation of the sample. The wavelength can be chosen from six discrete wavelengths varying between 1.45 to 2.67 Å by manipulating the monochromator allowing for the user to select a wavelength that will diffract a peak near 2θ = 90°[198]. In stress mapping, a single data point is an average of the response over the gauge volume illuminated within the sample and all of its corresponding grains. The volume is chosen depending on diffraction efficiency, size of the sample, grain size, and number of desired data points. Larger volumes require less data collection time and it is important that the gauge volume has a statically significant number of grains within the volume. Often the data collection time can be the largest factor since neutron time is limited. The goal is to produce just enough diffraction events for sufficient statistics so that additional data points can be collected. Furthermore, it is critical that the gauge volume is fully buried within the sample. Partially burying the sampled volume will produce anomalous shifts in the diffraction peaks that are difficult to account for [199, 200].

Each sample was precisely aligned on the instrument beginning with a theodolite to obtain a starting position to a precision of ±250 μm. The neutron beam was then incrementally translated across the sample by moving the sample with the goniometer to

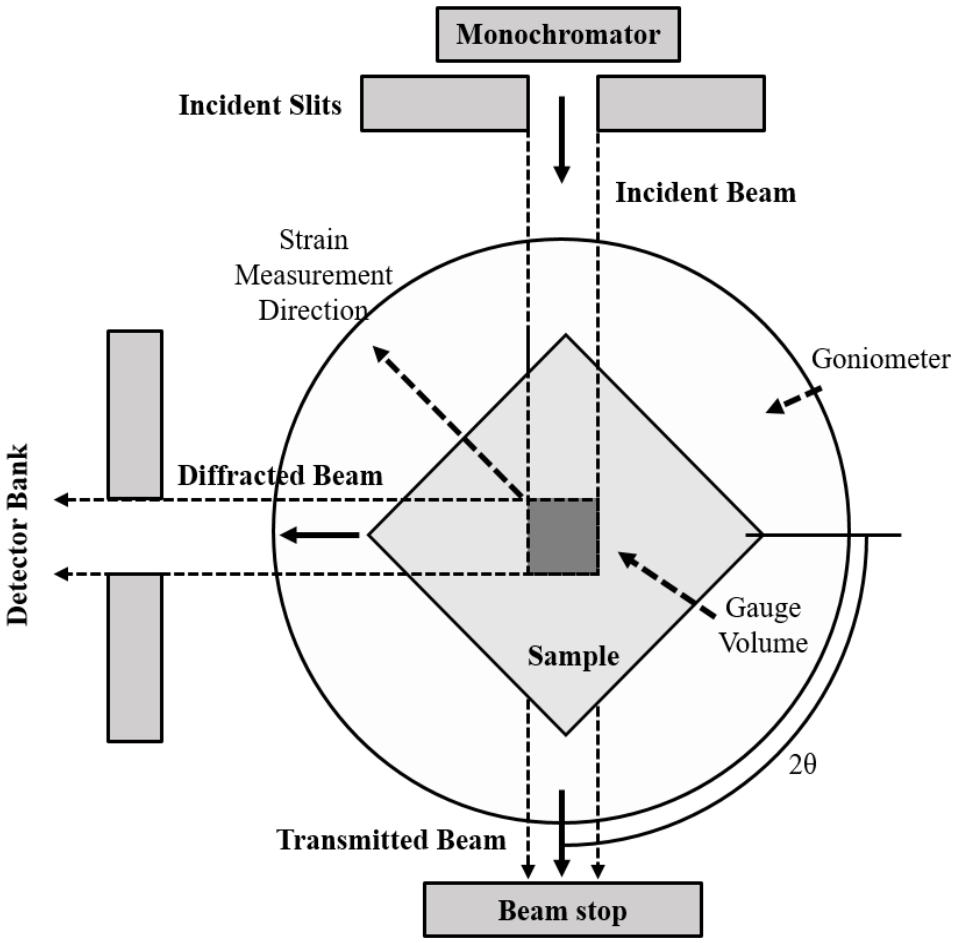

Figure 2.4. Diagram of the HB-2B diffractometer at Oak Ridge National Laboratory's High Flux Isotope reactor demonstrating the neutron beam path and geometry of the diffracted volume.

determine the sample edges with a high degree of precision. Care was taken during sample alignment to ensure accurate positions and mapping results. A 2 x 2 x 2 mm gauge volume was chosen that produced sufficient counts after 300 s in a single direction. The Si 422 monochromator setting was used to produce a ~1.54 Å constant wavelength of neutrons, the precise wavelength used in the analysis is calculated using a standard upon monochromator alignment and calibration. This put the Cu (311) plane at approximately 90° 2θ. The (311) plane is ideal for providing an average response of the bulk Cu phase and is not strongly affected by intergranular strains [160]. Since the as-built condition is known to have a limited diffraction quantity of Cr_2Nb, only the Cu phase was investigated at HB-2B. Based on prior TOF neutron work [195] with HIPed samples that had sufficient Cr_2Nb diffraction maxima for analysis, the Cr_2Nb phase is expected to contribute significantly to the overall stress state of GRCop-84, but its impact in the as-built condition is unknown.

Residual strain of the Cu (311) plane, ε_{hkl} where *hkl* represents the crystallographic plane, is calculated using what is referred to as the strain-free lattice spacing, d_{hkl}^0. This serves as the zero condition, similar to the starting length of a deformation experiment, for determining strain with experimental d_{hkl} values with

$$\varepsilon_{hkl} = \frac{d_{hkl} - d_{hkl}^0}{d_{hkl}^0} \quad (2.4.).$$

The d_{hkl}^0 value is usually dependent on the material and chemistry and can be determined with a stress-free sample or force balance calculation. With the residual strain, the residual stress can be calculated using Hooke's law but requires measuring strain in three orthogonal directions ε_{11}, ε_{22}, and ε_{33}, which are assumed to be principal strains and that correlate to stresses σ_{11}, σ_{22}, and σ_{33}. These follow a generalized form of Hooke's law for each stress by

$$\sigma_{ij}^I = \frac{E_{hkl}}{1 + v_{hkl}}\left(\varepsilon_{ij} + \frac{v_{hkl}}{1 - 2v_{hkl}}\left(\varepsilon_{11}^{hkl} + \varepsilon_{22}^{hkl} + \varepsilon_{33}^{hkl}\right)\right) \quad (3.4.)$$

where ij represents the orthogonal, assumed principal, directions 11, 22, and 33, σ_{ij}^I represents the estimate of macrostress, and E_{hkl} and v_{hkl} are diffraction elastic constants (DEC) of Young's modulus and Poisson ratio. The DECs of the as-built condition were determined in a previous (TOF) neutron study and are reported in Table 3.3. [195]. The accuracy of these values determines the magnitude of the stress calculation and are expected to have a confidence of roughly 10%. In practice, the strains were measured in three orthogonal directions, referred to as X, Y, and Z throughout. X and Y are arbitrary assigned and both perpendicular to the build direction while the Z direction is parallel to the build direction. The sample is physically rotated and the measurements are repeated a total of three times.

With the 2 mm gauge volume, the 300 s data collection time becomes 900 s for each individual data point, considering each direction. The distance between collected

data points was intentionally chose to keep the gauge volume a minimum of 0.5 mm from the sample edges. Twenty-seven data points were collected for the cube samples in a 3 x 3 x 3 array spaced; although, the 2 mm gauge volume resulted in significant overlap between the collected data of the 4 and 7 mm cube samples. The 7 mm cube was measured with a spacing of 2 mm, and the 10 mm cube was measured with a spacing of 3.5 mm. The as-built pillar sample was mapped with a data array using a 3 x 5 x 22 (X x Y x Z) grid producing a rectangular prism map. In this grid, the X data points were spaced 3.5 mm, the Y data points were spaced 1 mm, and the Z data points were spaced 1.7 mm. A similar grid was originally planned for a HIP pillar, but only a 3 x 1 x 22 grid was measured in the Z direction due to apparent homogeneity of the data (as low residual strains) and reallocation of resources. In analysis, the primary focus will be on the Z or build direction. In typical AM builds, the residual stress between layers is the main detriment to builds from generation of build defects [131].

The as-built $d_{311}^0 = 1.091517$ Å was calculated using a force balance on the data collected on the as-built 4mm cube sample. This d_{hkl}^0 was similar to a measurement of the wire EDMed matchstick sample which had an average d_{311}^0 of 1.0917(5) from four separate measurements of the strain parallel to the build direction (Z). The matchstick was expected to be a in a relatively strain-free condition but may have retained some internal strain. The d_{311}^0 of the HIPed condition reduced to $d_{311}^0 = 1.090(5)$ Å, but there is less certainty in this value. It should be noted that the accuracy of this value will mainly change the zero position and the relative magnitude will remain largely unaffected. High certainty in the d_{hkl}^0 value can be achieved through further testing but may be unnecessary.

Results and Discussion

Strain Mapping of As-built GRCop-84

Three dimensional contour maps of the residual strain the 4, 7, and 10 mm cubes are presented in Fig. 3.4., 4.4., and 5.4., respectively. The two dimensional contour maps used to generate the three dimensional maps are shown in Fig. 6.4., 7.4., and 8.4. for the 4, 7, and 10 mm cubes, respectively. The limits of the axes on the figures represents the sample geometry while the black dots represent the data points. These figures represent the general magnitude and location of residual strain within the samples for strain in the X, Y, and Z (or build) directions. When viewing this figures, it is important to recall that each data point is an average of the strain within a voxel and that the samples have been removed from their build substrate by EDM. The strain distribution of the samples from L-PBF should be significantly impacted due to stress relief. The stress and strain distribution will not resemble the exact state of as-built L-PBF samples and will instead be indicative of samples removed from the build substrate prior to additional heat treatments. Laser AM builds typically have compressive strains at the center of the build volume that is balanced by tensile strains at the edges [177]. Based on similar AM residual stress analysis by Mercelis [184] and Wu [201], we expect that a strong tensile strain was present at the boundary of the build substrate. These samples are relatively small, so the stress relief was likely to effect the entire sample. This should primarily affect the strain

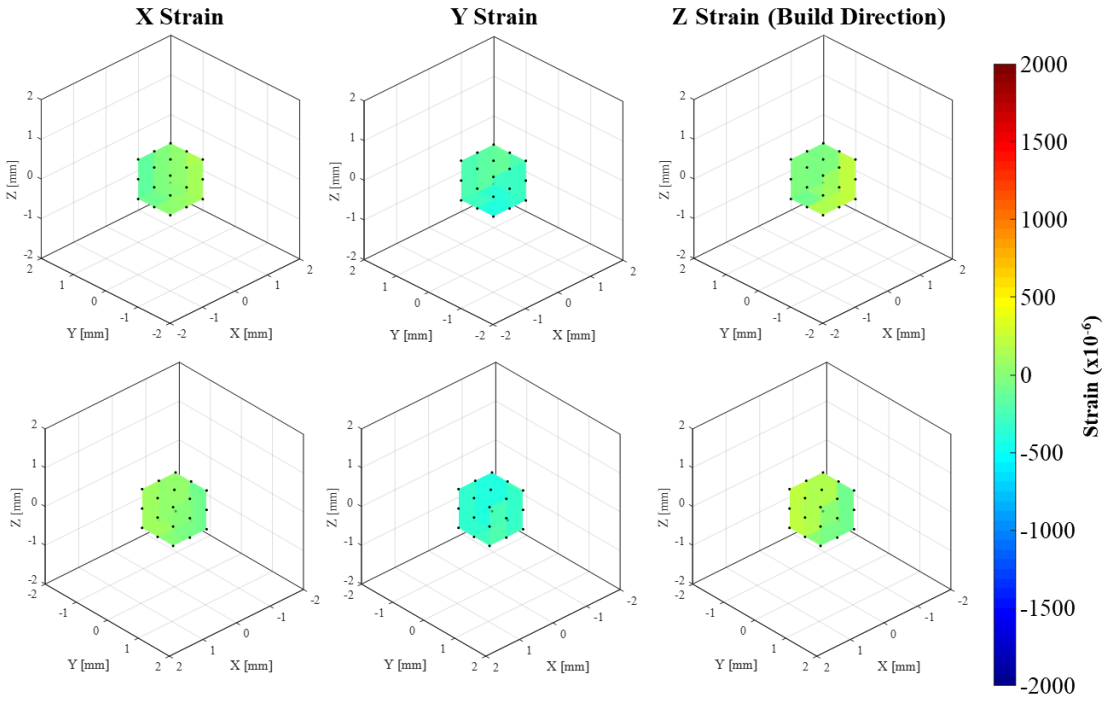

Figure 3.4. Three dimensional contour maps of strain for the as-built 4 mm cube sample with two opposite views of the measured volume and colorbar; the limits of the axes represent the sample edges, and the dots represent the center of the measured 2 mm gauge volume.

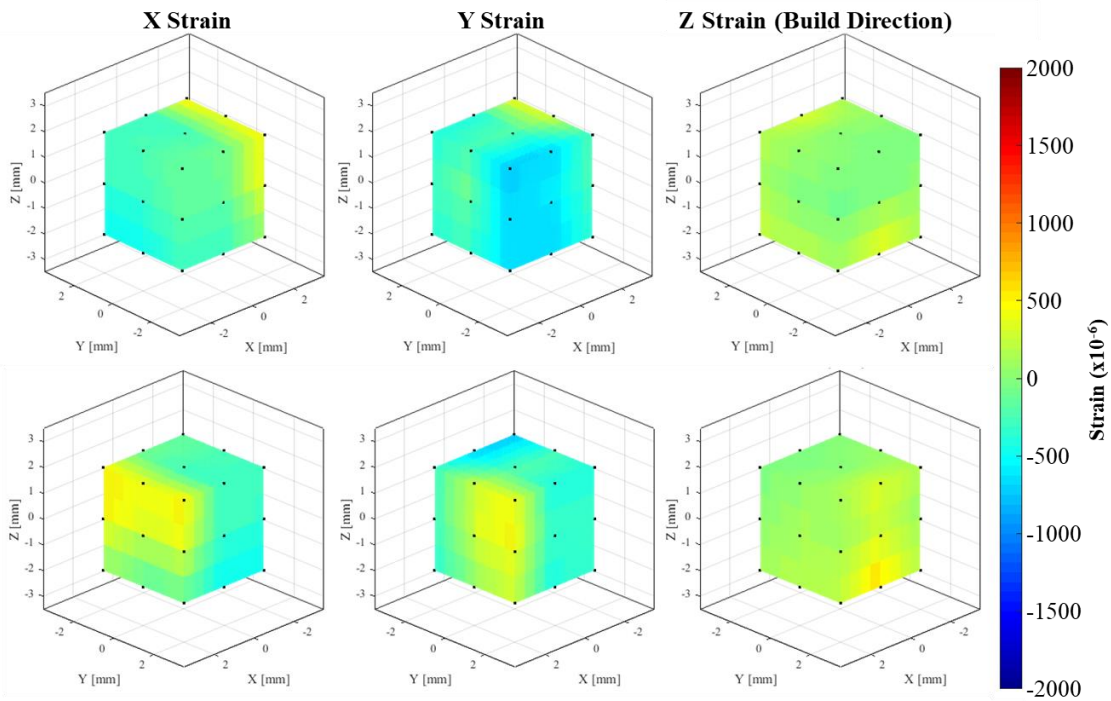

Figure 4.4. Three dimensional contour maps of strain for the as-built 7 mm cube sample with two opposite views of the measured volume and colorbar; the limits of the axes represent the sample edges, and the dots represent the center of the measured 2 mm gauge volume.

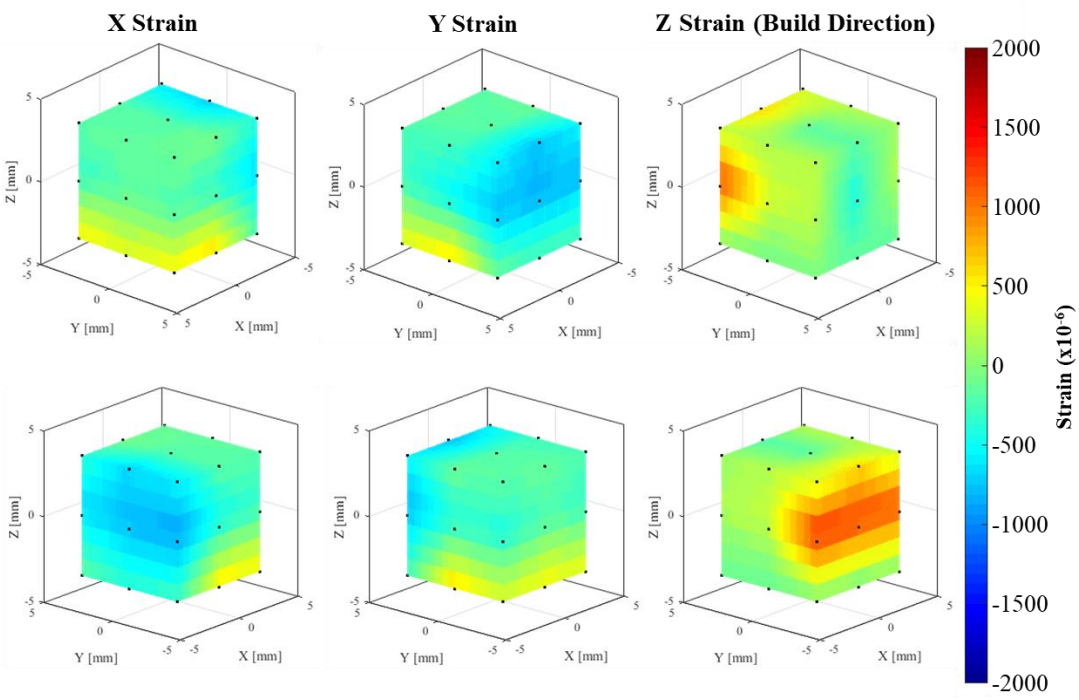

Figure 5.4. Three dimensional contour maps of strain for the as-built 10 mm cube sample with two opposite views of the measured volume and colorbar; the limits of the axes represent the sample edges, and the dots represent the center of the measured 2 mm gauge volume.

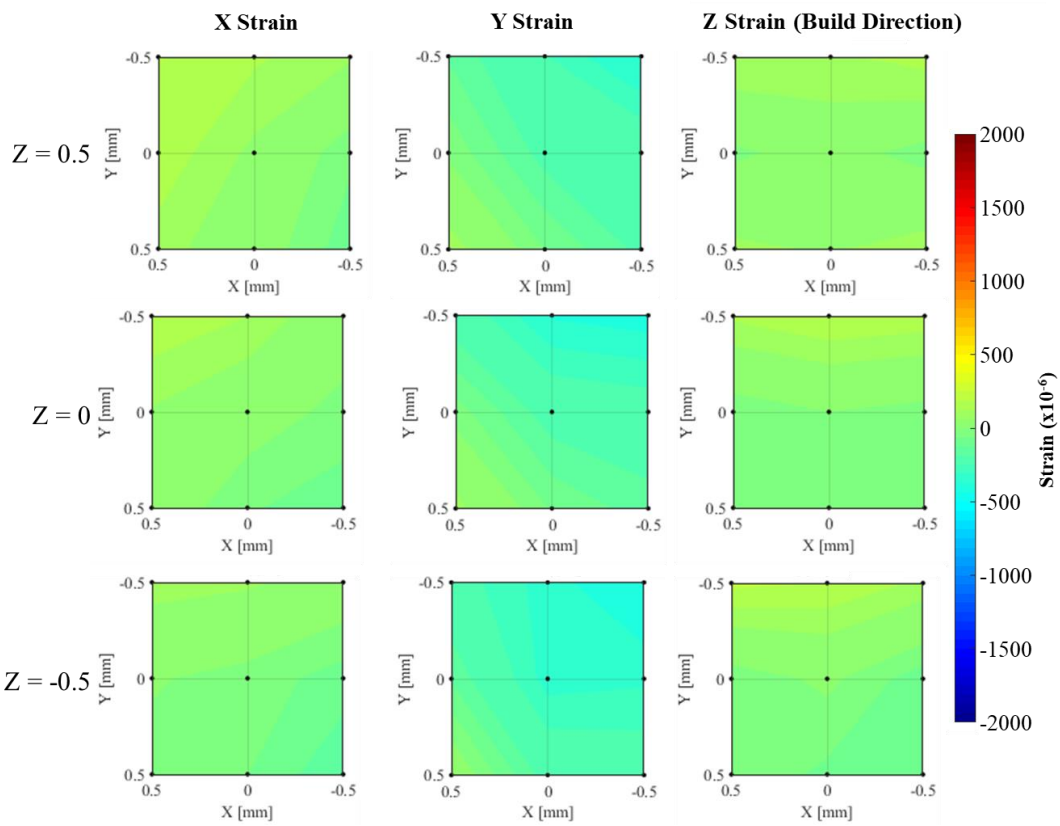

Figure 6.4. Two-dimensional contour maps of the as-built 4 mm cube sample with colorbar and labeled Z height from the center of the sample used to generate the three-dimensional contour map of Fig. 3.4.

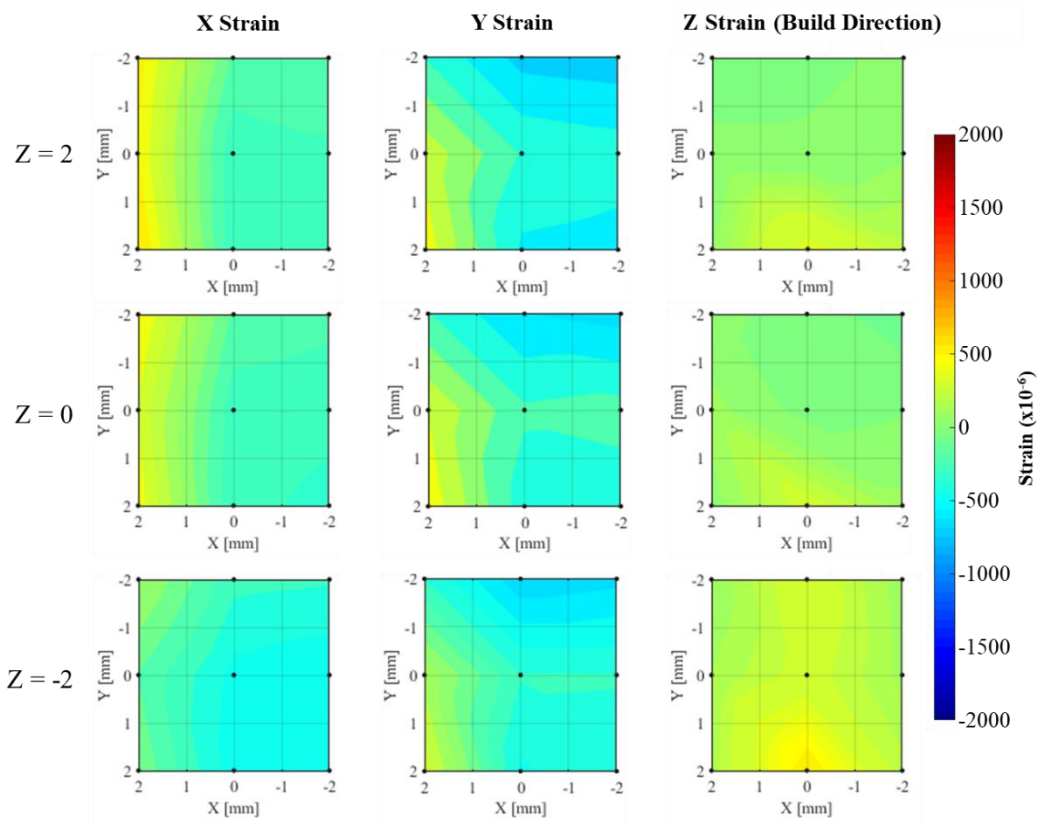

Figure 7.4. Two-dimensional contour maps of the as-built 7 mm cube sample with colorbar and labeled Z height from the center of the sample used to generate the three-dimensional contour map of Fig. 4.4.

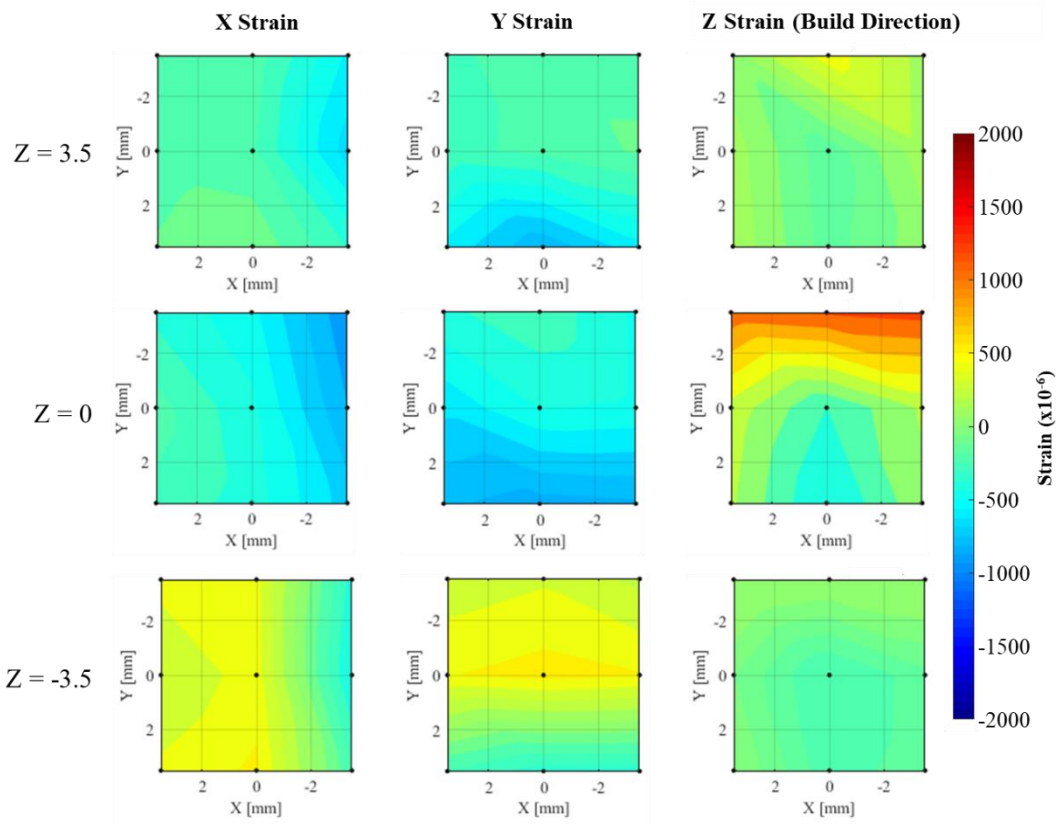

Figure 8.4. Two-dimensional contour maps of the as-built 10 mm cube sample with colorbar and labeled Z height from the center of the sample used to generate the three-dimensional contour map of Fig. 8.4.

parallel to the build direction since the samples were sectioned perpendicular to the build direction near the boundary. The tensile stress at bottom edge of the build volume should be largely relieved along with a correlating amount of compressive strain to reach equilibrium.

The 4 mm cube, Fig. 3.4. and 6.4., has low strains throughout the sample volume, but the gauge volume may be too large to accurately assess the strain distribution. The 2 mm gauge volume is $1/8^{th}$ the volume of the sample and localized strain may be present. Furthermore, the sample was likely too small to retain stress after relief during sectioning. The 7 mm cube, Fig. 4.4. and 7.4., should provide a better representation of present strain. The overall strain distribution is roughly double the 4 mm cube sample, and a small tensile strain in the Z direction is present near the bottom of the sample that may be a remnant of the tensile stress that was relieved during sectioning. Of the cube samples, the 10 mm cube, Fig. 5.4. and 8.4., has the highest degree of strain, and a high tensile stress was present on one of the sides of the sample, indicating that stress relief had not affected the entire volume.

Three dimensional contour maps of the residual strain of the pillar sample are shown in Fig. 9.4., and the corresponding two dimensional contour maps are shown in Fig. 10.4. The overall strain distribution is similar to prior literature results [177] with a strong compressive strain at the center of the sample in the Z direction balanced by tensile strains at the edges, and each reached a maximum of approximately 2000 μm. Compared to the top of the measured volume, the strain distribution at the bottom of the pillar is less uniform and a slight tensile strain is present in the X and Y directions. This is likely a result of stress relief when the sample was removed from the build substrate. In Fig. 10.4., the tensile strain at the edges of the Z direction significantly reduces between the slices at Z = -17 and -18.7 from the center of the sample. This should represent the range of stress relief and correlates with the stress relief observed in the cube samples. Above this height, the stress remains relatively uniform until reaching Z = 13.6 where it begins to become more tensile and should increase in magnitude closer to the top surface.

The strain mapping data of the pillar sample is plotted in Fig. 11.4. as a function of distance from the center of the sample. Fig. 11.4. compares the layers of the two-dimensional contour maps and difference between the stress parallel (Z) and perpendicular (X and Y) to the build direction. The maximum tensile and compressive strains of the Z direction are higher than the X and Y strains by over a factor of two. The majority of the residual stress in the pillar is vertical in nature and is typical of L-PBF builds.

In each of the cube samples, the strain distribution in the build direction appears to be primarily tensile, represented by positive strain. This perceived bias could either be due to an averaging effect from the relatively large gauge volume, from stress relief from removal from the build plate, or balanced by the unmeasured Cr_2Nb phase. Prior work with [195] in-situ neutron diffraction of HIPed GRCop-84, which had sufficient Cr_2Nb diffraction maxima, has demonstrated significant strain partitioning between the phases and is expected in the as-built condition. In contrast, the pillar sample demonstrates similar maximum tensile and compressive strains. For a better comparison, the maximum tensile and compressive strains are plotted in Fig. 12.4. for the cube samples and pillar

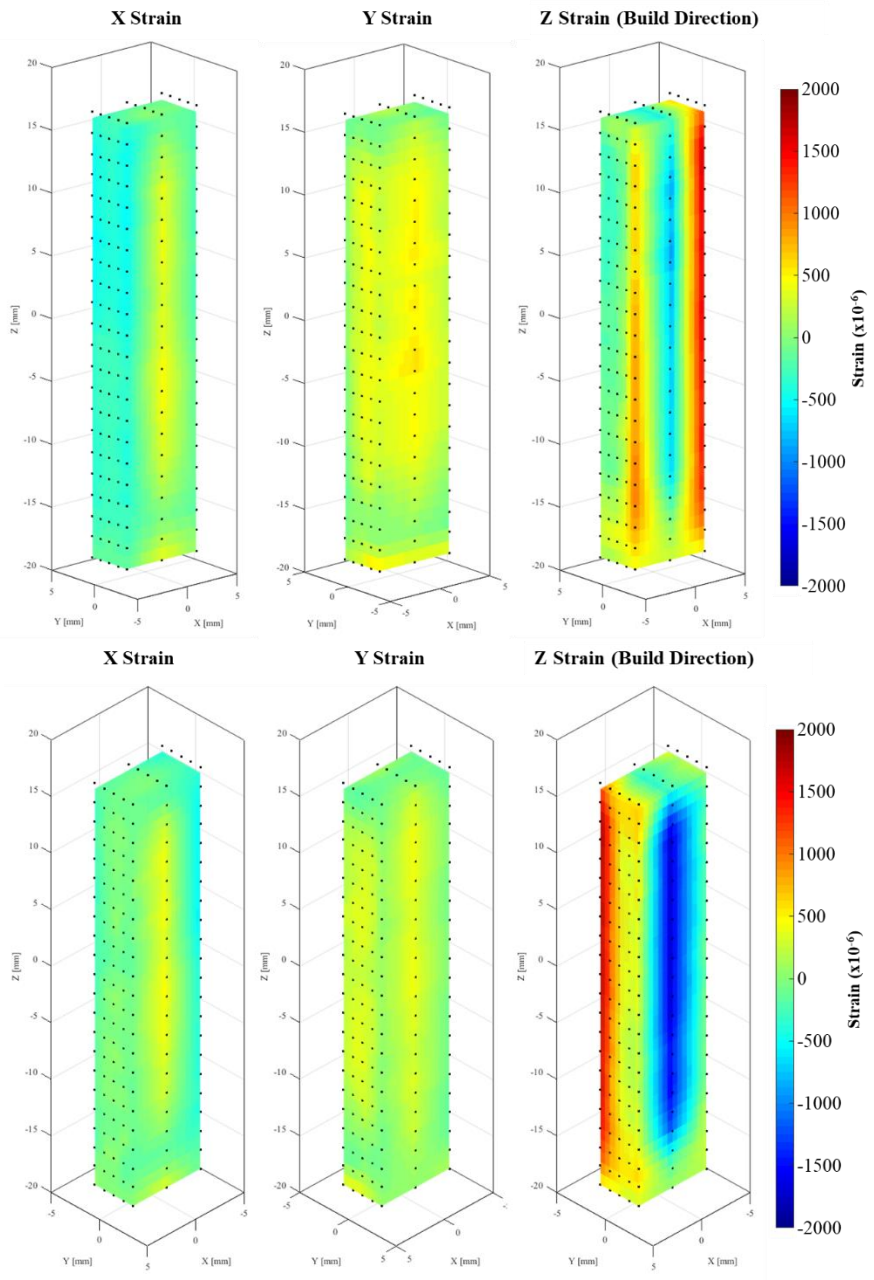

Figure 9.4. Three dimensional contour maps of strain for the as-built 10 x 10 x 40 mm pillar sample with two opposite views of the measured volume and colorbar; the limits of the axes represent the sample edges, and the dots represent the center of the measured 2 mm gauge volume.

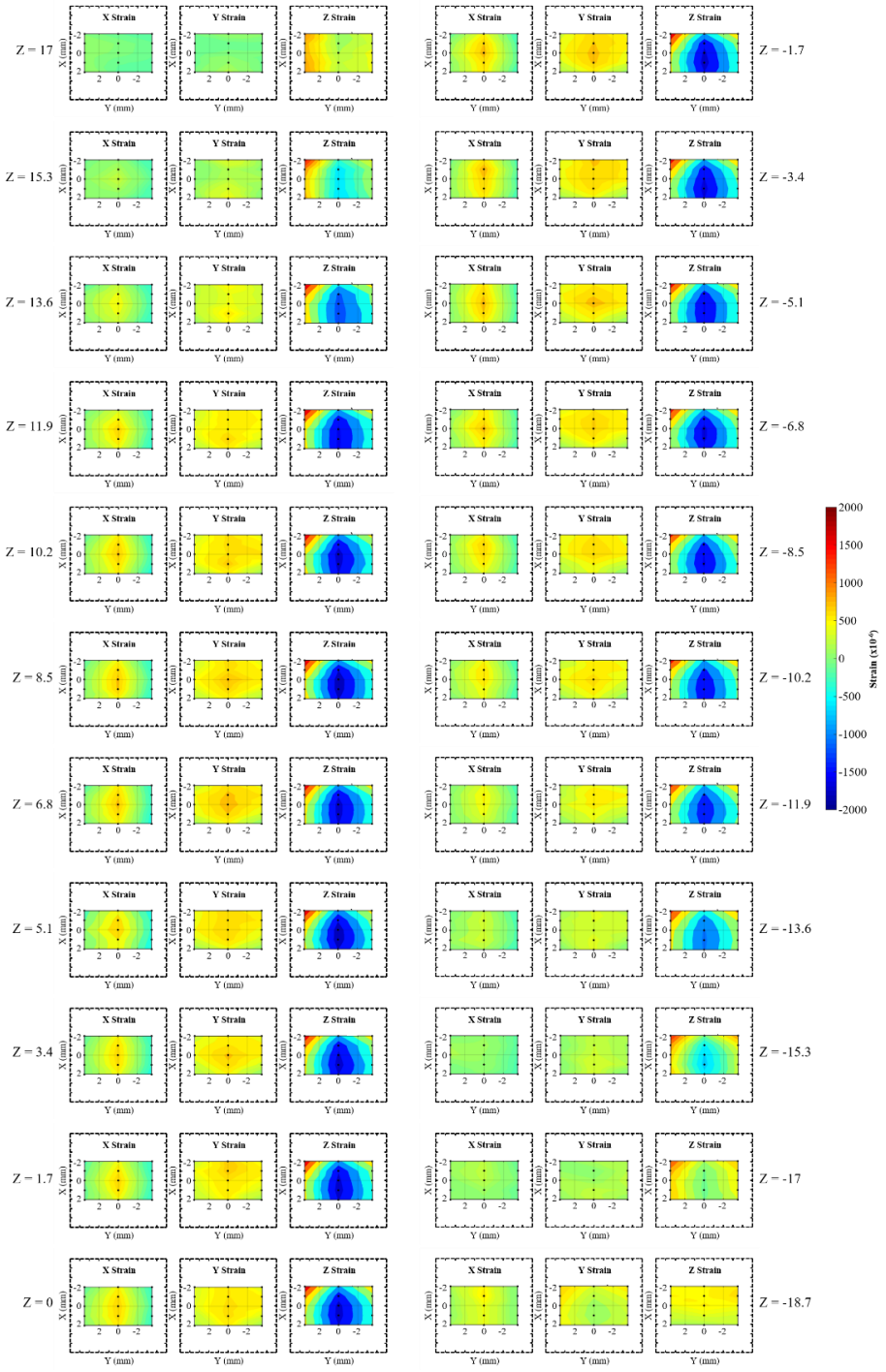

Figure 10.4. Two-dimensional contour maps of the as-built 10 mm cube sample with colorbar and labeled Z height from the center of the sample used to generate the three-dimensional contour map of Fig. 9.4.

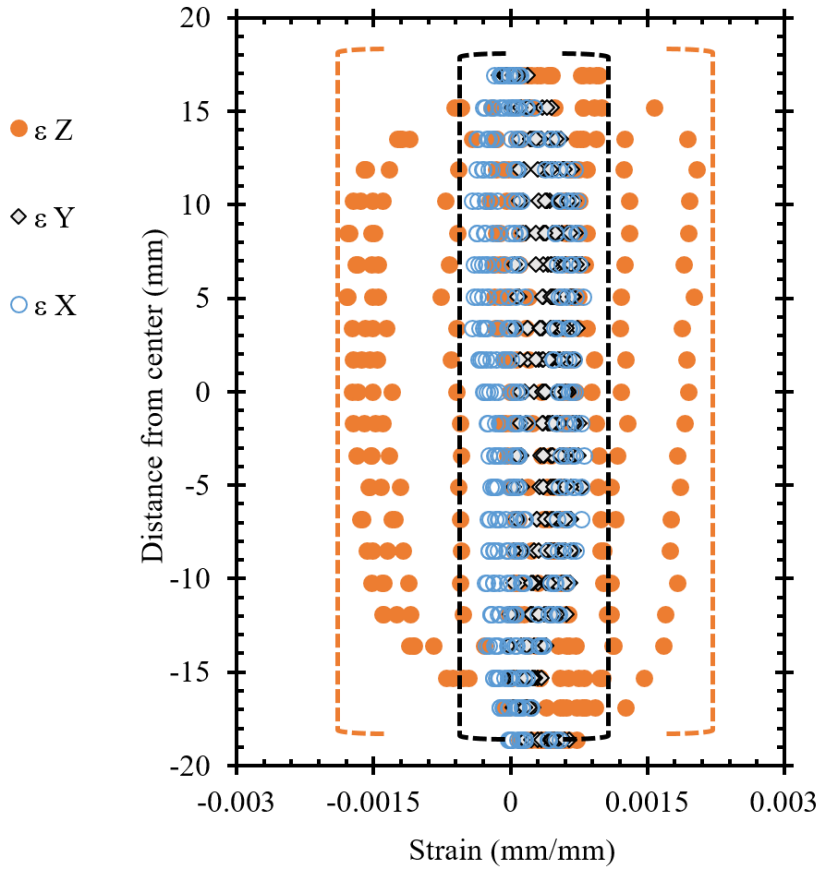

Figure 11.4. Strain distribution of the as-built 10 x 10 x 40 mm pillar sample with respect to the layer height for each orthogonal direction, shown as distance from the center of the sample; the Y axis represents the bounds of the sample and brackets are added to show the difference in distribution of the X and Y strains compared to the Z strain.

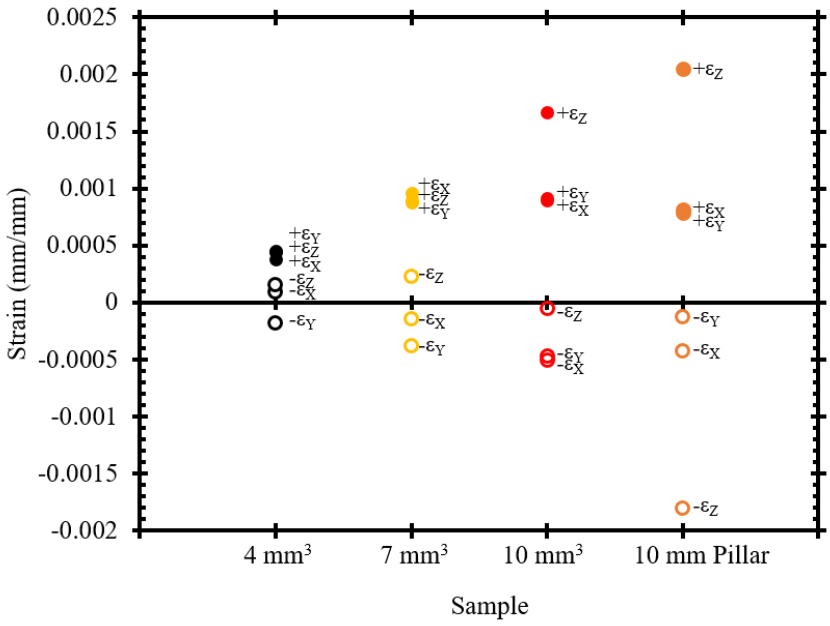

Figure 12.4. Maximum and minimum strain values, shown as open and closed data points, respectively, of the as-built samples with labels for the orthogonal strains.

sample with each orthogonal strain. In general as the volume of the sample increases, the maximum strains increase. Additionally, each of the cube samples demonstrates higher maximum tensile stress, but the pillar is relatively even. Li et al. [177] demonstrated with theoretical models and experimental results that typical L-PBF builds have a higher maximum tensile strain than compressive, so the results are likely typical and higher tensile strains should be present at the edge of the sample. Measuring strain with neutron diffraction near the edges of samples is difficult and prone to error, but surface level measurements with X-rays could be used to assess the maximum tensile strains.

In AM builds with features of rectangular prisms, the main factors of residual strain generation lie within the sample base area (X x Y) and height (Z). The maximum tensile strain should be present at the interface of the sample and the build substrate, so the larger the area of the interfacing region, the higher the stress should be. Evidence for this is shown by the increasing volume of the cube samples. The maximum strains of the 10 mm cube and pillar sample are of a similar (within 17%) magnitude and share the same the base area. If the 10 mm cube had not been stress relieved by removal from the build plate, the maximum strains would likely have been closer to the pillar's values. However, typical AM builds have highly complex features that will result in unusual strain distributions throughout, and modeling can help understand the stress generation and mitigation after validation.

Strain Distribution Post HIP

After a HIP cycle, the pillar sample was expected to be in an annealed state with low residual strains. The measured plane in the HIPed pillar sample demonstrated residual strains in the Z direction on the order of ±100 μstrain which is indicative of an annealed state and within the error of the neutron strain measurement. Compared to the as-built pillar sample's Z strain, Fig. 13.4., the overall reduction in strain is apparent. The HIP cycle is proven to be effective

Conversion of Strain to Stress

Each strain data point of the as-built samples was converted to stress using Eq. 3.4. and the correlating orthogonal strains. The strain distribution of the strain maps strongly resemble the stress maps. The only difference is the values of the color bar, so they are not presented individually. The maximum tensile and compressive strains are present in the Z strain of the as-built pillar, and each orthogonal strain correlating to those maximum values is shown in Table 1.4. Stress was calculated using three sets of modulus and Poisson values: (1) estimates of the bulk values from literature, (2) literature elastic loading diffraction elastic constants for the Cu_{311} plane of pure Cu calculated with the Kröner modeling scheme [160], and (3) experimental elastic loading diffraction elastic constants for the Cu_{311} plane from Table 3.3. The first method is best option for estimating the stress state without any planar data and is often used with more accurate macroscopic values. The elastic modulus value was estimated from available tensile data of L-PBF GRCop-84 [30], and the Poisson ratio is the typical ratio of Cu. The second method is more accurate to Cu's planar anisotropy but lacks any changes from alloying. The third method should provide the most accurate stress calculation from the measured

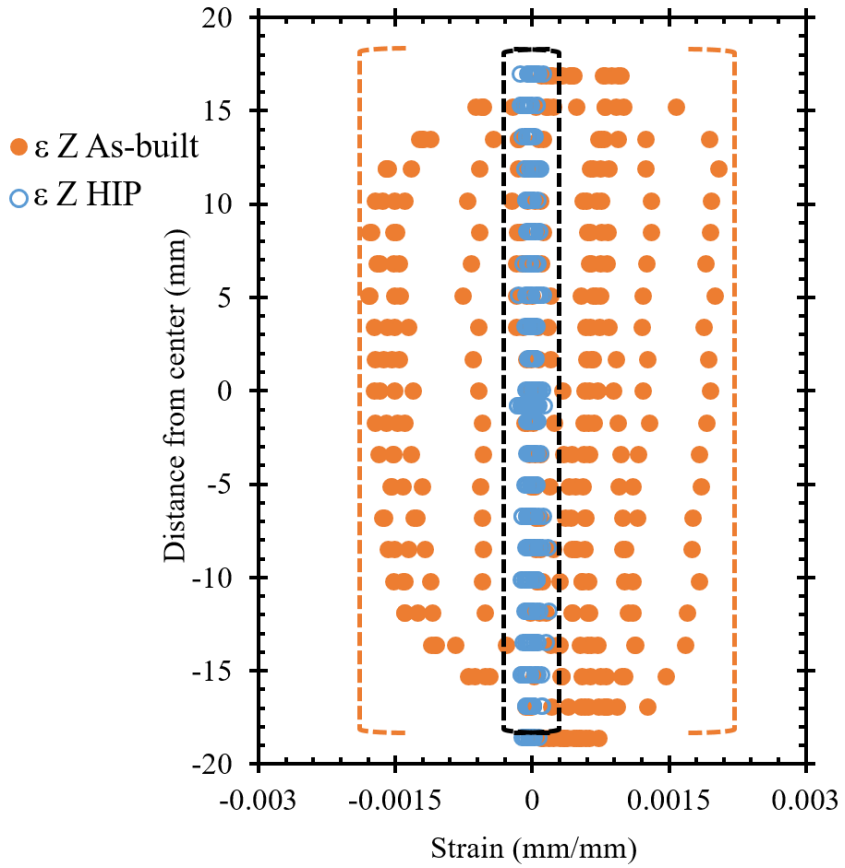

Figure 13.4. Strain distribution of the Z principal strain of both the as-built and HIPed 10 x 10 x 40 mm pillar samples; note that the HIPed data is only a single plane of the as-built data points.

Table 1.4. Elastic constants and strain values used with Eq. 3.4. to calculate maximum and minimum stress values for the 10 x 10 x 40 mm pillar sample with three different methods.

Estimated bulk values			
E (GPa)	110	υ	0.29
Literature Kröner values for pure Cu			
E_{311} *(GPa)*	122	υ_{311}	0.35
Experimental diffraction elastic constants			
E_{311} *(GPa)*	130	υ_{311}	0.345
Strain	$\mu\varepsilon_X$	$\mu\varepsilon_Y$	$\mu\varepsilon_Z$
Maximum +	-78	300	2042
Maximum -	613	652	-1797
Macroscopic Stress (MPa)	σ_X	σ_Y	σ_Z
Bulk (Method 1)	127	159	307
	21	24	-184
Modeled pure Cu DEC (Method 2)	232	266	423
	-1	3	-218
GRCop-84 DEC (Method 3)	236	272	441
	2	6	-231

data but is still considered an estimate and is not available for all materials. The calculated stress and corresponding strain data and constants are shown in Table 1.4. The stress calculations from (2) and (3) are the closest in value (within roughly ~5%) while (1) predicts stress approximately 27-30% less than the other methods. Although the lower modulus value contributes partially to the lower estimate, the difference in the Poisson ratio has the most impact on the calculated stress. This demonstrates that planar anisotropy should be considered in these types of calculations to achieve the most accurate results. Method (2) is a reasonable method for approximating stress but should only be applicable to binary or ternary alloys where the investigated phase is the bulk of the composition.

Excluding method (1), the estimated macroscopic residual stress is unusually high. The yield strength of L-PBF GRCop-84 built on the same AM system and build parameters from Gradl et al. [30] is approximately 207 MPa. AM parts tend to have high variance in the yield strength but this value should be close. The estimated maximum stress from the strain measurements is over double the yield value in the z-direction. Similarly high stresses exceeding the yield stress have been observed in other materials like Ti-6Al-4V and similarities between the alloys may help explain why this is possible [201, 202]. Ti-6Al-4V and GRCop-84 are both multi-phase alloys consisting largely of a major phase that is strengthened by a smaller volume fraction of a secondary phase. The secondary phase is most likely off-setting the high stresses and preventing the build from plastically yielding. In the as-built state, the high residual stresses should have a significant impact on the deformation behavior. Prior TOF work [195] demonstrated that as-built L-PBF GRCop-84 immediately begins plastically deforming from an observed increase in dislocation density. The high residual stress values estimated here are likely the reason for this behavior.

Implications of Stress/Strain Distribution

The stress/strain distribution of as-built L-PBF GRCop-84 resembles typical L-PBF builds with high tensile strains at the edges of the samples balanced by compressive strains towards the center. L-PBF GRCop-84 is intended for use in high-heat-flux applications where low-cycle thermal fatigue and creep are the primary life-limiting factor in operation, and the lifetime of as-built GRCop-84 would likely be insufficient for use in those applications [126]. Microstructure, porosity, surface finish, and residual stress are all expected to impact fatigue performance, but the high residual stresses in the as-built condition should be a primary factor [203]. NASA's current HIP cycle has been shown to reduce porosity, and the mapping data is evidence that the residual stresses are effectively eliminated [2, 166]. As a result, HIP is a necessary step for practical application of L-PBF GRCop-84 and demonstrates its necessity. The results found here can provide validation data for future modeling efforts but were beyond the original scope of the project.

Summary and Conclusions

Residual stress mapping of the Cu (311) plane was performed on L-PBF with 4, 7, and 10 mm cube samples and 10 x 10 x 40 mm pillar samples in the as-built and HIPed

condition. All of the samples were removed from the build plate by EDM which partially relieved an expected tensile stress at the interface of the build substrate and sample. Two and three-dimensional contour maps of the as-built samples were compared, and the maximum tensile and compressive strains were assessed. The measured strains were converted to macroscopic stress with three separate sets of elastic constants and compared which combined results from a prior in-situ mechanical TOF neutron study with the ex-situ study. The main findings are as follows.

(1) The stress/strain distribution of as-built L-PBF GRCop is typical of AM builds with high tensile strains at the edges and correlating compressive strains at the center. The measured volume within the samples does not account for the true maximum tensile strains. More residual stress measurements are necessary to evaluate surface level tensile stresses, and the expected tensile stress between the build substrate and the sample.
(2) Both volume and build height demonstrated a significant proportional change to the overall residual stress/strain state.
(3) The estimated maximum residual stresses in as-built L-PBF GRCop-84 are over two times the yield strength and are expected to be a major detriment to fatigue behavior.
(4) After HIP, the high residual stresses induced during L-PBF are effectively eliminated. Surface level testing is necessary to verify the reduction of surface strains.

Acknowledgements

This research used resources at the Spallation Neutron Source, a US Department of Energy Office of Science User Facility operated by Oak Ridge National Laboratory. The authors would like to acknowledge the Manufacturing and Materials Joining Innovation Center (Ma^2JIC), made possible through awards NSF IIP-1540000 (Phase I) and NSF IIP-1822186 (Phase II) from the National Science Foundation Industry University Cooperative Research Center program (IUCRC). RPM also acknowledges the financial support of Oak Ridge National Laboratory's Graduate Opportunities (GO!) Program.

CONCLUSION

The culmination of this research is characterization and improved understanding of additively manufactured GRCop-84 through novel methods. This work provided the first comprehensive review of GRCop-84 literature and the first neutron diffraction experiments on AM GRCop-84. Furthermore, this body of research provides fundamental understanding regarding microstructure evolution and phase interaction, mechanical loading characteristics, and residual stress evolution of AM GRCop-84. Throughout this work, many valuable insights and scientific findings were collected that directly benefit future efforts with GRCop-84 and similar high-heat-flux alloys.

The microstructural characterization and phase analysis in this research fills a gap in the current literature for future researchers and in understanding the results in the remaining body of work. L-PBF introduces complex microstructures and unusual phase fractions that are perceivable with diffraction methods. The gas-atomized powder used for SLM has a bimodal distribution of Cr_2Nb ranging from μm to nm scale with high loading fraction of 12 wt% which will provide a multitude of nucleation sites for the matrix grains, and high thermal conductivity of the alloy will provide extreme cooling gradients between the melt pool and surroundings. We hypothesize that these factors are the primary cause of non-equilibrium, heterogeneous grain structures and metastable precipitate phases observed in SEM, HTXRD, and EBSD results. The current HIP cycle has a significant impact on the microstructure and was shown to improve density, texture, and overall consistency of the grain structure and is likely an irreplaceable step in practical use.

The in-situ mechanical neutron diffraction efforts pushed the capabilities of the technique to the limits of analyzing real materials. Valuable information was acquired regarding diffraction elastic constants, anisotropic planar behavior, changes in deformation mechanisms, and influence of residual stress and texture. As-built and HIPed GRCop-84 are known to have significantly different macroscopic deformation behaviors, and the planar behavior helps explain the dissimilarity.

Ex-situ residual stress mapping with constant wavelength neutrons has revealed various features of the evolution of residual stress in L-PBF GRCop-84. The general distribution resembles typical L-PBF alloys with high compressive strains at the center of the volume balanced by high tensile stresses at the edges of the sample. Information obtained from the in-situ experiment was used to calculate residual stress and bridged complementary techniques. In larger samples, residual stresses were observed that exceed the yield strength by over a factor of two. This is believed to be possible due to a balancing effect from the Cr_2Nb phase that balances the high stresses. Development of L-PBF GRCop-84 has rapidly advanced due largely to ease of development as working process parameters were quickly found. The theorized balancing effect of Cr_2Nb could be responsible for the ease of printing and allows for a higher energy density during printing that produces more optimal microstructures.

Improved understanding of the processing and phase interactions of L-PBF GRCop-84 directly benefits reusable rocket technology in the aerospace industry where the alloy is currently applied. Within the 700-900 K temperature range, there is a dramatic loss of mechanical strength that makes the majority of high-heat-flux Cu alloys unviable or non-reusable as the microstructure deteriorates from high temperature exposure, but the higher temperature range can provide significantly better fuel efficiency and safety factors. GRCop-84's practical use and development has been limited by the preferred use of single-use

components, but its properties provide significantly longer fatigue and creep lifetimes that allow it to be useable within the 700-900 K range. This can result in a dramatic reduction of cost to the rocket and aerospace industry. Without L-PBF, GRCop-84's development would likely have stagnated due to its high material and machining costs. L-PBF and GRCop-84 allow for the production of highly customizable and reusable structural heat exchangers that can benefit a variety of industries. The advantages shown in this research are partly intended to improve awareness of the alloy and increase the quantity of interested researchers.

References

1. Lee, D.-Y. and K. Vafai, *Comparative analysis of jet impingement and microchannel cooling for high heat flux applications.* International Journal of Heat and Mass Transfer, 1999. **42**(9): p. 1555-1568.
2. Ellis, D.L., *GRCop-84: A high-temperature copper alloy for high-heat-flux applications.* 2005.
3. Dhokey, N.B., S.N. Sarve, and H.A. Lamsoge. *In Situ Synthesis of Cr2Nb Reinforced Copper Alloy by Liquid Metallurgy Route*. in *Materials Science Forum*. 2012. Trans Tech Publ.
4. Zinkle, S. and S. Fabritsiev, *Copper alloys for high heat flux structure applications.* Atomic and Plasma-Material Interaction Data for Fusion (supplement to Nuclear Fusion), 1994. **5**: p. 163.
5. Ebadian, M. and C. Lin, *A review of high-heat-flux heat removal technologies.* Journal of heat transfer, 2011. **133**(11): p. 110801.
6. Zinkle, S.J. and J.T. Busby, *Structural materials for fission & fusion energy.* Materials today, 2009. **12**(11): p. 12-19.
7. Berlin, G.N., *Managing the variability of fire behavior.* Fire Technology, 1980. **16**(4): p. 287-302.
8. Ellis, D.L. and B.A. Lerch, *Improvement of GRCop-84 through the addition of Zirconium.* 2012.
9. Ellis, D.L. and G.M. Michal, *Precipitation strengthened high strength, high conductivity Cu-Cr-Nb alloys produced by chill block melt spinning. Final Report Ph. D. Thesis.* 1989.
10. Protz, C., et al., *Additive Manufacturing of Low Cost Upper Stage Propulsion Components.* 2014.
11. Protz, C., et al., *Additively Manufactured Low Cost Upper Stage Combustion Chamber.* 2016.
12. Gradl, P.R., et al., *Progress in Additively Manufactured Copper-Alloy GRCop-84, GRCop-42, and Bimetallic Combustion Chambers for Liquid Rocket Engines.* 2019.
13. Williamson, R.A., *Developing the space shuttle.* Exploring the Unknown, 1999. **4**.
14. Ballard, R.O., *SSME to RS-25: Challenges of Adapting a Heritage Engine to a New Vehicle Architecture.* 2015.
15. Esposito, J.J. and R.F. Zabora, *Thrust chamber life prediction. Volume 1: Mechanical and physical properties of high performance rocket nozzle materials.* 1975.
16. Kazaroff, J.M. and G.A. Repas, *Conventionally cast and forged copper alloy for high-heat-flux thrust chambers.* 1987.
17. COOK, R. and G. COFFEY. *Space shuttle orbiter engine main combustion chamber cooling and life*. in *9th Propulsion Conference*. 1973.
18. Wadel, M.F., *Comparison of high aspect ratio cooling channel designs for a rocket combustion chamber with development of an optimized design.* 1998.
19. Andrus, J. and R. Bordeau, *Thrust chamber material technology program.* 1989.

20. NASA, *Report to the President Implementation of the Recommendations of the Presidential Commission on the Space Shuttle Challenger Accident Final Status Report.* 1987: p. 89.
21. Krishna, S.C., et al., *Microstructure and mechanical properties of Cu-Ag-Zr alloy.* Journal of materials engineering and performance, 2013. **22**(12): p. 3884-3889.
22. Thompson, J.R., *Space Shuttle Main Engine.* 1980.
23. Groza, J., *Heat-resistant dispersion-strengthened copper alloys.* Journal of Materials Engineering and performance, 1992. **1**(1): p. 113-121.
24. Dieter, G.E. and D.J. Bacon, *Mechanical metallurgy*. Vol. 3. 1986: McGraw-hill New York.
25. Porter, D.A., K.E. Easterling, and M. Sherif, *Phase transformations in metals and alloys (Revised Reprint)*. 2009: CRC press.
26. Martin, J.W., *Precipitation hardening: theory and applications*. 2012: Butterworth-Heinemann.
27. Ellis, D.L. and G.M. Michal, *Mechanical and thermal properties of Two Cu-Cr-Nb alloys and NARloy-Z.* 1996.
28. Singh, J., et al., *Mechanical properties and microstructural stability of wrought, laser, and electron beam glazed NARloy-Z alloy at elevated temperatures.* Journal of materials science, 1997. **32**(14): p. 3891-3903.
29. de Groh, H.C., D.L. Ellis, and W.S. Loewenthal, *Comparison of GRCop-84 to other Cu alloys with high thermal conductivities.* Journal of materials engineering and performance, 2008. **17**(4): p. 594-606.
30. Gradl, P.R., et al. *GRCop-42 Development and Hot-fire Testing using Additive Manufacturing Powder Bed Fusion for Channel-Cooled Combustion Chambers*. in *AIAA Propulsion and Energy 2019 Forum*. 2019.
31. Sanders, J., et al., *Microstructural investigation of the effects of oxygen exposure on NARloy-Z.* Materials Science and Engineering: A, 1995. **203**(1-2): p. 246-255.
32. Li, M. and S. Zinkle, *4.20-Physical and Mechanical Properties of Copper and Copper Alloys.* Comprehensive Nuclear Materials, 2012: p. 667-690.
33. Ellis, D., J. Carter, and M. Ferry, *A statistical study of the effects of processing upon the creep properties of GRCop-84.* Materials Science and Engineering: A, 2015. **640**: p. 1-15.
34. Holzwarth, U., et al., *On the recovery of the physical and mechanical properties of a CuCrZr alloy subjected to heat treatments simulating the thermal cycle of hot isostatic pressing.* Journal of Nuclear Materials, 2000. **279**(1): p. 19-30.
35. Kalinin, G., et al., *Assessment and selection of materials for ITER in-vessel components.* Journal of Nuclear Materials, 2000. **283**: p. 10-19.
36. Park, J.-Y., et al., *Effect of cooling rate on mechanical properties of aged ITER-grade CuCrZr.* Fusion Engineering and Design, 2008. **83**(10-12): p. 1503-1507.
37. Brandes, E.A. and G. Brook, *Smithells metals reference book*. 2013: Elsevier.
38. Subramanian, P. and J. Perepezko, *The Ag-Cu (silver-copper) system.* Journal of Phase Equilibria, 1993. **14**(1): p. 62-75.

39. Chakrabarti, D. and D. Laughlin, *The Cr-Cu (chromium-copper) system.* Bulletin of Alloy phase diagrams, 1984. **5**(1): p. 59-68.
40. Terekhov, G. and L. Aleksandrova, *Copper-niobium phase diagram.* Izvestiya Akademii Nauk SSSR, Metally, 1984: p. 210-213.
41. Okamoto, H., *Cu-Zr (copper-zirconium).* Journal of phase equilibria and diffusion, 2008. **29**(2): p. 204-204.
42. Callister, W.D. and D.G. Rethwisch, *Materials science and engineering: an introduction*. 2018: Wiley New York.
43. Anderson, K.R., *Effects of Thermal and Mechanical Processing on Microstructures and Desired Properties of Particle-Strengthened Cu-Cr-Nb Alloys.* 2000.
44. Anderson, K.R. and J.R. Groza, *Microstructural size effects in high-strength high-conductivity Cu-Cr-Nb alloys.* Metallurgical and Materials Transactions A, 2001. **32**(5): p. 1211-1224.
45. Jech, R.W., et al., *Rapid solidification via melt spinning: equipment and techniques.* JOM, 1984. **36**(4): p. 41-45.
46. Christian, J.W., *The theory of transformations in metals and alloys*. 2002: Newnes.
47. Lifshitz, I.M. and V.V. Slyozov, *The kinetics of precipitation from supersaturated solid solutions.* Journal of physics and chemistry of solids, 1961. **19**(1-2): p. 35-50.
48. Poirier, D.R. and G. Geiger, *Transport phenomena in materials processing*. 2016: Springer.
49. Tritt, T.M., *Thermal conductivity: theory, properties, and applications*. 2005: Springer Science & Business Media.
50. Groza, J. and J. Gibeling, *Principles of particle selection for dispersion-strengthened copper.* Materials Science and Engineering: A, 1993. **171**(1-2): p. 115-125.
51. Simon, S.H., *The Oxford solid state basics*. 2013: OUP Oxford.
52. Kasap, S.O., *Principles of electronic materials and devices*. Vol. 2. 2006: McGraw-Hill New York.
53. Touloukian, Y.S., et al., *Thermophysical properties of matter-the tprc data series. volume 1. thermal conductivity-metallic elements and alloys*. 1970, THERMOPHYSICAL AND ELECTRONIC PROPERTIES INFORMATION ANALYSIS CENTER ….
54. Anderson, W., J. Sisco, and I. Sung. *Rocket combustor experiments and analyses*. in *14th Annual Thermal and Fluids Analysis Workshop (TFAWS)*. 2003.
55. Halford, G.R., *Low-cycle thermal fatigue.* 1986.
56. *Standard Test Methods for Conducting Creep, Creep-Rupture, and Stress-Rupture Tests of Metallic Materials*. 2018.
57. Kassner, M.E., *Fundamentals of creep in metals and alloys*. 2015: Butterworth-Heinemann.
58. Kasper, H.J., *Thrust chamber life prediction.* 1985.

59. Dai, X. and A. Ray, *Damage-Mitigating Control of a Reusable Rocket Engine: Part I—Life Prediction of the Main Thrust Chamber Wall.* Journal of dynamic systems, measurement, and control, 1996. **118**(3): p. 401-408.
60. Popp, M. and G. Schmidt. *Rocket engine combustion chamber design concepts for enhanced life*. in *32nd Joint Propulsion Conference and Exhibit*. 1996.
61. Quentmeyer, R. *Rocket combustion chamber life-enhancing design concepts*. in *26th Joint Propulsion Conference*. 1990.
62. Zhu, J., et al., *Enthalpies of formation of binary Laves phases.* Intermetallics, 2002. **10**(6): p. 579-595.
63. Mayer, B., et al., *Ab-initio calculation of the elastic constants and thermal expansion coefficients of Laves phases.* Intermetallics, 2003. **11**(1): p. 23-32.
64. Callister, W.D., *Fundamentals of materials science and engineering*. Vol. 471660817. 2000: Wiley London.
65. Ogbuji, L., *A table-top technique for assessing the blanching resistance of Cu alloys.* Oxidation of metals, 2005. **63**(5-6): p. 383-399.
66. Woods, S. and J.A. Lee, *Hydrogen Embrittlement.* 2016.
67. Chandler, W. and R. Walter, *Testing to determine the effect of high-pressure hydrogen environments on the mechanical properties of metals*, in *Hydrogen embrittlement testing*. 1974, ASTM International.
68. Thomas-Ogbuji, L.U., *Oxidation Behavior of GRCop-84 Copper Alloy Assessed.* 2002.
69. Cook, M.B., K.L. Murphy, and T. Schneider, *Advanced Materials for Exploration Task Research Results.* 2008.
70. Quentmeyer, R.J., *Thrust chamber thermal barrier coating techniques.* 1988.
71. Batakis, A.P. and J. Vogan, *Rocket thrust chamber thermal barrier coatings.* 1985.
72. Bhat, B., H. Gilmore, and R. Holmes, *Thermal barrier coatings for the space shuttle main engine turbine blades.* 1985.
73. Quentmeyer, R.J., *Rocket thrust chamber thermal barrier coatings.* 1985.
74. Nesbitt, J.A. and W.J. Brindley, *Thermal analysis of thermal barrier coatings in a high heat flux environment.* 1988.
75. Holmes, R. and T. McKechnie, *Vacuum application of thermal barrier plasma coatings.* 1988.
76. Arnold, S.M., D.T. Butler Jr, and M.-J. Pinders, *Analysis of Factors Affecting the Performance of RLV Thrust Cell Liners.* 2004.
77. Ellis, D., *Private Communication.* Mar. 2020.
78. Nikolayev, A. and R. VM, *Investigation of Phase-Diagram of Copper-Rich Cu-Nb-Cr Alloys.* RUSSIAN METALLURGY, 1972(5): p. 118-121.
79. Anderson, K.R., *High temperature coarsening of Cr2Nb precipitates in Cu-8 Cr-4 Nb alloy.* 1996.
80. Liu, X., et al., *Experimental determination and thermodynamic calculation of the phase equilibria in the Cu–Cr–Nb and Cu–Cr–Co systems.* Journal of Alloys and Compounds, 2009. **478**(1-2): p. 287-296.

81. Stein, F., M. Palm, and G. Sauthoff, *Structure and stability of Laves phases. Part I. Critical assessment of factors controlling Laves phase stability.* Intermetallics, 2004. **12**(7-9): p. 713-720.
82. Okamoto, H., *Cu-Nb (Copper-Niobium).* Journal of phase equilibria and diffusion, 2012. **33**(4): p. 344-344.
83. Zhou, Z., et al., *Experimental determination and thermodynamic modeling of phase equilibria in the Cu–Cr system.* Journal of materials science, 2011. **46**(21): p. 7039-7045.
84. Venkatraman, M. and J. Neumann, *The Cr− Nb (Chromium-Niobium) system.* Bulletin of Alloy Phase Diagrams, 1986. **7**(5): p. 462-466.
85. Takasugi, T., M. Yoshida, and S. Hanada, *Deformability improvement in C15 NbCr2 intermetallics by addition of ternary elements.* Acta materialia, 1996. **44**(2): p. 669-674.
86. Lu, H.-J., et al., *Thermodynamic modeling of Cr–Nb and Zr–Cr with extension to the ternary Zr–Nb–Cr system.* Calphad, 2015. **50**: p. 134-143.
87. Jiang, Y., et al., *Thermodynamic re-assessment of binary Cr-Nb system down to 0 K.* Calphad, 2018. **62**: p. 109-118.
88. Vettraino, L., et al., *Influence of processing on the microstructure of Cu–8Cr–4Nb.* Journal of materials science, 2008. **43**(19): p. 6546-6555.
89. Ellis, D. and G. Michal, *Formation of Cr and Cr2Nb precipitates in rapidly solidified Cu-Cr-Nb ribbon.* Ultramicroscopy, 1989. **30**(1-2): p. 210-216.
90. Ellis, D.L., G.M. Michal, and N.W. Orth, *Production and processing of Cu-Cr-Nb alloys.* 1990.
91. Guseva, L. and L. Rusanova, *INTERMEDIATE PHASES IN THE CHROMIUMNIOBIUM SYSTEM.* Izvestiya Akademii Nauk SSSR, Neorganicheskie Materialy (USSR) For English translation see Inorg. Mater.(Engl. Transl.), 1966. **2**.
92. Bhat, B.N., et al., *Aerospace Materials Characteristics.* Aerospace Materials and Applications, 2018: p. 11.
93. Piatti, G. and D. Boerman, *Hot tensile characteristics and microstructure of a Cu-0.65 Cr-0.08 Zr alloy for fusion reactor applications.* Journal of nuclear materials, 1991. **185**(1): p. 29-38.
94. Conway, J., R. Stentz, and J. Berling, *High temperature, low-cycle fatigue of copper-base alloys in argon. Part 1: Preliminary results for 12 alloys at 1000 F (538 C).* 1973.
95. Conway, J., R. Stentz, and J. Berling, *High-temperature, low-cycle fatigue of advanced copper-base alloys for rocket nozzles. Part 1: Narloy Z.* 1974.
96. Conway, J.B., R. Stentz, and J. Berling, *High-temperature, low-cycle fatigue of advanced copper-base alloys for rocket nozzles. Part 2: NASA 1.1, Glidcop, and sputtered copper alloys.* 1974.
97. Anderson, K.R., et al., *Microstructural evolution and thermal stability of precipitation-strengthened Cu 8Cr 4Nb alloy.* Materials Science and Engineering: A, 1993. **169**(1-2): p. 167-175.
98. Lawley, A., *Atomization of specialty alloy powders.* JOM, 1981. **33**(1): p. 13-18.

99. Ellis, D., *Observations of a Cast Cu-Cr-Zr Alloy. MS&T Conference Presentation.* 2006.
100. Lawley, A., *Preparation of metal powders.* Annual Review of Materials Science, 1978. **8**(1): p. 49-71.
101. Russell, C.K., et al., *Friction stir welding of GRCop-84 for combustion chamber liners.* Journal of propulsion and power, 2007. **23**(4): p. 756-762.
102. Gradl, P.R., W. Brandsmeier, and S.E. Greene. *Channel Wall Nozzle Manufacturing and Hot-Fire Testing using a Laser Wire Direct Closeout Technique for Liquid Rocket Engines*. in *2018 Joint Propulsion Conference*. 2018.
103. Hayes, C., E. Brown, and B. Kappes. *Characterization of Selective Laser Melted GRCop-84*. in *2018 Joint Propulsion Conference*. 2018.
104. Ellis, D.L., W.S. Loewenthal, and H.-M. Yun, *Tensile Properties of GRCop-84.* 2012.
105. Tran, T.Q., et al., *3D Printing of Highly Pure Copper.* Metals, 2019. **9**(7): p. 756.
106. Gradl, P.R., et al. *Development and Hot-fire Testing of Additively Manufactured Copper Combustion Chambers for Liquid Rocket Engine Applications*. in *53rd AIAA/SAE/ASEE Joint Propulsion Conference*. 2017.
107. Gradl, P.R., et al. *Additive Manufacturing of Liquid Rocket Engine Combustion Devices: A Summary of Process Developments and Hot-Fire Testing Results*. in *2018 Joint Propulsion Conference*. 2018.
108. Cooper, K., et al., *Three-dimensional printing GRCop-42.* 2018.
109. Groza, J.R., *Microstructural features of a new precipitation-strengthened Cu 8Cr 4Nb alloy.* Materials characterization, 1993. **31**(3): p. 133-141.
110. Anderson, K.R., et al., *High-performance dispersion-strengthened Cu-8 Cr-4 Nb alloy.* Metallurgical and Materials Transactions A, 1995. **26**(9): p. 2197-2206.
111. Raj, S., et al., *High heat flux exposures of coated GRCop-84 substrates.* Materials Science and Engineering: A, 2007. **457**(1-2): p. 300-312.
112. Ellis, D.L., D.J. Keller, and M. Nathal, *Thermophysical properties of GRCop-84.* 2000.
113. Decker, M., J. Groza, and J. Gibeling, *Creep properties of an extruded copper–8% chromium–4% niobium alloy.* Materials Science and Engineering: A, 2004. **369**(1-2): p. 101-111.
114. Loewenthal, W.S. and D.L. Ellis, *Sources of Variation in Creep Testing.* 2011.
115. Lerch, B.A., S.M. Arnold, and D.L. Ellis, *Reversible and Irreversible Time-Dependent Behavior of GRCop-84.* 2017.
116. Touloukian, Y.S., et al., *Thermophysical properties of matter-the tprc data series. volume 12. thermal expansion metallic elements and alloys*. 1975, THERMOPHYSICAL AND ELECTRONIC PROPERTIES INFORMATION ANALYSIS CENTER ….
117. Takahashi, S., et al., *Fatigue life prediction for high-heat-load components made of GlidCop by elastic-plastic analysis.* Journal of synchrotron radiation, 2008. **15**(2): p. 144-150.
118. Ellis, D.L. and K. Hastings, *Effects of Hydrogen on GRCop-84.* 2006.

119. Ellis, D.L. and B.K. Hastings, *Hydrogen embrittlement resistance of GRCop-84.* International journal of hydrogen energy, 2008. **33**(20): p. 5661-5671.
120. Ellis, D.L., A.K. Misra, and R.L. Dreshfield, *Effect of hydrogen exposure on a Cu-8 Cr-4 Nb alloy.* 1993.
121. Thomas-Ogbuji, L.U., D.L. Humphrey, and L. Greenbauer-Seng, *Oxidation behavior of GRCop-84 (Cu-8Cr-4Nb) at intermediate and high temperatures.* 2000.
122. Zinkle, S.J., *Applicability of copper alloys for DEMO high heat flux components.* Physica Scripta, 2015. **2016**(T167): p. 014004.
123. Chen, Z., et al., *Surface roughness and fatigue properties of selective laser melted Ti–6Al–4V alloy*, in *Additive Manufacturing for the Aerospace Industry*. 2019, Elsevier. p. 283-299.
124. Ellis, D.L. and B.A. Lerch, *Increased Mechanical Properties through the Addition of Zr to GRCop-84.* 2011.
125. Seltzman, A.H. and S.J. Wukitch, *Brazing, Laser, and Electron-Beam Welding of Additively Manufactured GRCop-84 Copper for Phased Array Lower Hybrid Launchers.* IEEE Transactions on Plasma Science, 2020.
126. Minneci, R.P., et al., *Copper-based alloys for structural high-heat-flux applications: a review of development, properties, and performance of Cu-rich Cu–Cr–Nb alloys.* International Materials Reviews, 2020: p. 1-32.
127. Ellis, D.L., *Observations of a cast Cu-Cr-Zr alloy.* 2006.
128. Ellis, D., A. Misra, and R. Dreshfield, *Effect of Hydrogen on a Cu-8 Cr-4 Nb Alloy.* NASA TM-106429, NASA Lewis Research Center, Cleveland, OH (Dec. 1993), 1993.
129. Sames, W.J., et al., *The metallurgy and processing science of metal additive manufacturing.* International materials reviews, 2016. **61**(5): p. 315-360.
130. Gu, D., et al., *Densification behavior, microstructure evolution, and wear performance of selective laser melting processed commercially pure titanium.* Acta Materialia, 2012. **60**(9): p. 3849-3860.
131. Zhang, X., et al., *Microstructure evolution during selective laser melting of metallic materials: A review.* Journal of Laser Applications, 2019. **31**(3): p. 031201.
132. DuPont, J.N., *Fundamentals of weld solidification.* ASM Handbook 6a, 2011: p. 96-114.
133. Das, S., *Physical aspects of process control in selective laser sintering of metals.* Advanced Engineering Materials, 2003. **5**(10): p. 701-711.
134. Nelson, T., J. Lippold, and M. Mills, *Nature and evolution of the fusion boundary in ferritic-austenitic dissimilar weld metals, Part 1-Nucleation and growth.* WELDING JOURNAL-NEW YORK-, 1999. **78**: p. 329-s.
135. Yan, F., W. Xiong, and E.J. Faierson, *Grain structure control of additively manufactured metallic materials.* Materials, 2017. **10**(11): p. 1260.
136. Dezfoli, A.R.A., et al., *Determination and controlling of grain structure of metals after laser incidence: Theoretical approach.* Scientific reports, 2017. **7**: p. 41527.

137. Ventura, A.P., *Microstructural evolution and mechanical property development of selective laser melted copper alloys.* 2017.
138. Carter, R., et al., *Materials Characterization of Additively Manufactured Components for Rocket Propulsion.* 2015.
139. MSFC-STD, N., *Specification for Control and Qualification of Laser Powder Bed Fusion Metallurgical Processes.* 2017.
140. Scipioni Bertoli, U., et al., *In-situ characterization of laser-powder interaction and cooling rates through high-speed imaging of powder bed fusion additive manufacturing.* Materials & Design, 2017. **135**: p. 385-396.
141. Zheng, B., et al., *Gas atomization of amorphous aluminum powder: Part II. Experimental investigation.* Metallurgical and Materials Transactions B, 2009. **40**(6): p. 995.
142. Song, B., et al., *Vacuum heat treatment of iron parts produced by selective laser melting: microstructure, residual stress and tensile behavior*. Materials & Design (1980-2015), 2014. **54**: p. 727-733.
143. Brandl, E. and D. Greitemeier, *Microstructure of additive layer manufactured Ti–6Al–4V after exceptional post heat treatments.* Materials Letters, 2012. **81**: p. 84-87.
144. Toby, B.H. and R.B. Von Dreele, *GSAS-II: the genesis of a modern open-source all purpose crystallography software package.* Journal of Applied Crystallography, 2013. **46**(2): p. 544-549.
145. Toby, B.H., *EXPGUI, a graphical user interface for GSAS.* Journal of applied crystallography, 2001. **34**(2): p. 210-213.
146. Von Dreele, R. and A. Larson, *General structure analysis system (GSAS).* Los Alamos Natl. Lab. Rep. LAUR, 2004. **748**: p. 86-748.
147. Morey, A., *NIST Standard Reference Database 3.* 2019.
148. Otte, H.M., *Lattice parameter determinations with an x-ray spectrogoniometer by the debye-scherrer method and the effect of specimen condition.* Journal of Applied Physics, 1961. **32**(8): p. 1536-1546.
149. BUDBERG, P. and S. ALISOVA, *INVESTIGATION OF THE TACR 2-ZRCR 2 AND TACR 2-NBCR 2 SYSTEMS.* RUSS MET, 1969,--3--, 140-142, 1969.
150. Villafuerte, J.C., H.W. Kerr, and S.A. David, *Mechanisms of equiaxed grain formation in ferritic stainless steel gas tungsten arc welds.* Materials Science and Engineering: A, 1995. **194**(2): p. 187-191.
151. Schneider, C.A., W.S. Rasband, and K.W. Eliceiri, *NIH Image to ImageJ: 25 years of image analysis.* Nature methods, 2012. **9**(7): p. 671-675.
152. Bachmann, F., R. Hielscher, and H. Schaeben. *Texture analysis with MTEX–free and open source software toolbox*. in *Solid State Phenomena*. 2010. Trans Tech Publ.
153. Cullity, B.D.S., S. R. , *Elements of X-ray Diffraction*. Third ed. 2001, Upper Saddle River, NJ: Prentice Hall.
154. Babu, S., et al., *Toward prediction of microstructural evolution during laser surface alloying.* Metallurgical and Materials transactions A, 2002. **33**(4): p. 1189-1200.

155. Hong, T., et al., *Modeling of inclusion growth and dissolution in the weld pool.* Metallurgical and Materials Transactions B, 2000. **31**(1): p. 161-169.
156. Babu, S., *In pursuit of optimum welding system design for steels.* Science and Technology of Welding and Joining, 2011. **16**(4): p. 306-312.
157. Liu, P., et al., *Insight into the mechanisms of columnar to equiaxed grain transition during metallic additive manufacturing.* Additive Manufacturing, 2019. **26**: p. 22-29.
158. Denton, A.R. and N.W. Ashcroft, *Vegard's law.* Physical review A, 1991. **43**(6): p. 3161.
159. Kelly, T.F. and M.K. Miller, *Atom probe tomography.* Review of Scientific Instruments, 2007. **78**(3): p. 031101.
160. Hutchings, M.T., *Introduction to the characterization of residual stress by neutron diffraction*. 2005: CRC press.
161. Brown, D., et al., *In situ neutron diffraction study of the influence of microstructure on the mechanical response of additively manufactured 304L stainless steel.* Metallurgical and Materials Transactions A, 2017. **48**(12): p. 6055-6069.
162. An, K., et al., *First in situ lattice strains measurements under load at VULCAN.* Metallurgical and Materials Transactions A, 2011. **42**(1): p. 95-99.
163. Benafan, O., et al., *Design and implementation of a multiaxial loading capability during heating on an engineering neutron diffractometer.* Review of Scientific Instruments, 2014. **85**(10): p. 103901.
164. Wang, X.-L., et al., *VULCAN—the engineering diffractometer at the SNS.* Physica B: Condensed Matter, 2006. **385**: p. 673-675.
165. Page, K., et al., *Preface: Special Topic on Advances in Modern Neutron Diffraction at Oak Ridge National Laboratory*. 2018, AIP Publishing LLC.
166. Minneci, R., Haines, M., Gradl, P., Ellis, D., Lass, E. Bunn, J., Choo, H., Jones, Z., Babu, S., Rawn, C., *Microstructure Characterization of Laser-Powder Bed Fusion (L-PBF) Consolidated GRCop-84.* Manuscript Title, 2020.
167. An, K., *Data Reduction and Interactive Visualization Software for Event Mode Neutron Diffraction.* ORNL Report, ORNL-TM-2012, 2012. **621**.
168. Yu, D., et al., *Real-time in situ neutron diffraction investigation of phase-specific load sharing in a cold-rolled TRIP sheet steel.* JOM, 2018. **70**(8): p. 1576-1586.
169. Karato, S.-i., *Theory of lattice strain in a material undergoing plastic deformation: Basic formulation and applications to a cubic crystal.* Physical Review B, 2009. **79**(21): p. 214106.
170. Holden, T., A. Clarke, and R. Holt, *Neutron diffraction measurements of intergranular strains in MONEL-400.* Metallurgical and materials transactions A, 1997. **28**(12): p. 2565-2576.
171. Huang, E.-W., et al., *Slip-system-related dislocation study from in-situ neutron measurements.* Metallurgical and Materials Transactions A, 2008. **39**(13): p. 3079.

172. Shintani, T. and Y. Murata, *Evaluation of the dislocation density and dislocation character in cold rolled Type 304 steel determined by profile analysis of X-ray diffraction.* Acta Materialia, 2011. **59**(11): p. 4314-4322.
173. Ungár, T., *Microstructural parameters from X-ray diffraction peak broadening.* Scripta Materialia, 2004. **51**(8): p. 777-781.
174. Huang, E.-W., et al., *Plastic behavior of a nickel-based alloy under monotonic-tension and low-cycle-fatigue loading.* International Journal of Plasticity, 2008. **24**(8): p. 1440-1456.
175. Huang, E.-W., et al., *A neutron-diffraction study of the low-cycle fatigue behavior of HASTELLOY® C-22HSTM alloy.* International journal of fatigue, 2007. **29**(9-11): p. 1812-1819.
176. Clausen, B., *Characterisation of polycrystal deformation by numerical modelling and neutron diffraction measurements*. 1997, Risoe National Lab.
177. Li, C., et al., *Residual Stress in Metal Additive Manufacturing.* Procedia CIRP, 2018. **71**: p. 348-353.
178. Song, G., et al., *High Temperature Deformation Mechanism in Hierarchical and Single Precipitate Strengthened Ferritic Alloys by In Situ Neutron Diffraction Studies.* Scientific Reports, 2017. **7**(1): p. 45965.
179. Hong, S. and C. Fu, *Phase stability and elastic moduli of Cr2Nb by first-principles calculations.* Intermetallics, 1999. **7**(1): p. 5-9.
180. Ponraj, V., et al., *Graphene nanosheet as reinforcement agent in copper matrix composite by using powder metallurgy method.* Surfaces and Interfaces, 2017. **6**.
181. James, M.N., et al., *Residual stresses and fatigue performance.* Engineering Failure Analysis, 2007. **14**(2): p. 384-395.
182. Vayssette, B., et al., *Numerical modelling of surface roughness effect on the fatigue behavior of Ti-6Al-4V obtained by additive manufacturing.* International Journal of Fatigue, 2019. **123**: p. 180-195.
183. Yakout, M., et al., *Influence of thermal properties on residual stresses in SLM of aerospace alloys.* Rapid Prototyping Journal, 2020.
184. Mercelis, P. and J.P. Kruth, *Residual stresses in selective laser sintering and selective laser melting.* Rapid Prototyping Journal, 2006. **12**(5): p. 254-265.
185. Schajer, G.S., *Residual Stresses: Measurement by Destructive Testing*, in *Encyclopedia of Materials: Science and Technology*, K.H.J. Buschow, et al., Editors. 2001, Elsevier: Oxford. p. 8152-8158.
186. Buttle, D. and C. Scruby, *Residual Stresses: Measurement using Magnetoelastic Effects*, in *Encyclopedia of Materials: Science and Technology*, K.H.J. Buschow, et al., Editors. 2001, Elsevier: Oxford. p. 8173-8180.
187. Withers, P.J., et al., *Recent advances in residual stress measurement.* International Journal of Pressure Vessels and Piping, 2008. **85**(3): p. 118-127.
188. Young, R.J., *Residual Stresses: Measurement by Raman Shift*, in *Encyclopedia of Materials: Science and Technology*, K.H.J. Buschow, et al., Editors. 2001, Elsevier: Oxford. p. 8170-8172.
189. Chakoumakos, B.C., *Neutron scattering program at the high-flux isotope reactor, Oak Ridge National Laboratory.* Neutron News, 1999. **10**(2): p. 5-9.

190. Watkins, T., et al., *Neutron characterization for additive manufacturing.* Advanced Materials & Processes, 2013: p. 23.
191. Rustichelli, F., *Innovative technological materials Structural properties by neutron scattering, synchrotron radiation and modeling*. 2010, Germany: Springer.
192. Wang, Z., et al., *Residual stress mapping in Inconel 625 fabricated through additive manufacturing: Method for neutron diffraction measurements to validate thermomechanical model predictions.* Materials & Design, 2017. **113**: p. 169-177.
193. Körner, C., M. Markl, and J.A. Koepf, *Modeling and Simulation of Microstructure Evolution for Additive Manufacturing of Metals: A Critical Review.* Metallurgical and Materials Transactions A, 2020. **51**(10): p. 4970-4983.
194. Yap, C.Y., et al., *Review of selective laser melting: Materials and applications.* Applied physics reviews, 2015. **2**(4): p. 041101.
195. Minneci, R., Ellis, D., Chen, Y., An, Ke., Lass, E., Bunn, J., Gradl, P., Choo, H., Rawn, C., *Investigation of Deformation Mechanisms of L-PBF GRCop-84 with In-situ Neutron Diffraction.* Manuscript Title, 2020.
196. Sochalski-Kolbus, L.M., et al., *Comparison of Residual Stresses in Inconel 718 Simple Parts Made by Electron Beam Melting and Direct Laser Metal Sintering.* Metallurgical and Materials Transactions A, 2015. **46**(3): p. 1419-1432.
197. Chakoumakos, B.C., et al., *Diffraction at the HFIR.* Neutron News, 2008. **19**(2): p. 14-17.
198. Cornwell, P., et al., *Current capabilities of the residual stress diffractometer at the high flux isotope reactor.* Review of Scientific Instruments, 2018. **89**(9): p. 092804.
199. Spooner, S. and X.-L. Wang, *Diffraction peak displacement in residual stress samples due to partial burial of the sampling volume.* Journal of applied crystallography, 1997. **30**(4): p. 449-455.
200. Wang, X.-L., S. Spooner, and C. Hubbard, *Theory of the peak shift anomaly due to partial burial of the sampling volume in neutron diffraction residual stress measurements.* Journal of applied crystallography, 1998. **31**(1): p. 52-59.
201. Wu, A.S., et al., *An experimental investigation into additive manufacturing-induced residual stresses in 316L stainless steel.* Metallurgical and Materials Transactions A, 2014. **45**(13): p. 6260-6270.
202. Knowles, C., T. Becker, and R. Tait, *Residual stress measurements and structural integrity implications for selective laser melted Ti-6Al-4V.* South African Journal of Industrial Engineering, 2012. **23**(3): p. 119-129.
203. Edwards, P. and M. Ramulu, *Fatigue performance evaluation of selective laser melted Ti–6Al–4V.* Materials Science and Engineering: A, 2014. **598**: p. 327-337.

VITA

Robert Minneci was born in Clarksville, TN in July 1994. He received a Bachelor's degree in Materials Science and Engineering from the University of Tennessee, Knoxville in 2012. He was accepted as a graduate student afterwards under the advisement of Claudia Rawn. Robert's graduate work was supported by the Center for Material Processing, the National Science Foundation through an Industry-University Cooperative Research Center, the Manufacturing and Materials Joining Innovation Center, and the Graduate Opportunity program with the Neutron Scattering Division at the High Flux Isotope Reactor at Oak Ridge National Laboratory.